IVOCT Catheter Tracking and Targeted Drug Delivery using Magnetic Particle Imaging and Magnetic Particle Navigation

Vom Promotionsausschuss der
Technischen Universität Hamburg

zur Erlangung des akademischen Grades

Doktor-Ingenieur (Dr.-Ing.)

genehmigte Dissertation

von
Florian Griese

aus
Aachen

2020

Author's ORCID: http://orcid.org/0000-0003-3309-9783
DOI: https://doi.org/10.15480/882.3230

1. Gutachter: Prof. Dr.-Ing. Tobias Knopp
2. Gutachter: Prof. Dr.-Ing. Alexander Schlaefer
Tag der mündlichen Prüfung: 17.12.2020

Abstract

This thesis studies application scenarios for the medical imaging modality Magnetic Particle Imaging (MPI), especially in the field of device tracking and targeted drug delivery. MPI visualizes the quantitative distribution of magnetic nanoparticles by using static and oscillating magnetic fields. It further provides a high sensitivity combined with a high spatial and temporal resolution. Due to these qualities, MPI offers auspicious potential for preclinical and clinical applications, such as angiography, cell tracking, device tracking or magnetic navigation. Despite this, MPI has not yet made it out of the research community into a broader field of applications. A unique application scenario, where MPI can exploit of its unquestionable advantages as a highly sensitive, magnetic field-based, radiation-free modality has yet to be found.

MPI has the great advantage that it resolves only the magnetic nanoparticles without any background signal. However, for medical applications, the location of the particles in context of the anatomical structures is highly beneficial. Therefore, MPI images are commonly registered with images providing anatomical information, such as images acquired by Magnetic Resonance Imaging (MRI) or Computer Tomography (CT). Based on current state of development the MRI or CT measurements are performed before the MPI measurements. The imaged subject, such as a patient or an animal, is then transferred from one modality to the other. In order to align the two acquired datasets correctly, fiducial markers visible in both imaging modalities are necessary. They provide a reference for both coordinate systems. The handling and workflow of these steps can be quite challenging and time-consuming, especially in the context of preclinical research with living animals.

The first part of this work deals with the development of improved fiducial markers, the simplification of the workflow, and the image registration process in order to support the implementation of preclinical studies. Usually, the fiducial markers consist of liquid magnetic nanoparticles inside glass capillaries. The liquid condition of the fiducials has several disadvantages as the water component often evaporates due to imperfect sealing of the capillaries or contamination with bacteria. To overcome such issues, solid, long-lasting fiducial markers based on silicone and immobilized nanoparticles within a 3D printed fixation are presented in this work. As a further step, a robot-supported mouse bed has been constructed to precisely position the mouse bed inside the MPI scanner. It enables a reproducibility of the desired target position, if the mouse bed has to be moved

in or out of the scanner due to complications with the living animal. As the nanoparticles-based fiducials can sometimes interfere with the actual measurement, especially at low particle concentrations, the fiducials can be removed after the initial measurement. In the context of an automatic registration between MRI and MPI images, the position of the fiducial markers have to be precisely determined within the MPI field of view (FoV). Hence, a segmentation algorithm using subpixel strategies is developed to determine the fiducials positions with submillimeter accuracy. The MRI images can be loaded into an MPI online reconstruction framework to align both modalities before the MPI experiment.

In the second part of this work, MPI is applied for visualizing medical instruments, in particular for tracking intravascular optical coherence tomography (IVOCT) catheters. IVOCT is an optical imaging modality and uses the reflection of light to visualize anatomical structures in 3D. For IVOCT, the optical fiber is assembled inside a catheter. This catheter is rotated and pulled back by a proximal actuator. The 3D vessel volume reconstruction is based on the known rotation and pullback velocity. However, the actual position and rotation of the catheter within the global patient coordinate system is not known by IVOCT itself. This can lead to reconstruction artifacts. Thus, the IVOCT image reconstruction highly benefits from a second imaging modality that provides the 4D trajectory of the catheter in the global patient coordinate system. In this work, the catheter tip has been marked with a visible MPI marker to track its 3D position precisely in real-time. This combination enables the reconstruction to compensate for bending and heart beat artifacts. The artifacts are simulated with different pullback profiles to validate the potential of this method.

In the third part of this work, MPI is combined with Magnetic Particle Navigation (MPN) where large particles can be navigated via magnetic force. The combined method of Magnetic Particle Imaging and Magnetic Particle Navigation (MPIN) is investigated in the context of treating ischemic stroke. An ischemic stroke occurs when, for example, a carotid artery is blocked by a blood clot. Such an occlusion can be difficult to dissolve using an injected thrombolytic medication, because the flow is mainly through the unblocked branch of the bifurcation. As a solution, functionalized magnetic particles could be navigated by magnetic force towards the blocked vessel branch and could help to dissolve the blood clot or even to reduce the medication dose. The potential of MPIN is studied in flow experiments with artificial bifurcation phantoms. The injected particles are then navigated towards the stenosis, while their accumulation is imaged. The quasi-simultaneous navigation and imaging is successfully shown for flow velocities of up to $108.2\,\mathrm{mm\,s^{-1}}$ for a 100% blocked vessel. The flow velocities within the carotid arteries range from $46\,\mathrm{mm\,s^{-1}}$ to $268\,\mathrm{mm\,s^{-1}}$. Therefore, MPIN shows the potential to implement targeted drug delivery in clinical applications.

Besides the concentration, MPI is also capable of imaging the viscosity and temperature of particles as additional MPI contrasts. In the fourth part of this work, a novel

orientation MPI contrast is analyzed which is based on the shape anisotropy of particles and their energetically preferred axis called the easy-axis. It is demonstrated that this easy-axis aligned MPI contrast can determine the easy-axis orientation of immobilized particles. For this contrast magnetic particles are immobilized within a static homogeneous magnetic field to fixate and align the easy-axis of the particles. This novel MPI contrast has great potential for determining the pose and orientation of magnetic micro devices or the rotation orientation of an IVOCT catheter.

The research results of all four application scenarios show the potential to establish MPI as a part of the medical toolbox. In short, a submillimeter-accurate localization method is developed to identify fiducial markers more precisely for the registration of MRI and MPI volumes. With this method, an IVOCT catheter is tracked in 3D over time for bimodal imaging of IVOCT and MPI. Further, the method of Magnetic Particle Imaging and Magnetic Particle Navigation is used to navigate magnetic particles through a bifurcation within a vascular flow. Finally, the novel easy-axis aligned MPI contrast is used to determine the easy-axis orientation of samples.

Kurzfassung

Diese Arbeit beschäftigt sich mit Anwendungsszenarien für die medizinische Bildgebungsmodalität Magnetic-Particle-Imaging (MPI), insbesondere im Bereich des Instrumenten-Tracking und der gezielten Medikamentenabgabe. MPI visualisiert die quantitative Verteilung von magnetischen Nanopartikeln mit Hilfe statischer und oszillierender Magnetfelder. MPI bietet zusätzlich eine hohe Sensitivität kombiniert mit einer hohen räumlichen und zeitlichen Auflösung. Aufgrund dieser Eigenschaften hat MPI ein großes Potenzial für präklinische und klinische Anwendungen, wie z. B. Angiographie, Zell-Tracking, Instrumenten-Tracking oder magnetische Navigation. Trotzdem hat sich MPI noch nicht aus dem Forschungsumfeld heraus in ein breiteres Anwendungsfeld entwickelt. Ein vielversprechendes Anwendungsszenario, bei dem die Vorteile von MPI als hochempfindliche, magnetfeldbasierte und strahlungsfreie Modalität genutzen werden können, muss noch gefunden werden.

MPI hat den weiteren Vorteil, dass es nur die magnetischen Nanopartikel ohne Hintergrundsignal darstellt. Für medizinische Applikationen ist jedoch oftmals die Lokalisierung der Partikel im Kontext von anatomischen Strukturen relevant. Daher werden die MPI-Bilder z. B. mit Bildern der Magnetresonanztomographie (MRT) oder der Computertomographie (CT) registriert, weil diese anatomische Informationen liefern. Da MRT- oder CT-Messungen vor der MPI-Messung durchgeführt werden, wird das abzubildende Objekt, wie z. B. ein Patient oder ein Tier, von einer Modalität zur anderen gebracht werden. Um die beiden erfassten Datensätze korrekt auszurichten, sind sogenannte Fiducial-Marker notwendig. Diese sind in beiden Bildgebungsmodalitäten sichtbar und bilden eine Referenz für beide Koordinatensysteme. Die Handhabung und der Arbeitsablauf dieses Prozederes kann herausfordernd und zeitaufwendig sein, insbesondere in der präklinischen Forschung mit lebenden Tieren.

Der erste Teil dieser Arbeit befasst sich mit der Entwicklung verbesserter Fiducial-Marker, der Vereinfachung des Arbeitsablaufs und der Unterstützung der Bildregistrierung für die Durchführung von präklinischen Studien. In der Regel sind die Fiducial-Marker flüssige magnetische Nanopartikel. Der flüssige Zustand der Fiducial-Marker hat mehrere Nachteile, da die Wasserkomponente aufgrund unvollständiger Abdichtung oft verdampft oder es zu Kontaminationen mit Bakterien kommt. Dies verhindert eine Wiederverwendung der Fiducial-Marker. Deshalb werden in dieser Arbeit solide, langlebige Fiducial-Marker auf der Basis von Silikon und immobilisierten Nanopartikeln vorge-

stellt. In einem weiteren Schritt wurde ein robotergestütztes Mausbett konstruiert, um das Mausbett innerhalb des MPI-Scanners präzise zu positionieren. Dies ermöglicht eine Reproduzierbarkeit der gewünschten Zielpositionierung, wenn das Mausbett aufgrund von Komplikationen beim lebenden Tier aus dem Scanner heraus- oder hereingefahren werden muss. Zusätzlich können dann die Fiducial-Marker nach der anfänglichen Messung entfernt werden, da die Fiducial-Marker die eigentliche Messung manchmal stören können. Dies kann insbesondere bei niedrigen Partikelkonzentrationen im Experiment der Fall sein. Im Rahmen einer automatischen Registrierung von MRT- und MPI-Bildern muss die Position der Fiducial-Marker genau innerhalb des MPI-Sichtfeldes (FoV) bestimmt werden. Daher ist in dieser Arbeit ein Segmentierungsalgorithmus entwickelt worden, der die Positionen der Fiducial-Marker mit Submillimeter-Genauigkeit bestimmt. Zur Versuchsplanung können die MRT-Bilder in eine Rekonstruktionssoftware geladen werden, die die Bilddaten beider Modalitäten vor und während des MPI-Experimentes in Echtzeit registriert.

Im zweiten Teil dieser Arbeit wird MPI zur Visualisierung und zur Verfolgung von medizinischen Instrumenten genutzt. Dabei wird insbesondere das Verfolgen von Kathetern für die intravaskuläre optische Kohärenztomographie (IVOCT) untersucht. IVOCT ist eine optische Bildgebungsmodalität und nutzt die Reflexion von Licht, um anatomische Strukturen in 3D zu visualisieren. Bei IVOCT wird eine optische Faser in einem Katheter montiert. Dieser Katheter wird dann durch einen proximalen Aktuator gedreht und zurückgezogen. Die 3D-Volumenrekonstruktion basiert auf der bekannten Rotation und dem bekannten Rückzug des Katheters. Die tatsächliche Position und Rotation des Katheters innerhalb des globalen Patienten-Koordinatensystems ist bei der IVOCT selbst aber nicht bekannt. Dies kann zu Artefakten in der Rekonstruktion führen. Daher profitiert die IVOCT-Bildrekonstruktion in hohem Maße von einer zweiten Bildgebungsmodalität, die die 4D-Trajektorie des Katheters in einem globalen Patientenkoordinatensystem liefert. In dieser Arbeit wird die Spitze des Katheters mit einem sichtbaren MPI-Marker markiert, um seine 3D-Position in Echtzeit präzise verfolgen zu können. Diese Kombination ermöglicht es, Biege- und Herzschlagartefakte in der IVOCT Rekonstruktion zu kompensieren. Diese Artefakte werden mit verschiedenen Rückzugsprofilen simuliert, um das Potenzial dieser Methode zu validieren.

Im dritten Teil dieser Arbeit wird MPI mit der Methode Magnetic-Particle-Navigation (MPN) kombiniert, bei der große Partikel mittels Magnetkraft navigiert werden. Die kombinierte Methode von Magnetic-Particle-Imaging und Magnetic-Particle-Navigation (MPIN) wird im Zusammenhang mit der Behandlung des ischämischen Schlaganfalls untersucht. Ein ischämischer Schlaganfall tritt auf, wenn z. B. die innere Halsschlagader durch ein Blutgerinnsel blockiert ist. Ein solcher Verschluss kann mit einem injizierten thrombolytischen Medikament schwer aufgelöst werden, da der Blutfluss hauptsächlich durch die nicht-blockierte Verzweigung erfolgt. Als eine möglische Lösung bie-

ten sich funktionalisierte magnetische Partikel an, die durch die magnetische Kraft des MPI-Scanners zum blockierten Gefäß durch die Verzweigung navigiert werden können. Dadurch könnte das Blutgerinnsel leichter aufgelöst werden und die nötige Medikamentendosis reduziert werden. Das Potenzial von MPIN wird in Strömungsexperimenten mit künstlichen Verzweigungsphantomen untersucht. Die injizierten Partikel werden dann in Richtung der Gefäßverengung navigiert, während die Verteilung der magnetischen Partikel bildlich dargestellt wird. Diese quasi-simultane Navigation und Bildgebung wird erfolgreich für Flussgeschwindigkeiten von bis zu $108.2\,\mathrm{mm\,s^{-1}}$ für ein 100%-ig blockiertes Gefäß gezeigt. Die Strömungsgeschwindigkeiten innerhalb der inneren Halsschlagadern reichen von $46\,\mathrm{mm\,s^{-1}}$ bis $268\,\mathrm{mm\,s^{-1}}$. Damit stellt MPIN eine vielversprechende Methode für Targeted-Drug-Delivery-Anwendungen im klinischen Bereich dar.

Neben der Konzentration kann MPI auch die Viskosität und Temperatur von Partikeln als zusätzliche MPI-Kontraste abzubilden. Im vierten Teil dieser Arbeit wird ein neuartiger Easy-Axis-MPI-Kontrast analysiert, der auf der Formanisotropie der Partikel und ihrer energetisch bevorzugten Achse, der sogenannten Easy-Axis, basiert. Es wird gezeigt, dass der Easy-Axis-MPI-Kontrast verwendet werden kann, um die Orientierung von immobilisierten Partikeln zu bestimmen. Für diesen Kontrast werden magnetische Partikel in einem statischen homogenen Magnetfeld immobilisiert, um die Vorzugsorientierung der Easy-Axis zu fixieren. Dieser MPI-Kontrast hat großes Potenzial die Position und Orientierung von medizinischen Mikroinstrumenten oder die Drehungsorientierung eines IVOCT-Katheters zu bestimmen.

Die Forschungsergebnisse aller vier Anwendungsszenarien zeigen das Potenzial, MPI als Teil der medizinischen Toolbox im Kontext klinischer Anwendungen zu etablieren. In dieser Arbeit wird eine submillimetergenaue Lokalisierungsmethode entwickelt, um Markierungen für die Registrierung von MRT- und MPI-Volumen zu identifizieren. Mit dieser Methode wird auch ein IVOCT-Katheter in 3D über die Zeit bimodal mit MPI verfolgt. Des Weiteren wird MPIN verwendet, um magnetische Partikel durch eine Verzweigung zu navigieren. Zuletzt wird die Easy-Axis-Orientierung von Proben mit dem neuartigen Easy-Axis-MPI-Kontrast bestimmt.

Acronyms

ADC Analog-to-Digital Converter

AE Absolute Error

BBB Brain-Blood Barrier

CNR Contrast-to-Noise Ratio

CT Computed Tomography

DF Drive Field

DSA Digital Subtraction Angiography

EPR Enhanced Permeability and Retention effect

FF Focus Field

FFL Field Free Line

FFP Field Free Point

FWHM Full Width at Half Maximum

ICA Interna Carotis Artery

ICP Iterative Closest Point algorithm

IP Input Parameter

IP+LC Input Parameter and Lumen Center

IVOCT Intravascular Optical Coherence Tomography

LPS LipoPolySaccharides

MAE Mean Absolute Error

MCE MPI Centerline Estimation

MMT MPI Marker Tracking

MIP Maximum Intensity Projection

MPI Magnetic Particle Imaging

MPIN Magnetic Particle Imaging and Magnetic Particle Navigation

MPIO Micron-sized Particle of Iron Oxide

MPN Magnetic Particle Navigation

MPS Magnetic Particle Spectrometer

MRI Magnetic Resonance Imaging

mMRI Molecular Magnetic Resonance Imaging

NURD Non-Uniform Rotational Distortions

OCT Optical Coherence Tomography

PNS Peripheral Nerve Simulation

QM Quantum Mechanics

RE Relative Error

ROI Region Of Interest

SAR Specific Absorption Rate

SD Standard Deviation

SL StereoLithoraphy

SLS Selective Laser Sintering

SNR Signal-to-Noise Ratio

SPION SuperParamagnetic Iron Oxide Nanoparticles

TDD Targeted Drug Delivery

TEM Transmission Electron Microscopy

tPA Tissue Plasminogen Activator

UI User Interface

VA Vertebral Arteries

VCAM-1 Vascular Cell Adhesion Molecule 1

Symbols

List of Symbols

α_{e}	Estimated angle
α_{d}	Angle of the delta sample
α_{F}	Flipping angle
γ_{gmr}	Gyromagnetic ratio $\mathrm{Hz\,T^{-1}}$
$\boldsymbol{\delta}_k$	Localization error
ΔL	Difference between reference and measurement arm
ϵ	Convergence criterion
ϕ	Ratio repetition time to sampling time interval
η	Dynamic viscosity of liquids with particles
η_{water}	Dynamic viscosity of water
Θ	Signal to noise ratio
Θ_{T}	Relative threshold
λ_{OCT}	Wavelength of OCT
λ	Regularization parameter
$\tilde{\lambda}$	Regularization term
λ_0	Initial regularization parameter
$\boldsymbol{\mu}_{\mathrm{nmm}}$	Nuclear magnetic moment
μ_0	Vacuum permeability $\mu_0 = 4\pi \cdot 10^{-7}\ \mathrm{H\,m^{-1}}$
ξ_{r}	Ratio of magnetic energy to thermal energy
ξ	Magnetophoretic mobility
ρ_{p}	Density of the particles
ρ_{water}	Density of water
τ_{se}	Time period of spin echo
τ_{NB}	Combined Neel/Brownian relaxation time
τ_{N}	Neel relaxation time
τ_{B}	Brownian relaxation time
χ_{v}	Volume magnetic susceptibility χ_v
ω_0	Larmor frequency
A_{e}	Excitation amplitude
$\boldsymbol{A}$	Excitation amplitude in 3D

b_{w}	First fitting parameter for w
$\boldsymbol{B}$	Magnetic flux
B	Magnetic flux vector length
B_0	Magnetic flux vector length in MRI
c_{w}	Second fitting parameter for w
$\boldsymbol{c}$	Particle concentration vector
$\boldsymbol{c}$	Center of mass algorithm
c_l	Speed of light
$\boldsymbol{c}_{\mathrm{c}}$	Current center position
C	Number of receive channels
d_{c}	Magnetic core diameter
d_{h}	Hydrodynamic diameter
d_{CW}	Distance of catheter to vessel wall
$E_{\mathrm{r}}(t)$	Reference beam
$E_{\mathrm{s}}(t)$	Measurement beam
f_{cost}	Cost function
f_{e}	Excitation frequency
f_{b}	Base frequency
f_{s}	Sampling frequency
f_{temporal}	Temporal resolution of the MPI scanner
f_{rot}	Frequency of IVOCT catheter rotation
f_{OCT}	Frequency of OCT system
$F_{\mathrm{m},y}$	Magnetic force in y-direction
$F_{\mathrm{d},y}$	Drag force in y-direction
$F_{\mathrm{b},z}$	Buoyancy force in z-direction
$F_{\mathrm{g},z}$	Gravitation force in z-direction
g	Gravitation
$\boldsymbol{G}_{\boldsymbol{r}}$	Gradient field
G_f	Frequency gradient field
G_p	Phase gradient field
H_{e}	Excitation field
$\boldsymbol{H}_{\mathrm{L}}$	Lissajous based excitation field
$\boldsymbol{H}_{\mathrm{s}}$	Static gradient field
$\boldsymbol{H}$	Magnetic field strength
$\boldsymbol{H}_{\mathrm{FF}}$	Focus field
$\hbar$	Planck's constant $\hbar = 1.05 \times 10^{-34}\,\mathrm{J\,s}$
I	Dynamic MPI experiment
I_{o}	Intensity output of OCT
I_{q}	Quantum number

$_I^{\text{segBin}}$	Segmented dynamic MPI experiment
$\boldsymbol{I}_{\text{S}}$	Angular momentum or nuclear spin
k_{f}	Frequency component index
K	Magnetic anisotropy energy density
k_{B}	Boltzmann constant $k_B = 1.38064852 \cdot 10^{-23}$ J K^{-1}
K_{f}	Number of frequency components
K_{M}	Number of markers
l_{FoV}	FoV length of OCT
$\mathcal{L}$	Langevin function
L_{t}	Number of identified regions
m_{p}	Mass of particle
$\bar{\boldsymbol{m}}$	Mean magnetic moment
M	Magnetization
$\boldsymbol{M}$	Vectorial magnetization
M_{S}	Saturation magnetization
n_{blood}	Refraction index of blood
n_{water}	Refraction index of water
n_{iter}	Kaczmarz iterations
N_{p}	Number of particles
N_{L}	Lissajous density number
N_{S}	Number of system matrices
N_{G}	Number of grid points
N_{rot}	Number of A-scans of IVOCT catheter rotation
N_{nc}	Number of navigation cycles
N_{ic}	Number of imaging cycles
N_{c}	Number of Lissajous cycles / Number of frames
$\boldsymbol{p}_i$	Marker positions
$\boldsymbol{p}_{\text{rob}}$	Robot position
r_{mean}	Mean radius
r_{c}	Magnetic core radius
r_{h}	Hydrodynamic radius
r_{R}	Rotation radius
$\boldsymbol{r}$	Position vector with x,y and z compoments
$\boldsymbol{r}_k$	True marker position
$\boldsymbol{R}$	Rotation matrix
s_{delta}	Delta sample
s_i	Sample location with $i = 1, 2, 3$
s_{rot}	Distance of IVOCT catheter in one rotation
$\boldsymbol{S}$	Discretized system matrix

t	Time
$\boldsymbol{t}$	Translation vector
$\boldsymbol{t}_{\text{target}}$	Target position
T	Temperature in kelvin
T^t	Turbidity
T_{B}	Blocking temperature in kelvin
T_{L}	Repetition time Lissajous cycle
T_{rot}	Time of IVOCT catheter rotation
T_{s}	Temporal delay for switching
T_1	T_1 relaxation time
T_2	T_2 relaxation time
T_2^*	Effective T_2* relaxation time
T_{R}	Repetition time
T_{E}	Echo time
$u(t)$	Voltage signal in time-domain
$\hat{u}_{k_f}$	Voltage signal in frequency-domain
$\boldsymbol{u}$	Discretized frequency components
v_{pull}	Pullback velocity of IVOCT catheter
V_{c}	Magnetic core volume
V_{h}	Hydrodynamic particle volume
V_{p}	Particle volume
w	Peridic function

Acknowledgments

First and foremost I would like to thank all the amazing people who supported and inspired me during my journey over the last years. I deeply appreciate your time and effort. I also express my acknowledgement and sincere thanks to you!

Furthermore, I would like to thank especially Prof. Tobias Knopp, who gave me the opportunity to work in this exciting and innovative field. Your door was always open and you always took the time to help us find solutions for all kinds of scientific problems. You set the foundation for a caring, supportive, team-oriented and friendly work environment. I'm also grateful for the opportunities to learn techniques and methods beyond my projects.

I would like to thank Martin for the critical suggestions, the great help and the insightful, vivid discussions in the canteen. My sincere thanks also go to Nadine and Matthias G. for their open ears and extensive support in all matters of scientific work.

A big thanks also goes to my colleagues Patryk, Flo T., Marija, Franzi, Fynn, Mirco, Lina, Fabian, Flo S., Kolja and Ivo from the Institute of Biomedical Imaging, who always helped me with advice and deeds concerning MPS, mathematical problems, MPI scanner, measuring, construction, 3D printing, deep learning and paper writing. My sincere thanks also goes to Patryk for his infinite helpfulness. Additionally, I would like to thank Ivo for the pleasant indoor climate, both on the temperature and interpersonal level. It was a great time with you all!

Further, Annemarie deserves many thanks for providing us with cookies, cake and fruits during work. You had a great contribution in creating a nice and friendly work environment. The lavish birthday cards, the great summer and winter activities were always a highlight.

I greatly appreciate the support of Tobias M., Michael and Julia for their advice and constant technical assistance for the MPI scanner. Additionally, I would like to thank Dr. Peter Ludewig very much for the neurological input and the great enthusiasm for MPI

from the medical side.

A great thank you goes out to Matthias W. and Christian who helped me review the work and provided great council in MPI. I'm grateful for our friendship! Further, I would like to thank Daniel P., Ryan and all the others for proofreading my thesis. Thank you most appreciated!

I also want to express my gratitude to my parents Anne and Thomas and to my sister Marie for their constant support and encouragement.

Foremost, I owe my deepest sense of gratitude to my loving family Anna and Johannes. Without them this work would be meaningless. I'm tremendously thankful for your love, support and sacrifices during this time. I'm glad that you motivated and encouraged me during difficult times. Thank you for everything!

Contents

1. Introduction

Contents

1.1. Background and motivation

In modern medicine, a patient can often only be diagnosed with the help of medical imaging. Medical imaging is the process of visualizing the interior of the human body. Over the course of time, several medical imaging modalities have been developed that rely on different physical principles and are designed for different applications. The applications range from imaging bone fractures with X-ray [1] to the localization of brain tumors with magnetic resonance imaging (MRI) [2]. Usually, each modality features a core scope of applications where its full potential can be leveraged. In the examples above, X-ray is a great tool for emergency diagnostics and MRI provides an excellent soft tissue contrast to distinguish between normal brain tissue and tumor [3]. Overall, medical imaging plays an important role for the diagnosis, monitoring and treatment of patients [4, 5]. It enables the detection of cancer in early stages by screening with medical imaging technologies [6]. However, for special medical questions it is essential to combine the information of multiple imaging modalities. The imaging modalities X-ray, computed tomography (CT) [7], MRI, ultrasound (US) [8, 3] and optical coherence tomography (OCT) [9] are well established in the field of morphological imaging. All modalities make use of either sound waves or a specific range of the electro-magnetic spectrum to directly receive structural information about biological tissue.

The second category of medical imaging methods are functional imaging modalities. Typically, they are designed to image dynamic biological processes within the human body. Therefore, these functional modalities often rely on inhuman substances known as tracers, which are injected into the human body. Consequently, the tracers play the key role in visualizing biological processes with functional medical imaging [4]. However, also morphological imaging modalities such as digital subtraction angiography (DSA) [3] can make use of tracers. Dedicated functional imaging methods are mainly sensitive to

tracers as they are designed to only interact with their corresponding tracer, which leads to a very good contrast-to-noise ratio (CNR). Positron emission tomography (PET) [10] and single-photon emission computed tomography (SPECT) [11] are both using radioactive tracers. PET detects two gamma rays that have been released in opposite directions by an annihilation of a positron and an electron. The positron has been set free in the radioactive decay of an radioactive isotope. In SPECT, the gamma rays are directly detected, as tracers emit gamma rays from the beginning. These radioactive tracers can be coupled with proteins or other molecules to image dynamic interaction within the human body. Besides exposing radioactive radiation to the human body, PET and SPECT are linked to an extensive effort in logistics and cost, while their flexibility is limited. The radioactive isotopes usually have a short half-life time of a few hours and have to be produced nearby or on site in a cyclotron. Therefore, the timing of the planned injection has to be accurate and the possibilities of long-term measurements are limited.

In MRI, it is also possible to use magnetic tracers based on iron-oxides for imaging functional processes [12, 13, 14]. However, as MRI can have morphological and functional imaging abilities, the image contrast for magnetic particles is not very high. The magnetic particles change their relaxation times of the hydrogen protons in their vicinity and induce an negative contrast. Because the magnetic particles are not measured directly and only their influence on the relaxation properties of hydrogen is measured, the MRI background signal is tissue dependent and the quantification of the particle signal needs elaborate calibration.

In 2005, Gleich and Weizenecker presented a novel imaging modality called Magnetic Particle Imaging (MPI) specifically tailored to the use of magnetic nanoparticles [15]. Based on static and oscillating magnetic fields, MPI images only the distribution of the nanoparticles. The imaged distribution of particles is quantitative and linear in terms of signal intensity to the concentration of the particles [16]. As a tomographic method, MPI images the concentration of the nanoparticles within a volume as 3D data [17, 18]. Since MPI is magnetic field-based, its penetration depth depends on the magnetic field and is not limited by tissue as known from for optical methods [19]. The nanoparticles are long-term stable, biocompatible, and can be dissolved in the liver [20]. The applied magnetic fields can be operated safely in terms of peripheral nerve simulation (PNS) [21] and specific absorption rate (SAR) [22]. MPI provides a high sensitivity with a high temporal resolution of up to $46\,\mathrm{Hz}$ [23]. The theoretical potential of the spatial resolution is not fully utilized yet and is located within the millimeter range [24], but also submillimeter resolutions for smaller bore sizes have been reported [25]. MPI scanner designs are divided into two main concepts, the field free point (FFP) [26, 27, 15] and the field free line (FFL) [28] scanners, each with a different focus in terms of imaging characteristics. Several techniques including focus fields (FF) [29, 30] have been developed to increase the field of view (FoV) as upscaling of small scanners is a challenging process. The nanopar-

ticles can be coupled with other molecules to enable functional imaging [31]. MPI is even capable of determining additional physical parameters of the particles, such as their temperature [32, 33, 34, 35, 36], viscosity [37, 38], mobilization state [39], particle diameter [40], or particle type [41]. These approaches fall into the category of multi-contrast MPI and promise development of interesting future applications.

Up to now, potential applications of MPI have been studied in several medical application fields with the aim to find use cases with a diagnostic advantage for the patient and to become a valuable tool in the medical imaging toolbox. Some of the most promising medical applications have been investigated in the following fields:

- **Angiography:** In 2009, the beating heart of a mouse was first imaged with MPI in real time [23]. Since then, the suitability of blood pool tracers [42, 43, 44] and the half-life time of tracers within blood [45] has been investigated with MPI. In mice experiments, MPI has been investigated to determine the perfusion time of both brain hemispheres to detect acute strokes [46].

- **Hyperthermia:** MPI has been successfully utilized to heat magnetic particles for the purpose of cancer coagulation [47, 48, 49, 50, 51].

- **Cell tracking:** It was shown that stem cells can be labeled with magnetic particles and that their location and their quantitative concentration can be determined with MPI [52, 53, 54, 55].

- **Cancer and tumor detection:** MPI has been used to detect the location of cancer and tumor cells in mice experiments [56, 57, 31].

- **Device visualization and manipulation:** Magnetic particles have been used to coat catheters and to track their position and orientation with MPI [58, 59]. The catheters direction has even been manipulated by magnetic fields [60]. Based on multi-contrast approaches, MPI has been able to discern between blood pool tracer and balloon catheter as the tracer is used to find the stenosis and a coated balloon catheter is used to clear the stenosis [61, 62]. Further, MPI has been utilized to guide the deployment of stents [63].

- **Magnetic Navigation:** MPI has been used to navigate magnetic devices and small magnetic micro devices by rotating magnetic fields in a preclinical [64, 65, 66, 67] and clinical-sized setup [68]. Further, magnetic particles can be moved using MPI for the purpose of targeted drug delivery (TDD) [P1, 69, 70, 71, 72].

This work focuses on the application of MPI in the context of medical intervention and magnetic navigation. Medical intervention is referred to as the act of interfering with the human body with the intent of modifying the outcome of a disease. An intervention is

usually performed with medical instruments like scalpels, laparoscopic devices, stents, catheters and other medical devices. Catheters and stents are very important in the treatment of coronary angioplasty [73, 74], and percutaneous coronary interventions present the most effective technique to reduce the mortality rate of patients with acute myocardial infarction [75, 76]. For the guidance of the catheter, DSA is usually used [73]. However, DSA provides only 2D projection images and exposes radioactive radiation to the patient.

In the field of medical interventions, MPI as an alternative to DSA has already been operated together with catheters [58, 59], balloon catheters [61, 62] and stents [63]. This work combines MPI with an intravascular optical coherence tomography catheter (IVOCT). IVOCT is a special assembly of the OCT fibre. The optical fibre is placed inside a catheter, which can be rotated and pulled back inside a plastic shielding. With known rotation and pullback velocity, an IVOCT volume image is reconstructed. The main area of application is cardiovascular imaging, where the structure of plaques can be analyzed and characterized [77]. The rotation and pullback actuators are located outside the patient in an extra device, and their peripherical transmissions through the flexible catheter can lead to several artifacts. These motion artifacts, due to catheter bending and arterial vasomotion, can influence the quantification of plaques. To compensate the unknown motion of the catheter, the catheters position relative to the patients coordinate system has to be known in real-time. In this thesis, due to its real-time imaging capabilities, MPI is investigated to be used to track the position of the catheter globally. With the resulting 3D trajectory over time, the IVOCT reconstruction can be improved in terms of bending artifacts. In the field of magnetic navigation, this work studies the use of MPI for

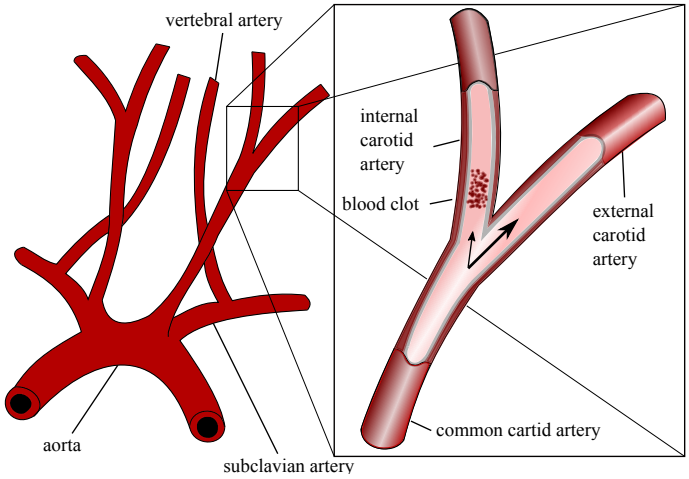

Figure 1.1.: Stenosis caused by a blood clot in internal carotid artery. Due to the blood clot, the blood flows mainly through the unblocked external carotid artery at the bifurcation.

TDD via magnetic particles. The treatment of ischemic stroke by dissolving blood clots acts as the main motivation. An ischemic stroke is usually caused by clotting blood that leads to a stenosis and an undersupply of oxygen-rich blood. The blockage of the blood vessel has the effect that medications injected into the blood stream are not able to reach

the blood clot, because the blood flows mainly through the unblocked vessel (see Fig. 1.1). This work investigates the potential to image and navigate the magnetic particles towards the stenosis at a bifurcation.

Further, this work studies a novel easy-axis aligned MPI contrast, which uses the shape anisotropy of the particles and their energetically preferred axis called easy-axis. Within immobilized particles the orientation of the easy-axis of particles is fixated and then the orientation of the particles can be determined with the easy-axis aligned MPI contrast. In order to prepare the alignment of all easy-axes, the magnetic particles are immobilized within a static homogeneous magnetic field. This novel MPI contrast shows great potential to precisely determine the rotation orientation of a previously described IVOCT catheter because the rotation is affected by non-uniform rotational distortions artifacts. Additionally, the pose and orientation of magnetic micro devices can be estimated with immobilized particle markers using the easy-axis aligned MPI contrast.

1.2. Structure of this work

The presented work is divided into eight chapters. After the introduction given in this chapter, the fundamental physical principles of MPI are explained in chapter 2. The properties of the magnetic particles used for MPI are described in the context of oscillating magnetic fields. In order to create a basic understanding of an MPI scanner, the theoretical aspects of signal and spatial encoding are derived. Further, the reconstruction process and more sophisticated MPI methods, such as multi-contrast MPI imaging, are introduced. At the end of this chapter, the magnetic force on the particles induced by the scanners' magnetic gradient field is outlined in relation to the magnetic particles.
In chapter 3, a method to determine the location of a small samples with submilimeter resolution is introduced. The algorithm uses a center of mass approach with a connected-component labeling.
In chapter 4, the concept of bimodal imaging with MRI and MPI is explained. The whole workflow of acquiring an MRI before the MPI measurement is presented in detail. This includes the use of novel fiducials, a precisely movable mouse bed and an extended online registration framework.
In chapter 5, the combination of MPI with IVOCT is introduced. The bimodal imaging results are investigated in terms of principle feasibility and artifact reduction.
Chapter 6 describes the method of imaging and navigating magnetic particles. In flow experiments, micro-sized magnetic particles are navigated towards a stenosis at a bifurcation. The accumulation of the particles at the stenosis is imaged via MPI.
Chapter 7 describes the novel orientation MPI contrast based on the aligned easy-axis of the particles. The easy-axis is immobilized with a homogeneous magnetic field. Afterwards, these properties are used to determine the orientation of the particles.

In chapter 8, the presented work is summarized and an outlook into further research possibilities is given.

1.3. Publications

The findings of the subvoxel algorithm for MPI have been published in a peer-reviewed journal [J1](first authorship). The algorithm determines the position of samples within the MPI FoV with submillimeter accuracy. The method is validated with single and multi markers by evaluating the systematical and statistical errors. Additionally, the temporal and spatial dependency of the systematic error is investigated.
The development of long-term stable fiducials, the robot based mouse adapter and the extended online reconstruction tool for the registration of MRI and MPI volumes have been published in a conference proceeding [P2].
The feasibility to combine MPI and IVOCT has been presented in a peer-reviewed journal [J2], with the article written in shared first authorship with S. Latus (Institute for Medical Technology, Hamburg University of Technology, Hamburg, Germany), and in two contributions to a conference [P3, C1]. Here, the angiography information of MPI are used to improve the IVOCT reconstruction. In a next step, the IVOCT catheter tip is tracked with MPI in 3D and real-time to compensate motion artifacts. The findings of this work are also published with S. Latus (Institute for Medical Technology, Hamburg University of Technology, Hamburg, Germany) in a peer-reviewed journal [J3](shared first authorship). In both peer-reviewed journals, S. Latus contributed greatly in the acquisition, reconstruction and post-processing of the IVOCT data, while the author of this thesis contributed mainly in the acquisition, reconstruction and post-processing of the MPI data.
The ability to image and navigate magnetic particles quasi-simultaneously with MPI has been published in a peer-reviewed journal [J4](first authorship) and has been presented at a conference [P1]. The method is validated in the context of ischemic stroke. The magnetic particles are navigated towards a stenosis of one branch of a bifurcation, while their distribution is imaged.

In addition, the author has published further MPI research findings, that are beyond the scope of this work. In multi-contrast experiments, the author has tested cobald embedded in Polylactide (PLA) as a catheter marker for MPI. The cobalt coated catheters could be discerned from other liquid blood pool tracer with corresponding concentration matching. The findings of this study are published in the proceedings of a conference [P4]. Furthermore, the author contributed in a conference submission that uses Deep Learning strategies to reduce the time effort to acquire MPI system functions [C2, C3]. Additionally, the author contributed to a conference submission that studies a moving table approach to increased the FoV of MPI by moving objects stepwise through the FoV [C4, C5, C6]. The author has been involved in the development of a human head MPI

scanner, which has been published in a peer-reviewed journal [C7, C8]. In the context of the human head MPI scanner, the author contributed to three conference submission that dealt with reconstruction [C9], perfusion parameter determination [C10] and stroke detection [C11]. Furthermore, the author participated in the development of Julia software packages for open access MPI data [C12], loading of MPI files [C13] and reconstruction of MPI data [C14].

2. Fundamentals of Magnetic Particle Imaging

Contents

Magnetic Particle Imaging is a tracer-based, quantitative imaging modality. Thus, it relies on the tracer to provide an image. In contrast to morphological imaging modalities, it resolves only the tracer with high contrast, but no other substances, such as tissue, organs, or bones. As a tracer, superparamagnetic particles are usually used, which are based on iron-oxides. MPI uses static and oscillating magnetic fields to image the distribution and concentration of the magnetic particles. By exploiting their non-linear magnetization the particles are excited with an oscillating magnetic field and their responding magnetization change is measured to determine the particle concentration. One way to achieve spatial

encoding is to saturate the particles by a static magnetic field in all positions in space except for one specific location. By receiving a responding magnetization change only from a specific location, the distribution of the particles can be determined within a volume.

2.1. Superparamagnetic particles

The image quality in MPI relies heavily on the performance of the magnetic particles [78]. The magnetic particles in MPI are typically superparamagnetic iron oxide nanoparticles (SPIONs), and magnetite (Fe_3O_4) is one example that is often used. To approach the behavior of magnetic particles in oscillating magnetic fields, we first consider the different types of magnetism in static magnetic fields. Therefore, we start with the magnetic properties of ferromagnetic particles. Ferromagnetic particles exhibit a spontaneous magnetization, and the magnetic moments of their atoms are aligned parallelly [79]. When ferromagnetic particles are exposed to an external magnetic field, they have a remaining magnetization called remanence when the external magnetic field is removed. The remanence becomes also evident in the hysteresis loop of ferromagnetic materials. For the hysteresis loop, an external magnetic field is increased until the magnetization reaches the saturation point. If the magnetic field strength is then reduced, the magnetization curve follows a different path back. When it reaches the magnetic field strength of zero, it has an offset to the starting magnetization, the remanence. When the magnetic field is decreased further in the opposite direction, the coercivity is reached by crossing the x-axis. The coercivity measures the ability of ferromagnetic materials to resist demagnetization when exposed to an external magnetic field. After the magnetization has reached the opposite saturation, the hysteresis loop is completed symmetrically, when the magnetic field is increased again. The hysteresis behavior of ferromagnetic materials shows a closed loop with an area inside (see Fig. 2.1a). Paramagnetic particles, on the other hand, show no

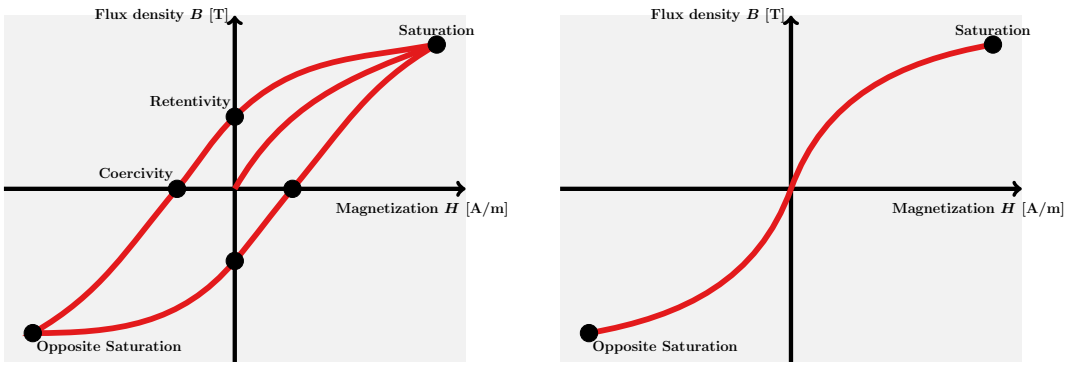

(a) (b)

Figure 2.1.: (a) Hysteresis behavior of ferromagnetic particles. (b) Hysteresis behavior of superparamagnetic particles.

remanence when a previously applied external magnetic field is removed. SPIONs with

single-domains behave like classical paramagnetic matter but with a very high macroscopic magnetic moment per particle [80](p.210). SPIONs also show no remanence or almost no remanence when a previously applied external magnetic field is removed [81]. In contrast to ferromagnetic materials, the magnetization curve of superparamagnetic materials has no area in the hysteresis loop and stays on the same track when an external magnetic field is increased and decreased. As shown in Fig. 2.1b, the particle magnetization has also a non-linear behavior.
Similar to paramagnetic particles on the atomic level, superparamagnetic particles align their macroscopic magnetic moment per particle when exposed to an external magnetic field. When the external magnetic field is removed, the magnetic moments of the nanoparticles orient themselves randomly again.

Superparamagnetism usually occurs in small nanoparticles with a single magnetic domain. Therefore, the nanoparticles need to have a magnetic core diameter below a threshold diameter of $d_{\text{thres}} < 50\,\text{nm}$, in which case the magnetocrystalline energy barrier is below the thermal energy at room temperature [78, 82, 83, 84]. Their thermal movement leads to unstable magnetization, which makes the particles act as single paramagnets [85].

The magnetic susceptibility of superparamagnetic nanoparticles is much larger than the one from paramagnets because they have only one magnetic domain with one large magnetic moment. The magnetic susceptibility is a dimensionless measure that determines how good a material can be magnetized within an external magnetic field. The magnetic susceptibility of magnetite Fe_30_4 is 70, which is relatively low compared to iron with $200\,000$ but relatively high compared to other iron oxides (hematite 0.0014). The magnetic susceptibility is frequency dependent but it is believed to be negligible for MRI with an excitation frequency in the MHz range [86] (p.825). Therefore, it is assumed to be insignificant for MPI with $25\,\text{kHz}$ as well.

To obtain its superparamagnetic behavior, the magnetic particles need to be below the Curie temperature T_C. The Curie temperature is a material-dependent threshold temperature at which ferromagnetic materials lose their spontanous magnetization and become paramagnetic. All iron oxides used in MPI have a Curie temperature far above the body temperature of $37\,^\circ\text{C}$ [87, 88]. Interestingly, gadolinium has a Curie temperature of $19\,^\circ\text{C}$ and thus cannot be used as an MPI contrast agent as it is used in MRI.
It is worth noting that ferromagnetic particles with larger diameters are also used as MPI tracer and their remanence is especially needed in hyperthermia applications [47, 48, 49, 50, 51]. An important characteristic for the MPI imaging process is the non-linear magnetization curve. The non-linear magnetization behavior, as seen in Fig. 2.1b, ensures that the particles respond with harmonics to the excitation frequency (usually $25\,\text{kHz}$). Particles with a linear magnetization curve would only response with the same frequency as the excitation frequency and, thus, their signal could not be distinguished from the excitation signal. The previous considerations refer to the behaviour in static magnetic fields.

The behaviour of magnetic nanoparticles in typical MPI fields is very complex and also depends on the frequency. Furthermore, the exact composition of the particles in terms of single core, multi-core, multi-domain and coating plays an important role. It is difficult to evaluate the suitability of nanoparticles as MPI tracers based on their magnetic properties in static magnetic fields. Therefore, the MPI suitability becomes usually only apparent in the signal response to oscillating magnetic fields.

2.1.1. Néel and Brownian relaxation

The magnetic moments of superparamagnetic particles have two possibilities to align themselves with an external magnetic field. As a first option, the magnetic moments can rotate internally, which is called Néel relaxation or Néel rotation. As a second option, the nanoparticles can rotate as a whole particle, which is called Brownian relaxation or Brownian rotation [89, 90]. In detail, superparamagnetic particles usually have a magnetic anisotropy in terms of their magnetic moment. It means that the magnetic moment points in two energetic preferred directions, which are antiparallel and only separated by an energy barrier. These directions are more stable and are often called easy-axis. With thermal fluctuation, the magnetic moment randomly switches between both orientations. The mean time it takes to switch is called the Néel relaxation time τ_{N} given by

$$\tau_{\mathrm{N}} = \tau_0 e^{\frac{KV_{\mathrm{p}}}{k_{\mathrm{B}}T}}, \tag{2.1}$$

where τ_0 is the material-specific attempt time to switch. k_{B} is the Boltzmann constant, T denotes the temperature, and KV_{p} describes the energy barrier. This energy barrier, consisting of the magnetic anisotropy energy density K and its volume V_{p}, has to be overcome to switch between orientations [84, 83]. In terms of the Néel relaxation, the magnetic moment flips only inside the magnetic particles as seen in Fig. 2.2a. If the Néel

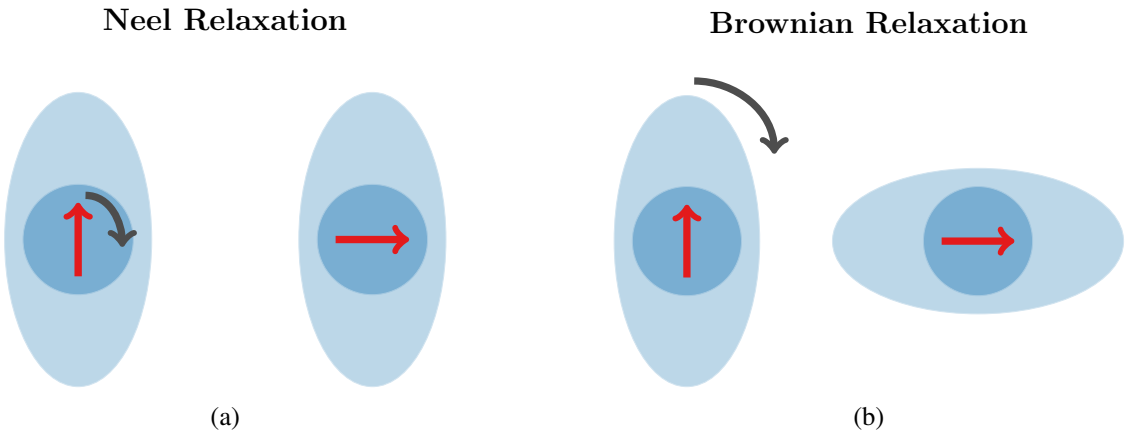

Figure 2.2.: (a) Néel rotation/relaxation. (b) Brownian rotation/relaxation.

relaxation time is very small compared to a defined measurement time τ_m ($\tau_{\mathrm{N}} \ll \tau_m$), the

magnetic moments flip a couple of times during the measurement. Consequently, in zero field the measured magnetization averages to zero. In this case, the nanoparticles appear superparamagnetic. However, if the measurement time is very small compared to the Néel relaxation time ($\tau_m \ll \tau_\mathrm{N}$), the magnetic moments do not flip during the measurement at all and the magnetization is the same as at the beginning of the measurement. In this case, the nanoparticles are blocked in their initial state. By setting the measurement time equal to the Néel relaxation time ($\tau_\mathrm{N} = \tau_m$) and solving for the temperature, the blocking temperature can be defined as follows

$$T_\mathrm{B} = \frac{KV_\mathrm{p}}{k_\mathrm{B} \ln(\frac{\tau_m}{\tau_0})}. \tag{2.2}$$

For iron oxides Fe_20_3 with magnetic core diameter of $10\,\mathrm{nm}$, the blocking temperature ($-238\,^\circ\mathrm{C}$ [91]) is way below the body temperature of the $37\,^\circ\mathrm{C}$ and therefore iron oxides can be used as MPI tracers in clinical applications.

The Brownian relaxation time τ_B describes the alignment of the particles magnetic moment when the particle rotates as a whole. It is defined by

$$\tau_\mathrm{B} = \frac{3V_\mathrm{h}\eta}{k_\mathrm{B}T} = \frac{\pi d_\mathrm{h}^3 \eta}{2k_\mathrm{B}T}, \tag{2.3}$$

where V_h denotes the hydrodynamic volume of the particles, η describes the dynamic viscosity of the liquid containing the particles [92] and d_h characterizes the hydrodynamic. The Brownian relaxation is shown schematically in Fig. 2.2b.

Whether the Néel or Brownian relaxation is predominant, depends on the particle size, particle anisotropy, particle mobilization state and viscosity of the medium. For spherical particles, for example, the transition from Néel to Brownian relaxation begins at the Shliomis size [93]. The particle mobilization state can be manipulated by embedding the particles in a structure of another material. As ferrofluids, the nanoparticles are in a liquid suspension and thus can rotate freely. This means that both, Néel and Brownian relaxation, occur for particles used in MPI because particles of different sizes are usually within a batch of MPI tracers. Hence, some of them are dominated by Néel and others by Brownian relaxation. However, Néel relaxation is likely predominant for MPI particles [94], as the choice of size ($d_\mathrm{c} = 15\,\mathrm{nm}$, $d_\mathrm{h} = 25\,\mathrm{nm}$) and frequency ($25\,\mathrm{kHz}$) of the oscillating magnetic field ($20\,\mathrm{mT}$) lead to more Néel relaxation. Yet, if the particles are immobilized by freezing or other immobilization techniques, only Néel relaxation occurs and the Brownian relaxation is suppressed [95]. The approximation of the combined Néel /Brownian relaxation time τ_NB is given by

$$\tau_\mathrm{NB} = \frac{\tau_\mathrm{N}\tau_\mathrm{B}}{\tau_\mathrm{N} + \tau_\mathrm{B}}. \tag{2.4}$$

For a more complex analysis on Néel and Brownian relaxation regarding particle size and shape distribution, please see [96, 94].

2.1.2. Structure of superparamagnetic particles

Suitable MPI tracers can have several different structures, ranging from single-core over multi-core to multi-domain particles (see Fig. 2.3). The typically desired structure of an MPI tracer is a single-core particle (see Fig. 2.3 single-core) with a single-domain and a high magnetic moment [78]. However, the current gold standard Resovist (Bayer Schering Pharma AG, Germany) generates a decent MPI signal, although it is a former MRI contrast agent and was not specifically designed for MPI. Here, the main performance of Resovist is mostly generated by clustered magnetic nanoparticles acting as multi-core particles rather than by smaller single-core particles [97]. The Resovist particles consist of a magnetic iron-oxide core Fe_3O_4 and a non-magnetic shell. The non-magnetic shell is made out of dextran, coated around the core, and inhibits the accumulation of particles [98]. Otherwise, the particles would lose their superparamagnetic properties. The shell is also responsible for the particles biocompatibility and ensures no interaction effects on the organism. The schematic structure of a particle with its inner core diameter d_c and its outer shell diameter d_h is shown in Fig. 2.3. As the availability of Resovist is limited, per-

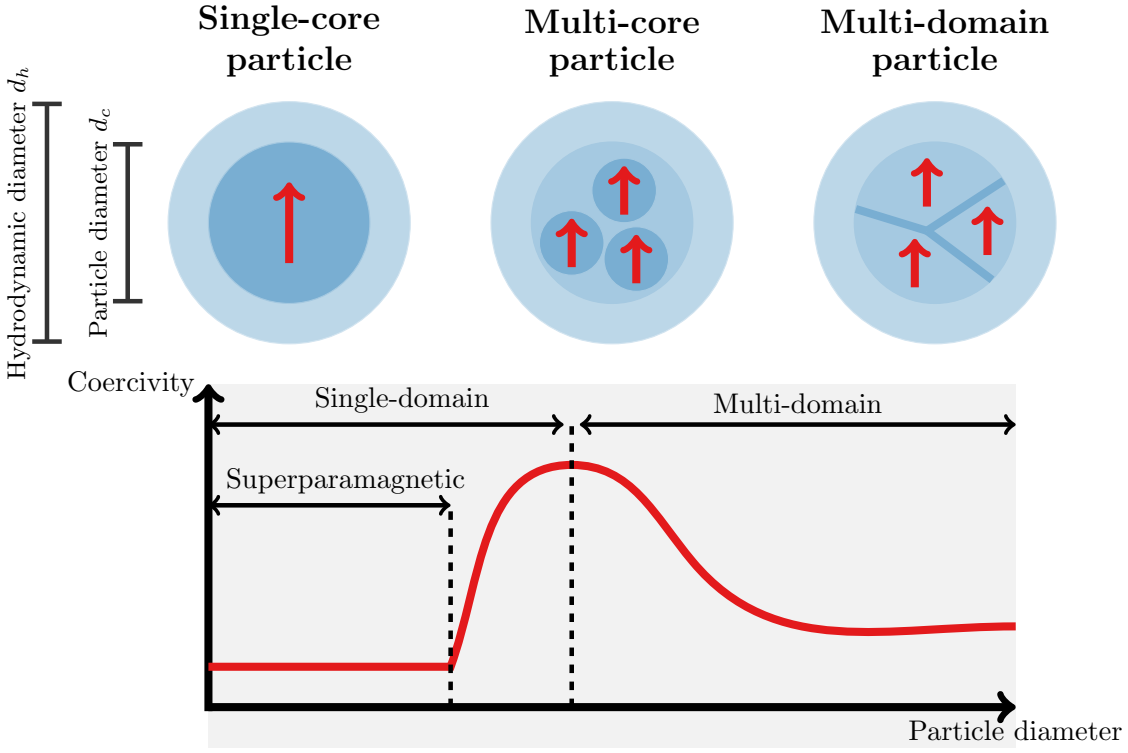

Figure 2.3.: Schematic particle structure of single-core, multi-core and multi-domain particles. The coercivity increases with increasing magnetic core diameter as long as the particles are single-domain. This theoretical connection is only valid in the case of static magnetic fields. In time-changing magnetic fields the relation is more complex.

imag (micromod Partikeltechnologie GmbH, Germany) can be used as an alternative. For the experiments presented in this work, mainly perimag is used as a tracer for angiography applications. Other common particles in the MPI literature are LS008 (LodeSpin Labs, USA) particles. These single-core particles provide a three-times better performance with respect to harmonic generation than Resovist and manage to have a longer circulation time *in-vivo* [43]. The drawback of LS008 is its availability. In terms of imaging properties, for MPI, the larger particles (over $d_\mathrm{c} = 25\,\mathrm{nm}$) are usually less sensitive in comparison to smaller particles. Since the critical hydrodynamic size diameter for Brownian relaxation is $39\,\mathrm{nm}$ in a single-domain particle, they probably response only with Néel relaxation to an oscillating magnetic field [99](p.586).

2.1.3. Langevin model

The superparamagnetic behavior of particles can be modeled by the Langevin theory [90, 27]. However, this basic model applies to a thermal equilibrium and assumes that the applied magnetic field is static [90]. The Langevin model does not account for changing magnetic fields, but is only concerned with the equilibrium magnetization. When applied to changing magnetic fields, it considers a direct alignment of the magnetic moment of particles. Thus, the Langevin model does not consider the relaxation time of the magnetic moment. For the Langevin model, the particles are assumed to be monodisperse single-domain particles, and each particle has a uniform magnetization [90]. These assumptions are rarely true for the particles used in MPI. Nevertheless, the Langevin model provides a good approach to understand the behavior of the particles within the limitations of the model. Each particle possesses a magnetic moment m, which determines its magnetic characteristics. In the absence of an external magnetic field, all magnetic moments point in random directions. This results from inner collisions between moving molecules due to Brownian motion. Then, the sum of all magnetic moments m is zero and the sum of all magnetic moments per volume V_p defines the magnetization M. For mean magnetization $\bar{\boldsymbol{m}}$, the magnetization is then divided by the number of particles N_p. The magnetization M as a function of the magnetic flux vector length B with $B = \|\boldsymbol{B}\|_2$ and with the magnetic flux $\boldsymbol{B} = \mu_0(1+\chi_\mathrm{v})\boldsymbol{H}$ is given by

$$M(B) \;=\; cm\mathcal{L}(\xi_\mathrm{r}) \tag{2.5}$$

with

$$\mathcal{L}(\xi_\mathrm{r}) \;=\; \begin{cases} (\coth(\xi_\mathrm{r}) - \frac{1}{\xi_\mathrm{r}}) & \text{with} \quad B \neq 0 \\ 0 & \text{with} \quad B = 0 \end{cases} \tag{2.6}$$

being the Langevin function. ξ_r is the ratio of magnetic energy to thermal energy of the particle

$$\xi_\mathrm{r} = \frac{mB}{k_\mathrm{B}T} \tag{2.7}$$

and the magnetic moment is defined as

$$m = \frac{1}{6}\pi d_\mathrm{c}^3 M_\mathrm{S}. \tag{2.8}$$

The permeability in vacuum is μ_0, the volume magnetic susceptibility is denoted as χ_v and the magnetic field strength is described by $\boldsymbol{H}$. The temperature T is given in kelvin and M_S denotes the saturation magnetization with $0.6\,\mathrm{T}/\mu_0$ [27]. An example visualization of the Langevin function is shown in Fig. 2.4. Besides the relaxation time of the

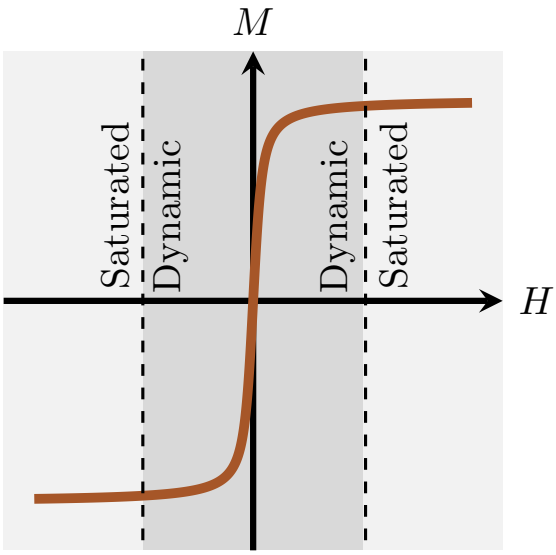

Figure 2.4.: Example visualization of the Langevin function that shows a non-linear dynamic graph that saturates to both sides.

magnetic moment, the Langevin model does also not take the shape of mono-domain particles into account. However, the anisotropy of the particles core influences the MPI signal strongly. It has been shown that with less particle anisotropy the MPI signal can be improved [100]. The Langevin model deviates from the real behavior of the magnetic particles since it assumes a simplified equilibrium magnetization. The reasons for these deviations can be explained by anisotropy or particle-particle interaction [101]. For high-frequency oscillating magnetic fields, the linearized Debye approximation can be used to model the behavior of the magnetic particles [102, 103].

2.2. Generation of the particle signal

In section 2.1, the non-linear hysteresis curve of superparamagnetic particles was introduced. In this section it is explained, how these characteristics of superparamagnetism are used to generate a responding signal from the particles. The non-linear magnetization is

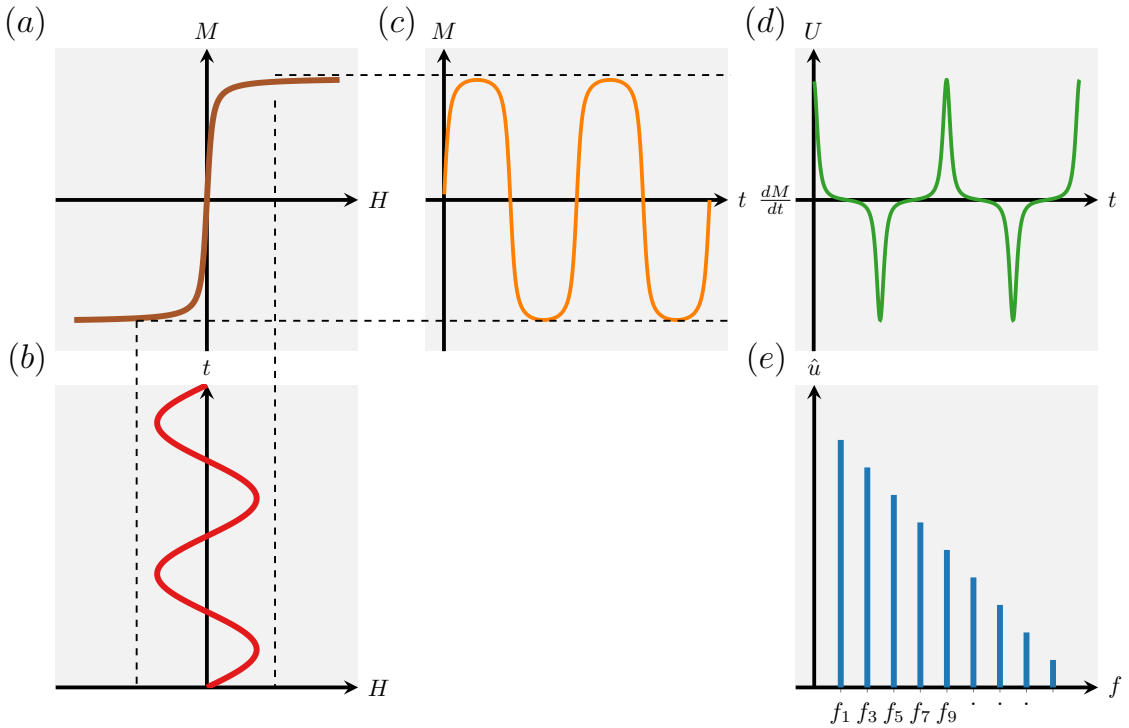

Figure 2.5.: Signal encoding: (a) The non-linear magnetization curve of superparamagnetic particles modeled by the Langevin function. (b) Time-dependent, sinusoidal, alternating magnetic field used to excite non-saturated particles. (c) Periodic, alternating magnetization behavior evoked by the sinusoidal excitation field. (d) The voltage signal induced by changing magnetization of the particle, i.e. the time derivative of the magnetization. (e) The responding time signal of the particles is transformed into Fourier space and is the spectrum of the particle signal.

modeled by Eq. (2.6) and illustrated in Fig. 2.5a. The particles can be excited by applying a time-dependent, sinusoidal alternating magnetic field

$$H_{\mathrm{e}}(t) = A_{\mathrm{e}} \sin(2\pi f_{\mathrm{e}} t) \tag{2.9}$$

with frequency f_{e} and amplitude A_{e} (see Fig. 2.5b). The magnetization of the particles is then depending on their core diameter, anisotropy and mobilization state following the alternating magnetic field with either mainly Néel or Brownian relaxation. The magnetization of non-saturated particles forms a time-dependent, periodic changing magnetization, depicted in Fig. 2.5c. The temporal change of the magnetization can be detected as an induced voltage signal with help of Faraday's law of induction $\nabla \times E = -\frac{\partial B}{\partial t}$. The voltage signal induced by the particles can be seen in Fig. 2.5d. It consists of the

initial excitation frequency superimposed with odd multiples of this excitation frequency called harmonics. These harmonics can be visualized even more clearly when the signal is transformed into Fourier space, also called the spectrum of the signal. The spectrum is illustrated in Fig. 2.5e and the intensity of the harmonics decreases with increasing harmonic number. The spectrum of magnetic particles is an important measure to analyze the performance of magnetic particles as a tracer for MPI. The more harmonics with a signal strength above the noise level are generated by the particles, the better the performance of the particles. Further, the decay of the amplitudes of the harmonics is also a good measure on how much of them end up being detected in the end.

2.3. Spatial encoding of the particle signal

Up to this point, all particles generate the same signal within the whole sample and it is only possible to determine the mean concentration or amount of particles within the entire volume. Hence, their spatial position is not known yet. As a next step, it is desired to determine the concentration of particles at a specific location within the sample. The basic idea is that particles at different locations generate signals, that can be discriminated from each other. For the FFP MPI scanner setup, spatial encoding can be achieved by saturating the particles in a way that these particles do not or marginally contribute to the MPI signal. If the particles are within a constant magnetic field, which is high enough, they are reaching their saturation state. In this saturated state, their magnetization no longer follows a sinusoidal excitation field. This concept is illustrated in Fig. 2.6 where saturated particles are superimposed by a sinusoidal excitation field (see Fig. 2.6a and Fig. 2.6b). In the saturated state, the magnetization remains constant and does not react to the alternating excitation field, as depicted in Fig. 2.6c. Since the particles are saturated, no voltage signal is induced in the receive coils and only noise is measured, as shown in Fig. 2.6d and Fig. 2.6e.

To receive a particle signal only from one specific location, the strength of a superimposed static magnetic field needs to be close to zero only at this specific location. All other locations need to experience a strong magnetic field that saturates the particles. This is given by a static gradient field

$$\boldsymbol{B}_s = \mu_0 \boldsymbol{H}_\mathrm{s} = \boldsymbol{G}_{\boldsymbol{r}} \boldsymbol{r} = \begin{bmatrix} G_x & 0 & 0 \\ 0 & G_y & 0 \\ 0 & 0 & G_z \end{bmatrix} \boldsymbol{r}. \tag{2.10}$$

An example illustration can be seen in Fig. 2.7a and as 2D image in Fig. 2.7b. This static

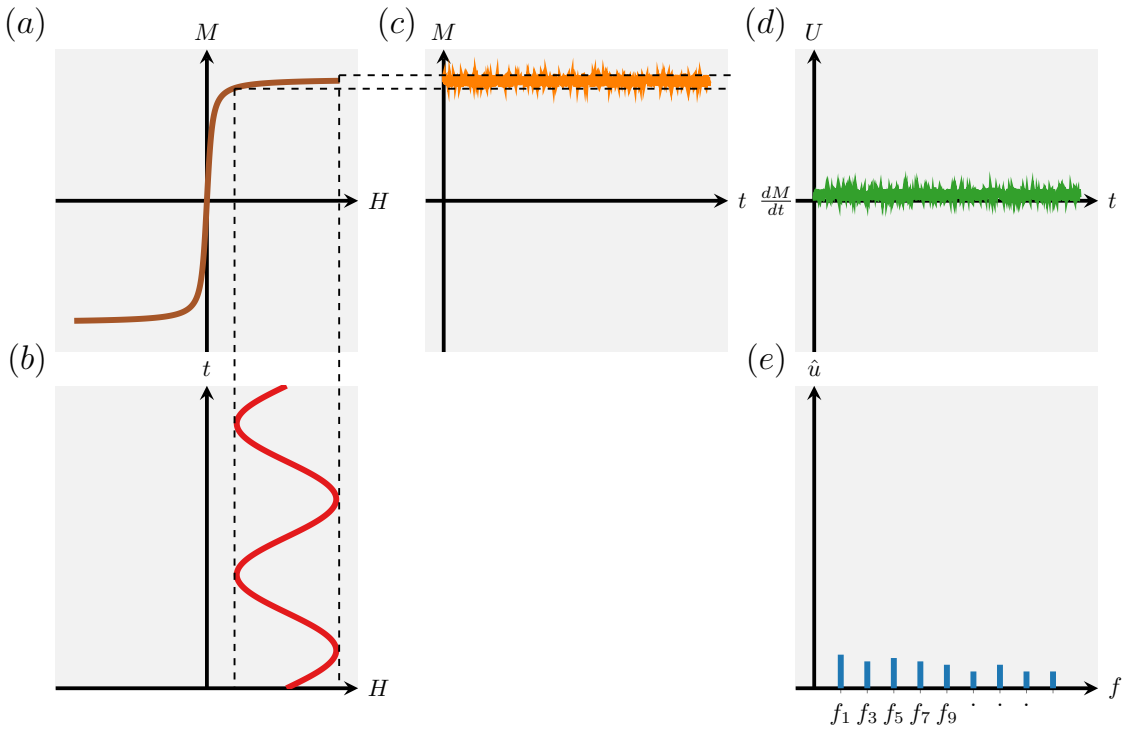

Figure 2.6.: Spatial encoding: (a) The particles are in a saturated state due to a strong constant magnetic field. (b) The sinusoidal magnetic excitation field is superimposed with the strong constant magnetic field. (c) The particle magnetization does not change according to the excitation field and shows a constant magnetization. (d) The voltage signal consists just of noise because only a change of magnetization can be detected by the receive coils. (e) The spectrum of the voltage signal shows only noise in all frequencies.

gradient field is usually generated by two coils in Maxwell setup where the currents in the coils run in opposite directions. Gauss's law of magnetism

$$\nabla \cdot \boldsymbol{B} = \frac{\partial B_x}{\partial x} + \frac{\partial B_y}{\partial y} + \frac{\partial B_z}{\partial z} = 0 \tag{2.11}$$

dictates that the divergence of the magnetic field has to be zero. It means that the sum of spatial derivatives in x, y and z direction have to nullify each other. Qualitatively, this translates to the fact that a magnetic vector field has to be source free and that no magnetic monopoles exist. Therefore, one possibility to choose the relation between the gradients strengths in x, y and z directions is

$$2G_x = 2G_y = -G_z \quad \text{with} \quad G_x = \frac{1}{2},\ G_y = \frac{1}{2} \text{ and } G_z = -1. \tag{2.12}$$

In MPI, this static magnetic field is called selection field because it basically selects the location from where the particle signal is received. The magnetic field strength increases linearly from the center. The location at which the magnetic field strength is zero is also referred to as the FFP. However, the signal from the particles is generated in an area

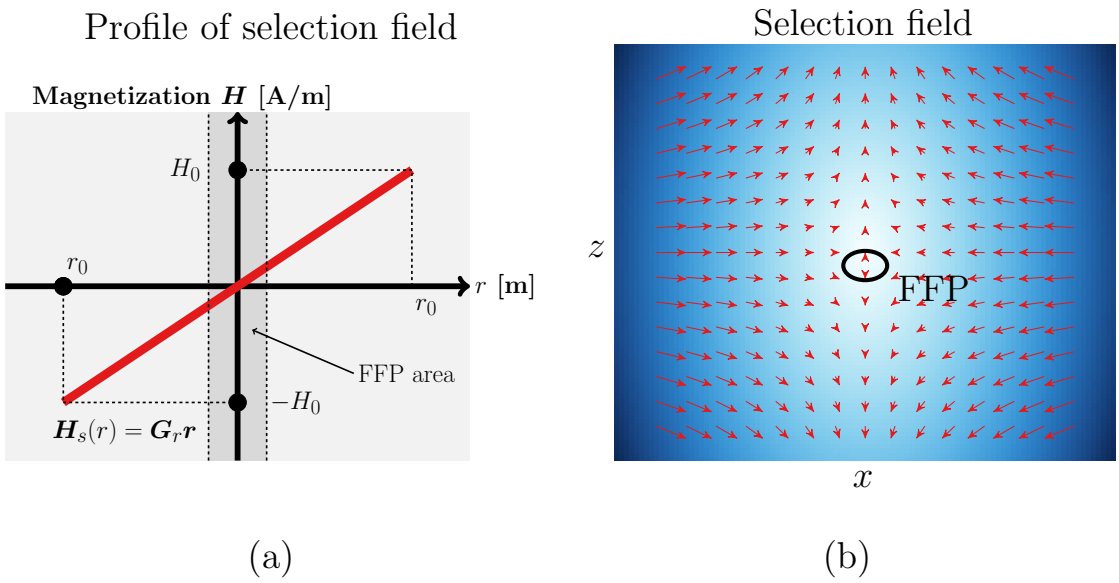

Figure 2.7.: (a) Profile of the static magnetic gradient field. (b) Selection field with FFP in x and z direction.

around the FFP because in that area the particles are not fully saturated. The influence of the selection field on particles at different positions within the selection field is shown in Fig. 2.8. The size of the FFP area is mainly determined by the gradient strength and it is an important parameter in MPI since the resolution and sensitivity are connect to this area. Even though the spatial encoding can also be achieved by a FFL [104], this work focuses on FFP MPI setups since all experiments habe been performed with an FFP scanner available at the UKE. More information on current FFL setups and the respective reconstruction technique can be found in [105, 106, 107, 108].

2.3.1. FFP sampling with Lissajous trajectory

In the 1D case the static gradient field H_s and the oscillating excitation field H_e are superimposed. This results in a FFP movement back and forth along a line in the direction of the excitation field. The FFP movement in 1D is shown in Fig. 2.9. One strategy to receive signals from locations within a 3D space and to perform 3D imaging is to add two additional excitation fields, perpendicular to each other. Depending of the frequencies of all three excitation fields the FFP can then be moved to each location in a 3D volume by the superimposed effective field. In MPI, the excitation field is called the drive field, in our case it is the combination of all three excitation fields. Since the excitation fields should be sinusoidal to simplify the filtering of the excitation frequency from the higher harmonics of the particle response, the excitation field consists of three sinusoidal excitations perpendicular to each other. If the same excitation frequency would be used for all directions, the FFP would only move along a diagonal trajectory in 3D with the same phase. Therefore, the base frequency is slightly shifted in each direction to create a tra-

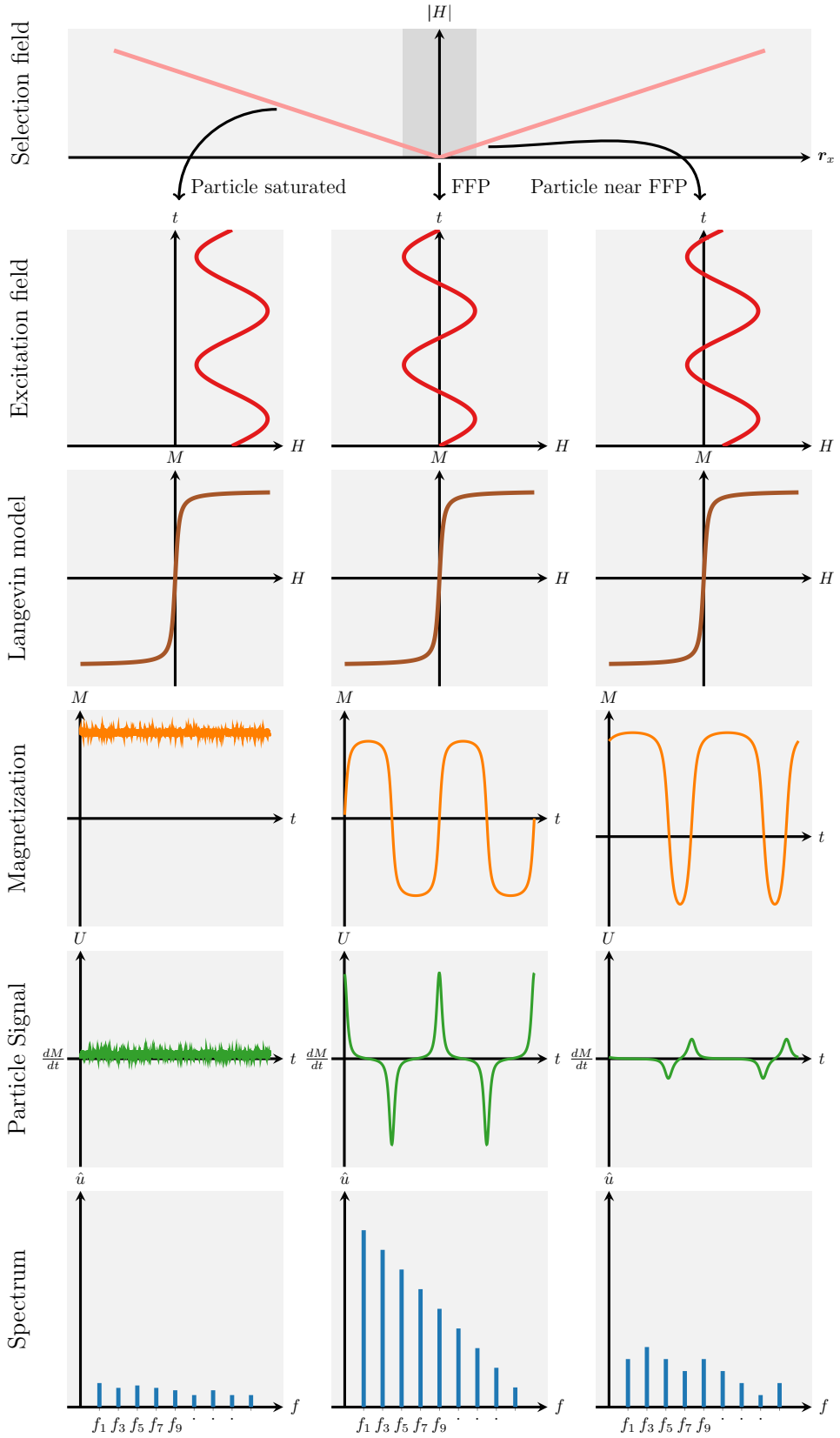

Figure 2.8.: Spatial encoding is established by a static gradient field. It generates an FFP where the particles can response to the excitation signal. Particles close to the FFP only contribute a small amount to the responding signal. Further away from the FFP, the saturated particles do not contribute to the responding signal.

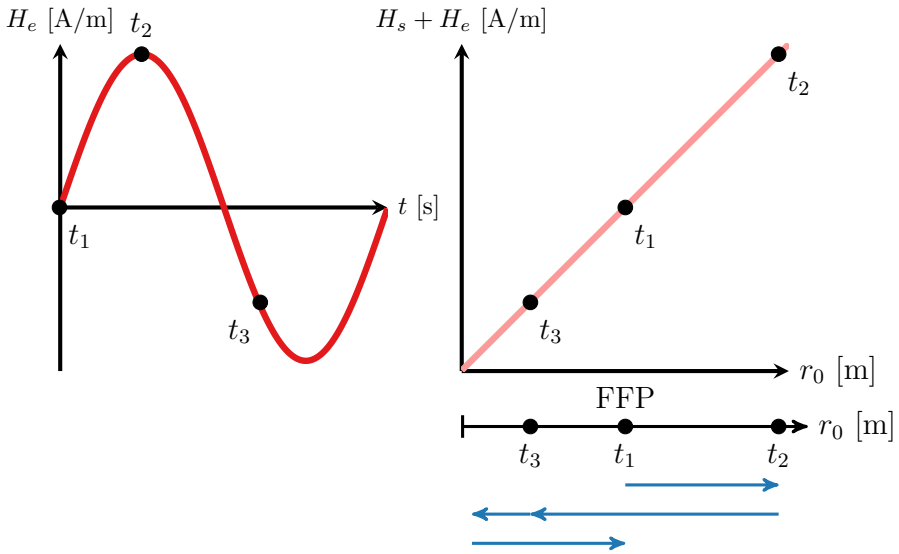

Figure 2.9.: In 1D the static gradient field H_s and the oscillating excitation field H_e are superposed. Thus, the FFP moves back and forth along a straight line in the direction of the excitation field.

jectory pattern that covers the entire 3D volume. One of the resulting trajectory pattern is called Lissajous trajectory. A Lissajous trajectory is described by

$$\boldsymbol{H}_{\mathrm{L}} = \begin{bmatrix} H_{L,x} \\ H_{L,y} \\ H_{L,z} \end{bmatrix} = \begin{bmatrix} A_x \sin(2\pi f_x t + \varphi_x) \\ A_y \sin(2\pi f_y t + \varphi_y) \\ A_z \sin(2\pi f_z t + \varphi_z), \end{bmatrix} \tag{2.13}$$

where the frequency ratios divident and divisor

$$\frac{f_x}{f_y} = \frac{N_{\mathrm{L}}}{N_{\mathrm{L}} - 1}, \quad \frac{f_x}{f_z} = \frac{N_{\mathrm{L}}}{N_{\mathrm{L}} + 1}, \quad \frac{f_y}{f_z} = \frac{N_{\mathrm{L}} - 1}{N_{\mathrm{L}} + 1}, \quad N_{\mathrm{L}} \in \mathbb{N} \tag{2.14}$$

are natural numbers. The Lissajous trajectory is only a closed loop, if the ratios are rational numbers. The natural number N_{L} determines the density of the Lissajous trajectory and defines the excitation frequencies

$$\begin{bmatrix} f_x \\ f_y \\ f_z \end{bmatrix} = f_{\mathrm{b}} \cdot \begin{bmatrix} N_{\mathrm{L}}^{-1} \\ (N_{\mathrm{L}} - 1)^{-1} \\ (N_{\mathrm{L}} + 1)^{-1} \end{bmatrix} \tag{2.15}$$

where f_{b} denotes the base frequency. The parameter N_{L} also helps to determine the repetition time T_{L} for one 3D Lissajous cycle calculated by

$$T_{\mathrm{L}} = \frac{N_{\mathrm{L}}(N_{\mathrm{L}} - 1)(N_{\mathrm{L}} + 1)}{f_{\mathrm{b}}} \tag{2.16}$$

since after N_L times $N_\mathrm{L} - 1$ times $N_\mathrm{L} + 1$ periods the cycle starts again. In this work, one Lissajous cycle is also referred to as drive field (DF) cycle. By increasing N_L, the repetition time becomes longer, but the FFP sampling of the 3D volume becomes more dense. Lissajous trajectories in 2D with parameters $N_\mathrm{L} = 2$ and $N_\mathrm{L} = 20$ are shown in Fig. 2.10a and Fig. 2.10b, respectively, and a 3D Lissajous trajectory with $N_\mathrm{L} = 8$ is visualized in Fig. 2.10c.

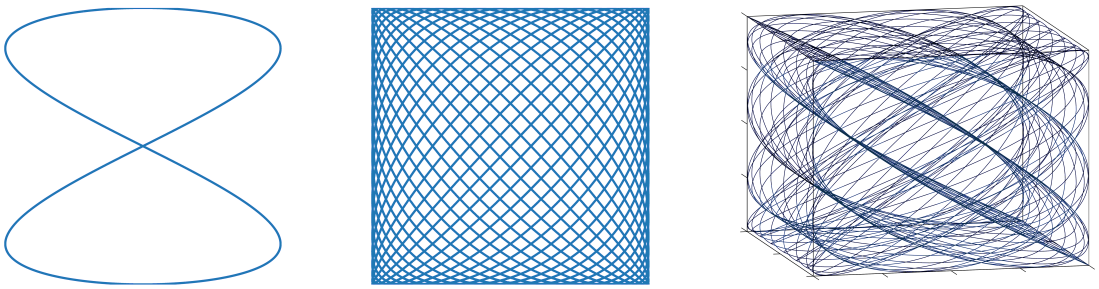

(a) (b) (c)

Figure 2.10.: (a) 2D Lissajous trajectory with $N_\mathrm{L} = 2$. (b) 2D Lissajous trajectory with $N_\mathrm{L} = 20$. (c) 3D Lissajous trajectory with $N_\mathrm{L} = 8$.

The drive field and the selection field superimpose and yield the total magnetic field

$$\boldsymbol{H}(\boldsymbol{r}, t) = \boldsymbol{H}_\mathrm{s}(\boldsymbol{r}) + \boldsymbol{H}_\mathrm{L}(t). \tag{2.17}$$

With the amplitude $\boldsymbol{A} = (A_x, A_y, A_z)^T$ of the drive field and the gradient strength $\boldsymbol{G_r}$ of the selection field, the size of the FoV can be determined by

$$\mathrm{FoV}(\boldsymbol{A}, \boldsymbol{G_r}) = \frac{2A_x}{G_x} \times \frac{2A_y}{G_y} \times \frac{2A_z}{G_z}. \tag{2.18}$$

Even though other trajectories, such as Cartesian, spiral and radial trajectories, can be generated using one base frequency, the Lissajous trajectory is preferred in terms of homogeneity and spatial resolution [109] but the spatial resolution can also be improved with bidirectional Carteasian trajectories [110, 111].

2.3.2. Focus fields

In a conventional MPI setup, the size of the FoV is determined by the drive field amplitude $\boldsymbol{A}$ and the gradient strength $\boldsymbol{G_r}$, which can be derived from Eq. (2.18). By increasing the amplitude, the size of the FoV could be increased, but then the safety constraints of the peripheral nerve stimulation (PNS) [21] and the limits for the specific absorption rate (SAR) would be disregarded [112, 113, 22]. Another way to increase the size of the FoV would be to decrease the gradient strength, but then the spatial resolution would be decreased as well (see Eq. (2.38)).

Gleich et al. [29, 30] developed another possibility and introduced the so called focus fields (FF). These FF are created by additional coils in each dimension in Helmholtz configuration. Helmholtz configuration means that the current flows in the same direction in both opposite coils. With the offset fields from these coils, the FFP and therefore the FoV can be moved in each dimension. The movement of the FF is performed with such a low frequency that the magnetic field changes are safe within the PNS and SAR. The FF

$$\boldsymbol{H}_{\text{FF}}(t) = \begin{bmatrix} H_{x,\text{FF}}(t)) \\ H_{y,\text{FF}}(t)) \\ H_{z,\text{FF}}(t)) \end{bmatrix} \tag{2.19}$$

is superimposed to the existing excitation field $\boldsymbol{H}_{\text{L}}$ and the static gradient field $\boldsymbol{H}_{\text{s}}$, resulting in the total field

$$\boldsymbol{H}(\boldsymbol{r}, t) = \boldsymbol{H}_{\text{s}}(\boldsymbol{r}) + \boldsymbol{H}_{\text{L}}(t) + \boldsymbol{H}_{\text{FF}}(t) \tag{2.20}$$

where $H_{x,\text{FF}} \in [-A_{x,\text{FF}}, A_{x,\text{FF}}]$, $H_{y,\text{FF}} \in [-A_{y,\text{FF}}, A_{y,\text{FF}}]$ and $H_{z,\text{FF}} \in [-A_{z,\text{FF}}, A_{z,\text{FF}}]$. Due to the additional movement of the FFP in both direction of each dimension, the FoV_{FF} can be enlarged. It can be calculated by

$$\text{FoV}_{\text{FF}}(\boldsymbol{A}, \boldsymbol{G_r}) = \frac{2(A_x + A_{x,\text{FF}})}{G_x} \times \frac{2(A_y + A_{y,\text{FF}})}{G_y} \times \frac{2(A_z + A_{z,\text{FF}})}{G_z}. \tag{2.21}$$

The maximal translation of the FFP by the FF can be determined by

$$\boldsymbol{t}_{\text{FF}} = \begin{bmatrix} \frac{A_{x,\text{FF}}}{\boldsymbol{G}_x} \\ \frac{A_{y,\text{FF}}}{\boldsymbol{G}_y} \\ \frac{A_{z,\text{FF}}}{\boldsymbol{G}_z} \end{bmatrix}. \tag{2.22}$$

This work uses only the functionality of the static multi-patch approach for the focus fields [30]. In the static multi-patch approach, the FoV is translated to several discrete positions and at each position, a measurement is performed with a Lissajous trajectory as described in section 2.3.1. The FoV at each position is called a patch. The patches can be either reconstructed individually, or they can be reconstructed all together with the joint reconstruction approach [114]. As shown in [30, 115], the individually reconstructed images are afterwards stitched together and usually suffer from artifacts at the border of the patches. The joint reconstruction approach is able to avoid the artifacts at the border region because it enforces consistency by solving the inverse problem with all measurements combined in one equation. The size of the linear system of equations increases quadratically with the number of patches, but the sparsity of the joint system matrix can be exploited to reduce the reconstruction effort [116]. A simple 2D example illustrates the

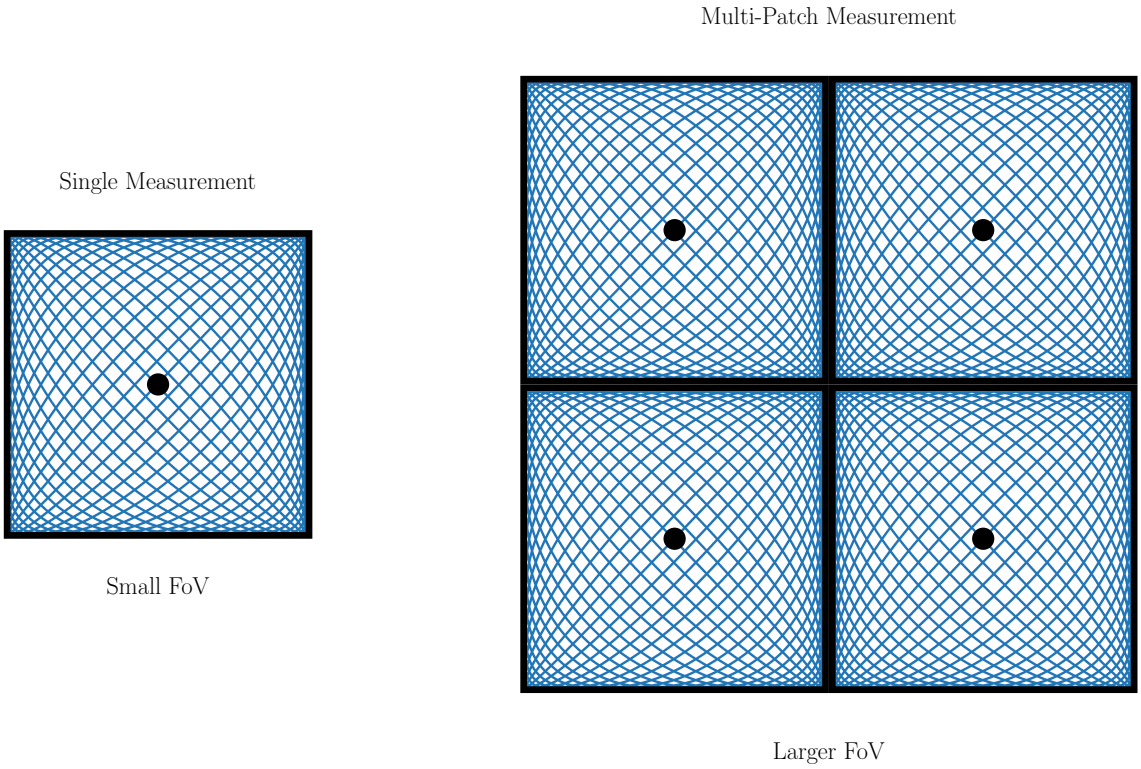

Figure 2.11.: The focus fields are used to measure four patches. With the help of the patches, a larger FoV can be reconstructed. This example shows the case for 2D image, but the same can be done in 3D.

use of the FF to enlarge the FoV in Fig. 2.11. The ability to position the patch by the FF at arbitrary positions can be applied for an adaptive feature detection [117]. First, a low resolution MPI image with a small gradient strength is acquired. Secondly, a region of interest is identified with help of the low resolution pre-scan. Thirdly, the FF are shifted to the region of interest. Lastly, a high resolution image with a larger gradient strength is acquired at the region of interest but with a smaller FoV. Consequently, less patches need to be measured.

2.4. Signal reception

The changing magnetization of the particles is detected in the receive coils via Faraday's law of magnetic induction

$$u(t) = -\mu_0 \int_\Omega \frac{\partial}{\partial t} \boldsymbol{M}(\boldsymbol{r}, t) p(\boldsymbol{r}) \mathrm{d}^3 r, \tag{2.23}$$

where $\boldsymbol{M}(\boldsymbol{r},t) = \bar{\boldsymbol{m}}(\boldsymbol{r},t)c(\boldsymbol{r})$ is the changing magnetization, $c(\boldsymbol{r})$ the particle distribution, $\bar{m}(\boldsymbol{r},t)$ the mean magnetic moment and $p(\boldsymbol{r})$ is the sensitivity of the receive coils [89](p.100). With $s(\boldsymbol{r},t) = -\mu_0 p(\boldsymbol{r})\frac{\partial}{\partial t}\bar{\boldsymbol{m}}(\boldsymbol{r},t)$, Eq. (2.23) can be written as

$$u(t) = \int_\Omega s(\boldsymbol{r},t)c(\boldsymbol{r})\mathrm{d}^3 r, \tag{2.24}$$

where $s(\boldsymbol{r},t)$ is denoted as the system function. When the voltage signal is transferred from time domain to frequency space via the Fourier-transform, it is formulated as

$$\hat{u}_{k_f} = \int_\Omega \hat{s}_{K_f}(\boldsymbol{r})c(\boldsymbol{r})\mathrm{d}^3 r, \tag{2.25}$$

where the Fourier-transformed system function is defined as

$$\hat{s}_{K_f}(\boldsymbol{r}) = -\frac{\mu_0}{T}\int_0^T p(\boldsymbol{r})\frac{\partial}{\partial t}\bar{\boldsymbol{m}}(\boldsymbol{r},t)e^{-2\pi i\frac{k_\mathrm{f} t}{T}}\mathrm{d}t, \tag{2.26}$$

with k_f as the index of the frequency component. In reality Eq. (2.25) has to be expanded by a complex valued transfer function, which takes filtering and damping of the excitation frequency into account. Further reading on the transfer function can found in [89](p.101).

Up to now, the voltage signal is considered to be a continuous time signal. However, to process the signal digitally on a computer, the signal has to be temporally discretized with a finite sampling rate f_s. The time interval of the sampling frequency is given with $\Delta t = \frac{1}{f_\mathrm{s}}$. Since the particles are excited with periodic sinusoidal signals, the magnetization response is also a periodic function in the time interval $[0, T_\mathrm{L})$. Therefore, to avoid data inconsistencies by conjoining data from different periods, the ratio $\phi = \frac{T_\mathrm{L}}{\Delta t}$ has to be a natural number $\mathbb{N}$. Finally, the discrete time signal is transformed to Fourier space with the discrete Fourier transform. As a next step, Eq. (2.23) has to be spatially discretized to process it further. Technically, the signal cannot be received from an infinite small location. Thus, Ω is discretizied by a 3D grid with side lengths l_x, l_y, l_z, dimensions $N_x \times N_y \times N_z$ and total number of grid positions $N_\mathrm{G} = N_x N_y N_z$. The volume of one voxel is then given by

$$\Delta V = \frac{l_x}{N_x} \times \frac{l_y}{N_y} \times \frac{l_z}{N_z}. \tag{2.27}$$

By using the temporal and spatial discretization the continuous MPI signal (2.25) is approximated by a sum yielding the discrete MPI signal equation

$$\hat{u}_{k_f} \approx \hat{u}^d_{k_f} = \Delta V \sum_{n=0}^{N_\mathrm{G}-1} \hat{s}_{k_f}(\boldsymbol{r}_n)c(\boldsymbol{r}_n) \tag{2.28}$$

where $\boldsymbol{r}_n$ denotes the discrete cell-centered grid position with index n.

In Fig. 2.12 the Fourier transform of the excitation signal, the particle signal and the superimposed signal of excitation and particle signal $u(t)$ into their spectral signals in frequency domain is shown. The excitation signal couples into the receive coils and su-

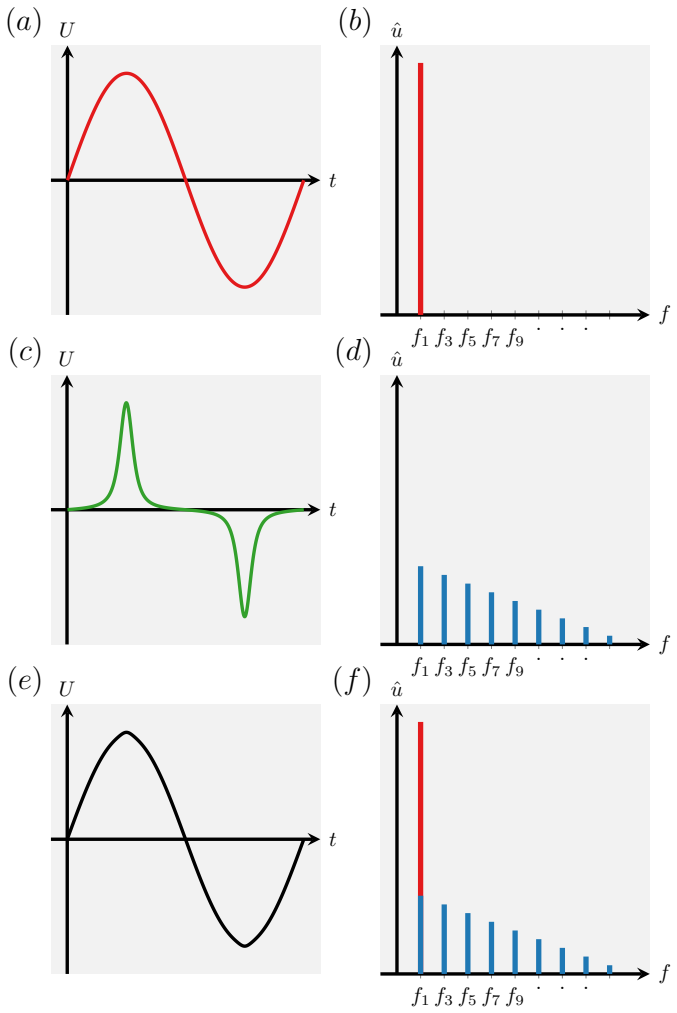

Figure 2.12.: Illustration of (a) the voltage signal of the sinusoidal excitation signal and its (b) Fourier-transformed spectrum. (c) The voltage signal of the particle signal and its (d) Fourier-transformed spectrum. (e) The superimposed voltage signal $u(t)$ of excitation and particle signal and its (f) Fourier-transformed spectrum $\hat{u}_{k_f}$ in the frequency domain. The Fourier-transformed spectrums are on a logarithmic scale.

perimposes the particle signal (compare Fig. 2.12e). Unfortunately, the excitation signal is several magnitudes higher than the first harmonic of the particle signal. In Fig. 2.12f, the Fourier-transformed excitation signal is superimposed with the first harmonic of the Fourier-transformed particle signal. Consequently, the excitation frequency has to be excluded from the spectrum since it is not distinguishable which part of the signal comes from the excitation and which part from the particles. Usually, an analog-to-digital converter (ADC) is used to convert the analog signal into a digital signal. With this conversion, the excitation frequency could be excluded in a post-processing step. However, the particle signal has a wide dynamic range, where the lowest frequency component above

the noise level can have a 10^{10} times lower amplitude than the excitation signal. Unfortunately, the most developed ADCs provide only a frequency range of 16 bits, resulting in a $10^5\,\mathrm{V}$ resolution [89](p.29). As this resolution range is not sufficient to cover the whole dynamic range of the particle signal, the excitation frequency has to be excluded prior to the digitalization process. In most MPI setups, the excitation signal is filtered with an analog band-stop filter. For more information on the band-stop filter and the technical details, please review the literature on filtering [89](p.89),[118](p.94).

2.5. Image reconstruction

In this work, the so-called system matrix reconstruction is used, which is the common reconstruction technique for FFP scanners. For the system matrix reconstruction the particle signal is often transformed from time domain to frequency domain as described previously. The FFP is moved along the Lissajous trajectory within the FoV. Thus, the received signal $u(t)$ and spectrum $\hat{u}_{k_f}$, respectively, contain particle information of the entire FoV. From one single measurement at one location, it would not possible to make an assumption about the particle distribution $c(\boldsymbol{r})$. Usually, a 3D volume image in MPI is discretized on the 3D grid presented in section 2.4. The task of image reconstruction is then to determine the particle concentration at each location and to assign it to a corresponding voxel. In other imaging modalities, like CT, the image reconstruction problem is an inverse problem, but unlike in CT we do not have analytical tools to formulate a closed expression for the solution of this problem [89](p.120). The reason for this lies mainly in the complex relaxation effects of the particles in connection with the 3D excitation, which are dependent on several physical parameters, such as excitation frequency and particle anisotropy. Therefore, to map the particles distribution spatially, a calibration scan has to be performed before reconstruction. The result of this calibration scan can be converted into the MPI system matrix by a linear scaling.

2.5.1. Acquisition of the system matrix

The system matrix needs to be acquired with a particle response signal from each location within the FoV, while every other position needs to be free of particles. This way the characteristic particle signal from each specific location is acquired in its purest form. In order to obtain the system matrix, a delta sample of known particle concentration c_0 and size is chosen. The concentration is usually chosen quite high to gain a good SNR but at a certain concentration and above (e.g. Resovist $0.15\,\mathrm{mol\,L^{-1}}$ [119]) the tracer can have a non-linear signal-to-concentration dependency. The size of the delta sample is usually chosen as large as one voxel of the desired image (see Fig. 2.13). Nevertheless, the grid can be adjusted freely in terms of discretization and size to meet the application

requirements. As seen in Fig. 2.13, the grid is often selected larger than the region covered by the FFP trajectory. This is due to the fact that particles outside the predefined trajectory FoV can cause artifacts along the border of the FoV [120]. The delta sample is then moved to each position of the grid. At each positions $\boldsymbol{r}_n$ with $n = 1, \ldots, N_\mathrm{G}$ of the grid, the particle responds is measured. Then, the Fourier coefficients $\hat{u}^n_{k_f} \in \mathbb{C}^{K_\mathrm{f}}$ with $k_\mathrm{f} = 1, \ldots, K_\mathrm{f}$ are determined via a Fourier transform. With each set of frequency components $\hat{u}^n_{k_f}$, the system matrix

$$\boldsymbol{S} = \begin{bmatrix} \hat{u}_{1,1} \cdots \hat{u}_{1,N_\mathrm{G}} \\ \vdots \ddots \vdots \\ \hat{u}_{K_\mathrm{f},1} \cdots \hat{u}_{K_\mathrm{f},N_\mathrm{G}} \end{bmatrix} \quad \text{with} \quad \boldsymbol{S} \in \mathbb{C}^{N_\mathrm{G} \times K_\mathrm{f}} \tag{2.29}$$

is filled column-wise, which can be seen in Fig. 2.13. The system matrix in Eq. (2.29)

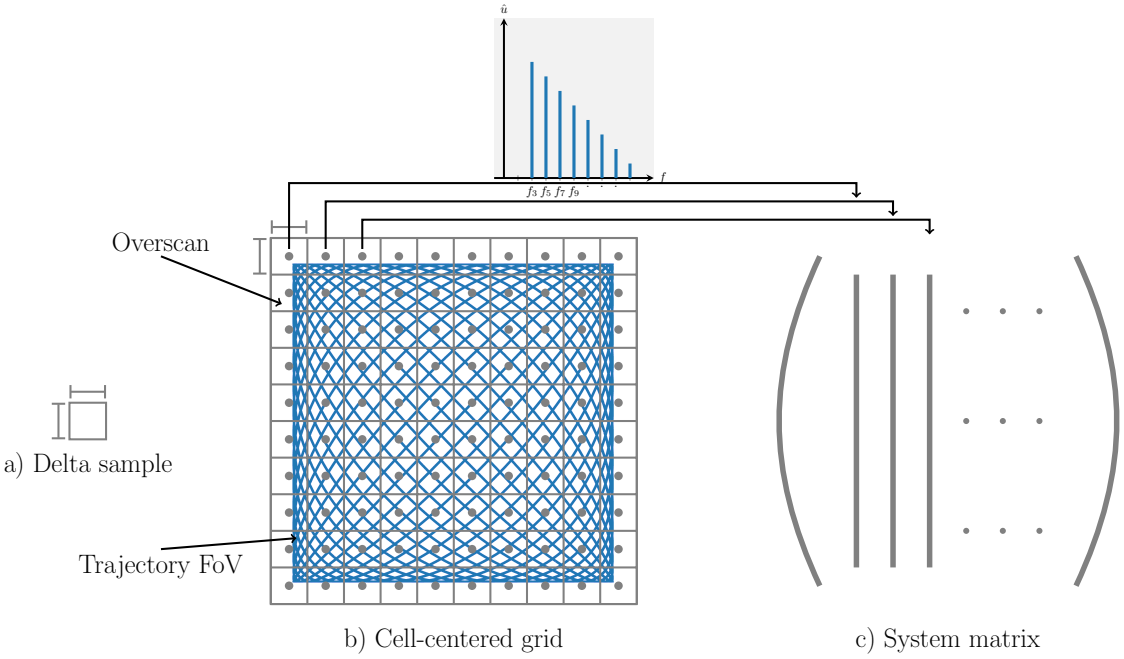

Figure 2.13.: The system matrix is acquired by use of a delta sample (a). The delta sample is moved to each voxel through the FoV in a cell-centered grid (b). The spectrum acquired at each position is filled column-wise into the system matrix (c).

describes the case that there is only one receive channel used. The system matrix can easily be extended to multiple receive channels. In practice is advantageous to use three receive channels, one for each direction in a 3D scenario. The system matrix has then the form $\boldsymbol{S} \in \mathbb{C}^{N_\mathrm{G} \times K_\mathrm{f} C}$, where $C = 3$ denotes the number of receive channels. Due to the linear relation between the particle signal and the concentration, a linear system of equation can be set up as follows

$$\boldsymbol{S}\boldsymbol{c} = \hat{\boldsymbol{u}} \tag{2.30}$$

that resembles the matrix-vector notation of Eq. (2.28). Again, $\boldsymbol{c} \in \mathbb{R}^{N_\mathrm{G}}$ describes the unknown particle concentration at each position inside the FoV and $\hat{\boldsymbol{u}}$ denotes the measured signals or rather measured spectra of the actual measurement.

The acquisition of the system matrix is a calibration process. This means the calibration has to be repeated, if one of the system parameters changes. Therefore, the system matrix depends on the gradient, the amplitude, the coil setup, the choice of trajectory and excitation frequency on the scanner side. On the particle side, the system matrix also depends on the particle type, the particle diameter, the particles anisotropy and the mobilization state. It can even be necessary to perform a re-calibration for a new particle batch, because the reproducibility of the particles cannot always be ensured.
However, the re-calibration for every parameter change would not impose a limitation of this method, if the calibration process would be quite fast and not so time consuming, especially in 3D. The calibration time mainly depends on the number of measured positions. In 3D space this number increases cubically. An image with an image resolution of 128 voxels in each dimension has $128^3 = 2.097.152$ positions. Assuming that it takes about $1\,\mathrm{s}$ to acquire the MPI spectrum at one position, the calibration scan would take about $25\,\mathrm{d}$ to finish. In reality, the movement of the delta sample is performed by a robot and several measurement cycles are acquired at each position to gain a better SNR by averaging. Therefore, the acquisition time per position is even in the range of $1\,\mathrm{s}$ to $3\,\mathrm{s}$ including robot movement, measurement cycles and data processing. Nevertheless, the measurement-based approach is still widely used for most MPI experiments, because it does not make assumptions about the scanner or particle properties. It is possible to reconstruct right after the system matrix is acquired. Further, the measurement-based approach does not suffer from model simplifications and all complex relaxation effects are taken into account in the system matrix.

Measurements with multiple FF positions are additionally affected by this time consuming calibration process, because usually a system matrix is acquired at each FF position to map the field characteristics precisely. Otherwise, if only the centric system matrix is utilized for the reconstruction at each FF position, the images contain artifacts. The reason for this are non-ideal magnetic fields, which means that the gradient field is not perfectly linear and the excitation field is not perfectly homogeneous. Consequently, the magnetic field has imperfections, especially towards the border of the FoV. Nevertheless, in some cases some of system matrices can be reused. If the FF positions are facing each other, the system matrix can be mirrored and phase corrected [121]. With clusters of similar system matrices [122], a trade-off between calibration time and artifact reduction can be achieved.

In order to reduce the enormous calibration time, a model-based approach has been investigated [123, 124]. The model-based approach uses a physical model for the particle dynamics. However, due to simplifications, the performance is not as good with respect

to the image quality as with the measurement-based approach. Geometrical displacement of the system matrix at the border of the FoV and noise are not represented by the model-based approach and limit the reconstruction results [89](p.126). The most promising approach to replace the measurement-based approach is a hybrid approach [125, 126]. It uses a magnetic particle spectrometer (MPS) with offset fields to emulate each position within an MPI scanner. It does not solve the problem of cubic scaling but the calibration time is reduced, as the movement of the robot is omitted. For the usage with the MPI scanner, only a transfer function needs to be acquired. Another advantage of this method is that the delta sample is closer to the receives coil, which results in a higher SNR. However, up to date, the 3D MPS is not commerically available. A second promising approach uses machine learning techniques to scale-up low resolution calibration scans [C2, C3]. The neural network learns the structure of a high resolution system matrix with a particle type A. Then, a low resolution system matrix with particle type B is acquired. The algorithm applies the structure of the system matrix from the neural network to the particle dynamics from particle B and scales the low resolution system matrix to high resolution matrix of particle B. Thus, the cubic scaling problem is reduced and leads to a short acquisition time for the lower grid.

2.5.2. Solving the inverse problem

The linear system of equations formulated in Eq. (2.30) describes an ill-posed inverse problem [127]. To solve this problem and to obtain the unknown particle concentration $\boldsymbol{c}$, a first-order Tikhonov-regularized least squares approach

$$\|(\boldsymbol{S}\boldsymbol{c} - \hat{\boldsymbol{u}})\|_2^2 + \tilde{\lambda}\|\boldsymbol{c}\|_2^2 \underset{\boldsymbol{c}}{\longrightarrow} \min \tag{2.31}$$

can be used.Usually, λ is reported as the regularization parameter, but here $\tilde{\lambda}$ is used, which is derived from $\lambda = \frac{\tilde{\lambda}}{\lambda_0}$, where $\lambda_0 = \text{trace}(\boldsymbol{S}^*\boldsymbol{S})N_\text{G}^{-1}$ and N_G is the number of voxels, where $\boldsymbol{S}^*$ is the conjugated transposed matrix of $\boldsymbol{S}$. The regularization term $\tilde{\lambda}\|\boldsymbol{c}\|_2^2$ penalizes solutions with a large Euclidean norm. Therefore, solutions emphasizing noise are neglected as they usually show a large Euclidean norm. The choice of regularization parameters is often a tradeoff between minimizing the noise and smoothing the solution.

There are many suitable algorithms to solve the weighted regularized least-square problem (2.31). Even though it is possible to use direct methods, such as a singular value decomposition (SVD) or a Cholesky decomposition, to solve the inverse problem, iterative methods, such as the Kaczmarz algorithm [128, 129], are implemented in most MPI reconstruction algorithms. The Kaczmarz alogrithm has the advantage that is does not require to load the entire system matrix into the main memory [89](p.144) and it converges

quite fast for MPI system matrices.
The Kaczmarz algorithm uses a fixed point iteration

$$\boldsymbol{c}^{k+1} = \boldsymbol{c}^{k} + \frac{\tilde{u}_i - \hat{\boldsymbol{s}}_i^* \cdot \boldsymbol{c}^k}{\|\hat{\boldsymbol{s}}_i\|_2^2} \hat{\boldsymbol{s}}_i^*, \tag{2.32}$$

where k describes the index of the inner iteration and i describes the index of the row $\hat{\boldsymbol{s}}_i^*$ of the system matrix . The row index i is increased after each inner iteration and $i = k \mod M$ is used. The start vector $\boldsymbol{c}^0$ is initialized by a vector containing zeros. The Kaczmarz algorithm iterates through the matrix rows and converges quite fast, if the rows are nearly orthogonal.More information on the adapted Kaczmarz algorithm can be found in [89](p.147).

In real-time applications, for example using the online reconstruction framework [130], the reconstruction time per MPI image is important. Therefore, the Kaczmarz algorithm is the method of choice for fast reconstructions. As the number of grid positions of the system matrix increases, the solution of the linear system of equation requires more memory and computational effort. As discussed earlier, in 3D, the number of positions increases cubically and so far a reconstruction with 25^3 positions is manageable in real-time [130]. Besides the grid size, which influences the number of rows of the system matrix, the choice of frequencies components and the number of receive channels influence the number of columns and determines the computational effort of the reconstruction. The number of iterations within the Kaczmarz algorithm plays a crucial role. For real-time purposes, the number of iterations n_{iter} is usually not set to more than 3.

Frequency selection

It should be mentioned that the number of frequency components K_{f} is usually reduced by filtering based on an SNR threshold. If a high number of frequencies components is chosen, components containing only noise might be selected as well. In contrast, if the number is too low, valuable particle information might be lost, because some frequency components holding essential image information are not included.

The value of λ_0 acts as an initial regularization parameter but does not take the noise of the measurement into account [89](p.139). Through over-regularization the underlying image information can be blurred too much such that the spatial resolution is reduced. It is quite challenging to find the best regularization parameters, as it is dependent on the conditioning of the system matrix and the noise level of the measurement. A suitable solution is often determined by visual inspection, which is usually time consuming and hinders the comparability of MPI images. It is also worth noting that a strongly regularized reconstruction alters the absolute quantitative concentration estimation. Ergo with increasing the regularization parameter λ, the estimated concentration is increased or decreased in some locations. Further, it can be advantageous to remove noisy frequency

component prior to reconstruction. Thus, a minimum SNR threshold Θ can be introduced that filters the noisy frequency components. All frequencies with an SNR below Θ are removed. The choice of Θ has to be done deliberately as a high value of Θ removes too many information-carrying frequencies and results in a loss of spatial resolution. Therefore, the combined choice of λ and Θ needs be to adjusted for each measurement since the noise and SNR change during a dynamic MPI sequence. Practically, the choice of λ and Θ is based on experience by trying out several parameter combinations and comparing their results.

2.5.3. Multi-contrast MPI

Due to various particle specific characteristics, different particles used for MPI are also responding differently to the excitation signal. For example, the different response in amplitude and phase of the harmonics for two types of particles with a different core material can be discerned [41]. However, the differing response is not limited to different materials, but can directly or indirectly depend on other tracer properties, such as the temperature, the viscosity, the particle shape, the mobilization state, the particle core diameter, the particle core coating and the immobilized easy-axis alignment. The temperature [32, 33, 34, 35, 36], viscosity [37, 38] and particle shape [40] influence the anisotropy energy that is highly linked to characteristics of the response signal. The particle shape mainly affects the anisotropy axis, whereas the viscosity also affects the immobilization state. The immobilization state describes whether the particles are mobilized within a solution or immobilized with a gel structure or bond to another molecule. If the particles are immobilized, Brownian relaxation is suppressed, and the particles only answers with Néel relaxation [39]. As explained in section 2.1.1, a particle exhibiting Néel and Brownian relaxation is discernable from a particle exhibiting only Néel relaxation. Particles with different core diameters can also be distinguished, because particles with a different core diameter respond differently to the excitation signal [131, 41]. However, at a certain core diameter, the particles respond only with Néel relaxation because the entire particle can no longer follow the changes of the magnetic field and rotates no longer as a whole. The same holds, if the particle coating is too large and the Néel relaxation dominates the relaxation process. Here, not only the size of the particle shell has an influence, but the structure and type of the shell as well. Finally, the easy-axis alignment can be immobilized to generate an additional MPI contrast [132, 95].

All these parameters influence the particle's relaxation process and enable the opportunity to separate different particles by their characteristical signal. In [41], the feasibility to separate between three different particle signals has been demonstrated in one of the first experiments towards multi-color MPI. Note that in this work, the term multi-contrast is used instead of the other terms multi-color or multi-spectral since it is similarly used

in MRI. To discern the signal from other constituents, a joint algebraic reconstruction approach [41] is used. For the joint algebraic reconstruction

$$\begin{aligned} \boldsymbol{S}_{P1}\boldsymbol{c}_{P1} + \boldsymbol{S}_{P2}\boldsymbol{c}_{P2} + \cdots + \boldsymbol{S}_{PN}\boldsymbol{c}_{PN_\mathrm{S}} &= \boldsymbol{u} \\ \begin{bmatrix} \boldsymbol{S}_{P1} & \boldsymbol{S}_{P2} & \cdots & \boldsymbol{S}_{PN_\mathrm{S}} \end{bmatrix} \begin{bmatrix} \boldsymbol{c}_{P1} \\ \boldsymbol{c}_{P2} \\ \vdots \\ \boldsymbol{c}_{PN_\mathrm{S}} \end{bmatrix} &= \boldsymbol{u} \\ \boldsymbol{S}_\mathrm{total}\boldsymbol{c}_\mathrm{total} &= \boldsymbol{u}, \end{aligned} \tag{2.33}$$

where $\boldsymbol{S}_\mathrm{total} = \begin{bmatrix} \boldsymbol{S}_{P1} & \boldsymbol{S}_{P2} & \cdots & \boldsymbol{S}_{PN_\mathrm{S}} \end{bmatrix}$ and $\boldsymbol{c}_\mathrm{total} = \begin{bmatrix} \boldsymbol{c}_{P1} & \boldsymbol{c}_{P2} & \ldots & \boldsymbol{c}_{PN_\mathrm{S}} \end{bmatrix}^T$ with $P = 1, 2, \ldots, N_\mathrm{S}$ being the number of constituents. After solving the corresponding regularized least squares problem for $\boldsymbol{c}_{total}$ with the standard Kaczmarz reconstruction (see Eq. (2.32)), $\boldsymbol{c}_\mathrm{total}$ is split again back to its component images $\boldsymbol{c}_{P1}, \boldsymbol{c}_{P2}, \cdots, \boldsymbol{c}_{PN_\mathrm{S}}$. They represent one image per constituent. In most setups, these multi-contrast images are converted into a one colorized image. Each contrast image is then assigned with a different color. In Fig. 2.14, an example of the multi-contrast principle is shown for two different particle types (e.g. red and green). In an application scenario with a maximal number of three constituents it is highly beneficial to superimpose the multi-channel images to one colorized image and use an appropriate color visualization (e.g. yellow for both particle types). For example, this visualiztion faciliates the handling in angioplasty experiments [61], where the information of a blood pool tracer and a marked balloon catheter are combined in one image. However, if the application setting requires more channels, for instance in easy-axis experiments, this colorized visualization approach is not constructive as information is lost during the conversion. For quantitative results, the information is directly taken from each multi-channel image. It should be noted that the Kaczmarz algorithm usually needs more iterations ($n_\mathrm{iter} \approx 100$) than usual to intensify the differences between multi-contrast images. The concept of multi-contrast MPI opens up various new applications for MPI. For instance, in interventional applications, Haegle et al. [133] coated the tip of a guide wire with Resovist particles and were then able to discern between the immobilized particles on the guide wire and the liquid Resovist inside a vessel phantom. Going one step further, Salamon et al. [61] used the multi-contrast approach to track a lacquer marked balloon catheter in real-time, while performing an angioplasty with MM4 as an injected contrast agent. Thus, multi-contrast MPI can help distinguishing between a marked interventional instruments and a regular used blood pool tracer for angiography. Even though further studies have also investigated the influence of temperature [32, 33, 34, 35, 36], viscosity [37, 38], and particle diameter [40], this work focuses mainly on the influences of the immobilization state of the tracer perimag.

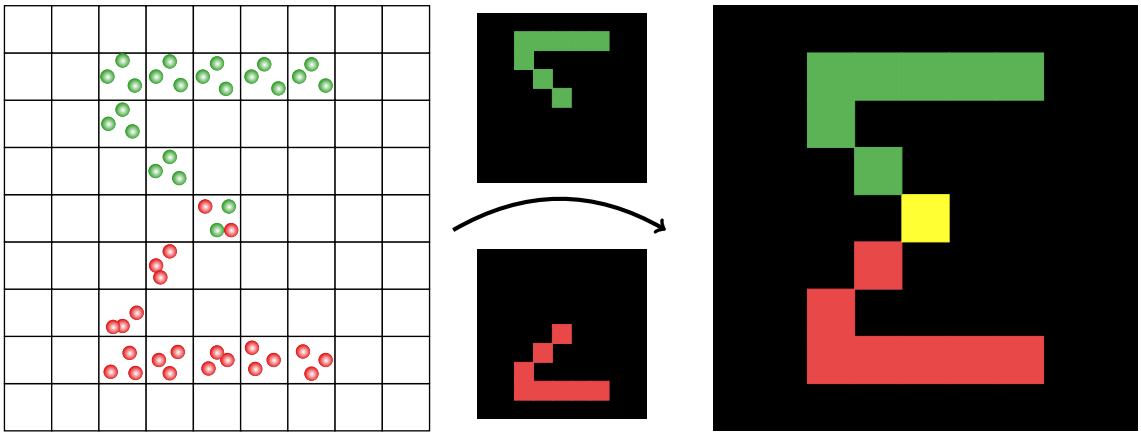

Figure 2.14.: Example illustration of the reconstruction in multi-contrast MPI, which first results in two multi-contrast images that can be superimposed. The first image only shows the distribution of the first particle type, while the second image depicts only the particle distribution of the second type. For the superimposed image, each contrast image is assigned to a different color. Note that one pixel is encoded yellow as a result of mixing red and green due to equal concentrations of both particle type.

2.5.4. Resolution and sensitivity in MPI

The resolution in MPI mainly depends on the particle size and the gradient strength since it determines the area around the FFP from where signal is received. To get an idea, how the particle size influences the resolution, we use the Langevin model described in section 2.1.3. A graphical illustration of the Langevin model for different particle core diameters is shown in Fig. 2.15a. The curve of the Langevin function becomes steeper with increasing particle core diameter. If the Langevin function is steep, it means that the

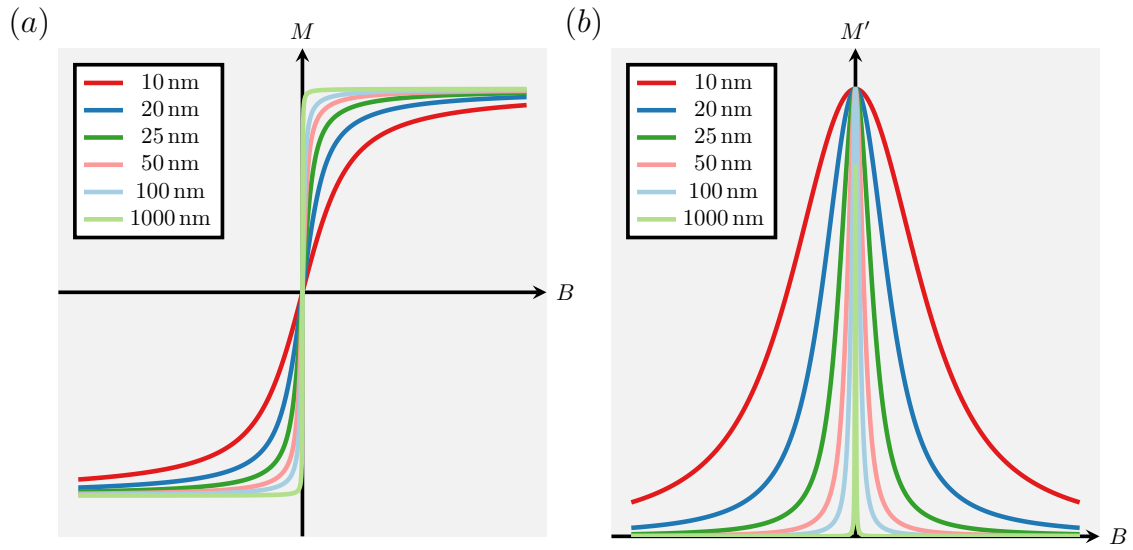

Figure 2.15.: (a) A graphical illustration of the Langevin model for particles with different core sizes. The dynamic range of the particles becomes narrower with increasing core diameter. (b) The derivative of the Langevin model for different core size diameters. The convolution kernel becomes narrower and sharper as the particle size increases.

dynamic range of the particle is quite narrow. A narrow dynamic range leads to a sharp answer in the response signal to an oscillating magnetic field. Additionally, the derivative of the magnetization helps to assess the possible resolution further. The derivative of the magnetization is described by

$$\frac{d}{dB}M(B) = cm\frac{m}{k_\mathrm{B}T}\frac{d}{dB}\mathcal{L}(\xi_\mathrm{r}), \tag{2.34}$$

where

$$\frac{d}{dB}\mathcal{L}(\xi_\mathrm{r}) = \begin{cases} \left(\frac{1}{\xi_\mathrm{r}^2} - \frac{1}{\sinh^2(\xi_\mathrm{r})}\right) & \text{with} \quad \xi_\mathrm{r} > 0 \\ \frac{1}{3} & \text{with} \quad \xi_\mathrm{r} = 0 \end{cases} \tag{2.35}$$

$$\tag{2.36}$$

is the derivative of the Langevin function. ξ_r is given by

$$\xi_\mathrm{r} = \frac{mB}{k_\mathrm{B}T} = \frac{\frac{1}{6}\pi d_\mathrm{c}^3 M_\mathrm{S} G_{r_x} r_x}{k_\mathrm{B}T}, \tag{2.37}$$

where Eq. (2.8) and Eq. (2.10) are substituted in Eq. (2.7). In Fig. 2.15b, the derivative of the Langevin function is shown for particles with different core sizes. The derivative of the Langevin function can also be seen as the point spread function (PSF) or convolution kernel of the particle response [27, 134], where the full width at half maximum (FWHM) can be used as a measure for the resolution (see Fig. 2.16). For a 1D case in x-direction,

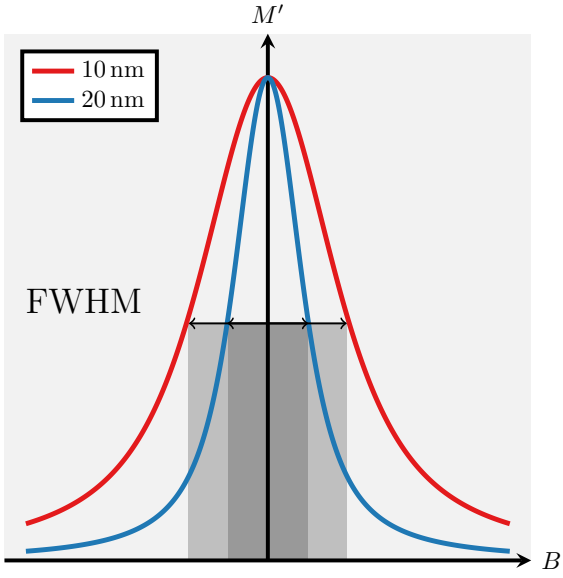

Figure 2.16.: The FWHM is shown for two particle core diameters. With increasing core diameters the FWHM becomes smaller. A smaller FWHM leads to a better spatial resolution.

the spatial resolution Δr_x is defined as

$$\Delta r_x = \frac{k_\mathrm{B} T}{\frac{1}{6}\pi d_\mathrm{c}^3 M_\mathrm{S} G_{r_x}} \Delta\xi_\mathrm{FWHM}, \tag{2.38}$$

where the FWHM $\Delta\xi_\mathrm{FWHM}$ of the derivative of the Langevin function is calculated numerically to approximately 4.16 [27]. Eq. (2.38) reveals the dependency on the involved physical quantities. The resolution is mainly dependent on

- the reciprocal of the gradient $\Delta r_x \propto G_{r_x}^{-1}$,
- the power of 3 reciprocal of the diameter magnetic core $\Delta r_x \propto d_\mathrm{c}^{-3}$,
- and linear on the temperature $\Delta r_x \propto T$.

This means that an increase in the gradient strength improves the spatial resolution, because the FFP becomes smaller and thus, the particle signal is generated from a more precise location. However, this assumption only holds if the particles are still providing a sufficiently high SNR. The greatest influence of the resolution has the particle core diameter, as the power of 3 reciprocal indicates. In [23], the particle/gradient combination of $30\,\mathrm{nm}$ and $5.5\,\mathrm{T\,m^{-1}}/\mu_0$ should allow a theoretical resolution of about $0.5\,\mathrm{mm}$ but due to the wide distribution of particles sizes and regularization, only a resolution of $\Delta r_x \approx 1.5\,\mathrm{mm}$ was achieved [27]. Additionally, the distribution of the particle core diameter distribution limits the prediction of the resolution by the particle diameter further because in practical scenarios particle distributions with mono-sized particles are not available [27]. At first sight, the temperature parameter seems to be a simple way to improve the spatial resolution as a bisection of the temperature, for example from $20\,^\circ\mathrm{C}$ to $10\,^\circ\mathrm{C}$, would lead to an resolution improvement of factor 2, but this is wrong. In reality, the temperature is denoted in kelvin and a temperature drop from $293\,\mathrm{K}$ to $283\,\mathrm{K}$ would only mean an improvement factor of 1.035.

It should be noted that the actual resolution is not linked to the image resolution encoded in the discretization of the system matrix. If the delta sample and the voxels of the system matrix are decreased, it does not necessarily increase the resolution. As the delta sample becomes very small, the SNR of the measured signal drops and the system matrix entries become noisier. Therefore, the SNR usually limits the voxel size and the choice of the grid [135, 125]. In this context, the resolution means that two objects or delta samples can be identified as such, if the intensity between the maxima of the respective PSFs drops below the FWHM. Otherwise, the two objects cannot be separated from each other and appear to be one larger object. If the two point are just separable, the distance from one maxima to the other maximum can be defined as the spatial resolution.

Beside the resolution, the sensitivity of an imaging technique plays an important role for many medical applications. In MPI, the sensitivity can be simplified described as the

minimum amount of magnetic material that is still detectable [89](p.69). In [136], it was shown that by use of gradiometer coils $5\,\mathrm{ng}$ of LS-008 are detectable in $2.14\,\mathrm{s}$. In this case, a moving delta sample has to be identified within a sequence of images to ensure that artifacts are not falsely misinterpreted as the sensitivity level. For some applications, the sensitivity is reported as the number of detectable cells that have uptaken the magnetic particles [53]. The sensitivity can be increased by averaging multiple measurements, but this is usually a tradeoff with the temporal resolution. Further readings on the definition and estimation methods of the sensitivity can be found in [136].

2.6. Magnetic force on magnetic particles

Lately, a continues shift of the FF has been used for MPI force applications as described in [66, 137, 64]. Here, the FF are utilized to rotate the FFP around an object to induce a torque. With these rotating FF it is possible to rotate single or multiple screws or a radiation source could be screwed out of its shielding at a target site [66]. Further, magnetic micro devices can be navigated toward target regions [67].

Beside using rotational FF to induced a magnetic force, it is possible to induced a directed magnetic force with the FF. With the FF introduced in the section 2.3.2, it is possible to move the FFP to an arbitrary position inside the scanner in each dimension. If the FFP is positioned very far towards the border of the scanner, the magnetic field strength on the other side increases equivalently [67]. As the magnetic field vector becomes stronger, the magnetic field induces a noticeable magnetic force on the particles. In the following, the force equation is derived based on the findings published in [99]. As described in section 2.1.3, the magnetization $\boldsymbol{M}$ is the resulting sum of all domain magnetizations within a volume containing magnetic particles. The magnetic moment

$$\bar{\boldsymbol{m}} = \boldsymbol{M} V_\mathrm{c} \tag{2.39}$$

of a particle is given by the product of the magnetization and the volume $V_\mathrm{c} = \frac{4}{3}\pi r_\mathrm{c}^3$ of its magnetic core with r_c being the radius. By applying an external magnetic field, the magnetization can be expressed as

$$\boldsymbol{M} = \Delta\chi \boldsymbol{H} \tag{2.40}$$

where $\Delta\chi = \chi_\mathrm{v} - \chi_w$ is the effective susceptibility of the particle χ_v and water χ_w for example. With magnetic flux density $\boldsymbol{B} = \mu_0(1+\chi_v)\boldsymbol{H}$, the magnetization becomes

$$\boldsymbol{M} = \Delta\chi \frac{\boldsymbol{B}}{\mu_0(1+\chi_\mathrm{v})} \tag{2.41}$$

and the magnetic moment is determined by

$$\boldsymbol{m} = \Delta\chi V_{\mathrm{c}} \frac{\boldsymbol{B}}{\mu_0(1+\chi_{\mathrm{v}})}. \tag{2.42}$$

If we assume that the magnetic moments of the particles are point dipoles, then the force $\boldsymbol{F}_m$ acting on the particles within a magnetic field can be expressed as

$$\boldsymbol{F}_m = (\bar{\boldsymbol{m}} \cdot \nabla)\boldsymbol{B}. \tag{2.43}$$

Hence, the magnetic dipole of the particles experiences a force proportional to the gradient in the direction of the vector field $\boldsymbol{B}$. The dipole of the particles only experiences a translation movement by the induced force within a gradient field. Within a uniform magnetic field, the dipoles of the particles align along the field lines. They perform a rotational movement due to the torque induced by the magnetic field. By combining Eq. (2.42) and Eq. (2.43), the force is given by

$$\boldsymbol{F}_m = \frac{V_{\mathrm{c}}\Delta\chi}{\mu_0(1+\chi_{\mathrm{v}})}(\boldsymbol{B} \cdot \nabla)\boldsymbol{B}. \tag{2.44}$$

The Ampere's circuital law $\nabla \times \boldsymbol{B} = \mu_0(\boldsymbol{J} + \frac{\partial \boldsymbol{E}}{\partial t})$ becomes $\nabla \times \boldsymbol{B} = 0$ with the constraints of no electrical current $\boldsymbol{J}$ and no oscillating magnetic field. The reason is that there is no source of magnetic induction within the particles. With the transformation

$$\nabla(\boldsymbol{B} \cdot \boldsymbol{B}) = 2\boldsymbol{B} \times (\nabla \times \boldsymbol{B}) + 2(\boldsymbol{B} \cdot \nabla)\boldsymbol{B} = 2(\boldsymbol{B} \cdot \nabla)\boldsymbol{B} \tag{2.45}$$

and the constrained Ampere's circuital law, the magnetic force on an isotropic suspension of magnetic particles in a magnetic gradient field [99](p.592) can be written as

$$\begin{aligned} \boldsymbol{F}_m &= \frac{V_{\mathrm{c}}\Delta\chi}{\mu_0}(\boldsymbol{B} \cdot \nabla)\boldsymbol{B} \\ &= V_{\mathrm{c}}\Delta\chi\nabla(\frac{\|\boldsymbol{B}\|^2}{2\mu_0}) \\ &= \frac{4}{3}\pi r_{\mathrm{c}}^3\Delta\chi\nabla(\frac{\|\boldsymbol{B}\|^2}{2\mu_0}). \end{aligned} \tag{2.46}$$

As described in section 2.3, the magnitude of the magnetic selection field of an MPI FFP scanner increases linearly with distance to the FFP. In the y-direction, the magnetic flux density is given by

$$B_y = \mu_0 H_y = \mu_0 G_y y, \tag{2.47}$$

where $G_y = \frac{\partial H_y}{\partial y}$ is the gradient strength and H_y is the magnetic field in y-direction. It is assumed that the origin of coordinates is the FFP. Therefore, the magnetic force induced by the gradient field on the magnetic particles [67] in the y-direction can be expressed as

$$\begin{aligned} \boldsymbol{F}_m &= \frac{4}{3}\pi r_\mathrm{c}^3 \Delta\chi \nabla \left(\frac{\|\boldsymbol{B}\|^2}{2\mu_0}\right) \\ &= \frac{2\mu_0}{3}\pi r_\mathrm{c}^3 \Delta\chi \nabla (G_y^2 y^2) \\ &= \frac{4\mu_0}{3}\pi r_\mathrm{c}^3 \Delta\chi G_y^2 y. \end{aligned} \tag{2.48}$$

From Eq. (2.48), it becomes evident that the magnetic force on particles is

- linearly dependent on the distance to the FFP ($\boldsymbol{F}_m \propto y$),
- quadratically dependent on the gradient strength ($\boldsymbol{F}_m \propto G_y^2$), and
- cubically dependent on the particle core radius ($\boldsymbol{F}_m \propto r_\mathrm{c}^3$).

These characteristics need to be considered if magnetic particles should be used for navigation applications in an MPI scanner.

2.6.1. Magnetic particle imaging and magnetic particle navigation

Originally, the FF have been designed to enlarge the FoV, but as outlined above, the FF can be utilized to induce a magnetic force on particles. This allows to navigate the particles to a desired position, if the FFP position is chosen appropriately. The use of the FF as a navigational force is called navigation mode in this work. Consequently, this navigation mode can be combined with the normal imaging mode because the FF positions can be switched quite fast with a frequency of $2.9\,\mathrm{Hz}$, which is a current hardware limitation on the Bruker MPI scanner resulting from a fixed time of the feedback loop. The combination of navigation and imaging mode, which is a core proposal of the presented thesis, enables to quasi-simultaneous navigation and imaging of magnetic particles. The particles can be moved toward a target position and it can be controlled by imaging whether the particles have reached it. The principle of switching between navigation and imaging mode is shown in Fig. 2.17. However, the imaging and navigation modes cannot be performed in parallel and have to be executed in an alternating manner. Thus, the magnetic force is

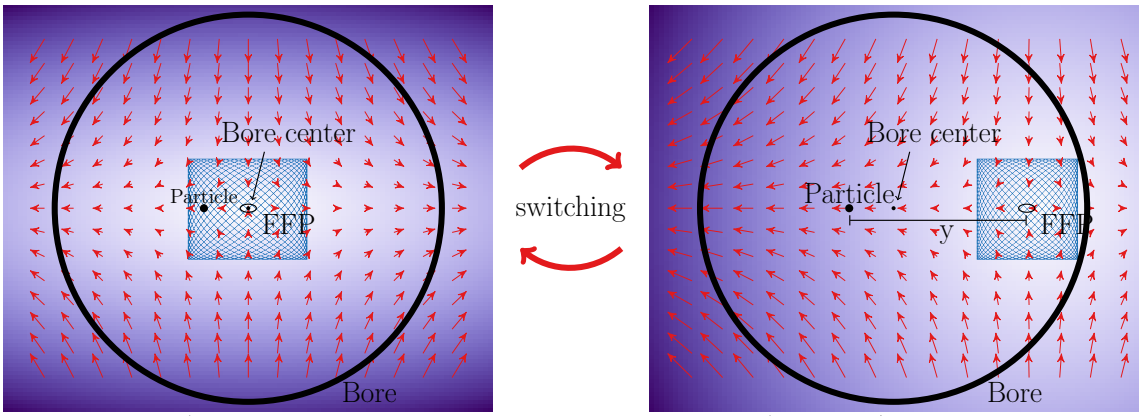

Figure 2.17.: (a) Visualization of the FFP position during imaging mode. The magnetic particles (indicated by a black dot) are within the FoV. (b) Illustration of the FFP position during the navigation mode. The magnetic particles are not within the FoV but the particles are moved due to the induced force by a distance y from the FFP.

only induced during the navigation time span. Consequently, Eq. (2.48) has to be extended with a switching function $s(t)$ yielding the following equation

$$F_{m,y}(y,t) = \frac{4}{3}\pi\mu_0 r_m^3 \Delta\chi_\mathrm{v} G_y^2 y s(t) \tag{2.49}$$

$$\text{with } s(t) = \begin{cases} 1 & \text{if } t \in [T_\mathrm{L}(i-1)N_\mathrm{nc} + T_\mathrm{L} i N_\mathrm{ic}, T_\mathrm{L} i (N_\mathrm{nc} + N_\mathrm{ic})] \\ 0 & \text{else} \end{cases}$$

where $i = 1, \ldots, n$, $T_\mathrm{L} = 0.021\,\mathrm{s}$ and N_ic is the number of imaging drive cycles and N_nc is the number of navigation drive field cycles. The time span of one acquisition cycle is denoted with T_L and y is the distance to the FFP. It is assumed that the object is within the FFP region during the imaging mode and no magnetic force acts on the particles. The maximal FFP movement is dependent on the gradient field strength and the DF strength as discussed in section 2.3.2. With a reduced gradient strength, the FFP can be moved further away from the bore center. However, as the dependencies ($\boldsymbol{F}_m \propto G_y^2, \boldsymbol{F}_m \propto y$) indicate, it is reasonable to choose the largest gradient strength in order to achieved the greatest magnetic force.

Eventually, the overall temporal imaging resolution is reduced during the combined navigation and imaging mode, because no useful images are acquired during the navigation mode. The temporal imaging resolution depends on the ratio between the imaging- and the navigation drive field cycles $N_\mathrm{nc}/N_\mathrm{ic}$. The temporal delay between switching the modes is denoted with T_s. The time span for a drive field cycle is given with T_L. The combination of both results in a temporal resolution of

$$f_\mathrm{ImagNavi} = \frac{1}{N_\mathrm{nc} \cdot T_\mathrm{L} + N_\mathrm{ic} \cdot T_\mathrm{L} + 2T_\mathrm{s}}, \text{ with } 0 < N_\mathrm{nc}, 0 < N_\mathrm{ic}. \tag{2.50}$$

The ratio between navigation and imaging mode is defined by the user. It can be chosen based on the application requirements. If the focus of the application is more on the navigational characteristics, the number of navigation Lissajous cycles can be increased, but consequently only a single image can be taken once in a while. Otherwise, if the imaging is important and the application requires only little navigational manipulations, the ratio can have the same number of Lissajous cycles for both.

2.7. Materials

In the following sections, materials like magnetic particles and scanners used in this thesis are described with their different properties and capabilities.

2.7.1. Magnetic particles

As the availability of Resovist and LS008 is limited, perimag (micromod Partikeltechnologie GmbH, Germany) is used as an commercially available alternative. The Dynabeads MyOne (ThermoFisher, US), Nanomag/synomag-D (micromod Partikeltechnologie GmbH, Germany) and magnetic lacquer particles (Magneto Magnetic Lacquer, Hand & Nail Harmony, US) are used in dedicated application scenarios.

Perimag

The perimag particles have a hydrodynamic diameter d_h of $130\,\mathrm{nm}$ with a dextran shell. The magnetic core has a diameter d_c of about $25\,\mathrm{nm}$ and the perimag can be coated with NH_2, COOH or Streptavidin. These surface structures are able to form covalent bindings to proteins, antibodies or other molecules.

Dynabeads MyOne

Parts of this work investigate the imaging properties and magnetic mobility characteristics of magnetic particles. Therefore, micro-sized particles called beads are used in several experiments. The Dynabeads MyOne particles have an hydrodynamic diameter of $1000\,\mathrm{nm}$. Their multi-core iron oxide structure can be seen in Fig. 2.3 where each iron core is spherically shaped [138]. Despite their large diameter, the particles act superparamagnetic [138]. All multi-cores are embedded in a polystyrene matrix. This polymer makes the beads not bio-degradable and thus, not suitable for *in-vivo* applications. The beads are mainly used to separate biological materials, such as cells, proteins and nucleic acids, in life science applications. The beads have a functionalized surface that can bond to the biological material, which is then extracted from the remaining material via an induced magnetic force. Per design, the beads have an excellent magnetic mobility. Due to these

magnetic mobility properties, the beads are used as a reference for imaging and navigation experiments in chapter 6. Besides being useful for magnetic manipulation, the beads have also been utilized in neurological studies with MRI where their larger size is a key feature [14]. Due to their larger size, the particles can be used for a passive targeting without suffering from the Enhanced Permeability Retention (EPR) effect. The EPR effect occurs when smaller particles cross the brain-blood barrier (BBB) and accumulate within a lesion or tumor. If one wants to target expressed antigens with functionalized beads, the specificity is reduced because one cannot rely on the correlation between intensity (concentration) of beads to express antigen [14]. Especially at inflammatory processes, the endothelial barriers can have leakages as large as $700\,\mathrm{nm}$ in their flammatory vessel and capillaries [99](p.546). The larger beads are not able to cross the BBB and show no EPR effect. It is worth noting that the toxicity of micro-sized particles is generally considered less compared to nano-sized particles since the surface to volume ratio is much smaller for a given mass. Therefore, a smaller reactive area gives less possibilities to interact with cell membranes [99](p.552), [139].

Nanomag/synomag-D particles

Since the beads are not biocompatible and not designed for MPI, a special particle combination is designed by micromod for the purpose of MPI and navigation through magnetic fields. These customized multi-core particles consist of nanomag and synomag with hydrodynamic diameters in the range of $700\,\mathrm{nm}$ (iron core $500\,\mathrm{nm}$ to $600\,\mathrm{nm}$) and have been designed and synthesized by micromod. Like Resovist they have a biocompatible dextran shell. Synomag-D has excellent MPI imaging characteristics but lacks sufficient magnetic mobility properties [140]. On the contrary, nanomag-D particles with diameters in the range of $250\,\mathrm{nm}$ to $500\,\mathrm{nm}$ reveal a high magnetic mobility [141]. In order to combine the imaging characteristic of synomag-D and the magneto-mobility characteristics of nanomag-D, synomag is embedded in the iron oxide multi-cores of nanomag. Afterwards, the combined particles are coated with dextran to protect them from agglomeration. The structure of the nanomag/synomag-D particles can be seen in a transmission electron microscopy (TEM) image in Fig. 2.18. The customzied nanomag/synomag-D particles are studied in detail in chapter 6.

Magnetic lacquer particles

As a third particle type, magnetic lacquer particles (Magneto Magnetic Lacquer, Hand & Nail Harmony, US) are used in chapter 5 for their coating abilities. These particles are usually used as nail polish. The lacquer particles can easily be coated on medical instruments as they dry very fast and do not dissolve in aqueous solutions. They are not suitable for *in-vivo* applications, but they are practical MPI particles for *in-vitro* experiments.

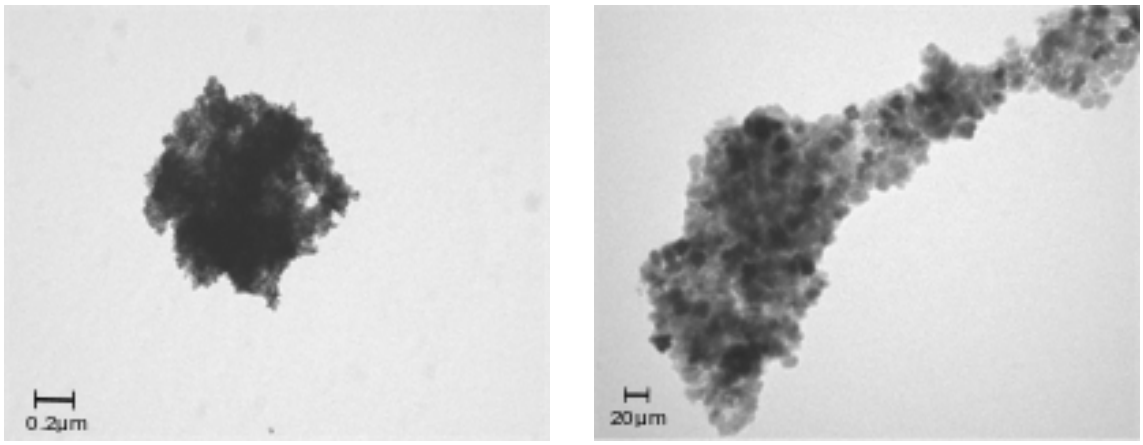

(a) (b)

Figure 2.18.: TEM images of nanomag/synomag-D particles. Measures for scale (a) $0.2\,\mu\mathrm{m}$ and (b) $20\,\mu\mathrm{m}$.

2.7.2. Magnetic particle spectrometer

An MPS has no spatial encoding and represents basically a 0-dimensional MPI scanner. As described in 2.2, it excites a sample of particles within a defined volume V_{MPS}. The excitation usually uses a frequency f_{MPS} around $20\,\mathrm{kHz}$ and an amplitude A_{MPS} of up to $30\,\mathrm{mT}$ [142]. During the excitation the received signal is filtered and noise matching steps are preformed to remove the excitation signal from the resulting signal. Then the filtered signal is transformed into Fourier space. By normalizing the particle samples with their iron concentration to a defined iron quantity, the spectra of several different particle types and batches can be compared in terms of signal-to-noise ratio (SNR) of the 3rd harmonic and the number of odd numbered harmonics above the noise level. The SNR of the 3rd harmonic is also an indicator to what extent the sample can be further diluted while still inducing a measurable signal. As an example, the spectra of perimag, nanomag/synomag-D and Dynabeads normalized to the same iron mass are visualized in Fig. 2.19a. An impor-

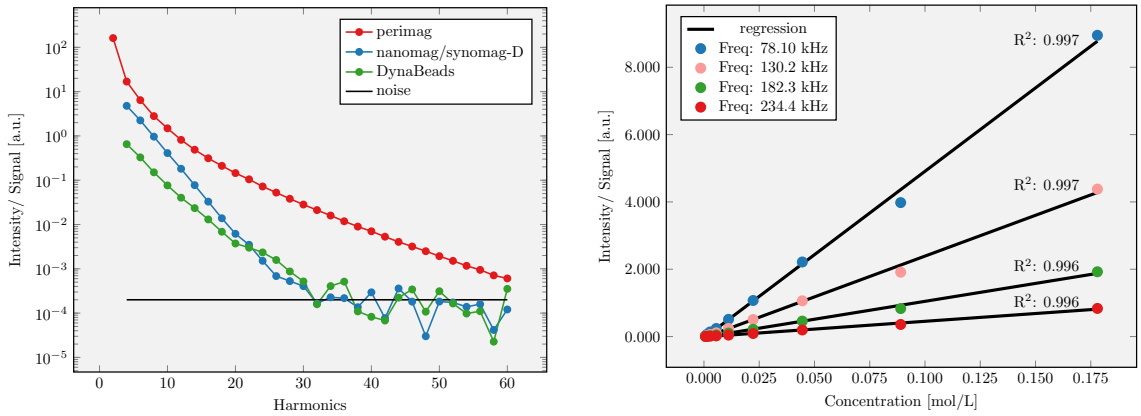

(a) (b)

Figure 2.19.: (a) MPS spectrum of perimag, nanomag/synomag-D and Dynabeads. (b) Intensities of selected frequencies for nanomag/synomag-D particles at different concentrations.

tant prerequisite for all MPI particles is the linearity of the MPI signal with respect to the particles concentration. This means that with linear decreasing particle concentration, the MPI signal intensity has to decrease linearly as well, which is a basic assumption for the MPI reconstruction. In Fig. 2.19b, the intensities of the selected frequencies for nanomag/synomag-D can be seen at different concentrations. At each frequency, the linearity of the MPI signal to the particles concentration is given, as the regression lines with coefficients of determination close to one indicate. This linear characteristic ensures the usability of MPI in a wide range of medical applications where quantification of the MPI signal is relevant. If the particles interact with each other or aggregate within an *in-vivo* enviroment, this linearity might be not given anymore [99](p.589), but the particle coating usually prevents an aggregation.

The MPS results presented in this work are measured with a custom-built MPS with $f_{\text{MPS}} = 26.042\,\text{kHz}$ and $A_{\text{MPS}} = 20\,\text{mT}$. The design is similar to Biederer et al. [143, 142]. Recently, more sophisticated, multidimensional MPSs are developed by Graeser et al. [118, 126] and v. Gladiß et al. [125]. Both multidimensional MPSs excite the particles in more than one direction and can reproduce the excitation of an MPI scanner.

2.7.3. Bruker MPI scanner

For an MPI scanner in contrast to an MPS, the determination of the spatial distribution of magnetic material is the essential functionality. All MPI measurements carried out in this work are acquired with a preclinical MPI scanner (Bruker Biospin MRI GmbH, Germany), which can be seen in Fig. 2.20. The scanner features a circular bore diam-

Figure 2.20.: Bruker scanner inside room with copper shielding.

eter of $d_{\text{Scanner}} = 118\,\text{mm}$, allowing experiments with small rodents such as mice and

rats. The scanner topology is an FFP setup and the system matrix reconstruction technique is mainly used for image reconstruction although it is also possible to do x-space reconstructions. The gradient strength can be adjusted to a maximal gradient strength G_z of up to $2.5\,\mathrm{T\,m^{-1}}$ in the z-direction. The maximal gradient strengths in x- and y-directions are $-1.25\,\mathrm{T\,m^{-1}}$ accordingly. The drive field amplitude can be regulated to a maximum of $14\,\mathrm{mT}$ in all three directions. The excitation frequencies are given by $f_x = 2.5/102\,\mathrm{MHz}$, $f_y = 2.5/96\,\mathrm{MHz}$ and $f_z = 2.5/99\,\mathrm{MHz}$. This choice of frequencies leads to a temporal resolution of one Lissajous cycle of $f_{\text{temporal}} = 46.43\,\mathrm{Hz}$. It follows that one 3D image takes $T_\mathrm{L} = 0.021\,\mathrm{ms}$ to acquire. The choice of the maximal gradient strength and amplitude leads to a relative small FoV with dimensions $\mathrm{FoV}_{\text{min}} = 22.4\,\mathrm{mm} \times 22.4\,\mathrm{mm} \times 11.2\,\mathrm{mm}$. Based on a more common gradient strength $0.75\,\mathrm{T\,m^{-1}}$ and an amplitude of $14\,\mathrm{mT}$, the FoV increases to FoV$= 74.6\,\mathrm{mm} \times 74.6\,\mathrm{mm} \times 37.3\,\mathrm{mm}$. The Bruker scanner has a maximal FF amplitude $A_{x,y,\text{FF}} = 18\,\mathrm{mT}$ in x- and y-directions and $A_{z,\text{FF}} = 42\,\mathrm{mT}$ in z-direction. This results in an enlarged FoV_{FF} with size of $51.2\,\mathrm{mm} \times 51.2\,\mathrm{mm} \times 44.8\,\mathrm{mm}$ and a maximal translation $t_{\text{FF},x} = 14.4\,\mathrm{mm}$, $t_{\text{FF},y} = 14.4\,\mathrm{mm}$, and $t_{\text{FF},z} = 16.8\,\mathrm{mm}$. Up to date, the temporal delay between switching the between focus field positions is $T_\mathrm{s} \approx 7 \cdot T_\mathrm{L} = 0.147\,\mathrm{s}$, which is a technical limitation of the Bruker scanner so far. With the time span for a 3D Lissajous cycle $T_\mathrm{L} = 0.021\,\mathrm{s}$, the temporal resolution for a drive field cycle ratio of 1/1 becomes around $3\,\mathrm{Hz}$.

3. Submillimeter-Accurate Marker Localization

Contents

3.1. Introduction and motivation

As stated in section 2.7.3, MPI achieves a high temporal resolution of $46\,\mathrm{Hz}$. This high temporal resolution qualifies MPI for a wide range of real-time medical applications, such as device tracking, image-based navigation and functional brain imaging. The suitability of MPI for interventional applications, such as catheter tracking, has been examined in several publications [59, 59, 61, 41]. At first, a catheter was coated with SPIONs and its position is tracked via MPI [59]. Further, a SPION-coated catheter was used to both track the position of the catheter and to clear vessel occlusions, where the position of the catheter and the condition of the stenosis are monitored with MPI [61]. In this context, multi-contrast techniques allow to visualize the instruments and vessels separately [41]. Interventional applications including the use of fiducial markers [144] require a precise localization of the medical instruments. These interventional applications rely on automated algorithms to identify the instruments position in medical images.

One way to achieve a precise localization is to perform imaging with a high spatial resolution. As stated in section 2.5.4, the spatial resolution in MPI mainly depends on the gradient strength and the tracer properties. Although the tracers have improved, the resolution gain is limited by physical contraints [101, 100]. According to [145, 26, 134], a spatial resolution better than $1\,\mathrm{mm}$ can be achieved for gradient fields in the range of $2.5\,\mathrm{T\,m^{-1}}$ to $7\,\mathrm{T\,m^{-1}}$. Unfortunately, the gradient strength of clinical MPI scanners with high temporal resolution will probably be in the range of $1\,\mathrm{T\,m^{-1}}$ to $3\,\mathrm{T\,m^{-1}}$. Stronger gradients are challenging to build because of the electrical power loss of the field generating coils. However, even a spatial resolution of $1\,\mathrm{mm}$ can hardly compete with the spatial resolution in X-ray-based DSA [3]. Therefore, accurate instrument localization is challenging with MPI. Nevertheless, other imaging modalities, such as CT and MRI, have circumvented the issue by applying automated subpixel-accurate localization approaches [146]. For this purpose, markers are initially localized within the images by a threshold-based segmentation algorithm. Afterwards, their positions are precisely estimated by determining the center of mass of the voxel intensities inside the pre-segmented areas.

In this chapter, the same approach is applied to MPI images to enhance the detection precision of the markers. A series of phantom measurements taken at full temporal resolution (46 Hz) is used to analyze random and systematical errors of this method. Further, the performance and stability of the automatic submillimeter-accurate marker localization algorithm are discussed. It is also worth noting that the high temporal resolution of MPI is promising for interventional applications since the X-ray-based DSA uses ionizing radiation. As this radiation should be minimized, a constant tracking of the instruments needs to be avoided [147].

3.2. Material and methods

3.2.1. Imaging parameters

All MPI measurements are performed with a preclinical MPI scanner as described in section 2.7.3. The gradient strength is set to $1.5\,\mathrm{T\,m^{-1}}$ in z-direction and $-0.75\,\mathrm{T\,m^{-1}}$ in x- and y-directions. This results in a DF FoV of $37.3\,\mathrm{mm} \times 37.3\,\mathrm{mm} \times 18.7\,\mathrm{mm}$. In order to reconstruct the images, a system matrix is acquired prior to the reconstruction. In this context, a delta sample of size $2\,\mathrm{mm} \times 2\,\mathrm{mm} \times 1\,\mathrm{mm}$ is filled with $4\,\mu\mathrm{L}$ ferucarbotran (Resovist, Irom Pharmaceuticals, Japan). The ferucarbotran has an iron concentration of $83\,\mathrm{mmol\,L^{-1}}$. To acquire the system matrix, the delta sample is moved to $20 \times 20 \times 20$ equidistant positions in a $40\,\mathrm{mm} \times 40\,\mathrm{mm} \times 20\,\mathrm{mm}$ FoV. At each position, the particle response signal is recorded for 30 Lissajous cycles.

For reconstruction, the algebraic approach, presented in section 2.5.1, is used. Further, in a post processing step, the frequencies of the Fourier-transformed particle signal below $80\,\mathrm{kHz}$ are discarded because the frequencies below $80\,\mathrm{kHz}$ carry unpredictable background signal. This background signal influences the reconstruction negatively as it cannot be reliably subtracted from the actual particle signal. Additionally, an SNR threshold of $\Theta = 3$ is applied to remove noisy rows from the system matrix, as done by the selection algorithm presented in [26]. Finally, the MPI images are obtained using a first-order Tikhonov-regularized least squares approach as discussed in section 2.5.2. The number of Kaczmarz iterations n_{iter} is set to 3. In Fig. 3.1, the effect of the regularization parameter λ is illustrated. In general, if λ is chosen too small, the image contains artifacts. The artifacts can be reduced by increasing λ. However, if λ is increased too much, the images are smoothed, which leads to a loss of resolution. For the data used in the following experiments, a good trade-off between a too noisy and an over-smoothed image can be achieved with $\lambda = 0.01$. For $\lambda = 0.01$, a spatial resolution in terms of the FWHM of $6.3\,\mathrm{mm}$, $8.0\,\mathrm{mm}$, and $3.7\,\mathrm{mm}$ in x-, y-, and z-direction is achieved. These results agree quite well with the estimated values of $5.97\,\mathrm{mm}$, $5.97\,\mathrm{mm}$, and $2.99\,\mathrm{mm}$ using the resolution formula discussed in [27], where a particle core diameter of $25\,\mathrm{nm}$ is assumed. Due to different characteristics of the x- and y-receive channels, differences of x- and y-resolutions can occur.

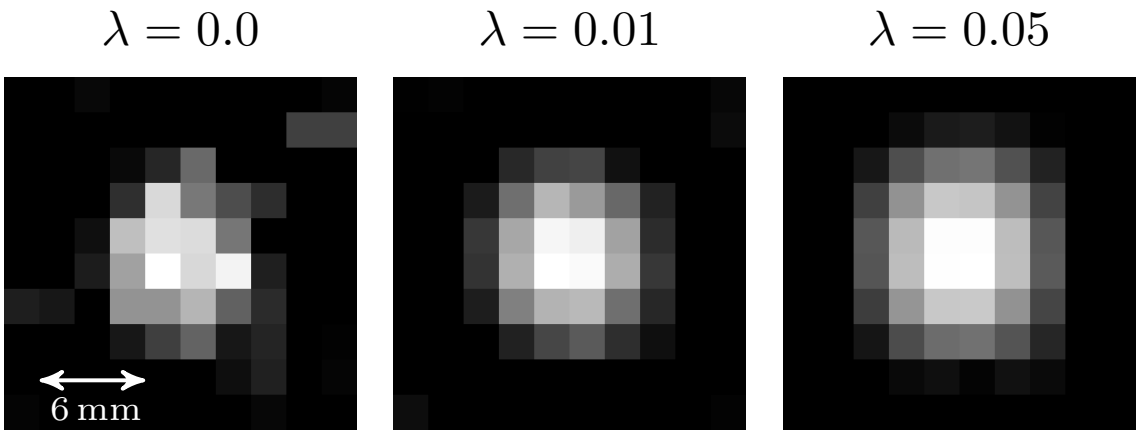

Figure 3.1.: Effect of the regularization parameter λ on the reconstruction images. The delta sample is presented in cropped xy-slices within a 3D MPI image with a FoV size of $37.3\,\mathrm{mm} \times 37.3\,\mathrm{mm} \times 18.7\,\mathrm{mm}$. From left to right, the images are reconstructed with regularization parameters $\lambda = 0$, $\lambda = 0.01$, and $\lambda = 0.05$. Without regularization (i.e. $\lambda = 0$), the image of the marker shows a lot of noise. The image in the middle with $\lambda = 0.01$ provides a good compromise between noise reduction and spatial resolution. The right image has almost no noise, but suffers from over-regularization that results in a loss of spatial resolution.

3.2.2. Automatic marker localization

Even slight adjustments in the position of a marker can lead to small changes in the image intensities. In Fig. 3.2, this effect is demonstrated for the spatial distribution of the particle signal in the reconstructed images. With this in mind, the established intensity-based subvoxel-accurate marker detection is motivated for the task. In detail, the well-known intensity centroiding approach is applied, which has been used in several imaging modalities and medical applications [148, 149]. For the automatic marker localization, a

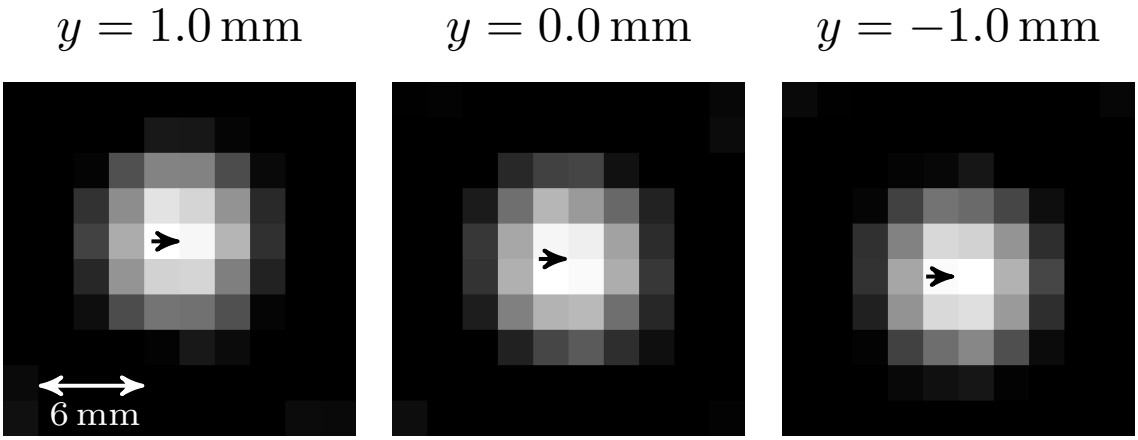

Figure 3.2.: Effect of the movement of the delta sample on the reconstruction images. The delta sample is shown in cropped xy-slices of a 3D MPI image within a FoV of $37.3\,\mathrm{mm} \times 37.3\,\mathrm{mm} \times 18.7\,\mathrm{mm}$. The markers are positioned at $y = 1\,\mathrm{mm}$ (left), $0\,\mathrm{mm}$ (middle) and $-1\,\mathrm{mm}$ (right) with the same x- and z-position. Although each voxel is $2\,\mathrm{mm}$ in size in y-direction, changes in the intensity distribution within the gray scale images are visible.

set of all MPI images from a dynamic MPI experiment is denoted with $I : \Omega_s \times \mathbb{R} \to \mathbb{R}$ ($\Omega_s \subset \mathbb{R}^3$). Thus, $I(\boldsymbol{x}, t)$ represents the reconstructed particle concentration at spatial position $\boldsymbol{x}$ and time t. Further, the described automatic marker localization is done in three steps. First, a threshold filter is applied to each image to separate the markers from the background. By this means, the high image intensity structures are left. The result is the data set $I^{\text{segBin}} : \Omega_s \times \mathbb{R} \to \mathbb{R}$ with

$$I^{\text{segBin}}(\boldsymbol{x}, t) = \begin{cases} 1, & \text{if } I(\boldsymbol{x}, t) \geq \Theta_{\text{T}} \cdot \max\limits_{\boldsymbol{x}} I \\ 0, & \text{otherwise,} \end{cases} \tag{3.1}$$

where $\Theta_{\text{T}} \in [0, 1]$ describes the relative threshold. This basic filter operation is visualized in Fig. 3.3a. In general, the influence of the threshold filtering is shown in Fig. 3.5. The reference xy-slice is not filtered, and the other slices correspond to filtered images with relative thresholds of $\Theta_{\text{T}} = \{0.1, 0.3, 0.5, 0.7, 1.0\}$.

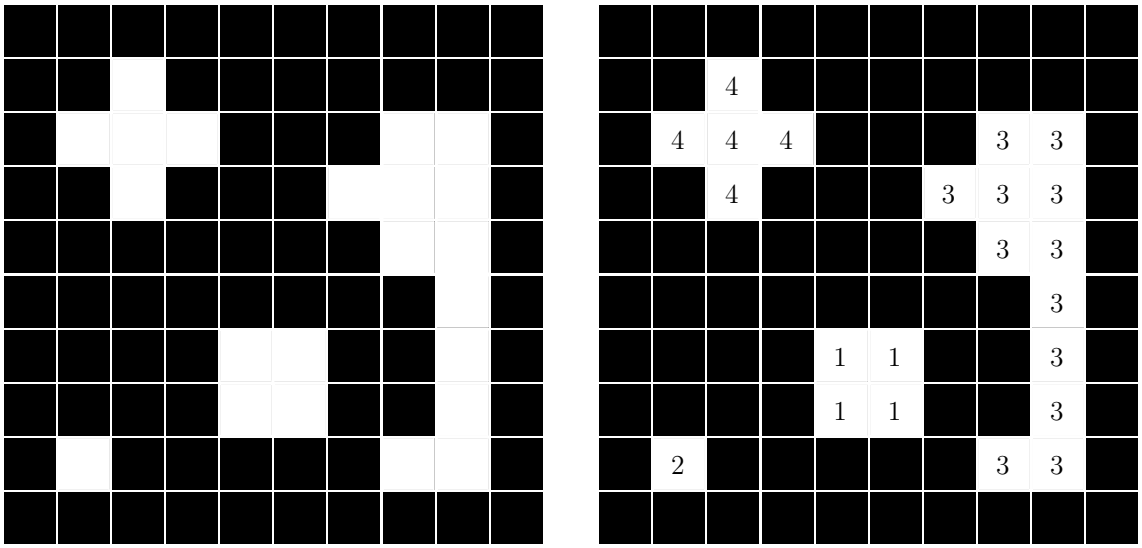

(a) (b)

Figure 3.3.: First two steps of the intensity-based subvoxel-accurate marker detection. (a) Basic threshold filtering is applied to the images in order to separate the marker signal from the background. (b) Connected regions are identified and labeled accordingly.

Secondly, the connected regions $\Omega_l^t \subseteq \Omega_s$, $l \in \{1, 2, \ldots, L_\mathrm{t}\}$ are identified by connected component labeling of $I^{\mathrm{segBin}}(\Omega_s, t)$, $t \in \mathbb{R}$ (see Fig 3.3b). L_t denotes the number of identified regions at time t. Further, the regions are ordered with respect to the maximum intensity value within the region: $\max\, I(\Omega_1^t, t) \geq \max\, I(\Omega_2^t, t) \geq \cdots \geq \max\, I(\Omega_{L_\mathrm{t}}^t, t)$. This ordering is illustrated in Fig. 3.4. In the last step, the number of markers K_M determines the selected regions from which K_M regions are chosen. It is assumed that the number of markers is smaller than the number of regions, i.e. $K_\mathrm{M} < L_\mathrm{t}$. Afterwards, the position of each of the K_M markers $1 \leq k \leq K_\mathrm{M}$ is estimated by determining the center of mass

$$\boldsymbol{c}_k(t) = \frac{\int_{\Omega_k^t} \boldsymbol{x} \cdot I(\boldsymbol{x}, t) \mathrm{d}\boldsymbol{x}}{\int_{\Omega_k^t} I(\boldsymbol{x}, t) \mathrm{d}\boldsymbol{x}} \tag{3.2}$$

of the voxel intensities of the corresponding connected region I. $\boldsymbol{c}_k$ is also referred to as the calculated positions.

3.2.3. Evaluation

For the evaluation, the true position of a marker k is denoted with $\boldsymbol{r}_k : \mathbb{R} \to \mathbb{R}^3$, while t_i, $1 \leq i \leq N$ are the points in time for which an image is reconstructed. With this in mind, the localization error $\boldsymbol{\delta}_k = (\delta_k^x, \delta_k^y, \delta_k^z)$ is calculated by the difference between true and calculated position

$$\boldsymbol{\delta}_k(t_i) = \boldsymbol{r}_k(t_i) - \boldsymbol{c}_k(t_i). \tag{3.3}$$

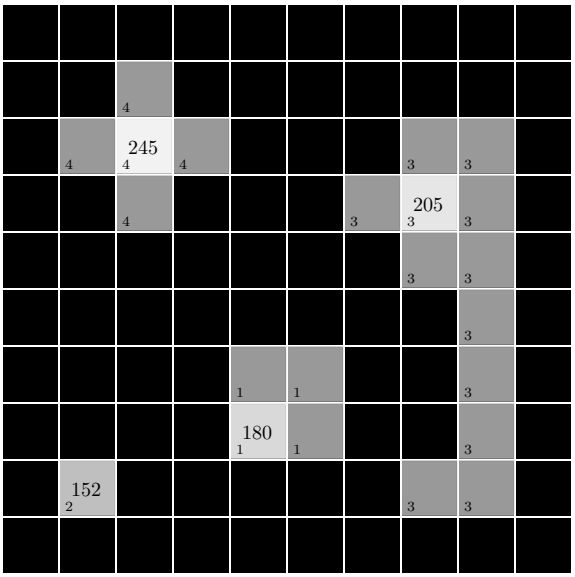

Figure 3.4.: The connected region are ordered with respect to their maximum intensity value within the region.

It has to be noted that this error is the superposition of a random error and a systematic error. Both errors depend on the spatial position and vary in time.

In order to determine the systematic error as a function of the marker position, $\boldsymbol{\delta_k}$ are averaged for all $T_k^{\boldsymbol{x}} = \{t_i | \boldsymbol{r}_k(t_i) = \boldsymbol{x}\}$ to get

$$\mu_k^{\alpha}(\boldsymbol{x}) = \frac{1}{|T_k^{\boldsymbol{x}}|} \sum_{t \in T_k^{\boldsymbol{x}}} \delta_k^{\alpha}(t), \tag{3.4}$$

for $\alpha = x, y, z$. The corresponding random error is calculated by the standard deviation

$$\sigma_k^{\alpha}(\boldsymbol{x}) = \sqrt{\frac{1}{|T_k^{\boldsymbol{x}}|} \sum_{t \in T_k^{\boldsymbol{x}}} \left(\delta_k^{\alpha}(t) - \mu_k^{\alpha}(\boldsymbol{x})\right)^2}. \tag{3.5}$$

3.2.4. Sample positioning

For the sample positioning, a 3 axes robot (Isel Automation GmbH, Germany) is used as it is already equipped to the MPI scanner. The robot is mounted with a $46.5\,\mathrm{cm}$ long fiberglas rod with a diameter of $10\,\mathrm{mm}$. Small tracer samples and other phantoms can be placed at the tip of the rod. The robot moves in three orthogonal directions (x, y, z) with a step size of $6.25\,\mu\mathrm{m}$. This allows for an accurate and reproducible phantom positioning during MPI measurements. In addition, it is used for sampling the system matrix. Consequently, all directions and coordinates can be reached in the robot coordinate system. The image coordinate system and the robot coordinate system are automatically aligned because the same robot is used for both purposes. The origin of the robot coordinate system is adjusted in a way that a $2\,\mathrm{mm} \times 2\,\mathrm{mm} \times 1\,\mathrm{mm}$ delta sample is centered in the DF FoV.

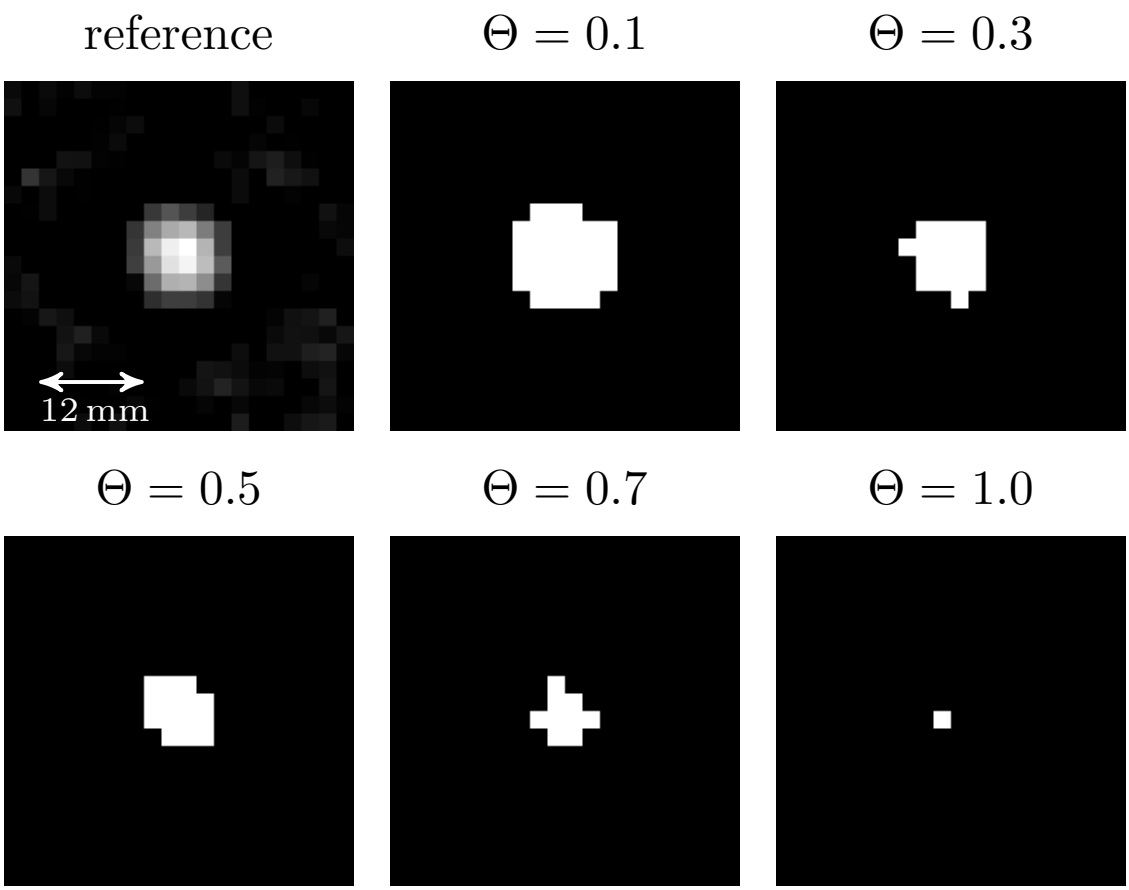

Figure 3.5.: The delta sample is shown in xy-slices of a 3D MPI image with FoV of $37.3\,\mathrm{mm} \times 37.3\,\mathrm{mm} \times 18.7\,\mathrm{mm}$. The image in the top left corner is a reference image reconstructed with $\lambda = 0.01$. The other images show the influence of the applied a threshold filtering with relative thresholds $\Theta_\mathrm{T} = \{0.1, 0.3, 0.5, 0.7, 1.0\}$. In the following experiments, a segmentation threshold $\Theta_\mathrm{T} = 0.3$ is selected.

3.2.5. Marker phantoms

In this chapter, two phantoms are used for the experiments. First, a single-marker-phantom is mounted at the tip of the robot rod. The ground truth of the marker position is provided by the robot coordinates for all experiments that are performed. As a second phantom, a multi-marker phantom is used. It contains three markers (c_1, c_2, and c_3) in a triangular arrangement (see Fig. 3.6a). To get a visual impression, the reconstructed 3D volume images of the multi-marker phantom are presented as maximum intensity projections in Fig. 3.6b. Each of the three markers consists of a hollow sphere with a $2.85\,\mathrm{mm}$ diameter. The spherical sample contains $7.27\,\mu\mathrm{L}$ ferucarbotran with an iron concentration of $83\,\mathrm{mmol\,L^{-1}}$. The phantom is mounted at the tip of the robot rod during measurement. The ground truth positions $\boldsymbol{r}_1$, $\boldsymbol{r}_2$, and $\boldsymbol{r}_3$ of the markers c_{1-3} is not known, but their respective distances $d_{12} = \|\boldsymbol{r}_1 - \boldsymbol{r}_2\|_2$, $d_{13} = \|\boldsymbol{r}_1 - \boldsymbol{r}_3\|_2$, an $d_{23} = \|\boldsymbol{r}_2 - \boldsymbol{r}_3\|_2$ are taken from the 3D CAD drawing of the phantom (see Table 3.1). 3D-printing was performed by selective laser sintering (SLS). SLS has an accuracy of $\pm 0.1\,\mathrm{mm}$. In contrast to the

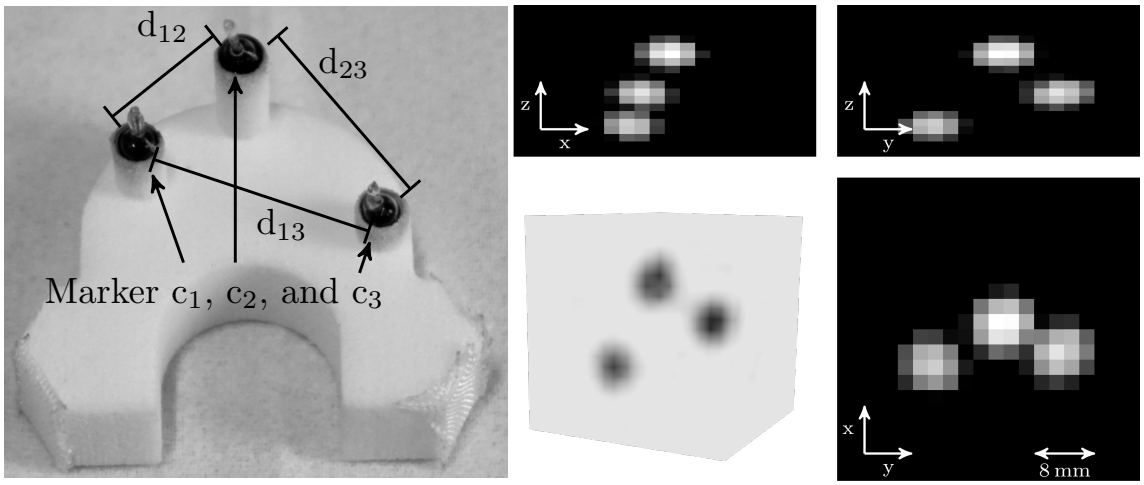

Figure 3.6.: a) Multi-marker phantom with three markers in a triangular setup. b) A reconstructed 3D volume image of the multi-marker phantom is presented as a maximum intensity projection for the xz-, yz- and xy-plane. The reconstructed multi-marker phantom is shown as 3D rendering in the lower left corner.

manufacturing tolerances of the glass spheres holding the tracer ($\pm 0.2\,\mathrm{mm}$), the fixation error of spheres within the socket is negligible low.

Table 3.1.: Distances between center positions of the spheres known from 3D CAD drawing.

	d_{12}	d_{13}	d_{23}
Distance [mm]	9.2 ± 0.3	17.3 ± 0.3	14.1 ± 0.3

3.2.6. Experiments

The feasibility and accuracy of the automated marker localization are first analyzed by performing a series of experiments with the single-marker-phantom. Afterwards, additional experiments with the three-marker-phantom demonstrate the feasibility of a reliable marker identification and localization in more complex multi-marker circumstances.

In the first experiment, the single-marker-phantom is positioned at the origin $\boldsymbol{r}_1 = \mathbf{0}$ of the robot coordinate system. Then, a series of 4000 Lissajous cycles is acquired. In a second experiment, the single-marker-phantom is positioned to 100 randomly chosen locations within the FoV. At each position, a series of 100 Lissajous cycles is measured. In the third, experiment the three-marker-phantom is moved to 100 positions with all three markers within the FoV. Again, the positions are chosen randomly before the experiment. For each position, a series of 100 MPI measurements is acquired.

3.3. Results: Accurate marker tracking

3.3.1. Systematic error and random error

In the first experiment, the center of mass positions of the single-marker are obtained for a sequence of 4000 volume images. The corresponding localization errors $\boldsymbol{\delta}_1(t_i)$, $1 \leq i \leq 4000$ are calculated for 101 equidistantly-spaced relative segmentation thresholds $\Theta_\mathrm{T} \in [0, 1]$. In Fig. 3.7, the x-, y-, and z-components of the localization error are visualized for $\Theta_\mathrm{T} = 0.3$ using only every 25th frame to maintain readability. Further, the

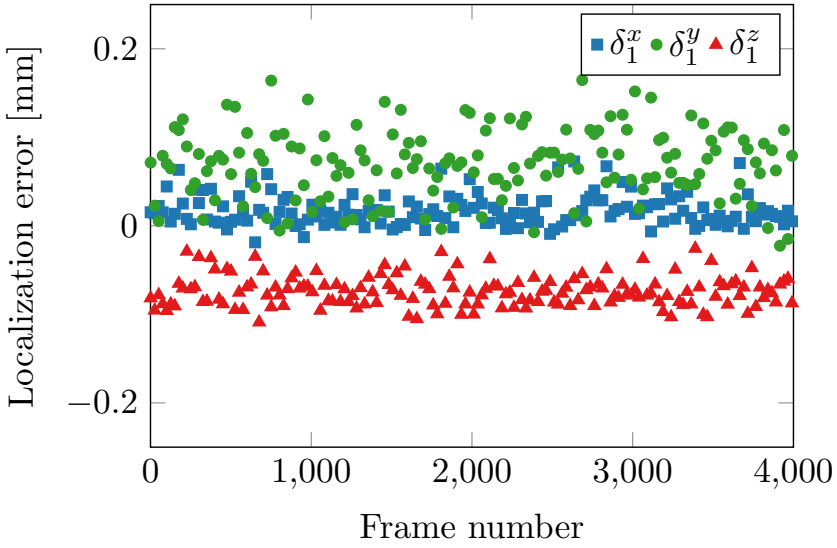

Figure 3.7.: A scatter plot demonstrated the localization error in the x-, y-, and z-directions for the relative threshold $\Theta_\mathrm{T} = 0.3$ of the first experiment. Only every 25th point is plotted to maintain readability.

systematic and the random localization errors $\boldsymbol{\mu}_1$ and $\boldsymbol{\sigma}_1$, respectively, are estimated from $\boldsymbol{\delta}_1(t_i)$. In Table 3.2, a small portion of these errors is presented for relative thresholds $\Theta_\mathrm{T} = \{0.1, 0.3, 0.5, 0.7, 1.0\}$. The analysis indicated that for all Θ_T there is a systematic deviation between ground truth and estimated marker position, which cannot explain the corresponding statistical error. As the localization error $\boldsymbol{\delta}_1$ is analyzed deeper, the underlying distribution reveals a variation in correlation with the relative threshold Θ_T. For example, the distribution seems to be mono-modal for $\Theta_\mathrm{T} = 0.1$ (see Fig. 3.8a) or could be overlaying multi-modal in one or more components for $\Theta_\mathrm{T} = 0.3$ (see Fig. 3.8b).

3.3.2. Temporal and spatial dependency of the systematic error

For the second experiment, a data set of 100×100 volume images is obtained, i.e. for each random robot position $\boldsymbol{r}_m$, $1 \leq m \leq 100$, 100 volumes images are reconstructed.

Table 3.2.: Estimations of the systematic and the corresponding random localization error $\boldsymbol{\mu}_1$. The $\boldsymbol{\sigma}_1$ is given for several relative thresholds for the first experiment using the single-marker-phantom.

Θ_T	$\mu_1^x \pm \sigma_1^x$ [mm]	$\mu_1^y \pm \sigma_1^y$ [mm]	$\mu_1^z \pm \sigma_1^z$ [mm]
0.1	0.04 ± 0.02	0.05 ± 0.02	-0.02 ± 0.01
0.3	0.02 ± 0.02	0.07 ± 0.04	-0.07 ± 0.02
0.5	-0.01 ± 0.04	0.05 ± 0.03	-0.05 ± 0.02
0.7	0.02 ± 0.02	0.06 ± 0.07	0.07 ± 0.02
1.0	0.36 ± 0.30	-0.19 ± 0.29	0.10 ± 5.34

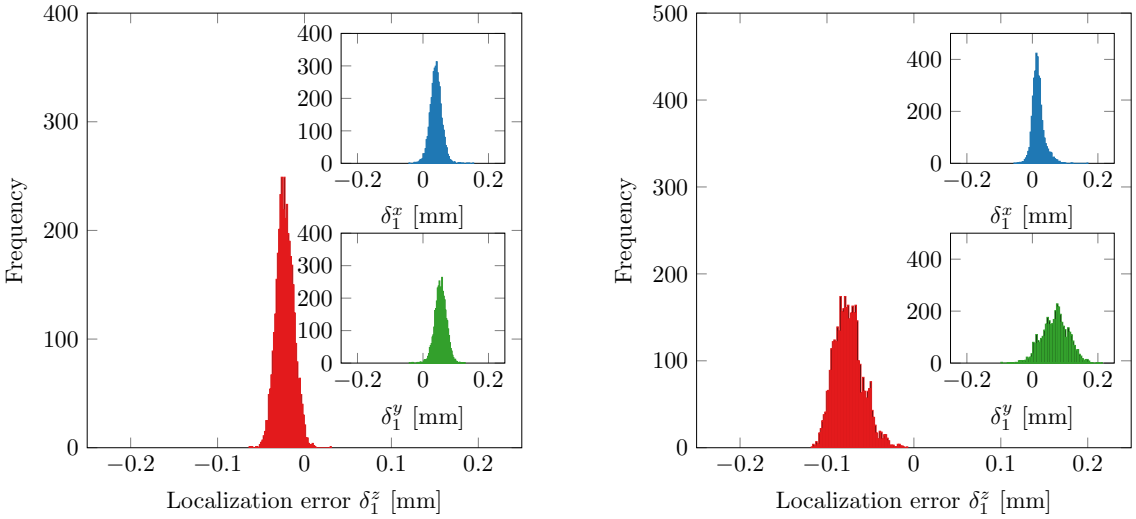

(a) Distribution of δ_1 for $\Theta = 0.1$.

(b) Distribution of δ_1 for $\Theta = 0.3$.

Figure 3.8.: For two relative thresholds Θ_T, the histograms present the distributions of the localization errors.

Equivalent to the first experiment, the single-marker is localized and the corresponding localization error $\boldsymbol{\delta}_1$ is determined for each volume image. A relative threshold of $\Theta_\mathrm{T} = 0.3$ is used for thresholding the volume images. The relative threshold is selected heuristically. It should ensure the comparability between the second experiment and the third experiment. For $0.9\,\%$ of the volume images, the automatic marker localization differs from the ground truth position by more than $1\,\mathrm{mm}$. In these cases, a faulty recognition of the brightest pixel as being the marker position can be identified as the reason due to strong noise influences. Consequently, these noisy volume images are removed from the data set and they are not considered in the statistics. Then, the systematic $\boldsymbol{\mu}_1(\boldsymbol{r})$ and random errors $\boldsymbol{\sigma}_1(\boldsymbol{r})$ are calculated for each random position $\boldsymbol{r}_m$. The results show that $\|\boldsymbol{\sigma}_1(\boldsymbol{r}_m)\|_2 \ll \|\boldsymbol{\mu}_1(\boldsymbol{r}_m)\|_2$. Therefore, the further analysis focuses on the systematic error $\boldsymbol{\mu}_1(\boldsymbol{r}_m)$.

As a first step, the $\boldsymbol{\mu}_1(\boldsymbol{r}_m)$ are sorted with respect to the data acquisition time, i.e. according to m (see Fig. 3.9). In this arrangement, a large spread in the systematic deviation

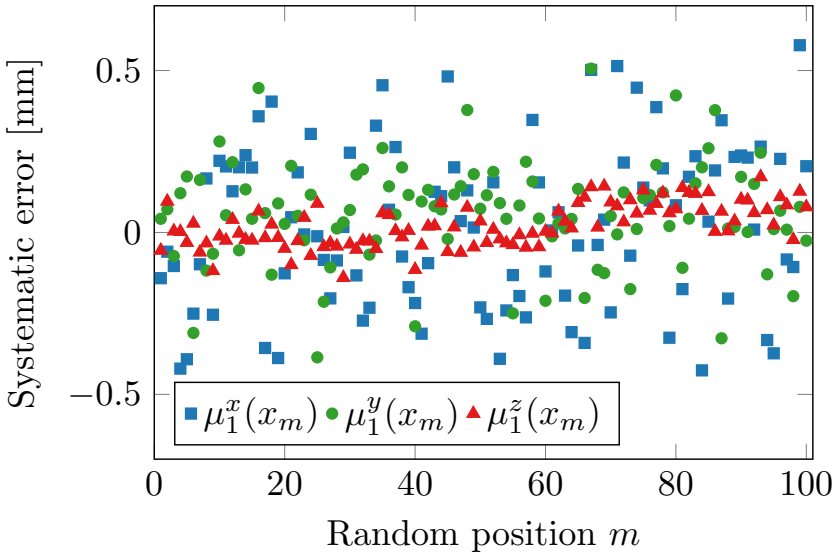

Figure 3.9.: The systematic errors are arranged with respect to acquisition time. The robot is moved to all random positions $\boldsymbol{r}_m$ in the second experiment.

of the x-position $\mu_1^x(\boldsymbol{r}_m)$ and y-position $\mu_1^y(\boldsymbol{r}_m)$ can be identified when comparing it to the component $\mu_1^z(\boldsymbol{r}_m)$. More accurately, the component-wise error limits are $-0.42\,\mathrm{mm} \leq \mu_1^x(\boldsymbol{r}_m) \leq 0.57\,\mathrm{mm}$, $-0.38\,\mathrm{mm} \leq \mu_1^y(\boldsymbol{r}_m) \leq 0.50\,\mathrm{mm}$, and $-0.14\,\mathrm{mm} \leq \mu_1^y(\boldsymbol{r}_m) \leq 0.17\,\mathrm{mm}$, and the absolute systematic error is limited by $\|\boldsymbol{\mu}_1\|_2 \leq 0.7\,\mathrm{mm}$. Overall, the whole measurement time is $400\,\mathrm{s}$. During this time, a minor temporal drift is revealed. The data is binned into groups of 10 consecutive positions. This binning reveals a systematic non-linear drift of the mean of $\mu_1^z(\boldsymbol{r}_m)$ by about $0.15\,\mathrm{mm}$ throughout the whole measurement time. Only the z-component experiences such a temporal drift, while the other components remain stable over time. This temporal drift is not corrected in the further analysis.

As a second step, the spatial dependence of the systematic error $\boldsymbol{\mu}_1$ is analyzed. All three components of the systematic error are plotted against the x-component of the robot position of the single-marker-phantom (see Fig. 3.10). Obviously, μ_1^x changes with the x-component. This variation could possibly explain the larger spread in the time-ordered data seen in Fig. 3.9. To test our presumption, the data set is subdivided into two subsets. The first consists of $\boldsymbol{c}_1, \boldsymbol{c}_3, \ldots, \boldsymbol{c}_{99}$ corresponding to odd numbered random positions $\boldsymbol{r}_1$, $\boldsymbol{r}_3, \ldots, \boldsymbol{r}_{99}$. The second consists of the even numbered random positions. With the first subset, a linear model $\boldsymbol{\mu}_1(\boldsymbol{c}) = A\boldsymbol{c} + \boldsymbol{b}$ is fitted to the data resulting in

$$A = \begin{bmatrix} 0.024 & 0 & 0 \\ 0 & -0.013 & 0 \\ 0 & 0 & 0 \end{bmatrix}, \boldsymbol{b} = \begin{bmatrix} 0.06\,\mathrm{mm} \\ 0.06\,\mathrm{mm} \\ 0.00\,\mathrm{mm} \end{bmatrix}, \tag{3.6}$$

where all coefficients are set to zero that have an absolute t-value less than 3.2 in the linear regression. The standard deviation of the coefficients in A and $\boldsymbol{b}$ is of the magnitude of

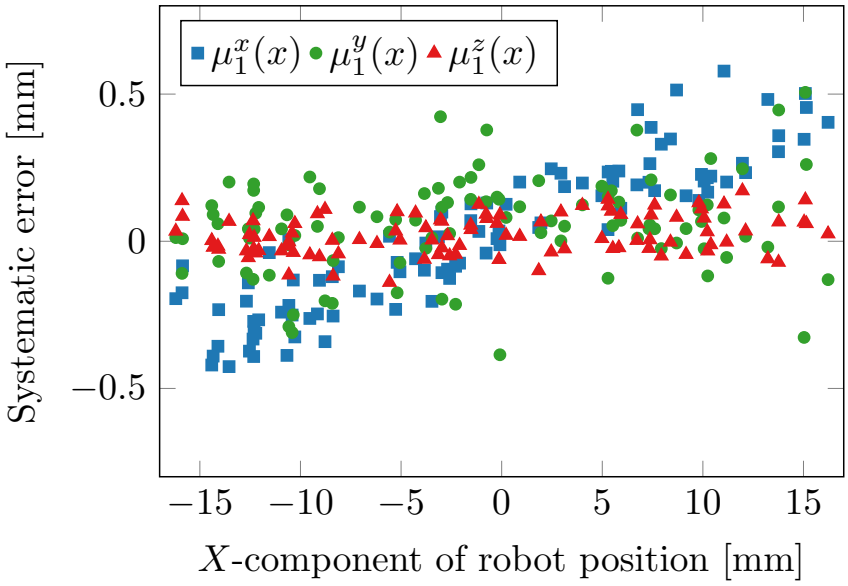

Figure 3.10.: The three spatial components of the systematic error μ_1^x, μ_1^y and μ_1^z are arranged with regard to the x-component of the robot position of the single-marker-phantom. A strong correlation between μ_1^x and x can be identified.

the last digit. After applying the linear model as a first-order correction to the marker localization $\boldsymbol{c}_k \mapsto \boldsymbol{c}_k + A\boldsymbol{c}_k + \boldsymbol{b}$ is applied to the second subset, the systematic error for the corrected data declines substantially. The error limit for the component-wise errors are reduced to $-0.20\,\mathrm{mm} \leq \mu_1^x(\boldsymbol{r}_m) \leq 0.34\,\mathrm{mm}$, $-0.20\,\mathrm{mm} \leq \mu_1^y(\boldsymbol{r}_m) \leq 0.25\,\mathrm{mm}$, and $-0.11\,\mathrm{mm} \leq \mu_1^y(\boldsymbol{r}_m) \leq 0.12\,\mathrm{mm}$, and for the absolute systematic error to $\|\boldsymbol{\mu}_1\|_2 \leq 0.4\,\mathrm{mm}$. For cross-validation of the linear model, the linear model is again applied to the second corrected data set. The results yields no coefficients with absolute t-value above 3.2.

3.3.3. Localization of multiple markers in a multi-marker phantom

In the third experiment, the multi-marker phantom is positioned at 100 randomly selected positions $\boldsymbol{r}_m$. The positions $1 \leq m \leq 100$ are chosen in a way that all markers are inside the FoV. As in the second experiment, 100 frames $1 \leq p \leq 100$ are acquired at each random robot position.

Further, the position of each marker $\boldsymbol{c}_1(m,p)$, $\boldsymbol{c}_2(m,p)$, and $\boldsymbol{c}_3(m,p)$ is identified for the p-th volume image measured at position $\boldsymbol{r}_m$. As a relative threshold, $\Theta_\mathrm{T} = 0.3$ is used, but in this particular experiment the choice of Θ_T is limited. If the Θ_T-values are too small, e.g. $\Theta_\mathrm{T} = 0.1$, the markers c_1 and c_2 cannot be distinguished. The marker positions are used to calculate distances between markers $d_{12}(m,p) = \|\boldsymbol{c}_1(m,p) - \boldsymbol{c}_2(m,p)\|_2$, $d_{13}(m,p) = \|\boldsymbol{c}_1(m,p) - \boldsymbol{c}_3(m,p)\|_2$, and $d_{23}(m,p) = \|\boldsymbol{c}_2(m,p) - \boldsymbol{c}_3(m,p)\|_2$ for each volume image (see Fig. 3.11). The corrections of the marker positions, which have been

gathered in the second experiment, are applied before the distance estimations. A more

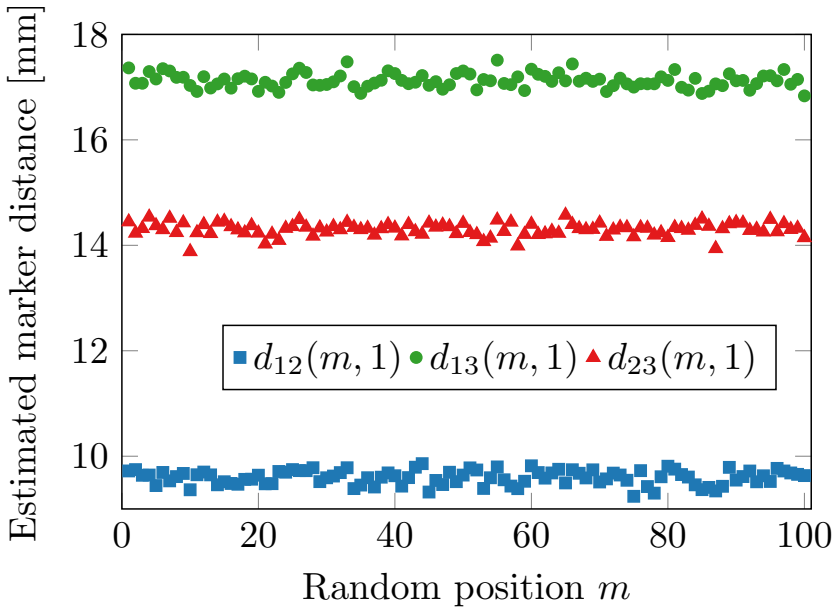

Figure 3.11.: Visualization of the estimated marker distances of the multi-marker phantom. Only every 25th point is plotted to maintain readability.

detailed examination of the results shows that the multi-marker phantom is not correctly recognized in a portion of $0.2\,\%$ of the volume images. As a criterion for a correct recognition of the multi-marker phantom, the distance estimates between the markers are not allowed to deviate by more than $1\,\mathrm{mm}$ from the ground truth distances given in Table 3.1. The main reason for the faulty recognition is the localization algorithm itself. The algorithm sorts the initially identified high-intensity connected components with regard to their brightest voxel and assumes that the markers correspond to these connected components. However, in a small number of volume images, a noisy voxel is falsely recognized as a marker. By removing these outliers from the data set, the marker distances result in an average of $d_{12} = 9.6\,\mathrm{mm} \pm 0.3\,\mathrm{mm}$ ($9.6\,\mathrm{mm} \pm 0.3\,\mathrm{mm}$), $d_{13} = 17.1\,\mathrm{mm} \pm 0.3\,\mathrm{mm}$ ($17.3\,\mathrm{mm} \pm 0.3\,\mathrm{mm}$), and $d_{23} = 14.3\,\mathrm{mm} \pm 0.3\,\mathrm{mm}$ ($14.3\,\mathrm{mm} \pm 0.3\,\mathrm{mm}$). For the result of the marker distances given in the brackets, no linear model correction is applied. These estimates agree quite well with the values from the 3D CAD drawing of the phantom (compare Table. 3.1).

3.4. Discussion

In this chapter, the proof of principle is shown that an automatic and reliable sub-millimeter marker localization within a real-time series of MPI volume images is feasible. Keep in mind that, the MPI system operates at a low field gradient of $1.5\,\mathrm{T\,m^{-1}}$ in z-direction and $-0.75\,\mathrm{T\,m^{-1}}$ in x- and y-directions as well as a DF amplitude of $14\,\mathrm{mT}$. With these

parameters, the achievable spatial resolution of the reconstructed MPI volume images is determined to be $6.0\,\mathrm{mm}$, $7.1\,\mathrm{mm}$, and $2.9\,\mathrm{mm}$. The analysis of the second experiment demonstrates that a submillimeter-accurate localization with an precision of about $\pm 0.27\,\mathrm{mm}$ in the x- and y-directions and $\pm 0.12\,\mathrm{mm}$ in the z-direction is reached. These results lead to a more than 10-fold increase in accuracy of the positioning compared to the positioning with the current native spatial resolution of the MPI scanner.

The very simple marker recognition used in the experiments infrequently identifies noise voxels as markers because, the MPI volume images are affected by noise. Nevertheless, the marker recognition proves to be very robust as the recognition failure rate for the single-marker indicates with only $0.9\,\%$. For the multi-marker phantom containing three markers, the failure rate is even smaller with only $0.2\,\%$. The randomly occurring noise is probably induced by the MPI scanner hardware. In the future, the faulty recognition could be compensated by identifying these noisy volume images by a noise recognition, but a more elegant solution would be the use of more stable algorithms, such as template matching for marker localization.

The automatic localization algorithm presented in this chapter mainly depends on the threshold parameters Θ_T. Here, the choice of Θ_T is restricted by the multi-marker phantom. Because below a certain threshold, the three markers could no longer be discerned from each other. Therefore, the parameter is selected heuristically to be $\Theta_\mathrm{T} = 0.3$. This value minimizes the influence on the localization result to a minimum. Nevertheless, the parameter Θ_T is algorithm-specific and could be left out by applying a more complex computer vision algorithm.

A more detailed investigation of the systematic localization error reveals a spatial dependence of this error and indicates a small non-linear temporal drift. The first order corrections of the spatial dependence reduces the systematic localization error to $0.4\,\mathrm{mm}$. Minor differences in the thermal or magnetic state of the MPI scanner during system matrix acquisition and marker measurements could possibly be the reason for this error. A further analysis of this problem is necessary to validate the automated marker localization completely. Nevertheless, the main findings in this chapter remain valid, even though a correction of these temporal and spatial deviations is not performed yet. If the marker localization is conducted offline in the current experiments, i.e. after the data acquisition, real-time marker localization would still be possible, because the marker localization can be performed in about $1.3\,\mathrm{ms}$ per volume image, which needs to be added to the reconstruction time. For comparison, the real-time reconstruction and real-time marker localization need to be performed in one cycle length of $21.54\,\mathrm{ms}$ per volume image.

The submillimeter-accurate marker localization can be useful for medical real-time applications, such as device tracking or navigation. The application would otherwise be restricted by the low spatial resolution of MPI in the current state. In terms of human real-time applications for MPI, the size of the FoV will be restricted due to the DF strength in

the current development state. Here, the safety constraints of the peripheral nerve stimulation (PNS) [21] are exceeded at the used drive field strength. The safety constraints of the PNS might be extended with higher excitation frequencies. However, then the specific absorption rate (SAR) becomes a restiction [22]. These restrictions could limit the implementation of MPI in interventional and navigation applications. In order to overcome these limitations, an automatic instrument localization could be used to continuously follow the instrument movement by shifting the FoV. The presented robust instrument localization algorithm is crucial for this kind of real-time imaging scenario.

4. MRI-based Target Planning for MPI using the Example of Inflammation Detection

Contents

4.1. Introduction and motivation

MPI reaches a high positive contrast by visualizing only the spatial distribution of SPIONs. However, these functional imaging abilities of MPI do not provide any information about the surrounding tissue morphology or anatomical structure. Yet, most instrumentation applications, such as device tracking and catheter navigation, need an anatomical map of the desired target region to be performed in real-time and to navigate a catheter or another medical device precisely and safely to the target destination. Thus, MPI images need to be registered with an image of a morphological imaging modality, such as CT or MRI. An MRI or CT scan is performed before the MPI measurement to obtain a static anatomical reference. Thus, the MPI signal can be associated with a specific anatomical location. To avoid misinterpretation, it is necessary to register both imaging volumes as precisely as possible. For this purpose, external markers referred to as fiducials can be used. Fiducials consist of a material or particles that are visible in both modalities. Werner et al. [144] have demonstrated the use of gadolinium as an MRI fiducial material

and Resovist as an MPI fiducial material. Both tracers were placed inside rods or glass capillaries of different sizes. Then, the smaller rod containing Resovist was placed inside the larger rod containing gadolinium. Magnetic nanoparticles diluted in only one glass capillary can be used as fiducials since water is visible in MRI, while the nanoparticles are MPI sensible. After both measurements have been performed, the rod structures or the glass capillary within the images are aligned either manually or automatically by applying a registration algorithm. The current workflow of aligning images from different modalities, such as MRI and MPI, can be quite challenging and time consuming, as it is often necessary to re-build the fiducials since they are not long-term stable. This chapter deals with solving the three main problems in the workflow and handling of the current preclinical experiments.

As mentioned before, the fiducials are made of liquid materials. This has the disadvantage that the markers will dehydrate over time, if they are not perfectly sealed. This is often the case, which implies that the fiducial liquid does not stay distributed equally within the container or rod. Beside the evaporation, the capillaries are often contaminated with bacteria. The bacterial contamination dissolves the dextran shell of the SPIONs, which causes the nanoparticles to accumulate and to no longer induce an MPI signal [150]. Consequently, a fiducial solution would be preferable where the fiducials would be long-term stable and could be reused for further experiments. Therefore, a solid fiducials arrangement with silicone and immobilized nanoparticles is proposed. The long lasting fiducials are placed inside a 3D printed fixation. Finally, the constructed fiducials facilitate the mounting and removal from the mouse bed. The mouse bed can be mounted to a sled and is used to move objects or animals out and in of the MPI scanner.

Currently, the mouse bed is operated manually, which means that the insertion distance and the height of the mouse bed are adjusted by screws from hand. This makes the planning of an experiment quite challenging and almost does not guarantee any precise repeatability of the once adjusted position. To facilitate a more robust fiducial placement, a robot supported mouse bed adapter is constructed. This robot-based mouse bed adapter enables a precise positioning of the mouse bed inside the MPI scanner. In doing so, a mouse bed position can be reproduced if the mouse bed has to be moved out and in due to complications with the living subject. A further aspect of fiducials is that for some experiments, a lower concentration or a different particle type are inducing a weaker MPI signal than the fiducials. It is highly beneficial to remove the fiducials during the actual MPI measurement. The robot-based mouse bed makes such a removal after the initial registration measurement possible, since the exact position is known and can be reproduced.

In the current workflow, the MRI and the MPI measurements are performed sequentially, which means that after a static MRI is obtained, the mouse bed is carried over to the MPI scanner to acquire the MPI sequences. The planning of the MPI FoV is purely

based on rough visual inspection of the geometry. However, since the FoV of the MPI is usually limited to only a few cubic centimeters depending of the selected parameters (see section 2.3.2), target planning can be challenging, especially if one wants to measure a specific part of the subject, e.g. a kidney in a mouse. Then, after both measurements are performed, the registration and the evaluation is done offline. This means that up to this point it is unclear if the desired position was actually measured or if the experiment, i.e. the MPI measurement, has to be repeated.

Thus, as a third solution, the online reconstruction framework proposed in [130] is extended to align MRI volume images and MPI volume images before the actual MPI experiment is completed. After the MRI measurements, the MRI volume images are loaded into the extended online reconstructions software. Then, one initial MPI measurement with the fiducials is performed. Based on this initial measurement, both data sets are registered either by adjusting the parameters manually or automatically. When both data sets are aligned, the user can plan the MPI target region based on the MRI images. Then, knowing the offset distances, the robot moves the mouse bed to the position where the target is inside the MPI FoV. During the MPI measurement, the real-time rigid registration to the MRI background is continued. Therefore, the user can observe the experiment online within the context of the anatomical background.

In the last part of this chapter, the previously developed solutions are evaluated in an experiment with mouse brains. For this experiment, the possibility to remove the fiducials is required since the used micron-sized particles of iron oxide (MPIO) (Dynabeads) for the experiment generate a quite low signal compared to the ones used in the fiducials (perimag). Additionally, their concentration is expected to be low as well. Their signal might be just above the noise level for an approximate SNR. The experiment aims to quantify a strong over-expression of endothelial vascular cell adhesion molecule 1 (VCAM-1) during a sterile inflammation in the brain [14]. To induce the sterile inflammation, lipopolysaccharides (LPS) are injected intra-striatal in the right hemisphere of the brain. Afterwards, MPIO-αVCAM are injected into the blood stream. The MPIO-αVCAMs are binding to the VCAM-1 antigens and the MPIOs are detected with MPI. MPIO-αVCAM, which are not bound during the first circulation of the blood, are cleared directly by the liver [14]. For comparison the over-expression of endothelial VCAM-1 is imaged by molecular MRI (mMRI) [151]. Further, this experiment tries to analyze the potential of MPI for neurology applications by imaging inflammation processes as reviewed in [152, 153, 154].

To sum up the contributions of this chapter, the developed long-term stable fiducials, the precise positioning of the robot-based mouse bed and the extended online reconstruction to plan the experiments more accurately are used to conduct the mouse brain studies analyzing the potential of MPI for neurology applications.

4.2. Material and methods

4.2.1. Basic principle of MRI

MRI is a well established morphological and functional imaging modality [155, 156]. MRI provides a high soft tissue contrast and induces no ionizing radiation. The spatial resolution can be below $1\,\mathrm{mm}$ and is dependent on the gradient strength and choice of physical parameters. The latest MRI developments also enable real-time acquisitions (FLASH - Fast Low Angle SHot) with a temporal resolution in the range of $33\,\mathrm{ms}$ [157, 158, 159]. In the following paragraphs, the physical basics, a selection of image reconstruction techniques and different imaging sequences are explained.

Physical basics

To understand the basic principle of MRI, the basic physics of a nucleus are explained first. A nucleus consists of protons, neutrons and electrons. The protons have a nuclear spin $\boldsymbol{I}_\mathrm{s}$ and they rotate with the same constant angular frequency [160]. This rotation results in an observable nuclear magnetic moment $\boldsymbol{\mu}_\mathrm{nmm}$ [160]. These phenomena cannot be explained by classical mechanics and need to be formulated by quantum mechanics (QM) [160, 161]. The magnetic moment is connected to the nuclear spin $\boldsymbol{I}_\mathrm{s}$ via $\boldsymbol{\mu}_\mathrm{nmm} = \gamma_\mathrm{gmr}\boldsymbol{I}_\mathrm{s}$, where γ_gmr describes the gyromagnetic ratio. Only particles with an odd number of protons or neutrons exhibit a nuclear spin in their ground state. Otherwise, the magnetic moments compensate each other. For example, hydrogen has mainly only one proton and possesses a high magnetic moment due to having the largest gyromagnetic ratio of all stable nuclei [155]. Further, all biological tissues, such as water or fat, consists to a large extend of hydrogen. The existence of the nuclear spin and the magnetic moment form the necessary prerequisite for MRI. However, to understand the phenomena of magnetic resonance, it is not necessary to use the explanation of QM. For magnetic resonance it, is sufficient to view the spins as an ensemble of spins and not the individual spins [160]. The following descriptions are classical but remain valid since only the mean values of physical quantities averaged over a large ensemble of nuclei are considered [155]. The equilibrium magnetization [155](p.12)

$$M_0 = |\boldsymbol{M}_0| = \frac{1}{V}\sum_{i=1}^{N}(\boldsymbol{\mu}_\mathrm{nmm,z})_i = \frac{N}{V}\frac{I_\mathrm{q}(I_\mathrm{q}+1)\gamma_\mathrm{gmr}^2\hbar^2 B_0}{3k_\mathrm{B}T} \tag{4.1}$$

is given as a macroscopic effect of the spin distribution of the ensemble, where $\hbar$ is the Planck's constant, k_B is the Boltzmann's constant, I_q is the quantum number, B_0 is the magnetic flux density of homogeneous magnetic field, T is the temperature, N is the number of spins and V is the volume of the sample. Without the influence of a magnetic field ($B_0 = 0$), the magnetic moments are oriented randomly and compensate each other.

Therefore, no magnetization is seen ($|\boldsymbol{M}_0| = 0$). However, if the spin distribution experience a homogeneous static magnetic field ($B_0 \neq 0$), the spin distribution is slightly skewed towards the direction of the magnetic field [160], which results in a macroscopic magnetization ($|\boldsymbol{M}_0| \neq 0$) [160]. This macroscopic magnetization increases with the proton density, the strength of the magnetic field and with a decreasing temperature, as stated by Eq. (4.1). For further descriptions, an analogy of a magnetic dipole is used to describe the behavior of the magnetization of the spins [155](p.10). Being in an external magnetic field, a cylindric magnetic dipole is defined by its magnetic moment, which experiences a torque to align parallel to the magnetic field direction. The magnetic dipole rotates around its longitudinal axis, which has an angular momentum. The magnetic dipole cannot align with the direction of the magnetic field, because it has to preserve its angular momentum. Instead, it leads to a precession of the magnetic spins on a cone around the direction of the magnetic field. The frequency of the precession is called the Larmor frequency [155](p.12)

$$\omega_0 = \gamma_{\text{gmr}} B_0 \tag{4.2}$$

and depends on the nucleus type and the strength of the magnetic field B_0. The Larmor frequency is $2\,\text{kHz}$ for magnetic spins of hydrogen within the magnetic field of the earth ($\approx 30\,\mu\text{T}$. For a homogeneous magnetic field with $1\,\text{T}$, this results in $42\,\text{MHz}$ and, respectively $63\,\text{MHz}$ for $1.5\,\text{T}$. A preclinical MRI Scanner (PharmaScan, Bruker, Germany) with a magnetic field of $7\,\text{T}$ has a Larmor frequcency of $294\,\text{MHz}$.

Up to now, all magnetization precessions have the same frequency around the direction of the magnetic field. For convenience, the direction of the magnetic field can be defined as the z-axis, and the plane perpendicular to the z-axis is the xy-plane. In the previously described state, all magnetic spins are precessing, but the equilibrium magnetization is stationary and induces no signal in a receive coil [160]. In order to obtain a magnetic resonant signal, the equilibrium state needs to be disturbed. Generally, energy transitions between the spins can be induced by an additional time-dependent electromagnetic radio frequency (RF) field [155](p.12). This circularly polarised wave interacts with the magnetic moments and rotates the magnetization of the spin ensemble as a whole [160]. The RF pulse needs to have the Larmor frequency to generate a resonance [155](p.13). Depending on the energy of the RF pulse, it can flip the magnetization around an angle α_{F}. A so called $180°$ pulse flips the magnetization $180°$ in opposite z-direction. Similar, a $90°$ pulse flips the magnetization by $90°$ in the xy-plane. For simplification, the longitudinal magnetization in the z-direction is defined as M_z and the transverse magnetization in the xy-plane is defined as M_{xy}. As the precession movement and the flipping of the angle are overlaid, the tip of the magnetization vector follows a helical pathway on the surface of a sphere around the magnetic field direction. Meanwhile, the length of magnetization

vector remains the same. After a short RF excitation, the magnetization returns to the more stable state of the equilibrium magnetization. This process is denoted as relaxation and can be separated into two relaxation types. The first relaxation of the magnetization is described by the longitudinal or spin-lattice relaxation in M_z-direction. The longitudinal relaxation time is denoted as T_1. The second relaxation of the magnetization is characterized by transverse or spin-spin relaxation in M_{xy}-direction. The transverse relaxation time is defined as T_2. The transverse magnetization rotates and induces an electrical current in a set of receive coils. The electrical signal over time defines the MR signal. Therefore, after the RF excitation, the transverse magnetization rotates freely, induces an MR signal and decays back to $M_{xy} = 0$ of its equilibrium magnetization. Following this behavior, the induced MR signal is also called free induction decay (FID). The T_2 relaxation of transverse magnetization M_{xy} shows an exponential behavior, and the T_1 relaxation build up of longitudinal magnetization M_z is also characterized by an exponential behavior. However, both relaxation process can be considered independently. The decay of the T_2 relaxation is usually shorter than the build up of the T_1 relaxation. The T_1 relaxation constant is tissue-dependent and magnetic field strength-dependent, e.g. fat tissue has a short T_1, while water has a longer T_1. During the T_1, relaxation the spins interact via translation and vibration with the lattice of other molecules and lose their energy in order to obtain their equilibrium state.

After a $90°$ pulse, the magnetization is rotated towards the transverse magnetization M_{xy}-plane. During the T_2 relaxation, the spins interact with other spins and lose their transversal magnetization. In contrast to the T_1 relaxation, the T_2 relaxation is also tissue-dependent but it is largely independent of the magnetic field strength. Again, the fat tissue has a short T_2 relaxation time, while water has a longer T_2 relaxation time. As the rotating transverse magnetization induces an MR signal, it would be expected that the signal decays with the relaxation time T_2, but due to inhomogeneities of the magnet field it decays much faster. The reason for the inhomogeneities are technical reasons of the coil setup and the patient itself, which causes local field variations. These local field variation are spatially and temporally constant and increase the dephasing of the spins. The actual decay is then described by the effective relaxation time constant T_2^*. Since the effective decay with its relaxation time T_2^* is much faster than the expected relaxation time T_2, the time for acquiring the MR signal is quite short. Therefore, a trick can be used to bring back the MR signal. After the initial $90°$ pulse, a $180°$ pulse is applied after a time period τ_{se}. The $180°$ pulse brings the spin distribution back in phase, and a new MR signal, the spin-echo, is induced. The spin echo increases and has its maximum after the echo time $T_{\text{E}} = 2\tau_{\text{se}}$. Afterwards, it decays again. Basically, the $180°$ pulse changes the phase order and restores the initial MR signal except for T_2-effects. With multiple $180°$ pulses, multiple spin-echos can be created. The amplitude and maximum of these multiple spin-echos decay with the relaxation constant T_2. The relation between the relaxation times

can be quantified as follows $T_2^* < T_2 < T_1$. The multiple spin-echos are then used for the MR imaging as they can be measured easily. The spin-echo is the first method to

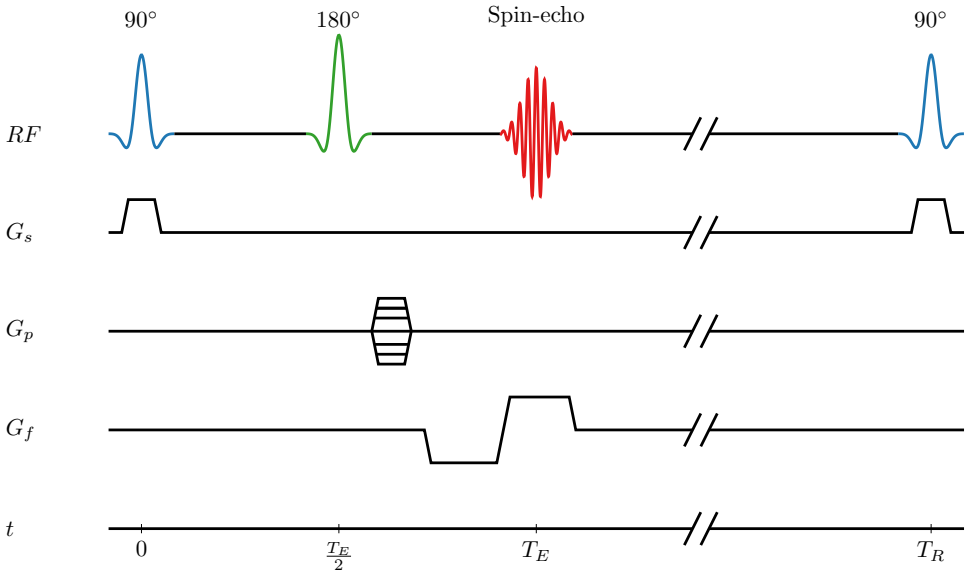

Figure 4.1.: Example of a spin-echo MR sequence.

obtain an MR signal (see Fig. 4.1). The second method is the so called gradient-echo method. Here, the magnetic field gradient is changed with additional gradient fields after the initial $90°$ pulse. The spin frequency changes through the gradient change since the Larmor frequency is proportional to the magnetic field strength. After the initial $90°$ pulse, a negative gradient dephases the spins faster. Then, the gradient is changed to the positive opposite, which brings the spins back in phase. The gradient-echo can be measured after an echo time T_E. Consequently, it is also possible to generate multiple gradient-echos and to induce more MR signals. However, the gradient-echos need to be generated within the fast relaxation time T_2^* because no $180°$ pulse changes the magnetization again. Thus, gradient-echo sequences enable a much faster imaging methodology. For the gradient-echo sequence, usually a smaller flipping angle α_F than $90°$ is chosen because there is less time for the measurement and it reduces the measurement time at the cost of SNR.

Image reconstruction and image sequences

So far, the MR signal from all areas of the tissue is obtained. As a next step, it is introduced how the spatial encoding is implemented within MRI systems. The basic idea is to vary the magnetic field locally to ensure different Larmor frequencies at different spatial positions. This local variation of the magnetic field is achieved with a gradient in the z-direction. The initial magnetic field strength B_0 is now only given in the middle of the z-axis. Thus, to enable slice selection, a gradient G_s in z-direction is applied simultaneously with the high frequency (HF) excitation pulse. The slice thickness is defined by a bandwidth $\Delta\omega$ around the Larmor frequency. Alternatively, the slice thickness is also

dependent on the strength of the gradient. By using gradient coils in all three directions of space, gradients in all directions of space can be generated. Up to here, the raw MR signal from slices is gained, but in order to assign each voxel an MR signal, a frequency encoding and a phase encoding need to be introduced. The mapping of the MR signal to each voxel is achieved via frequency and phase encoding. The frequency encoding is achieved by using a gradient G_f in the x-direction after the initial RF pulse and selection gradients. By this means, each voxel row in the x-direction is assigned a unique frequency. The same is done with the phase encoding in the y-direction. Here, the phase gradient G_p is also operated in between the initial RF pulse and the frequency gradient G_f. It assigns each voxel row in the y-direction a unique phase. In order to obtain a complete 2D image, the phase encoding has to be changed in repeated measurements to encode each pixel row with a different phase. The received signal encodes each pixel with a unique combination of frequency and phase [162](p.48) and can be written as

$$S(n,m) = \int_{-\infty}^{\infty}\int_{-\infty}^{\infty} M_{xy}(x,y)e^{jk_x(n)x+jk_y(m)y}dxdy, \tag{4.3}$$

where $k_x(n) = \gamma_{\text{gmr}}G_{0,x}\tau_\omega n$ and $k_y(m) = \gamma_{\text{gmr}}G_{0,y}t_{ph}m$ with τ_ω as sampling time and t_{ph} as duration of the phase gradient. Thus, the image $S(n,m)$ is encoded in frequencies and phases. The latter is also referred to as k-space. Afterwards, the Fourier transform transfers the MR raw signal to the image domain. As described in section 2.5, the Fourier transformation decomposes the superimposed signal in its single frequency components while also considering the different phases. The signal strength of the combination of frequency and phase is assigned to the spatial location and determines the grey values of the images. The result of a sagittal MRI image of a mouse is shown in Fig. 4.2. To sum up a pulse sequence, the spins are first excited with an RF pulse while a slice selection gradient is activated. Then, the phase encoding and the frequency encoding gradient are operated sequentially. During the frequency encoding gradient, the echo-signal is acquired. This pulse sequence is repeated multiple times with the repetition time (T_R), using a different phase encoding each time. Finally, the measurement time is determined by the number of phase encoding steps times the T_R. This description only covers the basic MRI concepts. Further information on advanced MRI sequences, such as multi-echo-sequences, turbo-spin-echos and echo planar imaging (EPI) technique, can, for example, be found in [156] and in [155](p.57), where the most important MRI sequences are listed.

Image contrast

The image contrast of an MRI image is defined by three different image contrasts, the T_1-contrast, the T_2-contrast and the proton density contrast. Each contrast contributes to the overall image contrast, but one contrast is usually predominant. The image contrast is mainly determined by the two relaxation constants T_1 and T_2. T_E and T_R are important

Figure 4.2.: Sagittal MRI image of a mouse.

parameters to control the image contrast. The proton density contrast can be reached with a long T_{R} (around $2500\,\mathrm{ms}$) and a short T_{E} (around $15\,\mathrm{ms}$). After a $90°$ RF pulse, the longitudinal magnetization M_z is restored differently fast for different tissue types. The maximal magnetization values are connected to the proton density of the tissue. For the T_2-contrast, T_{R} is also chosen long (around $2500\,\mathrm{ms}$), but T_{E} is set to long value (around $90\,\mathrm{ms}$). Here, the influence of the proton density is reduced because the T_2 relaxation constant declines faster and the T_2 relaxation is predominant in the transverse magnetization M_{xy}. The T_1-contrast is achieved with a short T_{R} (around $500\,\mathrm{ms}$) and a short T_{E} (around $15\,\mathrm{ms}$). The short T_{R} minimizes the influence of the proton density and the short TE reduces the effect of the T_2 relaxation. Therefore, the image contrast is mainly determined by the longitudinal magnetization, ergo the T_1 relaxation. The T_1 relaxation is often used to visualize anatomical structures because soft tissues rarely differs in their proton density but in their T_1 relaxation times. The combination of short T_{R} and long T_{E} yields no useful MR signal as the measurable signals decays very fast. For different tissue type, the typical T_1 relaxation times are in the range of $100\,\mathrm{ms}$ to $2000\,\mathrm{ms}$ and for the T_2 relaxation in the range of $10\,\mathrm{ms}$ to $1000\,\mathrm{ms}$. It is important to notice that the same tissue can have a high intensity values in a T_2 weighted image, while having low intensity values in a T_1 weighted image.

Molecular MRI

Molecular MRI (mMRI) sequences are specifically designed to enhance the constrast of injected contrast agents. The constrast agents are usually bound to a protein of interest [151, 14]. With this concept, functional processes can be visualized within the living organism in a noninvasive manner. In the following experiments, MPIOs, known from section 2.1 as Dynabeads, are used as a contrastophores. The larger iron oxide particles generate a negative contrast in the MRI image as they influence the local magnetic field in their environment. Thus, they induce a hypointense contrast in T_2^* weighted images and this phenomenon is known as blooming effect [151, 14].

4.2.2. Fiducials

As the different registration approaches, i.e. manual or automatic registration, are easier to be carried out using specific fiducials, two different fiducial types are constructed. The first type shown in Fig. 4.3a consists of three rods arranged perpendicular to each other [144]. Each rod is filled with a mixture of dental cement and perimag with a ratio of 1:1. The concentration c_{fid} of perimag is $2.8\,\mathrm{mg\,mL^{-1}}$. The inner rod has a diameter of $3\,\mathrm{mm}$, while the outer shell consists of a silicone tube with a $5\,\mathrm{mm}$ diameter. The perimag particles inside the dental cement are immobilized and induce less signal than mobilized particles. However, they become resistant to dehydration and the particles are staying equally distributed throughout the rod. By these means, the fiducials become more long-term stable and reusable. The rods are arranged in a way that each rod is visible from all three perspectives in a maximum intensity projection (MIP) image. With such a rod arrangement, it is easier to identify the position in three dimensions, but an automatic segmentation is more challenging because the length of the rods is not perfectly reflected in the MPI images. The second type of fiducials (see Fig. 4.3b) consists of three spheres arranged in a triangle. This fiducial arrangement is an improved version of the multi-marker phantom from [J1]. It is also constructed in a way that the three spheres c_1, c_2, c_3 are visible from all three orthogonal perspectives in a MIP image. Therefore, the orientation of the fiducials is always unique in space. The inner sphere with radius of $2.85\,\mathrm{mm}$ also consists of a mixture of dental cement and perimag with ratio 1:1. The outer silicone shell of $5\,\mathrm{mm}$ is 3D printed by inkjet technology (Agilista, Keyence, Japan). The silicone shell functions as a marker for MRI, because it is visible in most MRI sequence due to its hydrogen components. Perimag is used as a tracer for MPI and performs as a marker for MPI. The distances $d_{12} = \|\boldsymbol{r}_1 - \boldsymbol{r}_2\|_2$, $d_{13} = \|\boldsymbol{r}_1 - \boldsymbol{r}_3\|_2$, and $d_{23} = \|\boldsymbol{r}_2 - \boldsymbol{r}_3\|_2$ between the centers of the spheres are the same as the ones mentioned in chapter 3 and given in Table 3.1, accordingly. The fiducials with the three spheres arrangement are advantageous for an automatic registration, because an automatic segmentation of the spheres is

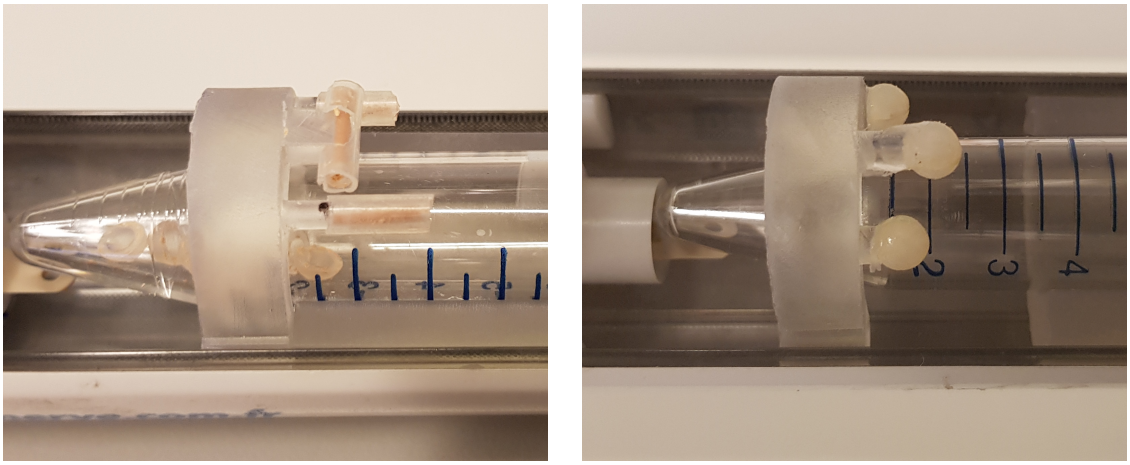

(a) (b)

Figure 4.3.: a) Fiducials with three rods with dental cement inside and silicone tube as shell. b) Fiducials with three spheres with dental cement inside and silicone in the shell.

much easier. The position of the sphere could be precisely determined with a 3D Hough-transformation for example.

4.2.3. Robot-adapted mouse bed

For the mouse bed a robot adapter has been designed, as shown in Fig. 4.4a. The robot adapter is 3D-printed by stereolithoraphy (SL) (Forms 2, Formlabs) and the result is shown in Fig. 4.4b. By mounting the mouse bed to the robot, it is possible to position the mouse bed precisely in all directions with a step size of $6.25\,\mu\mathrm{m}$. With this setup, it is also feasible to reproduce the measurement position once the subject has to be moved out and in again. This reproducibility becomes helpful when it is desirable to remove the fiducials in an experiment where the signal of the fiducials would limit the contrast range of the actual measurement. This can be the case, when the MPI signal is expected to be close to the sensitivity threshold. Then, the expected signal is just above the noise level and the fiducials would disturb the measurement.

4.2.4. MRI-based FoV selection with live MPI reconstruction

To enable an MRI-based FoV selection with live MPI reconstruction, the online reconstruction software tool [130] (Julia, Gtk) is extended. Thus, the MRI images can be loaded into the framework before the MPI experiments. With the first initial MPI measurement, both MRI and MPI images are registered manually by visual inspection. For the remainder of an experiment, the selection of the MPI FoV can be made based on the MRI images. During the experiment, the MPI images are aligned to the MRI images in real-time. A screenshot of the software user interface (UI), where the fiducials are visible in both modalities, can be seen in Fig. 4.5a. One yz-slice is enlarged in Fig. 4.5b. It is

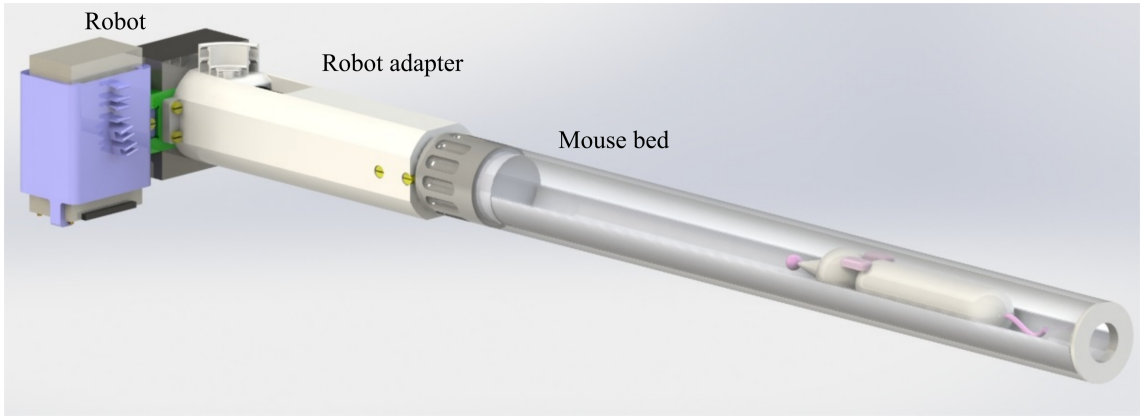

(a)

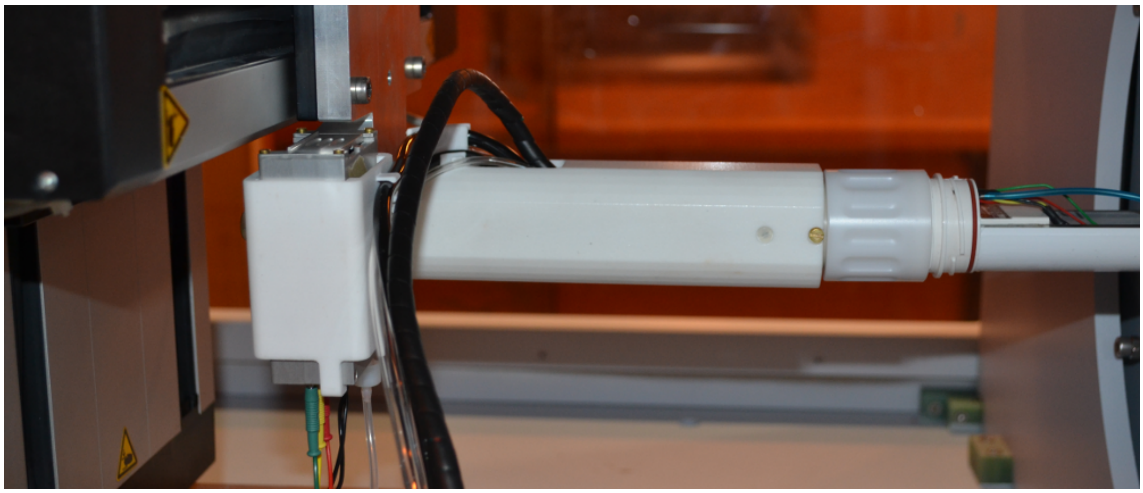

(b)

Figure 4.4.: a) CAD concept of the robot adapter for the mouse bed with holder for the acquisition unit. b) Constructed robot adapter for the mouse bed mounted to the robot with acquisition module for vital monitoring of the mouse.

worth noting that both images are not correctly aligned yet in Fig. 4.5b to show the visualization in both modalities. The extended software uses one worker process to perform the MPI reconstruction. The worker process fetches the reconstruction parameters from the remote channel, performs the MPI reconstruction and then pushes the results in a queue back to the remote channel. The remote channel shares memory space with the worker and the UI process. The UI process fetches the reconstructed image and performs a rigid registration to the static MRI. The rigid transformation [163] is defined as follows

$$\Phi_{\text{rigid}}(\boldsymbol{I}) = \boldsymbol{R}(\alpha, \beta, \gamma)\boldsymbol{I} + \boldsymbol{t}, \text{with } \boldsymbol{R} \in \mathbb{R}^{3\times3}, \boldsymbol{I} \in \mathbb{R}^{3\times N_G}, \boldsymbol{t} \in \mathbb{R}^{3\times N_G} \tag{4.4}$$

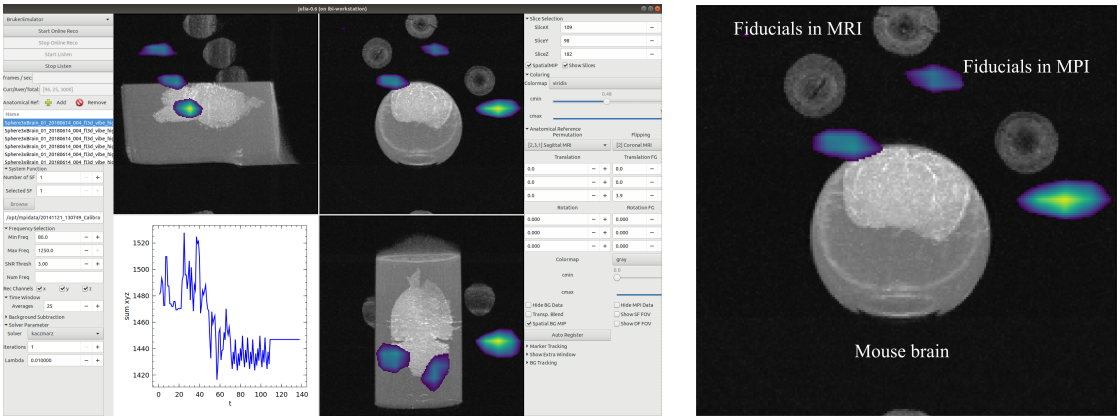

(a) (b)

Figure 4.5.: a) Extended online reconstruction software tool. Both images of MPI and MRI are not fully aligned yet. In the software, the registration parameters of the rotation matrix and translation vector between both images can be adjusted. Further, the reconstruction parameters and the visualization parameters can be adjusted during the experiment. b) Enlarged yz-slice of the data.

where

$$\boldsymbol{R}(\alpha,\beta,\gamma) = \boldsymbol{R}_z(\alpha)\boldsymbol{R}_y(\beta)\boldsymbol{R}_x(\gamma) = \tag{4.5}$$

$$\begin{bmatrix} \cos(\alpha) & -\sin(\alpha) & 0 \\ \sin(\alpha) & \cos(\alpha) & 0 \\ 0 & 0 & 1 \end{bmatrix} \begin{bmatrix} \cos(\beta) & 0 & \sin(\alpha) \\ 0 & 1 & 0 \\ -\sin(\beta) & 0 & \cos(\beta) \end{bmatrix} \begin{bmatrix} 1 & 0 & 0 \\ 0 & \cos(\gamma) & -\sin(\gamma) \\ 0 & \sin(\gamma) & \cos(\gamma) \end{bmatrix} \tag{4.6}$$

is the rotation matrix with rotation angles α around the z-axis, β around the y-axis and γ around the x-axis. $\boldsymbol{t}$ is the translation vector and $\boldsymbol{I}$ are the coordinates of the 3D grid of the images with N_G as the number of grid points. By doing the real-time alignment, the algorithm considers the parameters of the rotation matrix $\boldsymbol{R}$ and translation vector $\boldsymbol{t}$. These parameters are adjusted by the user. Finally, the overlayed aligned images are displayed.

Workflow of MRI-based FoV selection

In the following (see Fig. 4.6), the steps to align an MPI measurement in real-time to an MRI, where the FoV has been selected based on MRI images, are described in chronological order.

1. Initial situation: The MRI image has been acquired with the fiducial markers close to the target geometry.

2. Identify the fiducial markers in MPI: The mouse bed is moved inside the bore until the position and orientation of the markers are identified. The initial registration of

Figure 4.6.: The MRI-based selection of MPI FoV can be described in five steps. 1. Acquire MRI image, 2. Identify the fiducial in MPI, 3. Perform the registration, 4. Select target FoV, 5. Move to selected target FoV.

the MRI and MPI volume images are performed by aligning both FoV centers. The current robot position $\boldsymbol{p}_{\text{rob}}$ is saved.

3. Perform the registration: The manual rigid registration is performed by the user by adjusting the rotation matrix $\boldsymbol{R}$ and translation vector $\boldsymbol{t}$ to achieve a match (evaluated by visual inspection) of the markers in the two images.

4. Select target FoV: The user determines the translation $\boldsymbol{t}_{\text{target}}$ of the current MPI FoV within the MRI image to the requested MPI FoV overlaying the target in the MRI image. Note that the MPI FoV is usually smaller than the MRI FoV.

5. Move to selected target FoV: The user can either use the robot to move the mouse bed to the selected target FoV by adding $\boldsymbol{t}_{\text{target}}$ to $\boldsymbol{p}_{\text{rob}}$ (5.1) or the user can shift the focus fields by $\boldsymbol{t}_{\text{target}}$ to place the FoV over the selected part within the mouse bed (5.2). The rigid image registration uses then the parameters $\boldsymbol{R}$,$\boldsymbol{t} + \boldsymbol{t}_{\text{target}}$.

The user can determine the $\boldsymbol{t}_{\text{target}}$ translation by right clicking in the MRI image to mark the new MPI FoV center. Through pixel spacing of the MRI and pixel translation to the origin MPI FoV center, $\boldsymbol{t}_{\text{target}}$ is calculated in millimeters. The real-time registration takes about $0.9\,\text{s}$ per frame. Here, the $25 \times 25 \times 25$ MPI image has to be interpolated to the $192 \times 192 \times 192$ MRI image. In the video (see Fig. 4.7), the live registration of the MPI and MRI images is presented. For this visualization, the robot moves the mouse bed with the fiducials inside periodically to the corners of a square.

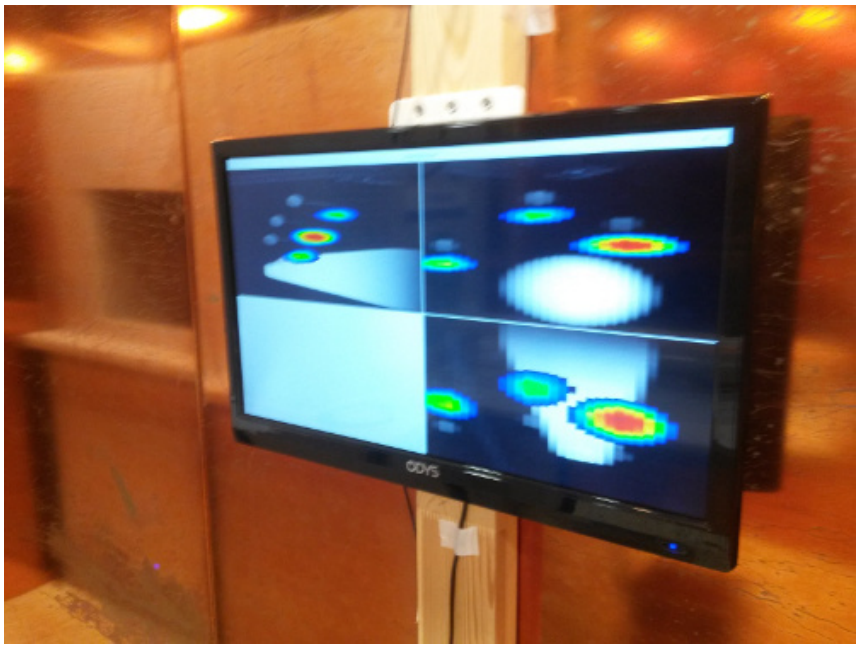

Figure 4.7.: The video shows the live registration between MPI and MRI images of the extended software frame work. The robot moves the mouse bed with fiducials inside from corner to corner of a square to visualize the registration process (video length: $48\,\text{s}$).

4.2.5. Experiments

For the experiments, nine mice are used and the preparation of the mice has been conducted in cooperation with the Université de Caen Normandie. The mice are divided into three groups A, B and C with three subjects each. The mice in group A are intrastriatal injected with $1\,\mu\text{g}$ LPS in the right hemisphere of the brain. The injection of LPS induces a sterile inflammation, which results in a strong over-expression of endothelial VCAM-1. After 24 hours, $800\,\mu\text{L}$ of MPIO-αVCAM are injected intravenously. The MPIO-αVCAM targets the endothelial VCAM-1 antigens. After $10\,\text{min}$, am mMRI scan is acquired with the parameters used in [151]. After further $20\,\text{min}$, euthanasia and harvesting of the brains and livers is performed. Finally, the brains are fixated in agarose gel. Group B is not injected with LPS but also with MPIO-αVCAM after 24 hours. Again, the mMRI and the harvesting are done in the same time interval. Group C is not injected

with anything and serves as control reference. The mMRI scan and the harvesting are also performed in the same time interval. In summary, the groups are described as follows

- Group A: Brain inflammation due to LPS injection, MPIO-αVCAM injection,
- Group B: No brain inflammation, MPIO-αVCAM injection,
- Group C: No brain inflammation, without MPIO-αVCAM injection.

The MRI images are acquired with the rod fiducials close to the mouse brain. Since the silicone rods are not visible in the mMRI images, a standard T_1-weighted MRI scan is done with the same geometrical parameters as the mMRI scan. After the MRI scans, the mouse bed with the mouse brain is mounted to the robot and moved into the MPI scanner. In an initial MPI, scan the fiducial position is determined and the robot position is saved. The manual registration is done by adjusting the registration parameters by visual inspection. Then, the mouse bed is moved out of the scanner and the fiducials are removed. After that, the mouse bed is moved back to the previous saved robot position. Finally, the actual MPI measurement is performed while the images are live registered to the MRI images. The experiments are designed to answer three questions:

- Is MPI capable of differentiating group A from groups B and C?
- Is MPI capable of differentiating between group B and C?
- Is MPI capable of differentiating the right hemisphere from the left hemisphere of the brain?

MRI and MPI parameters

At first, a localizer sequence is performed for the planning and selection of the MRI FoV. Afterwards, a standard T_1-weighted MRI sequence with a grid size of $128 \times 128 \times 128$ and a voxel spacing of $(0.25 \times 0.25 \times 0.25)\,\mathrm{mm}$ is conducted to identify the fiducials. Then, the mMRI sequence is performed with a 3D gradient-echo sequence with flow compensation and the following sequence parameters, $\alpha_{\mathrm{F}} = 22°$, $T_{\mathrm{R}} = 200\,\mathrm{ms}$ and $T_{\mathrm{E}} = 13.2\,\mathrm{ms}$. The grid size is chosen to be $320 \times 320 \times 36$ with a voxel spacing of $(0.09 \times 0.09 \times 0.6)\,\mathrm{mm}$. The MPI scanner is operated with a gradient strength of $G_z = 2.0\,\mathrm{T\,m^{-1}}/\mu_0$ in the z-direction and $G_x = G_y = -1.0\,\mathrm{T\,m^{-1}}/\mu_0$ in the x- and y-directions. The amplitude is set to $\boldsymbol{A} = (12\,\mathrm{mT}, 12\,\mathrm{mT}, 12\,\mathrm{mT})$, which leads to an MPI FoV of $24\,\mathrm{mm} \times 24\,\mathrm{mm} \times 12\,\mathrm{mm}$. Before the actual experiments, two system matrices with delta sample size $1\,\mathrm{mm} \times 1\,\mathrm{mm} \times 1\,\mathrm{mm}$ are acquired with Dynabeads and immobilized perimag. The grid size of the system matrix is chosen to be $25 \times 25 \times 25$, which covers an overall FoV of $25\,\mathrm{mm} \times 25\,\mathrm{mm} \times 25\,\mathrm{mm}$. As a receive coil, a highly sensitive mouse coil similar to the one used in [136] with bore diameter of $40\,\mathrm{mm}$ is used. The MPI sequences are reconstructed with the parameters $n_{\mathrm{iter}} = 3$, $\Theta = 5$ and $\lambda = 0.01$.

4.3. Results

In Fig. 4.8a, the axial MRI scan of the first subject from group A is shown. In this T_1-weighted MRI sequence, the fiducials are clearly visible and the mouse brain appears normal. In the second axial MRI image (see Fig. 4.8b), the same brain from group A is

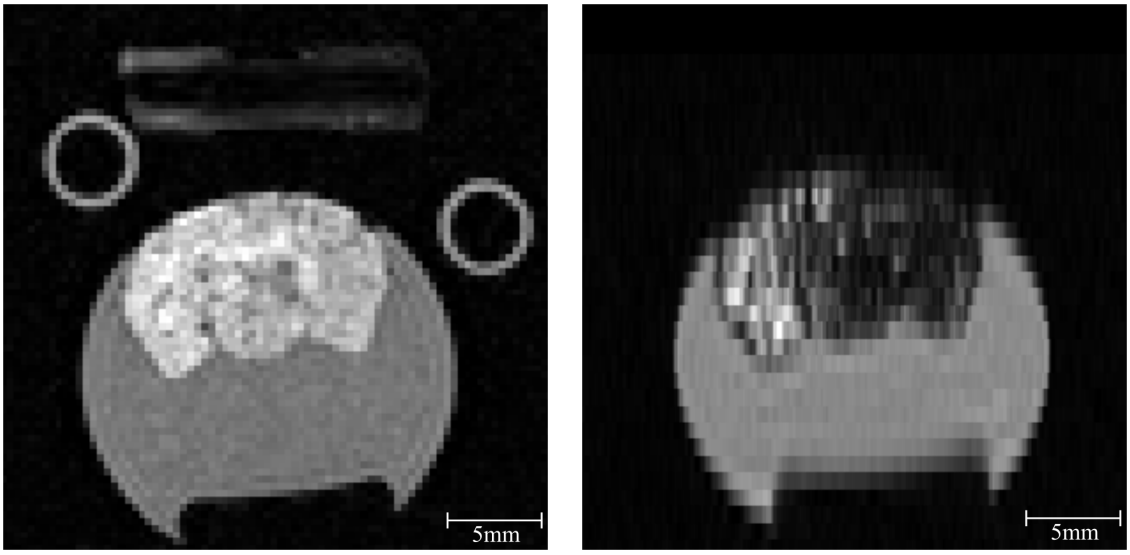

(a) (b)

Figure 4.8.: a) Axial MRI scan of mouse brain from group A. In this T_1-weighted sequence, the fiducials are clearly visible. b) Axial MRI scan of the same mouse brain from group A. In this sequence, the fiducials are not visible. Instead, the MPIOs-αVCAM are visualized by a black area in the central nervous system.

measured with the mMRI sequence. In this image, the fiducials do not appear, but the mMRI sequence reveals that the MPIOs-αVCAMs are spread through the central nervous system of the brain. The mMRI image in Fig. 4.9a shows the brain of the first subject from group A again. Here, a coronal slice is depicted because this data set shows the highest resolution in the coronal slices. The MPIOs-αVCAM can be identified even better than in Fig. 4.8b. For comparison, an mMRI scan of the brain of the first subject from group B is shown in Fig. 4.9b. Here, only a few MPIOs-αVCAM can be identified in the dark areas in the mid region of the brain. As expected, the mMRI scan of the subjects in group C shows no dark areas within the brain. The mMRI images of group C are not shown. In the Fig. 4.10, the MPI results are registered with the MRI images. The background MRI image have a grey scale colormap while the MPI images have colorized colormap. The brains of the three subjects from group A are presented in coronal slices. As the anatomical map from the MRI images indicates, the MPI signal strength and location varies between between the three brains. The strongest MPI signal is mostly located in the areas of the highest MPIOs-αVCAM density. Despite the fact that the MPI signal has only the shape of one or two circular areas, the left hemisphere and the right hemisphere can be differentiated. In Fig. 4.11, the MPI images for the first subject of group A are shown

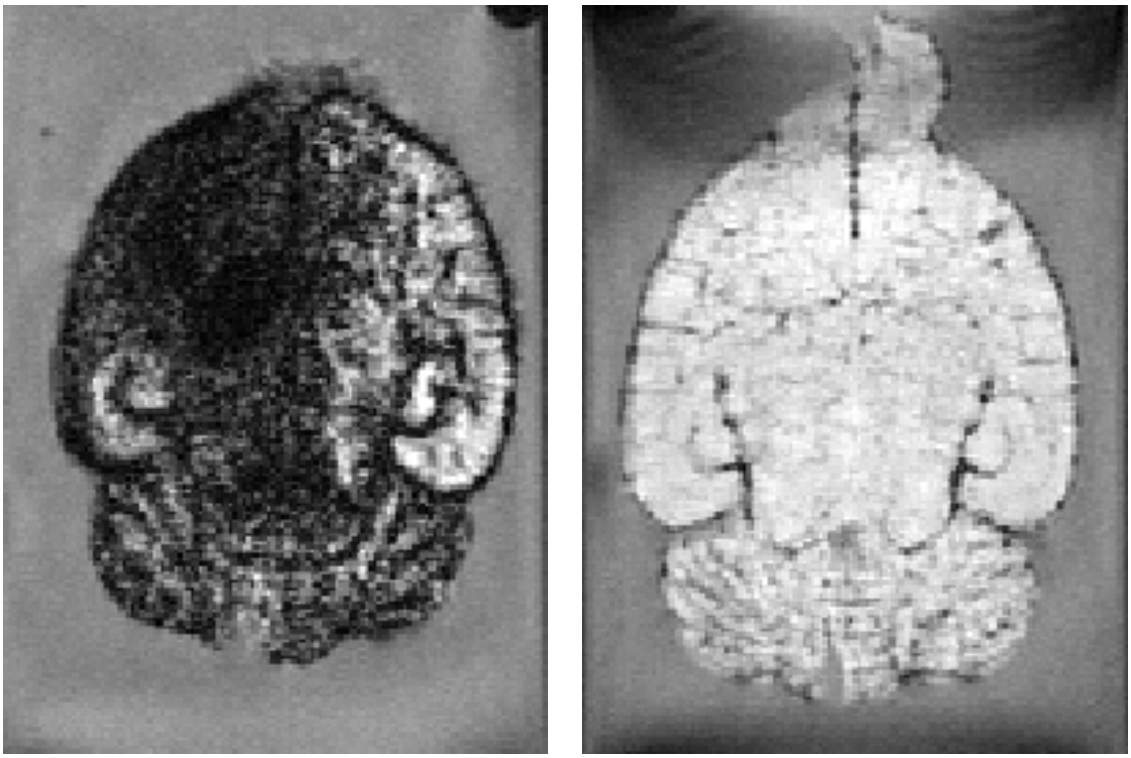

(a) (b)

Figure 4.9.: a) Coronal mMRI scan of first subject from group A. The dark areas of the brain indicate the binding of MPIOs-αVCAM. b) Coronal mMRI scan of the first subject from group B. Only a very few dark areas indicate the binding of MPIOs-αVCAM.

and they are additionally overlayed with the MRI images in sagittal, coronal and axial directions. The MPI signal fits quite well to the locations of the MPIOs-αVCAM locations within the MRI images in all three viewing directions. The MRI results from group B are presented in Fig. 4.12. The MPI results from group B also show an MPI signal, but the signal strength is very close to the noise level. Therefore, it is not possible to reliable connect the MPI signal to the location of the MRI background. For this reason and to avoid misinterpretation the noisy MPI images from group B are not shown. However, when the brains are moved in and out of the MPI scanner, a slightly higher signal as noise can be identified within each brain measurement from group B. The MPI signal increases and decreases minimally as the mouse bed is moved in and out. Not surprisingly, the brains from group C reflect only a noisy MPI signal and their results are also not presented for the same reason.

4.4. Discussion

The developed fiducials, the robot adapted mouse bed, and the extended software have all facilitated the handling and the workflow of this bimodal experiment. The fiducials are a promising, reliable, long-term stable solution and can easily be mounted to the mouse

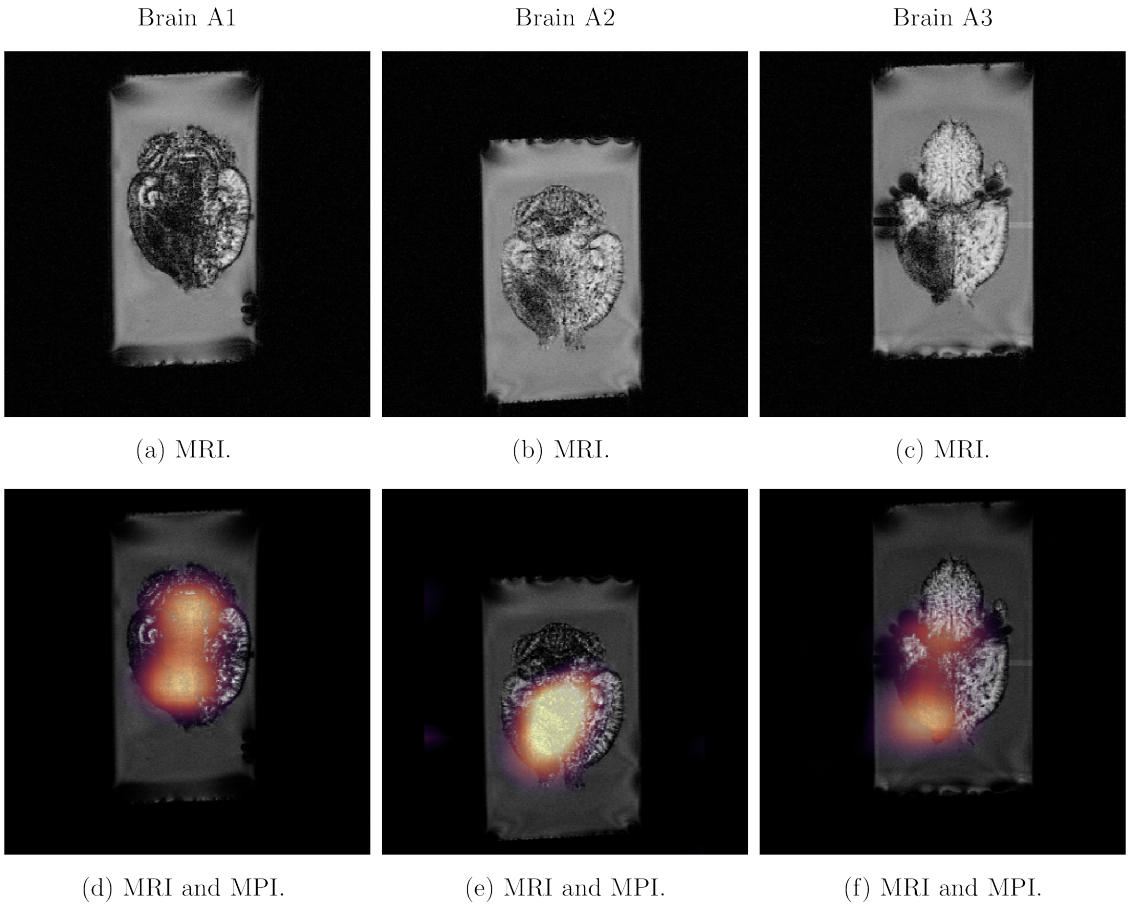

Figure 4.10.: Visualization of three brains of group A in coronal slice. In the first row a), b) and c), the MRI background image are shown. In the second row d), e) and f), the MRI background images are overlayed with the registered MPI images. The MRI image uses a grey value colormap, while the MPI image have a colored colormap.

bed. Additional preparation time of the fiducials for a next experiments is also saved. The robot adapter for the mouse bed works well and enables a precise positioning of a subject within the MPI FoV. Further, it increases the flexibility of the presented method, because the fiducials can be removed and the previous position remains reproducible. The extended software helps to register MRI images to MPI images before an actual MPI measurement. It enables a precise planning of the MPI FoV based on the MRI images.

In this case, the user has to adjust the registration parameters manually by visual inspection. This might lead to inaccuracies, but provides an acceptable solution. In the future, the registration will be performed automatically and the spherical type of fiducials form the basis for automatic registration. Even though some promising first experiments have been conducted, the preliminary results are not presented in this work. However, a possible work flow can be described as follows. First, the position and the orientation of the spherical fiducials have to be identified in each modality as precisely as possible. As a first step, the spherical fiducials have to be identified within the MRI image volume. The fiducials could be detected with image processing algorithms, such as a 3D Hough-

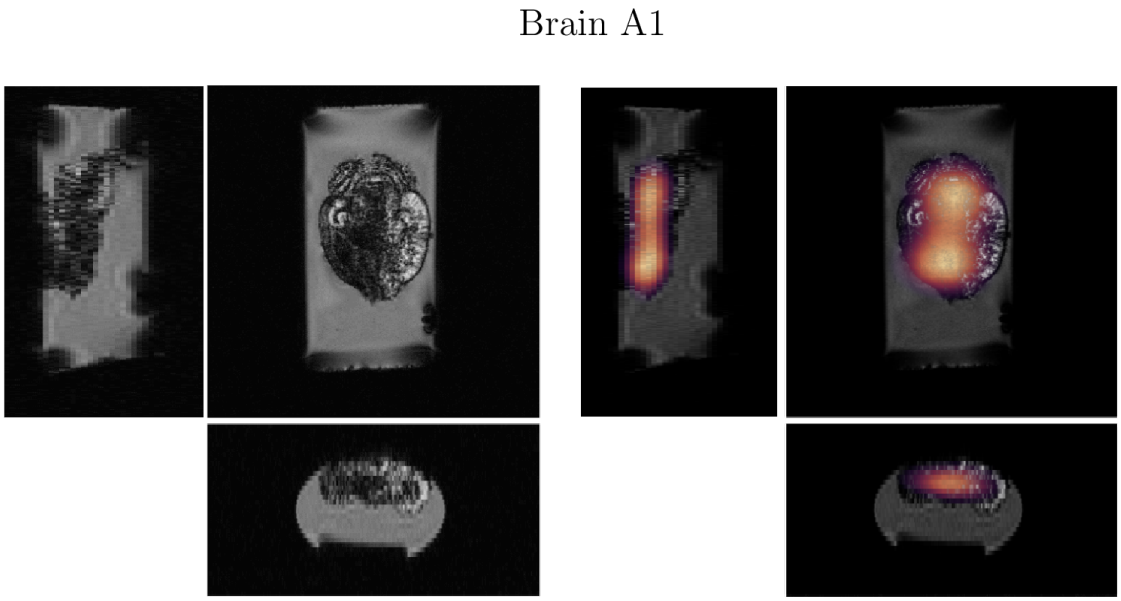

(a) MRI. (b) MRI and MPI.

Figure 4.11.: The brains of the first subject of group A are shown in sagittal, coronal and axial slice. The MRI background images are transparently overlayed with registered MPI images. a) The MRI image have a grey value colormap, b) while the MPI image have a colorized colormap.

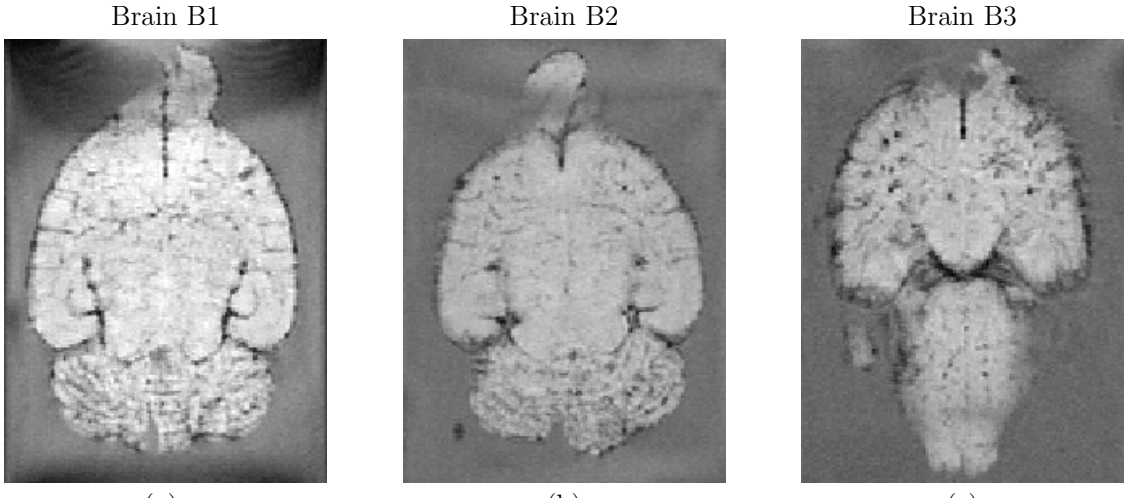

(a) (b) (c)

Figure 4.12.: Visualization of three brains a), b) and c) of group B in coronal slice as MRI images.

transformation, a 2D Hough-transformation on slices, a template matching approach or machine learning approaches. In this context, the image could be weighted to the area where the fiducials are usually placed. The challenge is to circumvent the identification of the spherical fiducials within the imaged brain or other structures of the MRI image. Another possibility would be to use an MRI sequence that only visualizes the spherical silicone structure. In a second step, the fiducials are precisely identified in the MPI images. This has already been demonstrated in chapter 3, where the positions of the spherical fidu-

cials with identical geometric parameters are determined with a precision in the submillimeter range. Similar techniques to increase the accuracy of the position determination have been applied in [146, 148] using subvoxel strategies. The precise identification of fiducials in MPI images has proven to work quite robustly. The algorithm depends only on the threshold parameter Θ_{T}, which could also be avoided by using more sophisticated algorithms. If the three marker positions in 3D have been identified, it needs to be validated that the correct markers are recognized. Therefore, a sanity check is implemented which checks the distances between the recognized markers and compares them to the distances of the markers in the CAD sketch. Additionally, a reasonable distance error tolerance is defined. Then, all distance errors need to be below this tolerance. Otherwise, the fiducials position and orientation is not regarded as correctly identified. This sanity check ensures that no position is falsely identified as a marker. However, after the identification of the three markers, their indexing and naming to the corresponding CAD sketch markers is not known. The three markers are just ordered with respect to their highest maximum voxel. Therefore, a transition needs to done which assigns each identified marker the correct label or name. Only with the correct labeling the distance error check can be performed. For the transformation and labeling of the markers the distances between the markers from the CAD are set up. Assuming the markers in the CAD sketch have the notations A, B and C, the distances are given by $\boldsymbol{d}_{\text{model}} = [d_{1,\text{AB}}, d_{2,\text{AC}}, d_{3,\text{BC}}]$. The difference between all measured distances $\boldsymbol{l}_{\text{meas}} = [l_1, l_2, l_3]$ and the model distances is then calculated. The difference matrix $\boldsymbol{Z}$ is set up with $z_{i1} = (d_{1,\text{AB}} - l_i)$, $z_{i2} = (d_{2,\text{AC}} - l_i)$ and $z_{i3} = (d_{3,\text{BC}} - l_i)$ with $i \in \{1, 2, 3\}$. Afterwards, the minimum in each row determines the distance error and the column index of each minimum value describes the transformation vector. For valid fiducial positions, each index can only occur once in the transformation vector. After the sanity check, there are two sets of three marker positions in 3D-coordinates. Then, these two sets can easily registered with an iterative closest point algorithm (ICP) [164, 165]. The ICP needs an initial starting guess for the transformation in order to provide robust transformations. This is ensured in this scenario as the fiducials are fixated to the mouse bed. Only minor rotations and translations can be expected. The ICP provides a transformation in homogeneous coordinates from one data set to the other. With the help of this transformation the MRI and MPI coordinate systems are registered quite fast and precisely.Especially in animal experiments, this automatic registration method could improve the workflow and reduce the time effort. Up to now, the automatic registration has been done with only one data set of MRI and MPI data. In order to analyze the robustness and the precision error more reliably, the automatic registration has to be tested with more data sets.

The MRI experiments show that the MPIOs-αVCAM particles have targeted the endothelial cells of the central nervous system. The MPIOs-αVCAM are bond to the surface proteins ICAM-1 as described in previous experiments [14]. Further, MPIOs-αVCAM

are not crossing the BBB and are circulating only once through blood system. After one circulation, the liver absorbs the particles. This is indicated by the strong MPI signal in the liver of all subjects that are injected with MPIOs-αVCAM particles. In group A, the ICAM-1 receptors are over-expressed because of the injection with LPS. This effect is visualized by the great amount of MPIOs-αVCAM bond to the ICAM-1 receptors. In group B, a minor amount of MPIOs-αVCAM particles are also bond to the normally expressed ICAM-1 receptors. The MPI results underline the MRI results and show an MPI signal at the same location as the MRI images. Even though the spatial resolution of the MPI images is not high, two of the three question can be answered positively. The sensitivity of MPI is high enough to differentiate between the groups A and B/C. Further, it is even possible to differentiate between the left and right hemisphere of the brain with MPI. However, the sensitivity of MPI is probably not capable of identifying a difference between group B and C robustly. It is worth noting that the injected dose of MPIOs-αVCAM is already quite high and usually only one quarter of that dose is injected. To enhance the MPI spatial resolution and thus, also the sensitivity, the experiments could be repeated with an MPI scanner with a higher gradient. Beside the MPI scanner, a different type of MPI particles could be used to improve the sensitivity, because the MPIO particles are not the ideal tracer for MPI. However, the use of smaller SPIONs might enhance the sensitivity, but then the EPR effect [166] is no longer avoided. The EPR effect introduces an ambiguity as it is no longer clear whether the SPIONs have concentrated passively or due to active binding to the receptors. Additionally, SPIONs might cross the BBB. Alternatively, it could be beneficial to focus the particle design towards larger sized particles. In the presented study, the MRI images provide a better spatial resolution as the MPI images and provide a higher sensitivity for the MPIOs due to the negative contrast to the rest of the brain tissue. Yet, MPI provides a quantitative signal and can be applied in organs, such as the lungs where almost no MRI signal can be acquired. Furthermore, several regions are challenging to image with MRI such as the skin, the lymph nodes, bone, hemorrhages and intestines. These organs usually provide only minor MRI signal and are strongly influenced by artifacts. The simple LPS model presented here could be expanded for more clinical relevant models, such as autoimmune encephalomyelitis, stroke and experimental autoimmune encephalomyelitis (EAE) models. Here, also the endothelial cell activation is important. This includes the target expansion on receptors such as VCAM-1, ICAM-1, P-Selectin, MAdCAM-1 in mice. The inflammation process could be imaged for myocardial, intestinal inflammations, but for pulmonary and bone inflammation MPI would be a dedicated image modality. The reason is that the MRI signal is limited in these regions due to the lack of protons. To better demonstrate the specificity of MPIOs-αVCAM particles, an additional control experiment with the injection of MPIO-isotopes with and without induced inflammation by LPS injection should be conducted for the

next study. This would definitely ensure the MPIOs-αVCAM binding to the VCAM-1 receptors.

In this chapter, a combination of fiducials, a robot adapted mouse bed and an extended online reconstruction to plan MPI experiments more precisely based on MRI images are presented. The presented tools facilitate the workflow and handling of the registration and planning process. The proposed methods are successfully tested in inflammation detection mice experiments. The inflammation of the brain is visualized by MPIOs-αVCAM particles that have bound to over-expressed ICAM-1 receptors. The combination provides the groundwork for a precise and automatic registration technique between MRI and MPI images. Additionally, the detection of MPIOs in the context of neuroinflammation provides a promising quantitative candidate for further medical applications in other organs and pathologies.

5. MPI-guided 4D IVOCT Catheter Tracking

Contents

5.1. Introduction and motivation

MPI has proven in several publications that it can be successfully used for vascular [59, 58, 61] and interventional imaging [60, 61, 62, 133, 45], such as catheter tracking, in real-time. In these applications, the offered spatial resolution of $0.5\,\mathrm{mm}$ to $5\,\mathrm{mm}$ is sufficient. In [45], magnetic nanoparticles enabled the visualization of catheters and guide wires with MPI. Since MPI provides 3D volume images, a 3D catheter trajectory can be directly extracted from the 3D MPI images over time. This is an advantage in contrast to DSA, because DSA provides only 2D projection images. Nevertheless, DSA is often utilized to estimate the path of the catheter movement [167, 168, 169, 170], but in order to gain a 3D trajectory of the catheter movement, additional bi-plane angiographic images have to be taken from different angles [171]. Afterwards, the 2D trajectories of

the catheter movement have to be identified in each DSA image and extruded perpendicularly to the angiographic planes forming two surfaces. The 3D trajectory is then estimated from the intersection of the two surfaces [172]. Besides this additional effort, DSA has the drawbacks that it uses ionizing radiation and that its contrast agent (iodine) cannot be injected to patients suffering from kidney diseases [173, 174, 175]. With this in mind, the ionizing radiation dose is also doubled for the previously described bi-planar 3D trajectory estimation. Furthermore, MPI works with long circulating tracers [43] that can be used to visualize the vascular system over several hours. This marks a great advantage to DSA tracers where iodine has to be given regularly.

DSA is usually used as a second imaging modality for IVOCT. Here, DSA is utilized to provide the position of the IVOCT catheter within a global coordinate system in real-time. Therefore, MPI is a promising candidate to be used as an alternative to DSA because it can provide the IVOCT catheter position directly and without radiation in a global coordinate system. The imaging technique IVOCT is based on the tomographic imaging modality optical coherence tomography (OCT). OCT can resolve tissue structures with a very high spatial resolution of $5\,\mu\mathrm{m}$ to $10\,\mu\mathrm{m}$ [19, 176]. In addition, OCT provides a very high temporal resolution of about $1\,\mathrm{MHz}$ [177, 178]. These high spatial and temporal resolutions apply for 1D imaging depth profiles, which are referred to as A-scans. However, since most of the OCTs light spectrum is attenuated by human tissue, OCT has only a limited penetration depth of $1\,\mathrm{mm}$ to $2\,\mathrm{mm}$. Therefore, OCT is mainly used for surface imaging. The main medical application areas are ophthalmology, dermatology, odontology, and intravascular imaging. In order to perform OCT imaging inside the vascular system, an OCT fiber needs to be integrated in a catheter that can be brought into the vascular system. To obtain a 2D volume image from the inside of the vessel, the catheter tip, which consists of a micro prism, is rotated with the whole catheter. By this means, A-scans are acquired virtually perpendicular to the catheter to form a circular 2D image. As a next step, the catheter can also be pulled back to image a 3D volume of the inside of the vessel. This assembled catheter is called IVOCT catheter. In the field of cardiovascular imaging, it is used to assess the vascular wall morphology of the coronary arteries [77]. This application scenario is illustrated in Fig. 5.1. As IVOCT is also capable of resolving anatomical structures behind the vessel walls in the range of a few milimeters, it is also possible to identify plaque formations [77]. Further, the length of a stenosis can be estimated from images acquired via IVOCT. That is important for the treatment of plaque formations when it comes to choosing the right length for the stent. Overall, the spatial resolution of IVOCT is more than one magnitude higher than intravascular ultrasound (IVUS), computed tomography angiography (CTA), or magnetic resonance angiography (MRA). Therefore, IVOCT is an established imaging modality for the diagnosis of atherosclerosis and thin-cap fibroatheroma [179, 77].

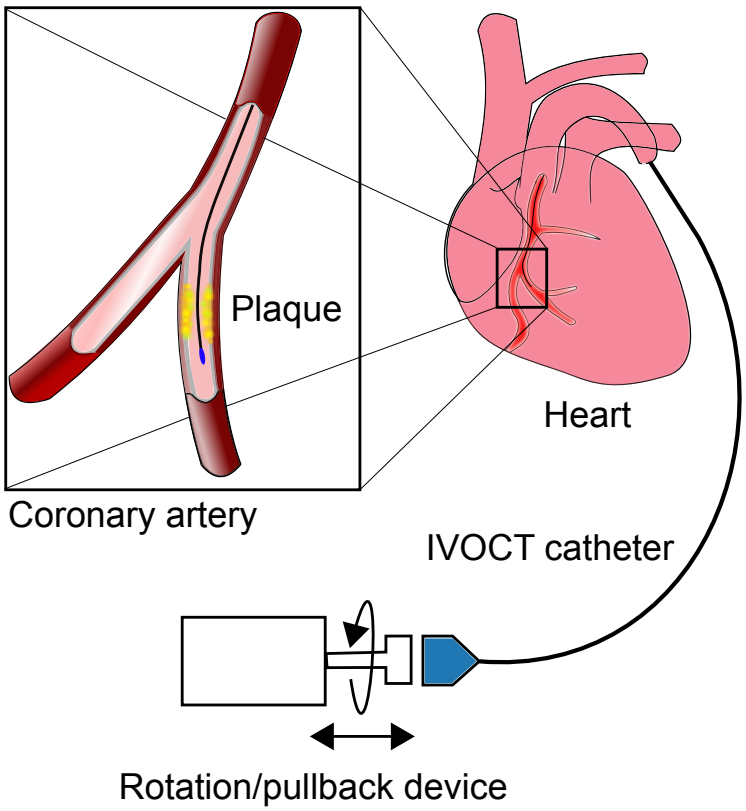

Figure 5.1.: Application of IVOCT catheter. The IVOCT catheter is used to assess plaques and stenoses in the coronary arteries.

As previously described, MPI and IVOCT are radiation free and provide a high temporal resolution. IVOCT features a high spatial resolution but its penetration depth is limited because the tissue attenuates the light. MPI, on the other hand, has a relatively low spatial resolution, but has a constant penetration depth throughout the tissue [180, 17]. Thus, both modalities compensate each others weaknesses quite well and synergize their strengths. As mentioned before, MPI uses only static and oscillating magnetic fields, which are safe within the saftey contraints [21, 113, 112, 22]. In addition, the SPIONs used as a tracer are biodegradable and can be decomposed within the liver [181, 182]. In this combination, MPI helps to overcome the problems of the standard reconstruction of IVOCT as a standalone imaging modality, which are described in the following. The standard reconstruction for IVOCT imaging uses the known rotation and pullback velocity to create a 3D volume image from 1D+t A-scan raw data. The rotation and pullback velocity can be set at the rotation/pullback device. However, the use of IVOCT as standalone modality is based on two assumptions

1. The catheter is moved a along a straight line in the center of the vessel.

2. The catheter tip is rotated and moved with the exact velocity set at the proximal rotation/pullback device.

The situation of the first assumption is shown in Fig. 5.2a. In reality, however, this as-

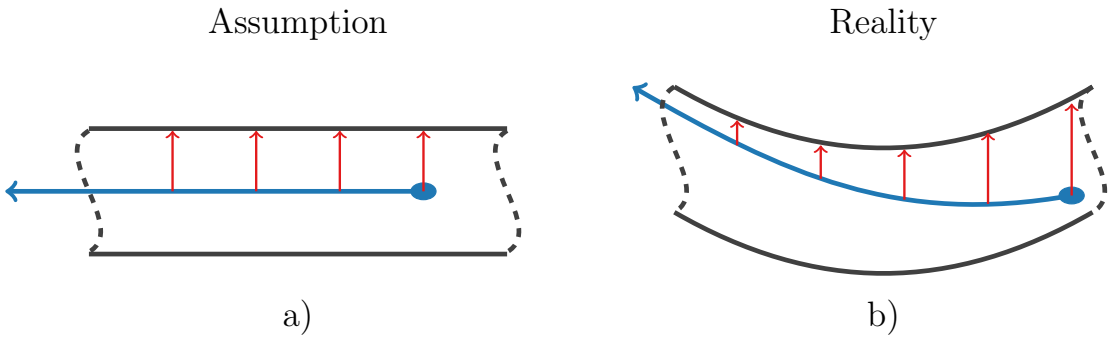

Figure 5.2.: a) The standard IVOCT reconstruction is based on the assumption that the catheter is pulled back along a straight line on the centerline of the vessel. b) In reality, the catheter often moves along the vessel walls to minimize its bending energy and shows less curvature as the vessel.

sumption is mostly not valid because the catheter never lies exactly in the center of the vessel on a straight line. It is often curved and lies close to the vessel walls as it minimizes its bending energy in curvatures. This scenario is shown in Fig. 5.2b.

The second assumption neglects that a flexible catheter has non-linear movements during the pullback. These non-linear movements occur when the elastic catheter is stretched and compressed afterwards. Further, non-uniform rotational artifacts can also arise through the elastic catheter material and the friction of the catheter. These artifacts are called non-uniform rotational distortions (NURD) and are caused by catheter motion itself. In addition to this, there are also heart beat motion and arterial vasomotion artifacts. These artifacts are caused by the heart beat and lead to the situation that parts of a vessel can be imaged twice or not at all. Several publications analyze the relevant influence of motion artifacts on the IVOCT volume reconstructions. In [183, 184], an irregular formation of stent struts is linked to heart beat motion. The scenario of a heart beat artifact is shown in Fig. 5.3. Due to the catheters and the artery movement, the resulting IVOCT volume images show a false shape of the stenosis and an underestimated length of the stenosis (see Fig. 5.3, time point t_6). The influence of heart beat motion can be reduced with ECG-triggered IVOCT imaging performed in less than one second [177]. Further, micro-motors in the tip of the catheter are presented as a solution for imaging artifacts due to a bending of proximally rotated catheters [177, 185]. Yet, it is a challenging task to miniaturize these micro-motors. Therefore, an IVOCT catheter with a micro-motor has not yet been approved clinically. As a consequence, the catheter bending and arterial vasomotion artifacts are still present in the clinical routine and influence the quantification of plaque formations.

The artifacts described before lead to the conclusion that the standalone IVOCT reconstruction approach is susceptible to artifacts, because the position of the catheter is not known in a global patient coordinate system. Therefore, IVOCT highly benefits from

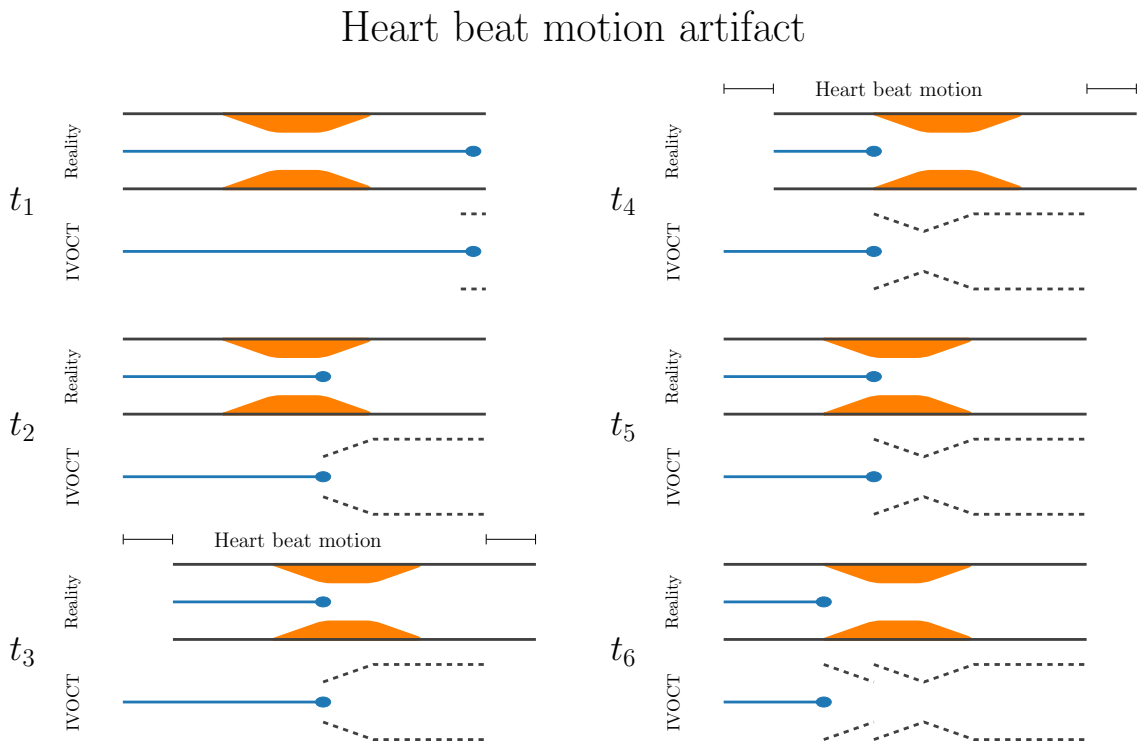

Figure 5.3.: Example sketch of a heart beat motion artifact. During the first two time points (t_1 and t_2), the catheter (blue) is pulled back inside the vessel. The IVOCT reconstruction represents the actual shape of the vessel and the beginning stenosis (orange). At time point t_3, the heart contraction deforms the artery and moves it relatively to the catheter. As a consequence, the catheter is pulled back continuously during time point t_4, but the reconstructed image misses a part of the stenosis. When the deformation of the artery is reversed during time point t_5, the catheter starts to acquire images from the end of the stenosis again. Finally, time point t_6 shows that the IVOCT reconstruction has underestimated the length of the stenosis and represents a false shape of the stenosis. The reason is that the middle part of the stenosis is not imaged at all, while the end of the stenosis is imaged twice.

a second imaging modality. The second imaging modality, such as DSA or MPI, can provide the catheter's position in global coordinate system. This helps to improve the accuracy of the reconstruction and reduces the described artifacts.

In this chapter, first the feasibility of combining IVOCT and MPI is established. For this purpose, the influence of MPI tracers on the OCT signal is analyzed. This investigation helps to identify a suitable concentration that allows simultaneous bimodal imaging of IVOCT and MPI. In a second step, the volumetric IVOCT images are reconstructed based on the catheter pathway gained from MPI data. In this context, the centric vessel pathway is estimated from the MPI image and compared to the standard standalone IVOCT reconstruction methods. By the means of the estimated vessel centerline, the IVOCT images are oriented in 3D to represent the vessel volume. This study uses different vessel shaped phantom to assess the effects of the different reconstructions. The shape and the estimated diameter of the vessel phantoms are compared with CAD sketches. Parts of these results are published in [J2]. As a third step, the IVOCT catheter tip is labeled with an MPI

visible marker to track the IVOCT catheter. The catheter position is provided by MPI in real-time and allows compensating for motion artifacts. In order to synchronize both modalities, a time trigger registers both modalities. Different catheter motion profiles are simulated by a custom-built IVOCT adapter. Afterwards, the MPI-tracked catheter trajectory helps to reconstruct a 4D IVOCT volume. For these experiments, only one straight vessel phantom with a stenosis is used. At first, the plausibility and statistical error of the MPI catheter tracking is evaluated in detail. Afterwards, motion artifacts caused by catheter bending and heart beat motion are investigated. The estimated stenosis lengths is compared to the ground truth length of the vessel phantom. Parts of these results are published in [J3]. In sum, it is demonstrated that simultaneous IVOCT and MPI imaging is feasible and that MPI as a second modality reduces the motion artifacts by precisely tracking the catheters position.

5.2. Material and methods

5.2.1. Principle of OCT

OCT has a spatial resolution in the micro-meter range and is able to penetrate tissue in a range of $1\,\mathrm{mm}$ to $5\,\mathrm{mm}$. Based on this micro-meter resolution, OCT is considered to be in between MRT/CT with a spatial resolution of a few millimeter, ultrasound with $0.1\,\mathrm{mm}$ to $1\,\mathrm{mm}$ and optical microscopes with a spatial resolution below one micro-meter. The same is valid for the penetration depth, but here optical microscopes have an even lower penetration depth, ultrasound a few centimeters and MRT/CT provide an unlimited penetration depth [176]. The fundamental principle of OCT is quite similar to ultrasound, but instead of sound, light is used. In general, light is emitted from a light source and then reflected or backscattered, depending on the optical characteristics of the tissue. Different tissue types show different reflection or backscatter patterns. Finally, the magnitude and echo time delay of reflected or backscattered light is measured by a detector. However, in contrast to sound, no sensor is fast enough to measure the short echo times of light, because light travels with a speed of $3 \times 10^8\,\mathrm{m\,s^{-1}}$. The measurement time for $10\,\mu\mathrm{m}$ resolution would be approximately $10^{-15}\,\mathrm{s}$. Therefore, a low-coherence interferometer, often called Michelson interferometer is used. Instead of measuring the direct reflection echo times, the Michelson interferometer measures the interference of light traveling different pathways. The principle of interferometry establishes an interference between backscattered or reflected light from tissue and light that has traveled a predefined reference distance. By this means, instead of measuring the intensity of the light, interferometry measures the electromagnetic field of light. The basic principle of interferometry by a Michelson interferometer is shown in a schematic diagram in Fig. 5.4. In a Michelson interferometer, the light source emits the initial light beam and this light is then split at a beam splitter into

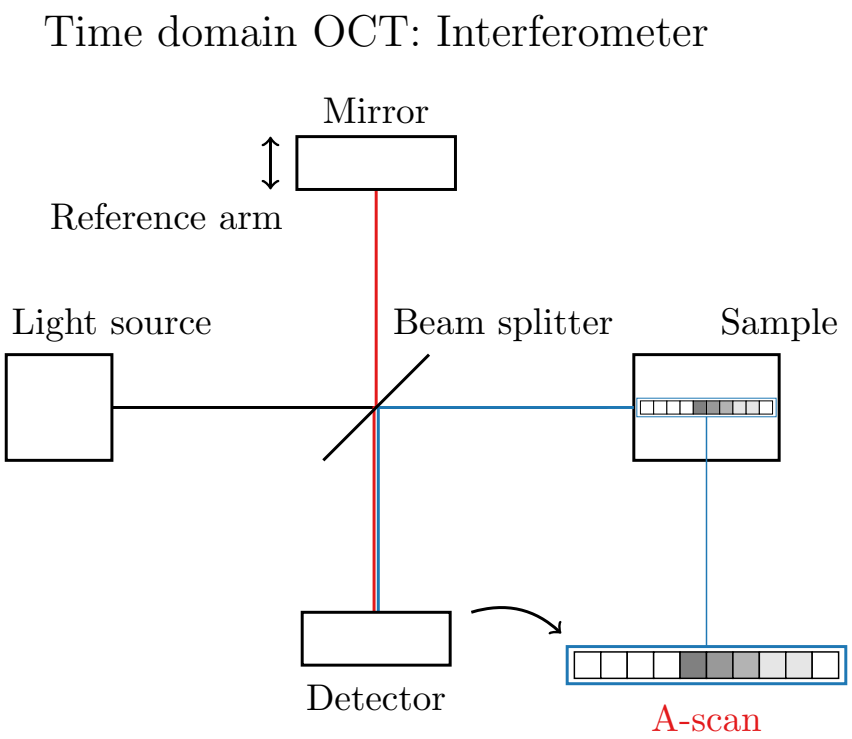

Figure 5.4.: Principle of an OCT Michelson interferometer. The light is emitted from the light source and is split into two pathways. The first pathway travels a known reference distance, where the light is reflected at a mirror. The second pathway travels through the sample and is reflected or backscattered in the tissue. Both light beams, the reference beam and the measurement beam, travel back to the beam splitter where they are both directed towards the detector. Then, the interference of both light beams is measured at the detector.

two beams, the reference beam $E_{\mathrm{r}}(t)$ and the measurement beam $E_{\mathrm{s}}(t)$. The reference beam travels the known distance to the mirror at the end of the reference distance and gets reflected. It travels the way back to the beam splitter, but this time it is directed through beam splitter towards the detector. The measurement beam travels to the sample and gets backscattered and reflected within the tissue. It travels then back to the beam splitter and there it is directed to the detector as well. On the way to the detector, both signals form their interferences. Both beams travel different distances within the interferometer and the sum of both electric fields $E_r(t) + E_s(t)$ is given at the output of the interferometer. The intensity of the output

$$I_{\mathrm{o}} = |E_r|^2 + |E_s|^2 + 2E_r E_s \cdot \cos(2k\Delta L) \tag{5.1}$$

can be measured by a detector, where ΔL is the difference in distance that the beams have traveled within the reference arm and the measurement arm. A low-coherence (broad-bandwidth) light is used as a light source since a coherent light source would induce interference over a wide range of path length differences [176](p.7). If a low-coherence light is used, optical echos can be detected because the interference is only observable

when the path difference between reference arm and measurement arm is within the coherence length

$$L = \frac{c_l}{n_{\text{re}} \cot \Delta f} \tag{5.2}$$

of the light. Here, c_l is the speed of light, n_{re} is the refractive index of the medium and Δf is the bandwidth of the light source. In order to measure interference of more than one position of the sample, the reference distances needs to vary. Thus, the reference arm is moved back and forth to allow a scanning through the sample and measure the magnitude and echo time delay of light. Effectively, the interferometer determines the electromagnetic field autocorrelation of the light. Finally, the interference signal is demodulated to receive the A-scan, a 1D profile through the sample. It is noteworthy that the coherence length of the light source from Eq. (5.2) defines the axial/spatial resolution in the image [176](p.8). OCT usually uses a wavelength of $1300\,\text{nm}$, because at lower wavelengths, melanin and hemoglobin absorb most of the light. At longer wavelengths ($1900\,\text{nm}$), water becomes a dominant absorber and limits the detection sensitivity [176](p.12).

The low-coherence interferometer described above outlines the basic principle of OCT based on time domain detection. Over the years, OCT has been developed further and the modern OCT devices use a Fourier domain detection. The Fourier domain detection allows a higher sensitivity and most importantly speeds up the acquisition time by a factor of 50 to 100. The reason for the speed up is that the Fourier domain detection measures all echos of light at the same time. Additionally, the improvement of the sensitivity by the Fourier domain detection over the time domain detection is about the ratio of the axial resolution to the axial imaging depth [176](p.31). The Fourier domain detections are divided into two main techniques, the spectral/Fourier domain OCT and the swept source/Fourier domain OCT. The spectral OCT [186, 187, 188, 189] also uses a low-coherence light source with an interferometer, as presented for the time domain OCT. However, the interference spectrum is measured by a spectrometer with a high-speed, line scan camera. The interferometer works as described for the time domain OCT, but in this case the reference arm length is fixed. The setup is shown in Fig. 5.5. As a consequence, the measurement beam and the reference beam have a relative time delay caused by the path length difference. That path length difference depends on the depth of the tissue structure from where the measurement beam is reflected or backscattered. The interference of the measurement beam and the reference beam results in a spectral modulation as a function of the frequency. This modulation is then acquired by the spectrometer. As the modulation is periodic, this periodicity is inversely connected to the echo time delay. Thus, one echo delay produces a different frequency modulation than another echo delay. As a next step, the spectrometer output is rescaled from wavelength to frequency. Finally, the interference signal is Fourier transformed (see section 2.5) to gain the axial measurement of the magnitude of the light signal from the sample. The OCT used in this work is a spectral

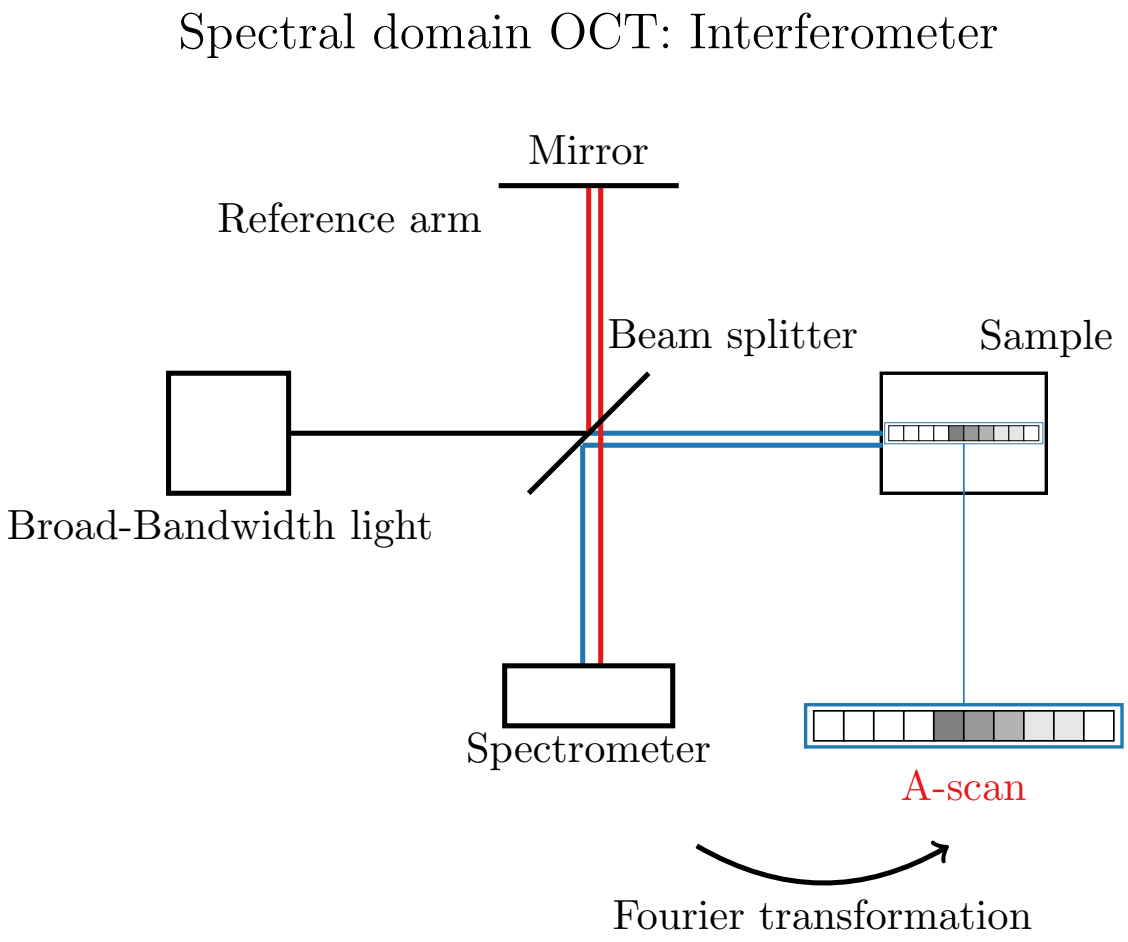

Figure 5.5.: Principle of spectral OCT. A broad-bandwidth light is emitted from the light source and is split into two beams. The reference beam travels a known distance, where the light is reflected at a mirror. The measurement beam travels through the sample and is reflected or backscattered in the tissue. Both light beams, the reference beam and the measurement beam, travel back to the beam splitter, where they are both directed towards the spectrometer. Finally, the spectrum measured at the detector is Fourier-transformed to the A-scan.

OCT and more detailed information can be found in [176]. The swept source OCT basically uses a narrow-bandwidth light source and an interferometer, but the light source sweeps through the frequencies. Here, the interference is measured as a function of time by the frequency-swept detector. Further readings on the swept source OCT can be found in [176] and [9] as the swept source OCT is not part of this work. One advantage of low-coherence interferometry is that it can be performed with continuous wave light sources, whereas swept source OCT needs short pulses of a laser.

5.2.2. Basic principle IVOCT

As described before, OCT provides excellent image quality and is able to resolve different tissue layers beyond the tissue surface [77]. Therefore, it is obvious to strive for an assembly with the OCT fiber inside a catheter, as it has been done with intravascular ultrasound

(IVUS). However, the microoptic fabrication of the optical components needs to be even smaller than for IVUS, since the optical fibers have only a diameter of $80\,\mu\mathrm{m}$ to $250\,\mu\mathrm{m}$. In the case of IVOCT, an optical fiber is placed inside a catheter. At the tip of the catheter, a microprism is assembled. The microprism directs the light radially outward. The light then points perpendicular to the catheter wire. The catheter is constituated within a plastic shell catheter, while the catheter can be rotated and moved freely within the plastic shell catheter. The IVOCT catheter is then attached to a custom-made rotation and pullback device built by S. Latus (Institute of Medical Technology and Intelligent Systems, Hamburg University of Technology, Hamburg, Germany) as described in [J2]. The rotation and pullback device can be seen in Fig. 5.6. It operates at a maximum frequency

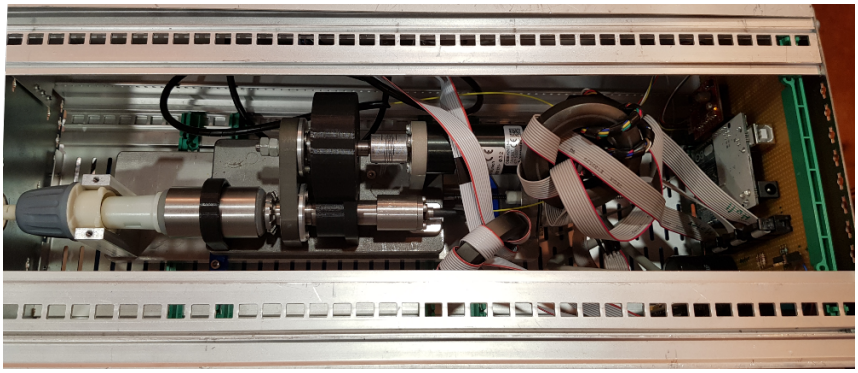

Figure 5.6.: Custom-build rotation and pullback device built by S. Latus (Institute of Medical Technology and Intelligent Systems, Hamburg University of Technology, Hamburg, Germany) as described in [J2].

of approximately $f_{\text{rot}} = 16.6\,\mathrm{Hz}$ and reaches a pullback velocity of $v_{\text{pull}} = 1.25\,\mathrm{mm\,s^{-1}}$. The different velocities for rotation and pullback can be adjusted in the control software of the custom-made device. The OCT beam leaving the microprism performs a helical movement when both movements, rotation and pullback, are superimposed. The helical movement is animated in Fig. 5.7. The optical fiber is connected via a rotational fiber coupler to the actual OCT device. As OCT device, the spectral-domain OCT system Telesto I (Thorlabs, US) is used. It operates with a wavelength of λ_{OCT} of $1315\,\mathrm{nm}$ and provides a A-scan rate of $f_{\text{OCT}} = 91\,\mathrm{kHz}$. The pixel number per A-scan is $P = 512$ pixels. This results in a 1D axial field of view of approximately $l_{\text{FoV}} = 2.66\,\mathrm{mm}$ within air. Within water, a constant refractive index of $n_{\text{water}} = 1.33$ ($n_{\text{blood}} = 1.301$) results in a pixel spacing of $\Delta = d_{\text{FoV}}/P/n_{\text{water}} = 4.0\,\mu\mathrm{m}$. For the spectral-domain OCT, the spectrum of the

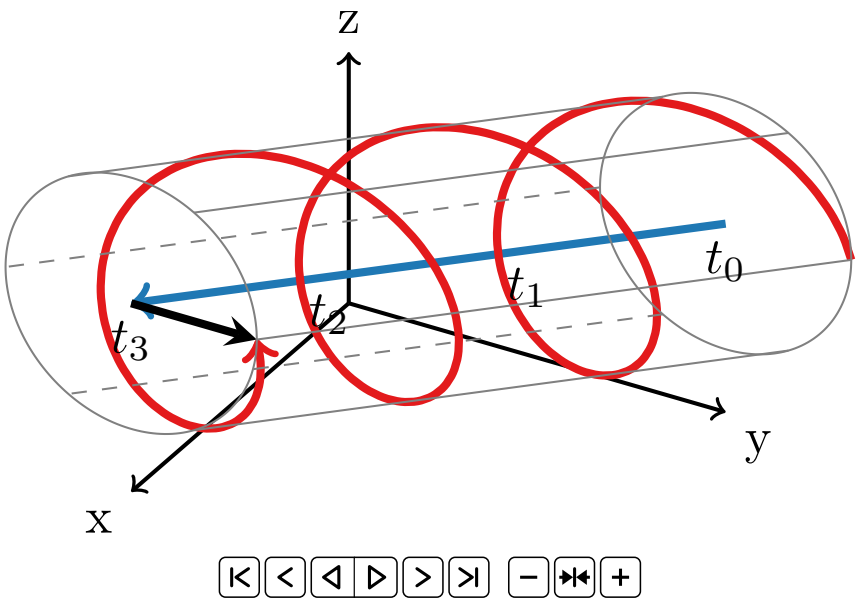

Figure 5.7.: Illustration of a helical movement of the A-scans (black arrow) if rotational (red) and transversal (blue) movements are superimposed. $t_0 - t_3$ marks time points when one rotation is completed.

light source is given by $S(k)$ with k as the wave number. The detected interference signal can be expressed by

$$\begin{aligned} I_D(k) =& S(k)\left(R_r + \sum_{m=1}^{M} R_m\right) + \\ & S(k)\sum_{m=1}^{M} 2\sqrt{R_r R_m}\left(\cos[2k(z_r - z_m)]\right) + \\ & S(k)\sum_{m=1}^{M}\sum_{n=1,n\neq m}^{M} \sqrt{R_m R_n}\left(\cos[2k(z_m - z_n)]\right), \end{aligned} \tag{5.3}$$

where M represents a finite number of ideal reflections in the sample beam way. R_i is the reflectivity, z_i the path length till reflection, and the index r refers to the reference arm [176](p.54). The first term in Eq. (5.3) is related to the light source and defines a static offset. The second term represents the interference between reference and measurement beam path. The third term encodes the various reflections within the measurement beam that interfere with each other pairwise. Each raw data spectrum acquired with the Telesto OCT device is reconstructed individually as described in [J2]. In the first post-processing step, the background signal is subtracted from the signal to compensate for the offset term in Eq. (5.3). As a second step, the data is re-gridded with respect to the wave number k, because the signal is not sampled equidistantly. Then, a Hann window is used for filtering and smoothing the data. Finally, the data is transformed by a fast Fourier transform to obtain the A-scan. Note that the A-scan value are complex, but only the absolute values are processed further as the A-scans.

IVOCT reconstruction

The raw signal of an IVOCT measurement consists of the 1D profiles, the A-scans over time. These A-scans are acquired by the OCT device as the catheter is permanently rotated while being pulled back. The temporal A-scans provided by the OCT device are shown in Fig. 5.8. The time span between each time point between t_0 and t_3 defines the time for one

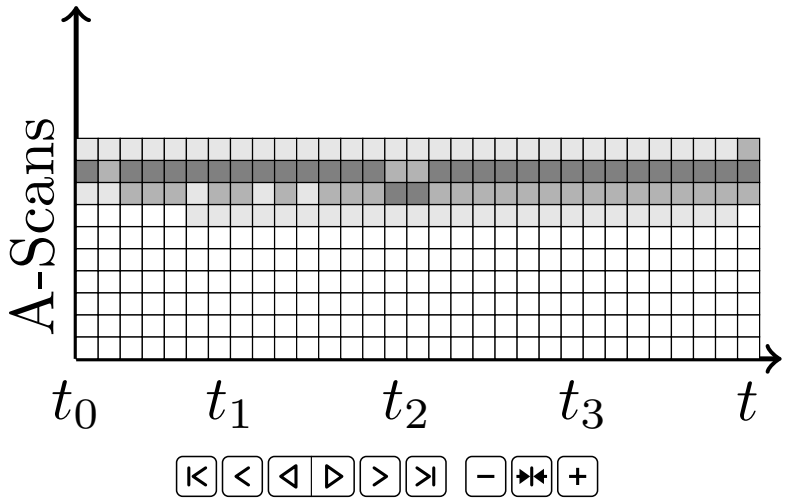

Figure 5.8.: The raw temporal A-scans received by the OCT device are acquired over time. The time span between each time points $t_0 - t_3$ defines the time for one full rotation of the catheter.

full rotation of the catheter. Although the A-scans are acquired on a helical pathway as shown in Fig. 5.7, the A-scans of one rotation are normally visualized on a 2D plane image called a B-scan. The helical pathway can be neglected because the pullback distance $s_{\text{rot}} = v_{\text{pull}}/f_{\text{rot}} = 45.1\,\mu\text{m}$ is very short during one rotation.

To assemble a B-scan, all A-scans from one rotation are selected. As one catheter rotation takes $T_{\text{rot}} = 1/f_{\text{rot}} = 60.2\,\text{ms}$, $N_{\text{rot}} = f_{\text{OCT}}T_{\text{rot}} = 5481$ A-scans are chosen per B-scan. Further, one rotation with the interval $[0, 2\pi)$ is equidistantly discretized with N_{rot} points. Each A-scan is then placed on each point. Afterwards, the depth of the A-scans is gridded from their polar representation to a cartesian grid. With the cartesian representation, the 2D cross-sectional image, namely the B-scan, is obtained. The procedure is repeated for each following rotation and is shown in Fig. 5.9. The transformation from polar coordinate representation to cartesian space maximally causes an interpolation error of $3\,\mu\text{m}$. For this assumption, a chord length $s_c = 2d_{\text{FoV}}\sin(\frac{\alpha}{2})$ of a circle segment with $\alpha = 360°/N_{\text{rot}}$ is identified.

To gain a three-dimensional representation of the reconstruction, the B-scans are stacked equidistantly with a distance of $45\,\mu\text{m}$. This arrangement forms a 3D volume image called the V-scan. The assembly of the V-scan is shown in Fig. 5.10. In general, the reconstruction transforms a continues 1D temporal signal to a static spatial 3D volume image.

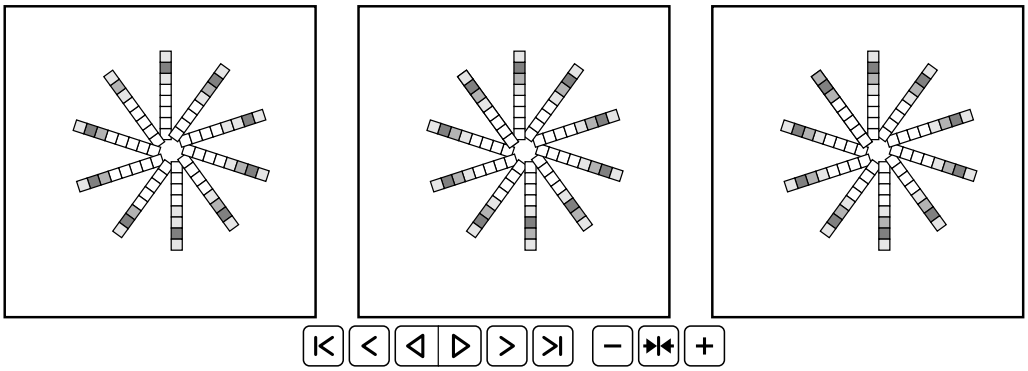

Figure 5.9.: The A-scans for one rotation are circularly discretized in the interval $[0, 2\pi)$. They are transformed from their polar coordinate representation to a carteasian grid. The animation shows the B-scans for three rotations.

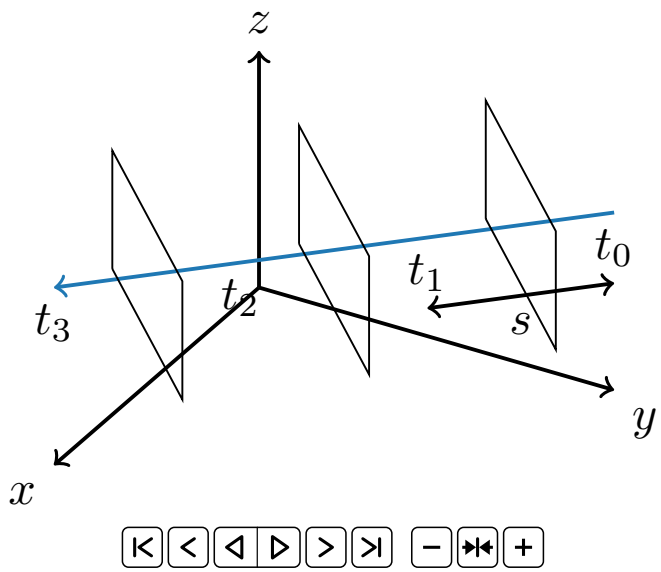

Figure 5.10.: The V-scan is assembled by stacking the B-scans equidistantly with a distance of $45\,\mu\mathrm{m}$. The V-scan is static representation of the 3D volume.

5.2.3. Experimental setup and *in-vitro* phantoms

The experimental setup used in [J2, J3] consists of a preclinical MPI scanner (see section 2.7.3), a custom-built IVOCT imaging adapter (see Fig. 5.6), a spectral domain OCT system (Telesto I, Thorlabs, US) and a control unit. The whole setup is schematically shown in Fig. 5.11. For the experiments, two different IVOCT catheters (Dragonfly Duo Kit, Abbott) with an outer diameter of $0.9\,\mathrm{mm}$ are used. The first catheter is a standard catheter, as it is shown in Fig. 5.12a and its catheter tip is shown in Fig. 5.12b. Inside the catheter, an optical fiber is covered by tight and flexible protection. Further, the whole catheter is able to rotate within a hollow plastic covering catheter. The catheter tip consists of a microprism that directs the light radially perpendicular outward. The second catheter is also a standard catheter, but the catheter tip (see Fig. 5.12b) is coated with a thin layer of magnetic lacquer ($1\,\mu\mathrm{L}$ Magneto Magnetic Lacquer, Hand & Nail Harmony,

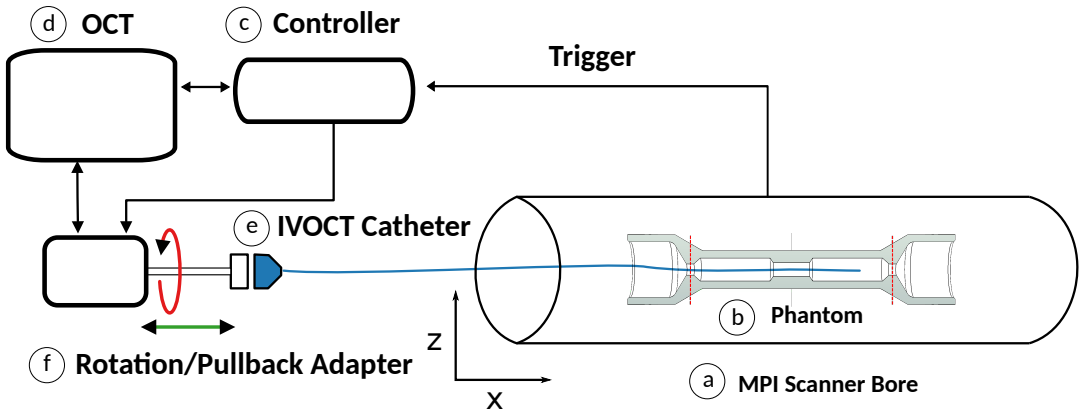

Figure 5.11.: Inside the MPI scanner bore a) a vessel phantom b) is placed. The MPI triggers the control unit c) when the measurement starts. Afterwards, the control unit initializes the OCT acquisition d) and starts to rotate and and pullback the IVOCT catheter e) with the rotation/pullback adapter f). The experimental setup is depicted as described in [J2, J3].

US). The magnetic lacquer dries on the catheter tip and does not dissolve in water. The marked catheter provides suitable image quality and the phantom borders are still visible for segmentation methods.

Both IVOCT catheters are used in different scenarios. In the first scenario, the phantoms are filled with magnetic particles and the standard IVOCT catheter is used for imaging. In the second scenario, the phantoms are filled with water and the marked IVOCT catheter performs the imaging. Here, the magnetic coating enables an MPI-based catheter tracking. In both scenarios, the MPI image acquisition and the IVOCT image acquisition are performed simultaneously. Both scenarios are shown in Fig. 5.13. For the experiments, three different types of phantoms are designed by S. Latus to mimic the vessels as published in [J2, J3]. The first type of phantom is a straight vessel phantom with an inner diameter of $2.5\,\mathrm{mm}$. This phantom type has a stenosis in the middle. Two stenosis phantoms with a stenosis diameter of $1.5\,\mathrm{mm}$ are constructed. The first stenosis has a length of $2.5\,\mathrm{mm}$ and the second stenosis has a length of $1.5\,\mathrm{mm}$. The length between the narrow parts for both phantoms is $20\,\mathrm{mm}$ (see Fig. 5.14). The phantom is then placed in the MPI FoV, as shown in Fig. 5.15a. The second vessel phantom type has a Z-shape form and can be seen in Fig. 5.14. The third vessel phantom forms a U-shape and is presented in Fig. 5.14. Both, the Z-shape and the U-shape phantom, have an inner diameter of $2.5\,\mathrm{mm}$ and a total length of $20\,\mathrm{mm}$.

All phantoms have narrow parts at the start and end of the phantom (in Fig. 5.14 illustrated with red circles) that can be used for co-registration of IVOCT and MPI images. The IVOCT volume is usually cut at these positions. The phantoms are 3D-printed by the stereolithography technique. For 3D-printing, the Form 1+ and the Form 2 (Formlabs, US) printers are used. Both printers offer a printing resolution of $0.05\,\mathrm{mm}$ in all three axes. A transparent resin FLGPWH01 from Formlabs is used to build the phantoms. The

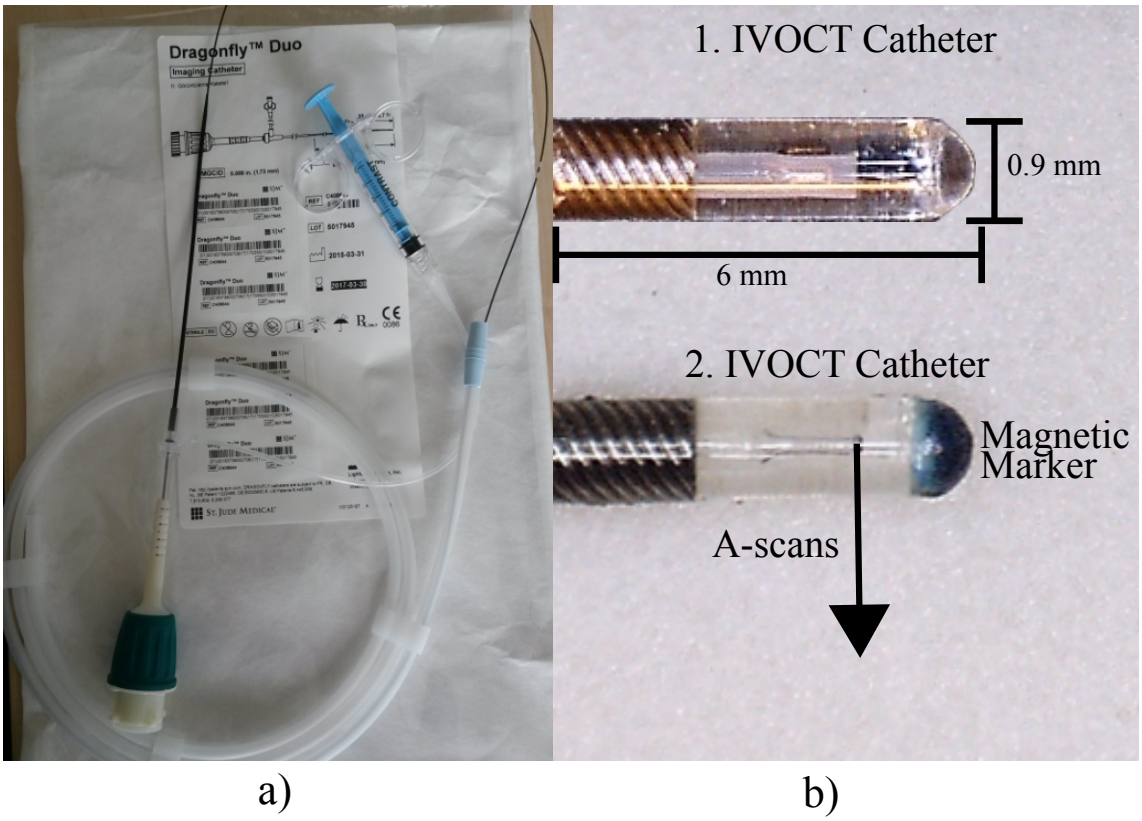

Figure 5.12.: a) Typical IVOCT catheter Dragonfly Duo Kit (Abbott, US). b) Magnified images of microprism at the tip of both IVOCT catheter. The second catheter tip is coated with 1 µL of magnetic lacquer.

resulting 3D-prints possess an ultimate tensile strength of $65\,\mathrm{MPa}$ and a Young's Modulus of $2.8\,\mathrm{GPa}$ after they have been cured with ultra violet light.

5.2.4. Acquisition and reconstruction parameters

The spectral OCT system operates with the parameters stated in section 5.2.2 ($\lambda_{\mathrm{OCT}} = 1315\,\mathrm{nm}$, $f_{\mathrm{OCT}} = 91\,\mathrm{kHz}$, $l_{\mathrm{FoV}} = 2.66\,\mathrm{mm}$ and pixel spacing of $4.0\,\mu\mathrm{m}$). With the help of the custom-built catheter adapter, the IVOCT catheter can be rotated and pulled back. The IVOCT catheter is rotated with a rotational frequency of $f_{\mathrm{rot}} = 6.25\,\mathrm{Hz}$. The standard pullback velocity is set to $v_{\mathrm{pull}} = -1.25\,\mathrm{mm\,s^{-1}}$, but the velocity is varied within the experiments, as it is described in section 5.2.6. The velocity variation simulates different motion artifacts. The catheter is pulled back over a total distance of $25\,\mathrm{mm}$ in all experiments, but only the data from the middle $20\,\mathrm{mm}$ are used further.

The MPI measurements are performed with the preclinical MPI scanner described in section 2.7.3. To gain a better signal quality, a custom-built receive coil [136] is inserted inside the scanner bore. The receive coil inlay reduces the bore diameter to $40\,\mathrm{mm}$. The magnetic field strength is adjusted to $12\,\mathrm{mT}$ in all three directions. The gradient strength is set to $2.0\,\mathrm{T\,m^{-1}}$ in the z-direction and $-1.0\,\mathrm{T\,m^{-1}}$ in the x- and y-directions. The

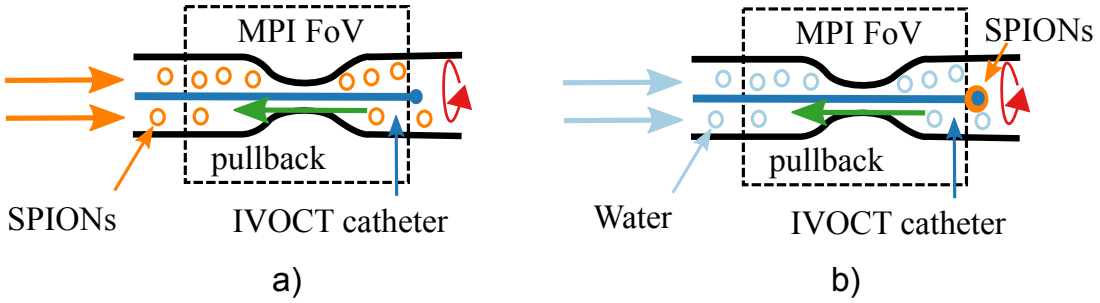

Figure 5.13.: a) In the first scenario, the standard IVOCT catheter is pulled back within a phantom filled with SPIONs. b) In the second scenario, the marked IVOCT catheter is pulled back within a phantom filled with water. In both cases, the measurement of the MPI and IVOCT imaging is performed simultaneously.

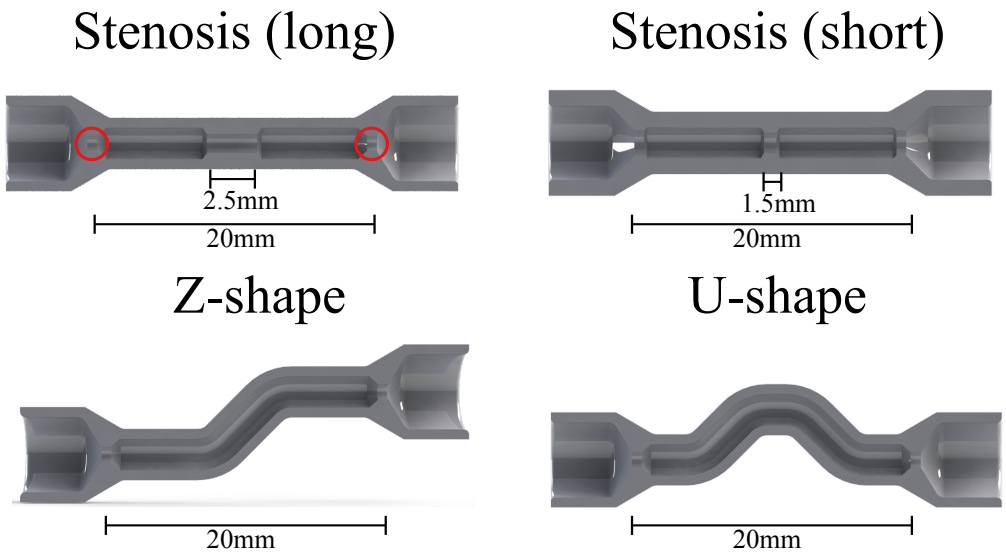

Figure 5.14.: Visualization of the CAD model cross sections of the 3D-printed long and short stenosis as well as the Z-shape and U-shape phantoms. The red circles show the narrow parts that illustrate the start and end of the phantom length of l_{pha}=20 mm. The phantoms have been designed by S. Latus as presented in [J2, J3].

frame rate is $46.43\,\text{Hz}$ and it takes $21.54\,\text{ms}$ to acquire one frame. The FoV derives from the magnetic field and the gradient to a size of $24\,\text{mm} \times 24\,\text{mm} \times 12\,\text{mm}$.

For the reconstruction of the MPI images, the frequency space approach [17], as presented in section 2.5.1, is used. The necessary calibration scan is acquired with a delta sample of size $1\,\text{mm} \times 1\,\text{mm} \times 1\,\text{mm}$. Two system matrices are acquired. For the first system matrix, the delta sample is filled with $1\,\mu\text{L}$ perimag, whereas for the second system matrix $1\,\mu\text{L}$ undiluted magnetic lacquer is used. Both system matrices are acquired at $35 \times 25 \times 13$ positions to cover a volume of $35\,\text{mm} \times 25\,\text{mm} \times 13\,\text{mm}$. Artifacts are reduced by choosing the calibration scan volume larger as the FoV in all directions [120].

The reconstruction solves the inverse problem with a first-order Tikhonov-regularized least-squares approach as described in section 2.5.2. The number of Kaczmarz iterations is chosen to be $n_{\text{iter}} = 3$ and the regularization parameter λ is set to 0.01. These recon-

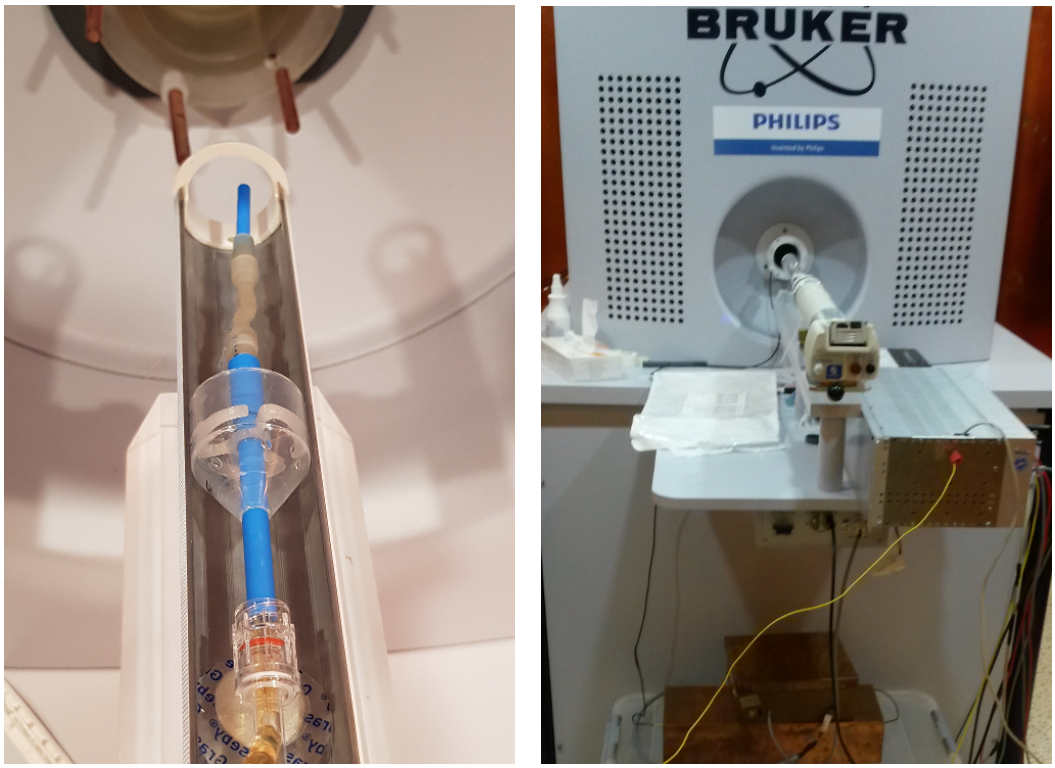

(a) (b)

Figure 5.15.: a) The phantom on the mouse bed is to be placed inside the MPI scanner bore. b) The control unit with the rotation/pullback device in front of the scanner.

struction parameters are optimized based on visual impressions. To gain a higher signal, the temporal MPI signal is block-averaged with a factor of two before the reconstruction. That bisects the temporal resolution to $f_{\text{temporal}} = 23.2\,\text{Hz}$. For the pathway estimation and tracking of the catheter, the automatic marker localization from section 3.2.2 is used. The relative intensity threshold is chosen to be $\Theta_{\text{T}} = 0.35$.

5.2.5. IVOCT volume reconstruction methods

In the following paragraphs, four different IVOCT volume reconstruction methods are presented analogously to [J2, J3]. The reconstruction methods are named input parameter (IP), input parameter and Lumen Center (IP+LC), MPI centerline estimation (MCE) and MPI marker tracking (MMT) volume reconstruction. For all four reconstruction methods, the inner phantom border is segmented in the IVOCT data using a semi-automatic algorithm [J2, C1, 190]. A lumen boundary detection [191] is already performed on the temporal A-scan representation (see Fig. 5.8), which simplifies the segmentation process. However, in some cases, manual corrections are applied to the segmentation algorithm, especially in the narrow parts of the phantom. For the segmentation, an edge detection algorithm uses several preprocessing steps including filtering, removal of catheter, thresholding and morphological operations. Afterwards, the transformation from A-scans

to B-scans is done as described in section 5.2.2. The transformation from B-scans to V-scans is performed by one of the reconstruction methods described in the following. Finally, the segmentation algorithm estimates the distance d_{CW} between the catheter and the phantom wall for each A-scan. Afterwards, 3D point clouds are generated based on the four methods. Their envelopes are utilized to assess the volume reconstructions.

Input parameter (IP) reconstruction method

The IP-based volume reconstruction is based on the assumption that the catheter is moving along a straight trajectory. The non-linear motion of the catheter or the shape of the vessel is neglected. The catheter movement is expected on the basis of the known input parameter for rotational speed and pullback velocity. Consequently, the B-scans are aligned equidistantly perpendicular along a straight line. The line goes through the origins O_c of each B-scan (see Fig. 5.16a). However, even for a straight vessel phantom, the

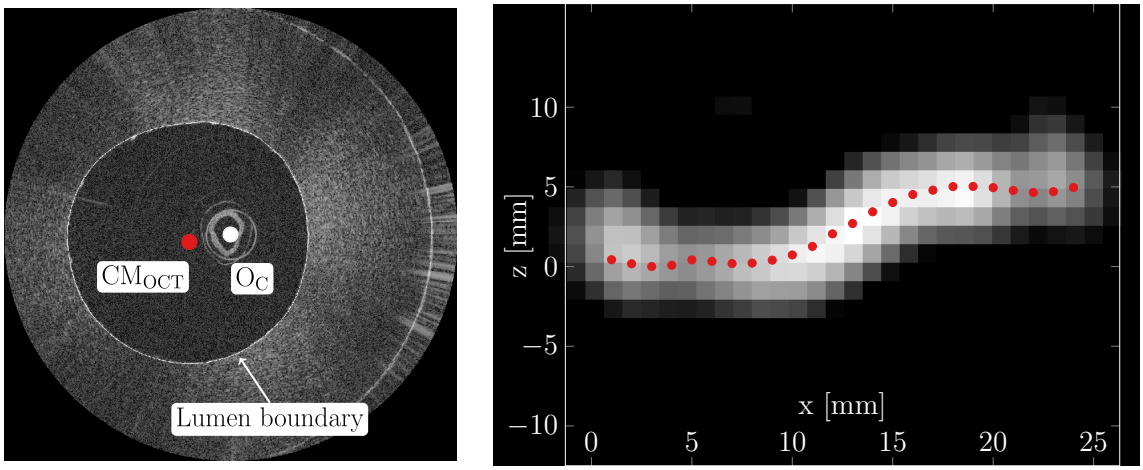

Figure 5.16.: a) The image origin O_C of each B-scan is used to align the B-scans for the IP-based volume reconstruction. The methods IP+LC and MCE place their lines in the center of mass CM_{OCT} of the lumen boundary. b) Center of mass CM_{MPI} in each MPI yz-slice (red squares) for an U-shape vessel phantom depicted as xy-slice. The pathway is used to align the B-scans to a volumetric V-scan image. Both images have been published in [J2].

catheter pathway does not lie precisely on a straight line in reality. As described eariler, the catheter tip is affected by motion artifacts and the catheter minimizes its bending energy.

Input parameter and lumen center (IP+LC) reconstruction method

The IP+LC reconstruction method uses the segmented lumen boundaries to calculate the lumen's center of mass CM_{OCT} [192], as seen in Fig. 5.16a and Fig. 5.16b. The lumen center is identified within each B-scan. Afterwards, the B-scans are equidistantly stacked

with their CM_{OCT} placed on a straight line. The IP+LC method assumes that the catheter is moving mostly on the centerline of the vessel cross-section . This method is able to reconstruct a straight shaped vessel phantom, even if the catheter has not been placed perfectly centric on the vessel centerline in each cross-sectional image.

MPI centerline estimation (MCE) reconstruction method

To stack the B-scans, similar to the IP+LC method, the MCE reconstruction method uses the center of the segmented lumen. However, for the MCE method, the catheter pathway is not assumed to be on a straight line. Here, the catheter centerline is estimated based on the MPI images. As a first step, the static 3D MPI images are post-processed slice-wise along the x-direction. The center of mass CM_{MPI} is determined for each yz-slice with the algorithm presented in section 3.2.2. As a second step, the positions CM_{MPI} per slice are interpolated to the number of B-scans. As a third step, each B-scan is stacked with its lumen center CM_{OCT} on the estimated pathway of the vessel centerline (see Fig. 5.16b). The estimated MPI centerline resembles the actual structure of the measured phantom vessel. Overall, the MCE method extracts the centerline from the MPI data and estimates the catheter pathway. By this means, arbitrary vessel shapes can be reconstructed in the IVOCT volume.

MPI marker tracking (MMT) reconstruction method

The MMT reconstruction method uses the IVOCT catheter marked with SPIONs. Through this magnetic marker, the IVOCT catheter can be tracked via MPI. Therefore, the actual IVOCT catheter trajectory is acquired. In contrast to the other reconstruction methods, the A-scans are arranged along the catheter trajectory. For two successive catheter positions, the distance in space Δx and time Δt_{MMT} is calculated and the acquired A-scans are distributed equidistantly. Due to substantial noise of the y- and z-components of the estimated 4D catheter trajectory, only the x-coordinate (in pullback direction) is considered as catheter position over time. With respect to the catheter rotation f_{rot}, the OCT frequency f_{OCT} and the MPI volume rate $f_{temporal}$, up to four catheter positions are assigned to one catheter rotation. Afterwards, the A-scans are oriented with a fixed angle difference θ_0 around the estimated catheter trajectory, because a constant catheter rotation is assumed. In a final step, the distances d_{CW} for each A-scans are placed in a 3D coordinate system. The A-scans are placed on the 3D phantom boundary points on a helix with constant pitch $p_{pull} = v_{pull}/f_{OCT}$ and angle $\theta_0 = 360° \cdot f_{rot}/f_{OCT}$. It means that the reconstruction actually respects the helical form as the transformation from A-scan to V-scan is done directly without creating B-scans. For this purpose, both imaging modalities have to be temporally synchronized to ensure an image registration. The temporal synchronization is done via a trigger signal and each event is shown in Fig. 5.17. The MPI device sends

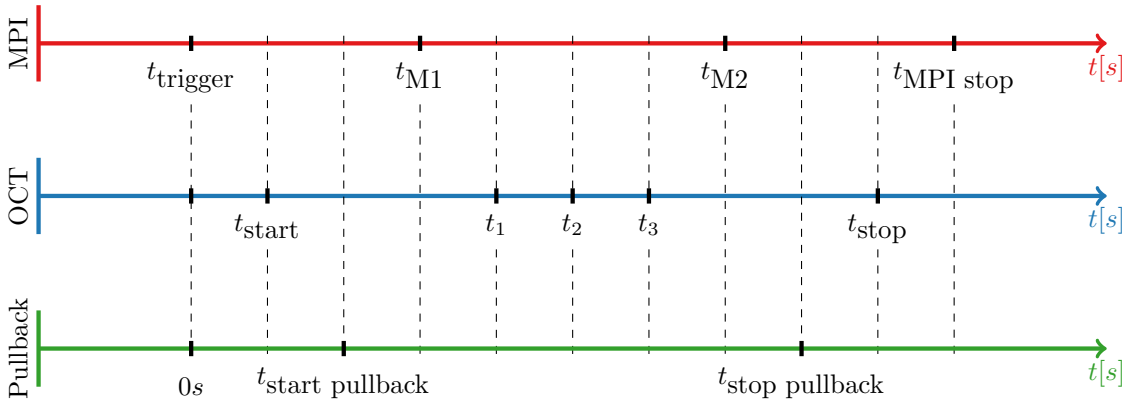

Figure 5.17.: Time axis to synchronize the OCT device and pullback device with the help of the MPI trigger signal.

the trigger (t_{trigger}) and one second afterwards, the catheter starts to pull back. Meanwhile, the A-scans are acquired by the OCT device ($t_{\text{OCT,0}}$). For the catheter movement, different motion profiles are applied as further described in the experiment section 5.2.6. The time stamps t_{M1} and t_{M2} mark the entrance and the exit of the catheter into and out of the MPI volume. The MPI measurement is stopped ($t_{\text{MPI,end}}$) when the catheter motion is finished ($t_{\text{OCT,end}}$). The registration of the IVOCT volume data and the MPI catheter tracking is shown in Fig. 5.18. The used automatic marker tracking has an accuracy in the sub-millimeter range, but the catheter position is only robustly determined within a cropped MPI FoV. Therefore, the MPI FoV is cropped for 4D reconstruction methods. In the x-direction, the cropped MPI FoV possesses a length of $10\,\text{mm}$. Outside this cropped MPI FoV, the catheter position could not be estimated as robust due to artifacts that are introduced by the rotation of the catheter. Positions outside this cropped MPI FoV are not considered for reconstruction. In addition, extreme outliers are excluded by setting a threshold to realistic values. Further, a Ransac algorithm removes slight outliers. In extreme cases, the images are affected by noise. Then, the localization algorithm falsely detects a high intensity noise voxel as a marker position. The trajectories are smoothed to ensure a continuous trajectory.

5.2.6. Experiments

The experiments are designed to investigate four aspects. The first aspect analyzes whether the magnetic particles influence the OCT signal strength and whether it is feasible to perform bimodal imaging of MPI and IVOCT. The second aspect investigates whether it is beneficial to estimate the vessel centerline from the MPI data and use it for the reconstruction of the IVOCT images. The third aspect studies the feasibility to track the IVOCT catheter directly with MPI and utilize the determined trajectory for the IVOCT reconstruction. The last experiments investigates the possibility to track the rotation of the catheter with an asymmetric magnetic marker at the catheter tip.

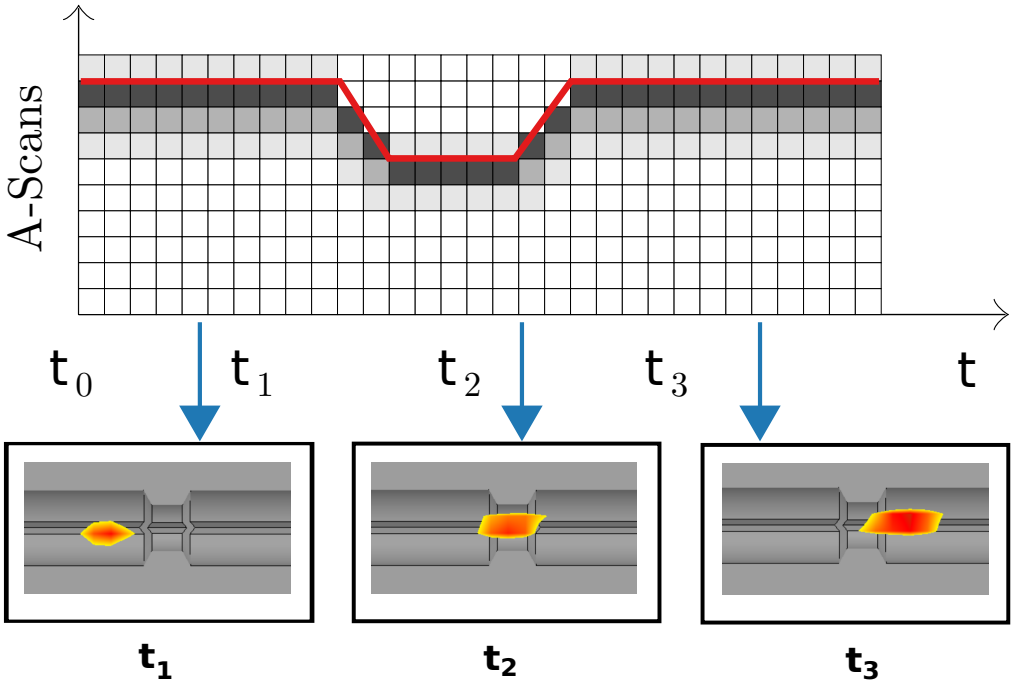

Figure 5.18.: Example registration of IVOCT and MPI data. The OCT A-scans are arranged over time (top). The segmented phantom boundary is highlighted in red. For three time stamps t_i, the related MPI signals from catheter tip are shown within the CAD sketch (bottom).

Influence of SPIONs on the OCT signal strength

When the bimodal data acquisition of MPI and IVOCT is performed simultaneously, the OCT has to function even though a diluted SPIONs solution is injected into the vessel. Therefore, the scattering, absorption and reflection of the light with this solution has to be investigated in optical fraction measurements. For this purpose, a series of different perimag SPION concentrations is set up, as listed in Table 5.1. The chosen concentrations provide enough MPI signal, but the signal strength and image quality increases with the SPION concentration [136]. For each concentration, a respective solution is filled inside a straight vessel phantom with diameter of $2.5\,\mathrm{mm}$. The IVOCT catheter is placed inside this phantom and OCT data are acquired while the catheter is only rotated and not pulled back. The OCT signal is analyzed for the influence of the magnetic particles with respect to the mean OCT signal strength at the vessel walls. As a result, a suitable SPION concentration is experimentally determined by the optical assessment and the course of the mean signal intensity. The determined concentration provides a compromise between a sufficient MPI signal strength and good OCT signal.

Table 5.1.: Concentrations of the dilution series used for optical fraction measurements. As a reference concentration c_{10}, water without perimag SPIONs is used.

	c_1	c_2	c_3	c_4	c_5
dilution factor	1	2	4	8	16
iron concentration [$\mathrm{mmol\,L^{-1}}$]	50	25	12.5	6.75	3.13
	c_6	c_7	c_8	c_9	c_{10}
dilution factor	32	64	128	256	–
iron concentration [$\mathrm{mmol\,L^{-1}}$]	1.56	0.78	0.39	0.19	0

Feasibilty of bimodal MPI and IVOCT imaging

In this experiment, the feasibilty to perform biomodal MPI and IVOCT imaging is investigated by using three differently shaped phantoms. The stenosis-like phantom with stenosis length of $2.5\,\mathrm{mm}$, the Z-shaped and the U-shaped phantom are used for the experiments (see Fig. 5.14). For the IVOCT volume reconstruction, the reconstruction methods IP, IP+LC and MCE are studied. To evaluate the results, the shape of the reconstructed vessels and the vessel diameter are compared to the CAD ground truth .

Feasibilty of MPI-guided IVOCT catheter tracking

In these experiments, the feasibility to track the IVOCT catheter via MPI is analyzed. Therefore, three experiments with the stenosis phantom with a stenosis length of $1.5\,\mathrm{mm}$ are conducted. The experiments are repeated three times. For the first experiment, the catheter is moved with a standard pullback profile (SP). The standard profile has a constant pullback velocity $v_0 = -1.25\,\mathrm{mm\,s^{-1}}$ and is pulled over a distance of s. The second experiment aims to simulate a bending artifact. Therefore, the bending artifact profile (BA) consists of a non-linear pullback of the catheter. The catheter is decelerated and then accelerated to mimic the catheter bending due to elastic material. For this purpose, the catheter is pulled back with a velocity $v_0 = -1.25\,\mathrm{mm\,s^{-1}}$ over a distance of $10\,\mathrm{mm}$. Then, the catheter velocity is adjusted to $v_1 = -0.625\,\mathrm{mm\,s^{-1}}$ over a distance of $5\,\mathrm{mm}$. This simulates the situation that the catheter is stuck. In the last step, the catheter velocity is adjusted back to the initial velocity $v_0 = -1.25\,\mathrm{mm\,s^{-1}}$ for the last $10\,\mathrm{mm}$. This mimics the elastic contraction of the catheter. The BA profile is shown in Fig. 5.19a. The third experiments aims to simulate a heart beat motion artifact (HBA). The HBA occurs when a heart contraction initiates a relative vessel motion relative to the IVOCT catheter. The HBA causes that some parts of the blood vessel are measured multiple times or not at all (see Fig. 5.3). For the simulation of this artifact, the catheter is moved with a heart beat motion profile that shows relative motion. First, the velocity is adjusted to $v_0 = -1.25\,\mathrm{mm\,s^{-1}}$ for a distance of $15\,\mathrm{mm}$. Afterwards, the velocity is changed to the opposite negative velocity to $-v_0 = 1.25\,\mathrm{mm\,s^{-1}}$ for a distance of $5\,\mathrm{mm}$. This imitates

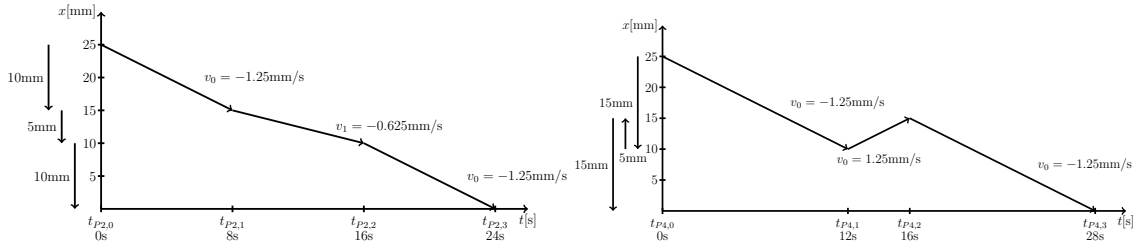

Figure 5.19.: a) In the case of the BA profile, the catheter is pulled backwards with a velocity $v_0 = -1.25\,\mathrm{mm\,s^{-1}}$ over the distance of $10\,\mathrm{mm}$. Afterwards, the velocity is reduced to $v_1 = -0.625\,\mathrm{mm\,s^{-1}}$ for the following distance of $5\,\mathrm{mm}$. Then, the velocity is set back to v_0 for the remaining distance of $10\,\mathrm{mm}$. b) In the case of the HBA profile, the IVOCT catheter is pulled backwards for the distance of $15\,\mathrm{mm}$. Afterwards, the catheter is pulled forward for the next $5\,\mathrm{mm}$. Finally, the catheter is pulled backwards in the original direction again for next $15\,\mathrm{mm}$. The catheter is pulled back with the initial velocity $v_0 = -1.25\,\mathrm{mm\,s^{-1}}$ for all motion directions.

the actual heart beat movement. Finally, the velocity is set back to $v_0 = -1.25\,\mathrm{mm\,s^{-1}}$ for the remaining distance of $15\,\mathrm{mm}$. The distance over time of the HBA profile is presented in Fig. 5.19b.

IVOCT catheter tip rotation analysis with MPI

In the following experiment, the capabilities to track the rotation of the IVOCT catheter with an asymmetric marker at the tip of the catheter is analyzed. Strictly speaking, it is desirable to determine the threshold radius of an asymmetric marker up to which it is possible to track the rotation. For this purpose, a noval rotation device is developed (see Fig. 5.20). In contrast to the rotation device presented in section 5.2.3, the rotation device developed here has an unflexible rotation axis. This ensures that any precession bias of a flexible catheter is avoided. The device consists of an Arduino (Arduino LLC, Italy), two stepper motors (Nema 14, Nanotec, Germany) and two aluminium shieldings. The axis and the supporting rods are made of Tufnol and most of the other parts like the sled are 3D-printed by SL (Forms 2, Formlabs, US). A delta sample can be mounted orthogonally to the rotation axis with a defined radius to the rotation axis. In this case, the delta sample mimics the asymmetric marker at the tip of the catheter. The first motor stepper is capable of rotating the rotation axis, while the second stepper can pull back the sled and with it the centric rotation axis. When these movements are superimposed, the asymmetric marker emulates the directed helical movement as the light beam leaving the prism. The axis is rotated with a rotation frequency of $f_{\mathrm{rot}} = 1\,\mathrm{Hz}$ and the sled is pulled back with a velocity of $v_{\mathrm{pull}} = 4\,\mathrm{mm\,s^{-1}}$. After the MPI data is reconstructed using parameters $\lambda = 0.01$, $n_{\mathrm{iter}} = 3$ and $\Theta = 5$, the marker position per frame is determined by use of the subvoxel strategy presented in chapter 3. As a next step, the helical movement

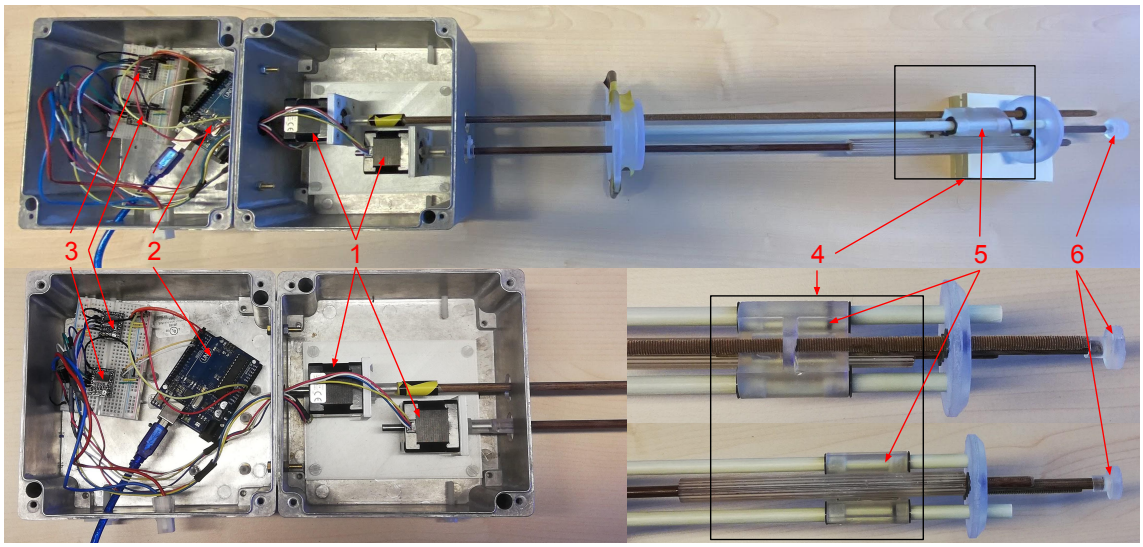

Figure 5.20.: Image of the rotation device (4), control unit (2,3) and steppers (1). The Arduino (2) transmits the control signal to the stepper. The power supply uses a LAN cable for better shielding. The aluminium boxes ensure the electromagnetic shielding from the MPI scanner. Within the black box, the gear for rotation of the asymmetric marker (6) is shown. The gear enables a axial movement of the sled (5) through a spindle.

is projected in the yz-plane. Then, the center of the circle is estimated by solving the least squares minimization problem

$$f_{\text{cost}}(\boldsymbol{c}_\text{c}) = N_\text{c}^{-1} \sum_{i=1}^{N_\text{c}} \left(\|\boldsymbol{p}_i - \boldsymbol{c}_\text{c}\|_2 - r_{\text{mean}}(\boldsymbol{c}_\text{c}) \right)^2 , \tag{5.4}$$

where $\boldsymbol{p}_i$ describes the marker position at frame i and N_c the total number of frames. The current position of the circle center is denoted with $\boldsymbol{c}_\text{c}$. With r_{mean}, the current circle radius is given and it is defined as follows

$$r_{\text{mean}}(\boldsymbol{c}_\text{c}) = N_\text{c}^{-1} \sum_{j=1}^{N_\text{c}} \left(\|\boldsymbol{p}_j - \boldsymbol{c}_\text{c}\|_2 \right) . \tag{5.5}$$

Further, the gradient of the cost function is given as

$$\nabla f_{\text{cost}}(\boldsymbol{c}_\text{c}) = \frac{2}{N_\text{c}} \sum_{i=1}^{N_\text{c}} \left(\left(\|\boldsymbol{p}_i - \boldsymbol{c}_\text{c}\|_2 - r_{\text{mean}}(\boldsymbol{c}_\text{c}) \right) \cdot \left(\frac{(\boldsymbol{p}_i - \boldsymbol{c}_\text{c})}{\|\boldsymbol{p}_i - \boldsymbol{c}_\text{c}\|_2} - r_{\text{mean}}(\boldsymbol{c}_\text{c}) \right) \right) . \tag{5.6}$$

The least squares minimization problem is solved iteratively with a conjugated gradients descent method [193]. As a starting position, the mean of all measurement positions is used. The method stops, when the cost function f_{cost} converges. This is the case when the difference between two consecutive iterations is smaller as the convergence criterion ($\epsilon = 0.001$). After the algorithm converges, it results in an estimated circle center with an estimated radius. The experiment is conducted with two different rotation radii, $r_\text{R} = 1\,\text{mm}$ and $r_\text{R} = 2\,\text{mm}$, for the asymmetic marker.

5.3. Results: MPI-IVOCT studies

5.3.1. Influence of SPIONs on the OCT signal strength

To investigate the influence of the SPIONs on the OCT signal strength, the IVOCT images are normalized with respect to the global maximum and minimum intensity and shown as A-scans in polar coordinates (see Fig. 5.21a-e). For illustration purposes, only the concentrations c_1, c_3, c_5, c_7 are presented. The highest concentration of SPIONs, c_1, in Fig. 5.21a exhibits more scattering as the other concentrations. This effect leads to lower reflection intensities at the vessel walls compared to the ones for the concentrations c_3, c_5, c_7, and c_{10} in Fig. 5.21b-e. For the concentrations $c_5 - c_{10}$, hardly any difference with respect to scattering and reflection at the vessel walls can be identified. Further, the visual impression agrees with the quantitative analysis of the mean intensities in the area containing the vessel walls (red boxes in Fig. 5.21). The mean intensity values inside

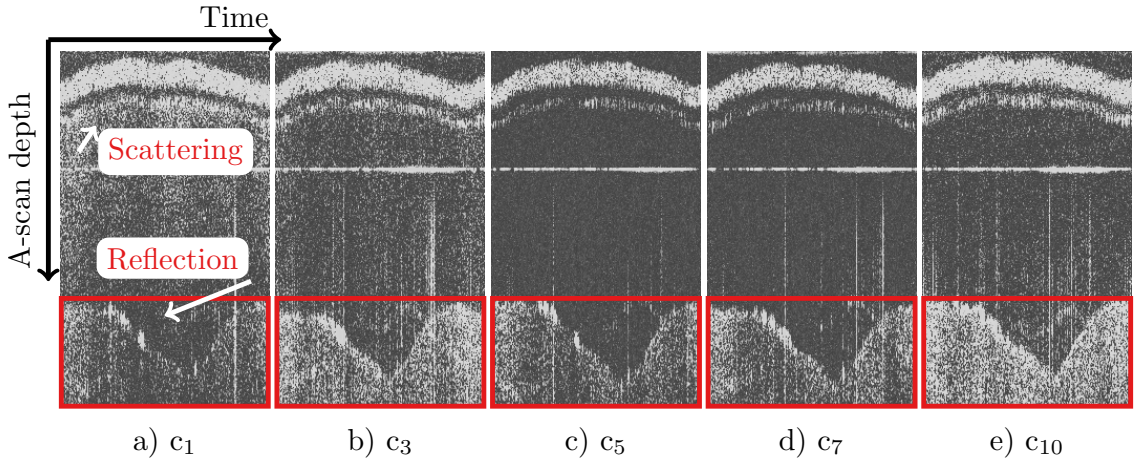

Figure 5.21.: A-scans of IVOCT images in polar coordinates for perimag concentrations c_1, c_3, c_5, c_7, and c_{10} (water) inside the phantom. At the highest concentration c_1, a more pronounced scattering can be identified. The edges of the phantom show also less signal compared to the other concentration. Almost no different in the intensities can be noticed for the other concentration. The results have been published in [J2].

the red boxes are shown in Fig. 5.22 for all concentrations. It can be seen that up to the concentration c_4, the mean intensities increases. Afterwards, the mean intensities remains on the same level. This leads to the conclusion that a higher dilution factor than $n = 16 - 32$ is not beneficial for the OCT signal at the vessel wall. Consequently, for further experiments a concentration $c_{\text{exp}} = 2.5\,\text{mmol}\,\text{L}^{-1}$ with a dilution factor of $n = 20$ is used. A concentration between c_5 and c_6 satisfies a trade-off between a good OCT signal strength and a sufficient MPI signal strength. In summary, an influence on the refractive index of water (1.33) could not be noticed. Therefore, the OCT pixel spacing remains unchanged (compare section 5.2.1).

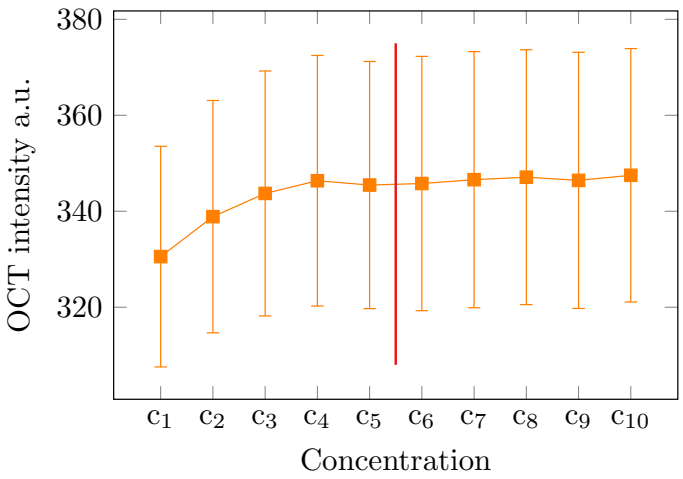

Figure 5.22.: Mean intensities with standard deviations from area of the vessel walls (dashed red boxes in Fig. 5.21) for perimag dilution series $c_1 - c_{10}$. The mean intensity increases up to the concentration of c_4 and remains on the same level for the following concentrations. The red line marks the concentration $c_{\text{exp}} = 2.5\,\text{mmol}\,\text{L}^{-1}$ used in the following experiments. The results have been published in [J2].

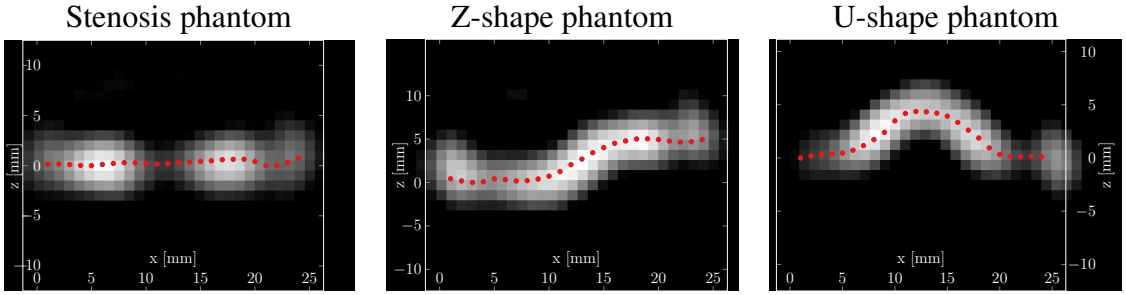

Figure 5.23.: From left to right, the xz-slice of the reconstructed MPI volumes are shown as xz-slice of stenosis, Z-shape, and U-shape phantoms. These results have been published in [J2]. The dotted red line indicates the center of mass CM_{MPI} positions per yz-slice. It resembles the centerline of the estimated three-dimensional IVOCT pullback pathway used for MCE method.

5.3.2. Feasibility of bimodal MPI and IVOCT imaging

The xz-slices of the reconstructed 3D MPI volumes are presented for the stenosis, Z-shape and U-shape phantoms in Fig. 5.23. The estimated centerlines determined by center of mass CM_{MPI} positions per yz-slice are shown as dotted red line. In Fig. 5.24, the estimated centerlines from Fig. 5.23 are plotted against to the ground truth centerlines of the CAD models. It can be seen that the estimated centerlines agree quite well with the centerlines from the CAD models. The mean absolute error (MAE) for all three phantoms is in the range of $0.25\,\text{mm}$ to $0.28\,\text{mm}$ as summarized in Table 5.2. The standard deviation (SD) σ ranges from $0.21\,\text{mm}$ to $0.35\,\text{mm}$ for all phantoms. Overall, the estimated MPI centerline seems slightly flattened compared to the CAD centerline. The reconstructed IVOCT volumes are shown based on the IP, IP+LC and MCE reconstruction methods in Fig. 5.25.

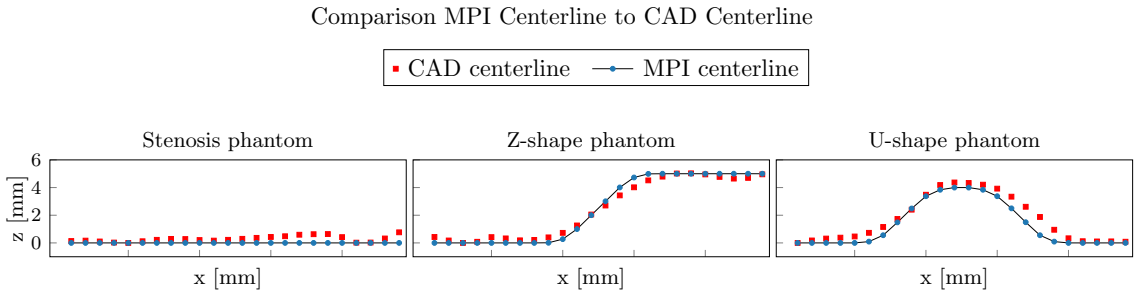

Figure 5.24.: The estimated MPI catheter centerlines are compared to the CAD centerlines for all three phantoms stenosis, Z-shape, and U-shape. The 3D centerlines are only shown in xz-planes. The blue lines indicate the centerlines of the CAD models and the red dots mark the center of mass $\mathrm{CM}_{\mathrm{MPI}}$ positions per yz-slice. These MPI centerlines are used to reconstruct the IVOCT volume via the MCE reconstruction method. These results have been published in [J2].

Table 5.2.: MAE and SD determined for the MPI estimated centerline to the CAD centerline.

Phantoms	Stenosis	Z-shape	U-shape
MAE [mm]	0.28	0.26	0.25
σ [mm]	0.21	0.32	0.34

IP reconstruction method The reconstructed phantom IVOCT volumes for all three phantoms reveal high deviations from the CAD models. Some twists and bendings alongside the volume can be identified. The stenosis phantom reflects the wide and narrow parts but the shape of Z-shape and U-shape phantom cannot be detected correctly.

IP+LC reconstruction method The volumes reconstructed with the IP+LC method resemble the phantom shape more accurately at least in the stenosis phantom. In case of the stenosis, the reconstruction resembles the phantom shape very much. In case of the Z-shape and U-shape phantoms, the reconstructed volumes look like shaped cylinders. However, they still do not resemble the shape of the CAD models.

MCE reconstruction method For the MPI centerline estimation method, the reconstructed volumes reproduce the shape of all three phantoms well. For the stenosis phantom, the volumes of the MCE method and the IP+LC method appear similar. A clear difference can be identified for the Z-shape and the U-shape volumes. The reconstructed volume shape is conform with the ground truth shapes of the phantom. The xz-slices of the reconstructed volumes based on the MCE reconstruction method together with the cross-sections of the CAD sketches are shown in Fig. 5.26. In case of the IVOCT volume of the stenosis, the lumen boundaries almost entirely agree with the walls of the phantom. For the IVOCT volumes of the Z-shape phantom, the deviations from the CAD model are presented and the lumen boundaries seem more flattened. The lumen boundaries for the

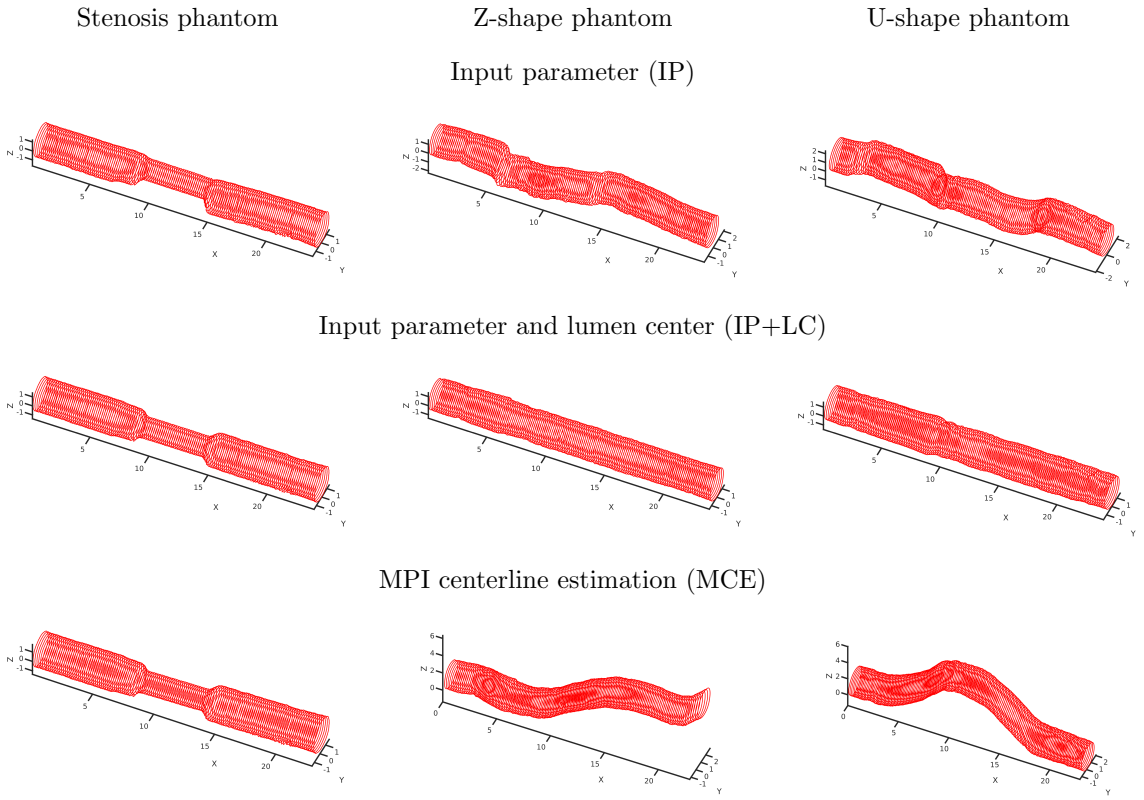

Figure 5.25.: The reconstructed IVOCT volumes processed with the IP, IP+LC and MCE reconstruction method for the three phantoms (stenosis, Z-shape, U-shape). These results have been published in [J2].

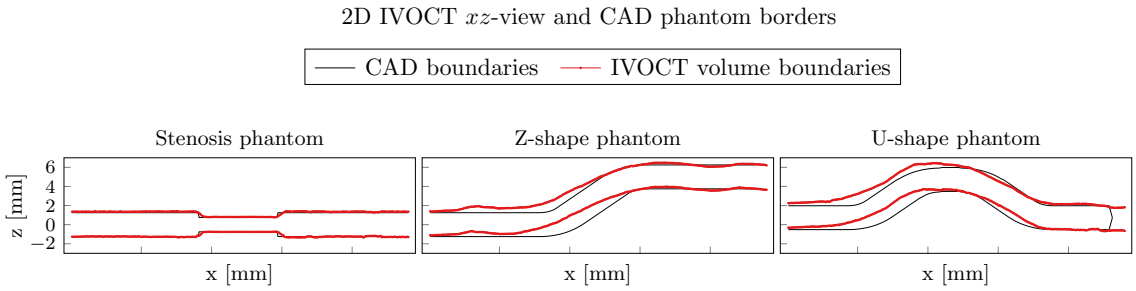

Figure 5.26.: The xz-slice of the lumen boundaries of the IVOCT volume reconstructions for the stenosis, the Z-shape and the U-shape phantoms in red and the CAD borders in black. These results have been published in [J2].

U-shape phantom resemble some deviations from the CAD model. Overall, they coincide well with the phantom shape. A comparison of the diameters for all three phantoms to the ground truth diameter of the CAD sketches is published in [J2] but is not presented in this work.

5.3.3. Feasibilty of MPI-guided IVOCT catheter tracking

In order to investigate if it is feasible to track an IVOCT catheter coated with an MPI sensitive marker, the following results are separated into three parts. At first, the positions

over time and the determined velocities of the 4D MPI catheter tracking are verified for the three motion profiles SP, BA and HBA. For this purpose, the MAE is calculated for the distance traveled only in x and the vectorial traveled distance in x, y, z. The MAE is also estimated for the velocities of all three profiles. To get an visual impression, the result

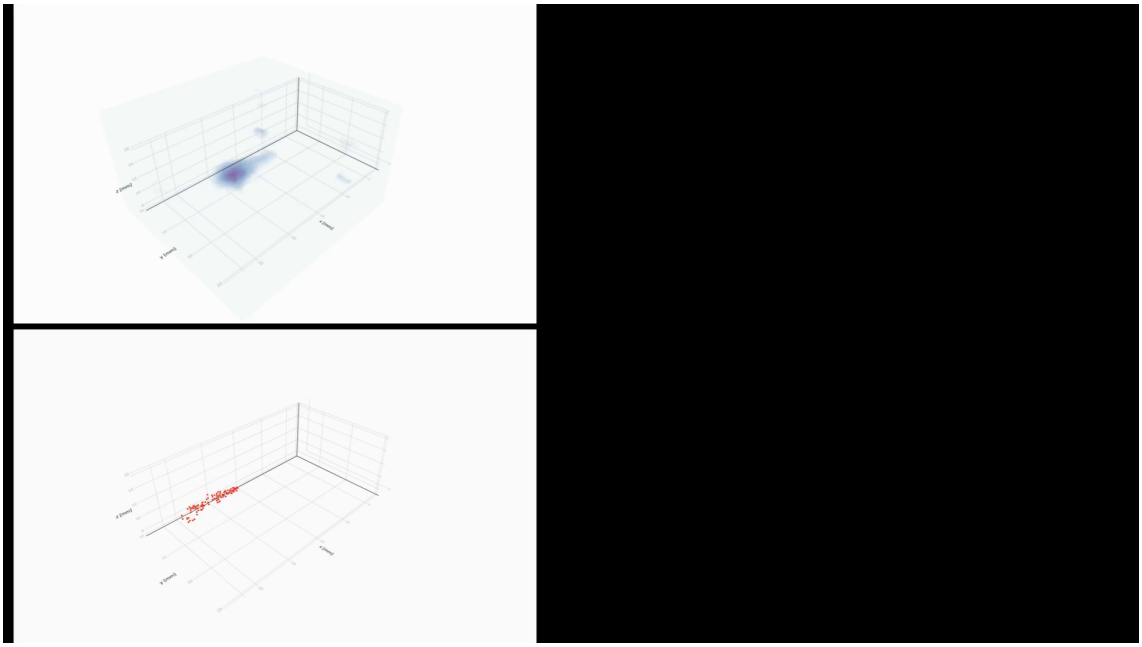

Figure 5.27.: Top left: MPI raw data of a marked IVOCT catheter pullback. Bottom left: Extracted catheter tip position from the raw data over time (video length: 13 s).

of one IVOCT catheter trajectory over time is presented as a video in Fig. 5.27. In the top left part, the MPI raw data is shown and in the bottom left part, the estimated catheter tip position is determined over time. In the second result part, the MPI-guided IVOCT catheter trajectory is used to reconstruct the IVOCT vessel volume. Then, the MMT-based volume reconstruction is compared with the standard IP volume reconstruction. This comparison is performed for the SP, the BA profile and the HBA profile. In the case of the BA profile, both reconstruction methods are analyzed regarding bending artifacts. For the HBA profile, both volume reconstruction methods are analyzed in terms of heart beat artifacts. In the third part of the results, the quantified stenosis length is compared for all reconstruction methods and profiles to its ground truth values from the CAD model.

Statistical validation of 4D MPI catheter tracking

The SP tracking results are presented in Fig. 5.28a and show the distance in the x-direction over time between $M_1 = 18\,\mathrm{mm}$ and $M_2 = 6\,\mathrm{mm}$. The tracked x-positions (black) agree well with the expected x-positions (red) between $18\,\mathrm{mm}$ and $11\,\mathrm{mm}$, whereas the tracked x-positions between $11\,\mathrm{mm}$ and $6\,\mathrm{mm}$ (black) slightly diverge from the expected values (red). Additionally, a regression line (blue) is fit through the mean values of the measured positions. Overall, an MAE of $0.44\,\mathrm{mm} \pm 0.44\,\mathrm{mm}$ is calculated for the distance in the

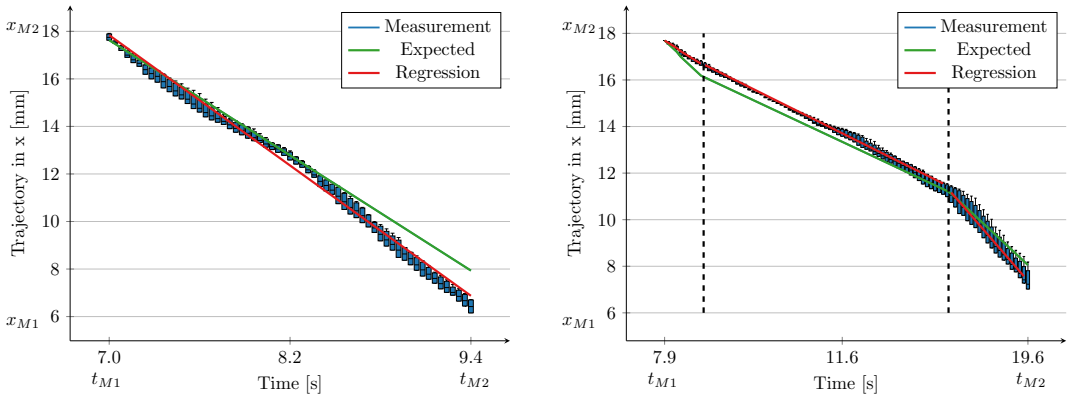

Figure 5.28.: a) The MPI measurements for SP show a good agreement of the measured distance with the expected values in the x-direction over time between $18\,\mathrm{mm}$ and $11\,\mathrm{mm}$. In the last part of the trajectory, the positions in the x-direction differ marginally. b) The MPI measurements for the BA profile indicate that the first change of velocity is not detected by the measurement. After the first velocity change, the tracked distances in the x-direction over time agree with the different velocities v_0 and v_1 with only minor deviations.

x-direction. With help of the regression line, an absolute error (AE) of $0.21\,\mathrm{mm\,s^{-1}}$ is determined for the velocity. As given in Table 5.3, the AE translates in a RE of 16.8%. For the BA profile, the distance in the x-direction over time between $18\,\mathrm{mm}$ and $6\,\mathrm{mm}$ is shown in Fig. 5.28b. The first segment indicates a small deviation from the expected values, but overall, the tracked x-positions (black) agree with the expected x-positions (red). As stated before, all three measurements are illustrated as box plots and show the distribution of the tracked positions. The mean values of the three repeated measurements are used to fit a regression line (blue). The MAE for the distance in x-direction is

Table 5.3.: The MAE is calculated for the distance in the x-direction with its SD. In addition, the AE along with the RE of the velocity is given. These errors are determined with help of the 3D regression line between t_{M1} and t_{M2}.

Errors	Standard profile
MAE Trajectory 1D-x [mm]	0.44 ± 0.44
AE (RE) Velocity [mm/s]	0.21 (16.8%)

$0.26\,\mathrm{mm} \pm 0.16\,\mathrm{mm}$ for the first segment, $0.35\,\mathrm{mm} \pm 0.11\,\mathrm{mm}$ for the second segment and $0.20\,\mathrm{mm} \pm 0.22\,\mathrm{mm}$ for the third segment. The AE and RE in terms of the velocity of the regression line for the BA profile are presented in Table 5.4 for all three segments. For the HBA profile, the distance in the x-direction over time between $18\,\mathrm{mm}$ and $6\,\mathrm{mm}$ is presented in Fig. 5.29a. It can be seen that the motion of the catheter being pulled back and forth is resembled by the tracked x-positions. The turning points when the catheter changes the direction of its movement can be clearly detected. Nevertheless, the velocity

Table 5.4.: MAE and SD for the distance in the x-direction as well as AE along with the RE of the velocity for the BA profile. The errors are calculated by use of a 3D regression line between t_{M1} and t_{M2}.

Errors	BA profile segment 1	BA profile segment 2	BA profile segment 3
MAE Trajectory 1D-x [mm]	0.26 ± 0.16	0.35 ± 0.11	0.20 ± 0.22
AE (RE) Velocity [mm/s]	0.44 (35.4%)	0.07 (10.8%)	0.22 (17.9%)

in the first two segments seems to be underestimated because the tracked x-positions are not in full accordance with the expected x-positions (red). Only in the third segment, the tracked x-positions are in full agreement with the expected x-positions. Besides the x-positions, the distances in y and z over time are shown in Fig. 5.29b-c, respectively. The turning points are visible as well and it becomes evident that the stenosis phantom was inserted slightly diagonal. This can be deviated from the increasing y-values and the decreasing z-values depending on the x-position. Otherwise, a straight insertion leads to straight line in both dimensions y and z. Again, the three repeated measurements are presented as box plots to show the variation of the measurements. The tracked positions in the x-direction mainly differ from the expected positions as the velocities changes. The regression lines are fit to the mean values of the three measurements. The MAE for the distance in the x-direction is $0.64\,\mathrm{mm} \pm 0.36\,\mathrm{mm}$ for the first segment, $0.51\,\mathrm{mm} \pm 0.55\,\mathrm{mm}$ for the second segment and $0.38\,\mathrm{mm} \pm 0.45\,\mathrm{mm}$ for the third segment. The velocity in the x-direction over time confirms the inversion of the velocity (see Fig. 5.29d). The AE (RE) of the velocity in the x-direction are calculated based on their regression lines. The errors are $0.38\,\mathrm{mm\,s^{-1}}$ (30.0%) for the first segment, $0.49\,\mathrm{mm\,s^{-1}}$ (39.4%) for the second segment and $0.04\,\mathrm{mm}$ (3.2%) for the third segment. The errors for the HBA profile are presented in Table 5.5.

Table 5.5.: The MAE for the distance in x-direction with its SD is shown for the HBA profile. The AE and RE of the velocity based their 3D regression lines is evaluated between t_{M1} and t_{M2}.

Errors	HBA profile segment 1	HBA profile segment 2	HBA profile segment 3
MAE Trajectory 1D-x [mm]	0.64 ± 0.36	0.51 ± 0.55	0.38 ± 0.45
AE (RE) Velocity [mm/s]	0.38 (30.0%)	0.49 (39.4%)	0.04 (3.2%)

Volume reconstructions

The 4D volumes are reconstructed with the IVOCT volume reconstruction methods IP and MMT for the motion profiles ST, BA and HBA. A comparison of the results can be

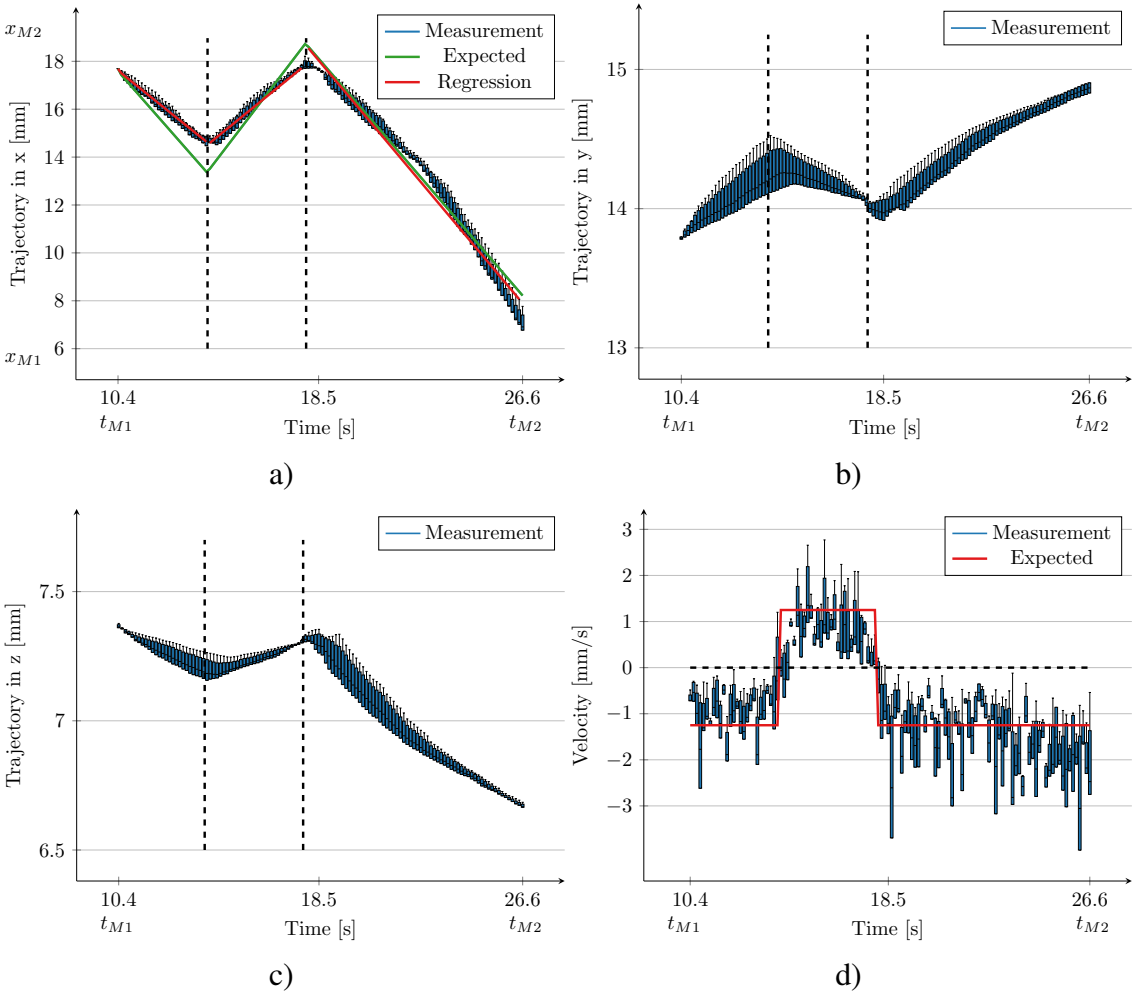

Figure 5.29.: a) The measured distances in x-direction are in good agreement with the adjusted catheter motion. The turning points can be clearly identified. Nevertheless, the velocity is underestimated in the first two segments. In the third segment the measured distances in x are in good agreement with the expected positions in x. b) The measured distances in y and z-directions c) indicate that the stenosis phantom is inserted slightly diagonal. The turning points of the back and forth movement of the catheter can also be noticed and the values in y increase and the values in z decrease depending on the x position. d) The inversion of the velocity is clearly recognizable. Further, the mean velocity values are within the range of the expected velocities. However, the variation of the velocity is quite high.

seen in Fig. 5.30. The volumes are cropped to the size of the MPI FoV in x-direction. In the first row, a ground truth volume with parameters from the CAD model is shown. The 4D boundary points are colored based on the elapsed time. Additionally, the colormap is shifted with regard to the time values of the positions at $x_{M_1} = 18\,\mathrm{mm}$. Overall, the envelopes of all volume reconstructions deviate from the ground truth volume. For comparison, the stenosis lengths are marked with red arrows and their quantitative length estimations are given in Table 5.6. The stenosis lengths of the MMT reconstructed volumes are almost equal to the ground truth for all motion profiles. The IP volume reconstruction method indicates a larger deviation of the stenosis length and relative position of it. Further, the IP volume reconstruction causes a strong deviation of the stenosis length for the BA and HBA profiles. Especially for the BA profile, the stenosis length is prolonged. It does not reflect the underlying deceleration of the catheter of the BA profile. To emphasize the complete pullback time for the BA and HBA profile, the related 4D volumes are presented in Fig. 5.31 and Fig. 5.32 without cropping the x-axis. Regarding the BA profile (see Fig. 5.31), the complete IP reconstructed volume shows an increased length with a constant helical pitch p_0. The MMT volume, however, does not overestimate the total volume and the stenosis length in particular. The catheter velocity varies for the MMT method as presented in Fig. 5.28b. This variation can be identified by different densities of boundary points between $x = 9\,\mathrm{mm}$ and $x = 12.5\,\mathrm{mm}$ compared to the points between $x = 13\,\mathrm{mm}$ and $x = 14.5\,\mathrm{mm}$.
For the HBA profile (see Fig. 5.32), the IP volume also overestimates the total volume. Additionally, in the volume reconstruction beyond $x = 8\,\mathrm{mm}$ a second stenosis occurs. The MMT volume again reconstructs the volume more realistically. As the motion of the catheter is tracked, the 3D boundary points are ordered over time in a way that several boundary points overlay each other between $x = 13\,\mathrm{mm}$ and $x = 15\,\mathrm{mm}$. Hereby, the colored 4D volume (bottom) shows a catheter trajectory where the turning point is located within the stenosis.

Quantitative stenosis length results

The stenosis length in x-direction is quantified with help of the full at half width of the envelope decay of the volume shapes. It is estimated for all reconstruction methods, profiles and experimental repetitions. In order to quantify stenosis length of the HBA profile, the two stenosis lengths are summed up.

5.3.4. MPI-based IVOCT catheter tip rotation analysis

The results of the rotation analysis are shown in Fig. 5.33. The estimated radius for the experiment with $r_\mathrm{R} = 2\,\mathrm{mm}$ is $1.5\,\mathrm{mm} \pm 0.3\,\mathrm{mm}$. The distribution of the marker positions in yz-plane and the estimated center of the circle is presented in Fig. 5.33a. The

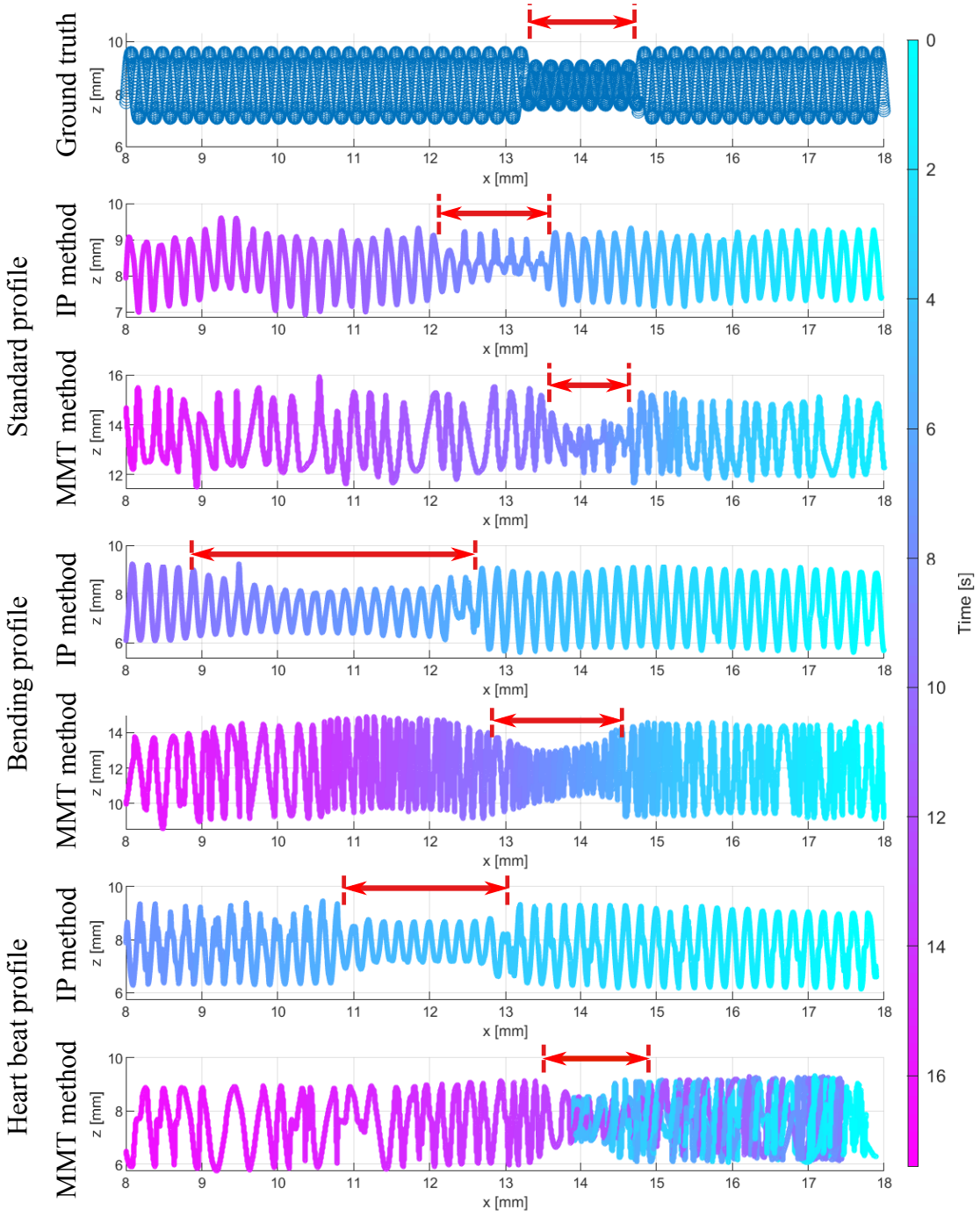

Figure 5.30.: The reconstructed volumes are shown for all motion profiles and reconstruction methods. In the first row the ground truth volume for the cropped MPI FoV is given. The distances $x = 18\,\mathrm{mm}$ and $x = 8\,\mathrm{mm}$ coincide to the time points t_{M1} and t_{M2}. The IP and MMT volume reconstructions are labeled on the left side. The phantom boundary points are colored with regard the elapsed time (right). Additionally, the stenosis lengths are indicated with red arrows. These results have been published in [J3].

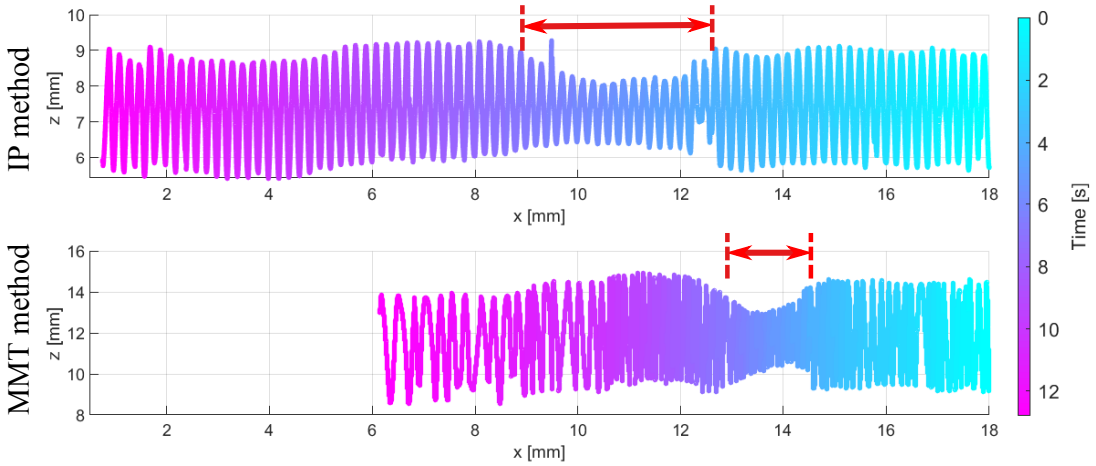

Figure 5.31.: Comparison between entire IP volume reconstruction and MMT volume reconstruction for the BA profile. These results have been published in [J3].

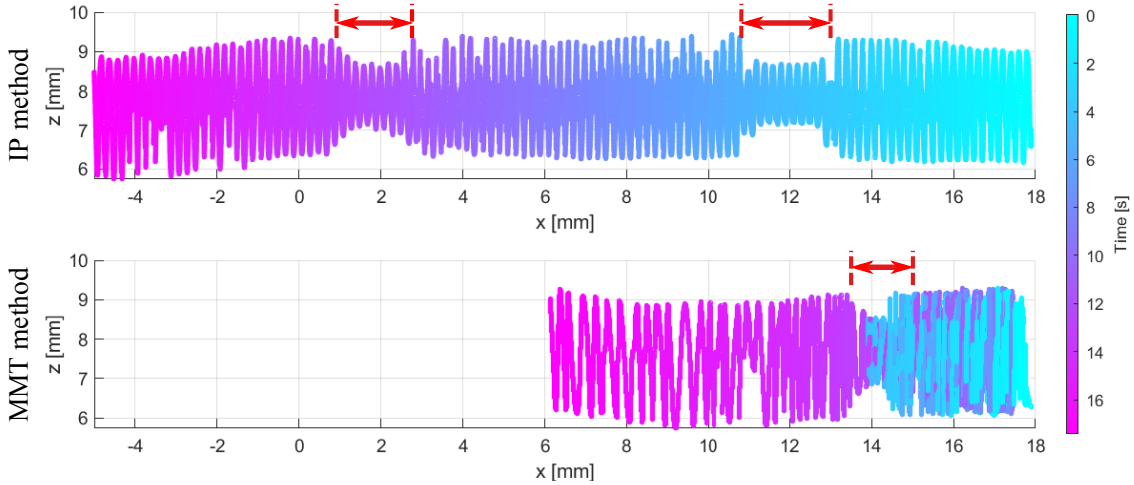

Figure 5.32.: Comparison between entire IP volume reconstruction and MMT volume reconstruction for the HBA profile. These results have been published in [J3].

Table 5.6.: The determined stenosis lengths in mm are presented for all reconstruction methods and the motion profiles SP, BA, and HBA.

	SP profile	BA profile	HBA profile
Stenosis IP (RE)	1.52 (1.3%)	3.91 (160%)	3.82 (154%)
Stenosis MMT (RE)	1.15 (23%)	1.49 (0.6%)	1.19 (21%)

measured marker positions form a circle with slight deviations. The estimated radius for the $r_{\mathrm{R}} = 1\,\mathrm{mm}$ experiment results in $1.00\,\mathrm{mm} \pm 0.17\,\mathrm{mm}$. Here, the shape of a circle is also visible. The measured marker positions along with its estimated center are shown in the yz-plane in Fig. 5.33b.

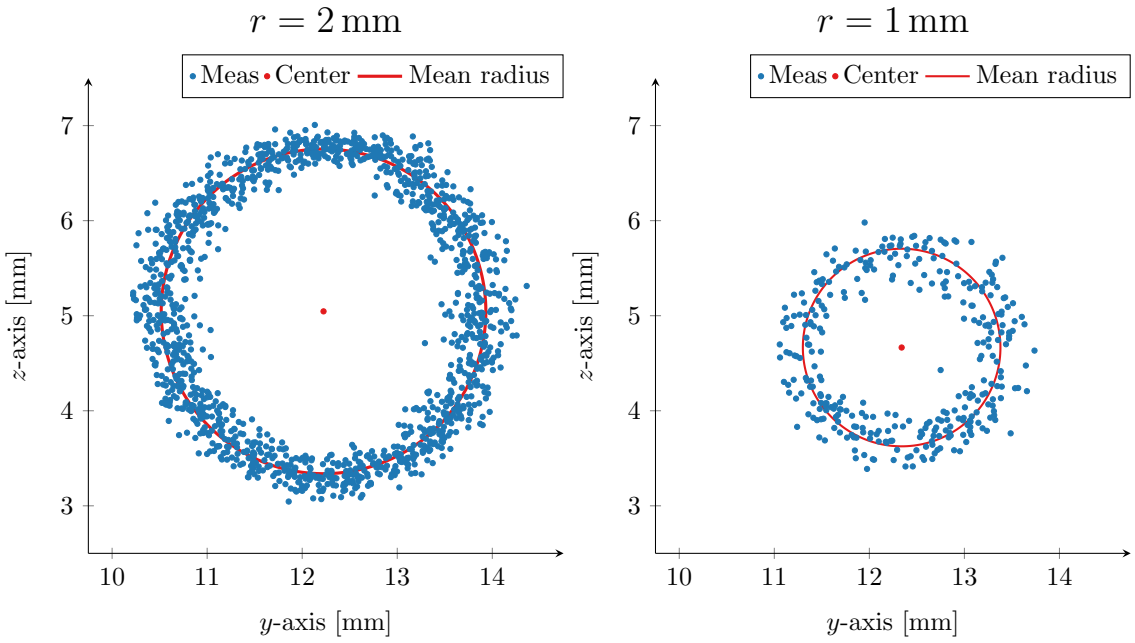

Figure 5.33.: a) Measured marker positions (blue) and the estimated center (red) for the $r_{\mathrm{R}} = 2\,\mathrm{mm}$ experiment projected in the yz-plane. b) The same plot for the $r_{\mathrm{R}} = 1\,\mathrm{mm}$ experiment.

5.4. Discussion

In this chapter, the influence of SPIONs on the optical signal of the OCT was investigated to establish a bimodal imaging scenario of MPI and IVOCT. Usually, a vessel is flushed with NaCl to allow the IVOCT measurement. In the presented scenario, the vessel would be flushed with a solution of NaCl and SPIONs to enable a simultaneous bimodal measurement of MPI and IVOCT. Experiments based on a concentration series with a SPION concentration in the range between $1.56\,\mathrm{mmol\,L^{-1}}$ to $31.3\,\mathrm{mmol\,L^{-1}}$ showed that the SPIONs have no substantial negative impact on the IVOCT imaging. The observed scattering effect is only very small and the signal of the border walls of the used phantoms could be clearly detected. At the highest level of dilution of the SPIONs the solution is nearly transparent and allows high IVOCT signals; in addition, the SPIONs still provide enough MPI signal.

The general feasibility of combining MPI and IVOCT in simultaneous bimodal imaging is experimentally shown with three vessel phantoms and three different reconstruction methods. At first, the results validate that MPI is a suitable modality to complement IVOCT. MPI can be used to estimate the vessel centerline of the pulled back catheter and this estimated centerline is beneficial for the IVOCT reconstruction. Comparing the three volume reconstruction methods IP, IP+LC and MCE, it becomes clear that the IVOCT volumes based on the MCE centerline resemble the true vessel shape more accurately than the IP and IP+LC volume reconstructions. They are only based on the IVOCT itself and show

substantial deviations to the ground truth CAD models. This becomes especially evident for the curved shaped phantoms. Not surprisingly, the catheter position is often not centered within the phantom and therefore twists, bends, and rotation irregularities occur alongside the volume for the IP method. The results based on the IP+LC method appear with smoother surfaces due to its center of mass approach based on the B-scans, but the curvature of the Z-shape and U-shape phantom is not resembled. The MCE reconstruction method still does not show a perfect accordance but the additionally estimated centerline from the MPI data improves the conformity to the CAD model greatly (compare 5.26).
The quantitative analysis of the trajectories supports the overall agreement between the reconstructed and ground truth shape. The centerline of the vessel phantoms are effectively estimated by MPI with an MAE of less than $0.3\,\mathrm{mm}$ (see Table 5.2). These results are comparable to the ones achievable with angiography [194, 170]. The errors presented here are end-to-end errors to the CAD models, which means that they include the errors from the 3D printing, the registration and the segmentation.
The curved phantom showed a greater deviation in the estimated diameter at the positions where the catheter had to be bend. These deviations can prevail because the current approach does not include the gradient of the B-scans along the centerline. Consequently, the misplacement could be minimized if the B-scans are placed perpendicular to the 3D estimated pathway. Nevertheless, the actual catheter tip motion does not follow the vessel centerline and can only be a rough estimation for the pathway. The use of the centerline is motivated by angiography [170], where a permanent tracking of the catheter tip induces radiation. However, as MPI is not limited by these circumstances, the catheter is labeled with a specific MPI marker to track its motion inside the vessel in the next experiments. Even though the described results so far do not show the capability to correct IVOCT artifacts such as non-uniform pullback motion artifacts and non-uniform rotations, they do show the potential of MPI as a co-modality for IVOCT.

The feasibility of MPI-guided IVOCT catheter tracking for IVOCT volume reconstruction was performed with three different motion profiles. The repetitions of the motion profile experiments reveal a relatively small MAE in x-direction of around $0.5\,\mathrm{mm}$. This statistical validation agrees quite well with the estimated determination accuracy from [J1]. It is worth noting that the ground truth for the trajectory with respect to the position in x, y and z-directions is not known, because it is quite challenging to track the catheter's position within the MPI scanner with a second modality, e.g., an optical system. One option could be a constructed vessel phantom with just enough space for the catheter, but even that would be susceptible to inaccuracies. Consequently, the ground truth for the trajectory is only given by the pullback velocity and distance in 3D over a defined time period. That is why the calculated MAEs in x-direction are afflicted with a small uncertainty, as the y and z ground truth positions are assumed to be constant zero.
The pullback velocities are determined with a regression line in 3D. The AE and RE of

the velocities are within the range of the ground truth velocities. The RE fluctuates in the range of $3.2\% - 39\%$ for all motion profiles and their segments. Obviously, the first change of the velocity in the BA profile is not resembled by the measured values. One explanation might be that the velocity alternation was performed too close to the border of the FoV. The center of mass localization algorithm might misinterpreted the position of the catheter tip, because the circle shaped voxel intensities had not entered the FoV entirely. Then, only a part of these voxel intensities are used to determine the position.
Furthermore, the velocity of the HBA profiles is underestimated because the measured values for the HBA motion profile show deviations around the turning points (compare Fig. 5.29). This underestimation can be explained by the catheter setup with a proximal actuator. During the HBA profile, the pullback direction is reversed and the flexible catheter exhibits a shrinkage and stretching. The inversion of the pullback direction can also be observed in the y- and z-positions seen in Fig. 5.29b-c because the stenosis phantom is not truly positioned in compliance with the x-axis.
In general, the presented MMT volume reconstruction method demonstrates a qualitative enhancement to the IP reconstruction method (compare Fig. 5.30), because it includes the additional information from the MPI catheter tracking. Only for the SP profile, where no motion artifacts are intended, the MMT method shows does not show better results regarding the stenosis length. The presented reconstruction results for the artifact-affected profiles BA and HBA underline the importance of a catheter tracking over time. Otherwise, the stenosis is reconstructed either too long or appears twice. In case of the IP reconstruction method, the stenosis lengths in Table 5.6 quantify these errors and confirm the qualitative impression. Nevertheless, shape deviations appear for all reconstruction methods and motion profiles. An explanation could be other imaging artifacts that influence the acquisition of IVOCT and MPI images, such as non-uniform rotational distortions of the catheter. They occur frequently and have their origin in the proximal rotation of the flexible catheter. With MPI it might be possible to track the rotation of the catheter with an asymmetric marked catheter. The proof of concept results from the rotation analysis indicate that it is possible to track the rotation of an asymmetric marker with radius of $1\,\mathrm{mm}$. Further deviation can be identified in the boundary segmentation of the IVOCT data. Additional inaccuracies can be introduced by the catheter tip localization, when the center of mass algorithm misinterprets noisy MPI images.
Overall, the time synchronization of the IVOCT and the MPI enables an optimized arrangement of OCT A-scans to form the 3D V-scan directly without the intermediate step over B-scans [171, J2, C1, 168].
To sum up, MPI provides a suitable, non-ionizing imaging modality for a combination with IVOCT. MPI can improve the IVOCT volume reconstruction either by estimating the centerline of the vessel with its tracer or by direct tracking of the catheter itself. In further experiments, the multi-contrast ability [63, 60, 61, 62, 133, 41] of MPI could be

used to track the IVOCT catheter with one particle type and image the vessel tree angiographically with a second MPI tracer type. The second blood pool tracer could be a long circulating tracer [43]. Then, MPI could monitor the vessel tree continuously for longer periods of time and a repeated injection as with DSA would be avoided. Therefore, MPI would provide a radiation free imaging and prevent the potential risks of DSA [173, 174, 195]. Especially, the high temporal resolution of IVOCT and MPI [180, 17, 177] allows to compensate the motion artifacts caused by catheter and vessel contractions.
An open question remains the compensation of the NURD artifacts. A tracking of the actual rotation of the catheter would be highly beneficial for the volume reconstruction. One approach could be implemented by the manufacturer of the IVOCT catheters. If two non systematic grooves would be designed inside the outer plastic catheter, a periodic signal of the rotation would be encoded in the A-scans. A similar effect is observed in the current IVOCT catheters. In some catheters, the microprism is not adjusted symmetrically on the catheter. Therefore, the actual rotation can be identified within the A-scans. However, these asymmetric manufacturings are not present in all used catheter and lie probably within the production tolerance. If a solution with two grooves would provide a reliable solution remains unanswered because the plastic catheter is also influenced by twists, bending and stretches.
Another possible solution could be provided by MPI, if the catheter is labeled with an rotational asymmetric marker. So far, it is possible to track the rotation as presented in section 5.3.4, but further analysis has to be done to achieve a robust angle determination. If it is possible to track the phase of the actual rotation, the NURD artifacts could be corrected, as the volume is reconstructed via a helical shape. The accuracy of this rotation tracking needs to be investigated in future works, but the first proof of concepts experiments are quite promising. Similar to a micromotor, the use of MPI could even be taken one step further by rotating only the microprism in front of the optical wire with rotational focus fields. The rotation of screws with the magnetic forces of an MPI scanner has already been demonstrated in [66]. Obviously, that would make the proximal rotation of the catheter superfluous, but it remains an open question whether these high rotation velocities can be reached with the rotational focus fields and whether it remains safe in terms of PNS and SAR.

In conclusion, IVOCT and MPI synergize well and compensate each others limitations. The presented MPI-guided IVOCT catheter tracking is able to reconstruct the volumes of known vessel phantoms and to reduce bending and heart beat artifacts. The time synchronization of IVOCT and MPI data helps to combine both imaging modalities. The quantification of the length of stenosis underline the improved compensation of the artifacts in comparison to the standard method.

6. Magnetic Particle Imaging and Magnetic Particle Navigation

Contents

6.1. Introduction and motivation

In general, Targeted Drug Delivery (TDD) in nanomedicine pursues several goals. The first goal is dose reduction. The drug targets only specific parts of the body and avoids the interaction with others. Due to this specific targeting, the efficacy is improved, because the medication is not distributed throughout the whole body. Consequently, potential side-effects of the medication can be reduced. Further, the therapeutic effects are prolonged since the drugs stay longer at the specific location and are not taken away by systemic blood circulation. In this work the potential of TDD based on Magnetic Particle Imaging and Magnetic Particle Navigation (MPN) is motivated by the example of acute ischemic stroke.

In the case of acute ischemic stroke, one of the blood vessels of the carotid artery is blocked by a blood clot (see Fig. 1.1), usually the internal carotid artery. Due to this, the area behind the occluded blood vessel will not be supplied with sufficient oxidized blood, because the blood will mainly flow through the unblocked branch of the bifurcation between external carotid artery and internal carotid artery. Not surprisingly, the injection of a thrombolytic medication does not resolve the blood clot effectively, because almost no thrombolytic medication reaches the blood clot. The consequence is that the blood clot has to be removed in a minimally invasive intervention in some cases. As every invasive intervention, such a procedure can have a substantial risk. This is where TDD based on Magnetic Particle Imaging and Magnetic Particle Navigation, together (MPIN), could potentially provide an alternative less invasive solution. The ability to image and navigate magnetic particles is worth to be investigated for application in ischemic stroke. The magnetic particles could be attached with therapeutic substances, such as fibrinolytic medication [196, 197]. One class of the fibrinolytic drugs is the tissue plasminogen activator (tPA), which resolves blood clots very effectively [196]. During an acute ischemic stroke, the magnetic particles attached to the tPA could be injected intravascularly into the body. Then, the magnetic particles would be navigated and concentrated locally in the vascular territory of the vessel occlusion. Thus, the MPIN method would enhance the disintegration of the blood clot. The imaging ability could be used to control the re-opening of the vessel and track the correct targeting. Therefore, usage of tPA functionalized magnetic particles could help to clear the blood vessel and make an invasive procedure redundant.

In order to make the MPIN method work as an alternative for stroke treatment, the magnetic particles have to be navigated towards the blocked blood vessel at the bifurcation junction. In women, the diameter of the internal carotid artery (ICA) is $4.66\,\mathrm{mm} \pm 0.78\,\mathrm{mm}$ and $6.10\,\mathrm{mm} \pm 0.80\,\mathrm{mm}$ for the common carotid artery. Significantly larger are the diameters in men with $5.11\,\mathrm{mm} \pm 0.87\,\mathrm{mm}$ and $6.52\,\mathrm{mm} \pm 0.98\,\mathrm{mm}$ [198]. The blood flows with a velocity of $275\,\mathrm{mL\,min^{-1}} \pm 52\,\mathrm{mL\,min^{-1}}$ in the ICA, while it flows only

with $91\,\mathrm{mL\,min^{-1}} \pm 18\,\mathrm{mL\,min^{-1}}$ in other vertebral arteries (VA) [199]. These values indicate the requirements for the MPIN method in flow experiments.

Besides imaging applications, MPI has so far been used in several magnetic navigation studies. These studies focus on the magnetic manipulation of millimeter sized objects, such as catheters, mini-spheres and helical micro-devices. Additionally, the objects are usually tracked via imaging. For the navigation of a catheter, a soft magnetic sphere has been coated with nanoparticles and is then attached to the catheter. The tip of the catheter could then be imaged by MPI due to the nanoparticles and it could further be manipulated by the magnetic field. With these characteristics, it is feasible to maneuver the catheter through a bifurcation of a phantom blood vessel [60]. In [67], soft magnetic spheres have been placed inside a small magnetic device. This small device is then navigated to a target area within the FoV. The magnetic force is adapted based on the current position that is provided by the MPI images. This approach implements a closed-loop navigation of the small device. In [66], rotating focus fields are controlled selectively to rotate helical micro-devices. In terms of application, these screw-like devices could be used to unscrew a radioactive source out of its shielding in the vicinity of a target area, e.g. for specific cancer radiation. The same principle of rotational magnetic fields has been demonstrated with a human-sized MPI scanner for multiple screws [68]. In [65], rotational focus fields have also been utilized to control the actuation of magnetically coated swimmers. They are moved through bifurcations while their position is simultaneously imaged.

In contrast to moving millimeter-sized objects, the magnetic fields of MPI have also been used to navigate large magnetic particles for targeted drug delivery [69, 70, 71, 72, 64]. A proof of concept to utilize the magnetic fields for MPIN has been demonstrated in [P1]. Micron-sized magnetic particles have been quasi-simultaneously moved and imaged to one side of a glass tube. The combined temporal resolution for the imaging part has reached a rate of $2.9\,\mathrm{Hz}$.

In this work, the method MPIN from [P1] is investigated in more detail. At first, the choice of particles is analyzed systematically. Two particle types with different core diameters are investigated in terms of magnetic manipulability and imaging performance. The navigation characteristics are quantified outside of the MPI system by determining the magnetophretic mobility. The imaging characteristics are identified with Magnetic Particle Spectrometer (MPS) measurements. In a second step, the MPIN method is validated in bifurcation flow experiments. The limiting flow velocity, up to which velocity it is possible to navigate the particles to one side, is determined. In a further step, these experiments are extended by a investigating the flow in a phantom with two different stenosis degrees.

6.2. Material and methods

6.2.1. Magnetic force on particles in flow

In section 2.6, the magnetic force on particles in an undefined medium is described. However, if the magnetic particles are within a liquid medium, such as water, a counter force acts in opposite direction of the magnetic force. This force is called drag force and acts if the particles are moved through water. The drag force, for simplicity given here in the y-direction (classical coordinate system), is defined by

$$F_{\mathrm{d},y}(v) = 6\pi\eta_{\mathrm{water}} r_{\mathrm{h}} \Delta v_{m,y} \tag{6.1}$$

with η_{water} being the fluid viscosity, r_{h} being the hydrodynamic radius of the particles, and $\Delta v_{m,y}$ being the flow velocity difference $\Delta v_m = v_m - v_{\mathrm{water}}$ of the particles to the flowing liquid. By looking at the motion of the particles in the xy-plane, namely the horizontal plane, the drag force and the magnetic force $F_{\mathrm{m},y} = F_{\mathrm{d},y}$ using Eq. (2.48) can be balanced. By setting both forces equal, the equilibrium difference of the flow velocity of the particles and the fluid can be obtained. This results in

$$\begin{aligned}
& F_{\mathrm{m},y} = F_{\mathrm{d},y} \\
\Leftrightarrow\ & \frac{4}{3}\pi r_{\mathrm{c}}^3 \Delta\chi_{\mathrm{v}} \nabla \left(\frac{\|\boldsymbol{B}\|^2}{2\mu_0} \right) = 6\pi\eta_{\mathrm{water}} r_{\mathrm{h}} \Delta v_y \\
\Leftrightarrow\ & \Delta v_y = \frac{\Delta\chi_{\mathrm{v}} r_{\mathrm{c}}^3}{9\mu_0\eta_{\mathrm{water}} r_{\mathrm{h}}} \nabla B_{0,y}^2 && (6.2) \\
\Leftrightarrow\ & \Delta v_y = \xi \nabla B_{0,y}^2 && (6.3) \\
\Leftrightarrow\ & \Delta v_y = \xi \nabla (\mu_0 H(y))^2 \\
\Leftrightarrow\ & \Delta v_y = \xi \frac{\partial}{\partial y} (\mu_0^2 (G_y y)^2) = \xi 2\mu_0^2 G_y^2 y,
\end{aligned}$$

where the magnetophoretic mobility [200], [201], [99](p.593) is defined as

$$\xi = \frac{\Delta\chi_{\mathrm{v}} r_{\mathrm{c}}^3}{9\mu_0\eta_{\mathrm{water}} r_{\mathrm{h}}} \tag{6.4}$$

with unit $[\frac{\mathrm{m^2 s^3 A^2}}{\mathrm{kg^2}}]$ for the described magnetic particles. The magnetophoretic mobility is determined based on explicit knowledge of characteristic parameters of the particles, such as flow velocity, hydrodynamic radius, core radius and viscosity. The magnetophoretic mobility is independent of the magnetic surroundings and measures how well magnetic particles can be navigated by a magnetic gradient field. With increasing radius r_{c}, the manipulability of the particles is increased $\xi \propto r_{\mathrm{c}}^2$. In this case, the difference between r_{c} and r_{h} is neglected. Additionally, the superparamagnetic characteristics for larger par-

ticles need to be ensured [202, 99](p.593). The magnetophoretic mobility dependency of the particle core diameter is illustrated in Fig. 6.1 for water and blood. In order to

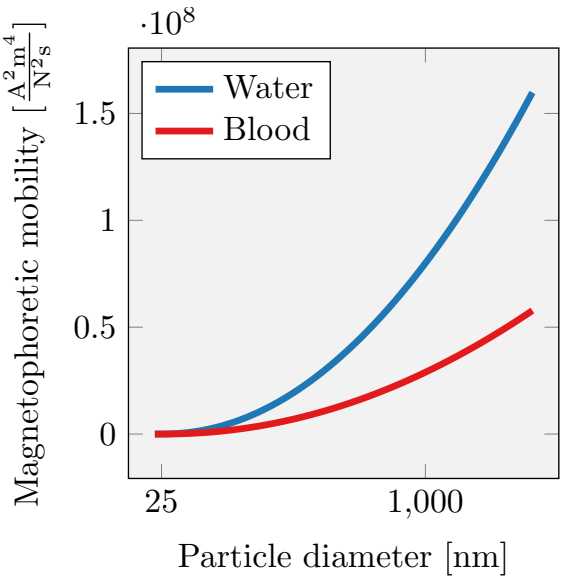

Figure 6.1.: Magnetophoretic mobility for water and blood.

raise the forces on the magnetic particles by keeping the same gradient strength, the size of the particles needs to be as large as possible [99](p.591). However, tracking the path of individual particles by a clearly defined gradient field is challenging. Therefore, the magnetophoretic mobility is measured indirectly, as presented in section 6.2.2. For our purpose, a relative measure for the magnetic mobility is sufficient.

6.2.2. Navigation characterization using a separation apparatus

For the relative measurement of the magnetic mobility, a magnetic cell separation procedure is applied, which has been conducted by micromod. An apparatus for magnetic cell separation is used to separate particles from a surrounding medium with the help of magnetic fields. The duration time, which is required to separate the particles, is inversely proportional to the magnetophoretic mobility. Therefore, a classification evaluating their suitability for navigation is based on the comparison of the particle's separation times. The separation apparatus is presented in [203, 204], whereas the procedure is explained in [205]. An analytical model for the separation process and the resulting separation times is also derived in [205]. From their model, the turbidity T^t at time t is given by

$$T^t = T^t_\infty + \frac{T^t_0 - T^t_\infty}{1 + (\frac{t}{t_{50}})^2} \tag{6.5}$$

for mono-sized Langevin particles with the initial turbidity T_0^t, the final turbidity T_∞^t, and the half separation time t_{50} [206]. According to [205], the half separation time for mono-sized Langevin particles is described by

$$t_{50} = \left(1 - \frac{1}{\sqrt{2}}\right) \frac{L}{v_s}, \tag{6.6}$$

where v_s is the saturation flow velocity of the particles at magnetic saturation and L is the radius of the cavity. It is assumed by Eq. (6.6) that the magnetic field strength at the border of the apparatus is much higher than the required magnetic field to saturate the particles. Recall that the saturation magnetization is defined as $M_\mathrm{S} = 0.6\,\mathrm{T}/\mu_0$. The flow velocity at saturation v_s is given by

$$v_s = \xi \frac{M_\mathrm{S}\mu_0}{\Delta\chi_\mathrm{v}} \nabla B_0 = \xi \frac{M_\mathrm{S}\mu_0^2}{\Delta\chi_\mathrm{v}} G_y, \tag{6.7}$$

which contains the magnetophoretic mobility ξ. To derive this equation, one B in B^2 in Eq. (6.3) is replaced with $B = \frac{\mu_0 M}{\Delta\chi_\mathrm{v}}$ and $M = M_\mathrm{S}$. From Eq. (6.6) and Eq. (6.7), it can be concluded that the half separation time t_{50} and the magnetophoretic mobility are inversely proportional to each other. Therefore, the comparison of the half-separation times of particles gives a a relative measure of the magnetic navigation capabilities.

6.2.3. Magnetic force on particles against gravitation

When the magnetic particles are navigated perpendicularly to the xy-plane in the z-direction, two additional forces act on the particles, as they are navigated by the magnetic force. The buoyancy force

$$F_{\mathrm{b},z} = V_\mathrm{p} \rho_\mathrm{water} g \tag{6.8}$$

describes the force acting on the particles within a liquid medium of different densities as in water. V_p denotes the volume of the particles, ρ_water is the density of water and g is the gravitational constant. This force is exerted by the fluid and opposes the weight of the particles and therefore counteracts against the gravity. It usually determines whether an objects floats or not. The gravitation force is given by

$$F_{\mathrm{g},z} = m \cdot g = V_\mathrm{p} \rho_\mathrm{p} g, \tag{6.9}$$

where ρ_p is the density of the particles. If the magnetic particles should be navigated upwards in z-direction, the magnetic force acts against the drag force and the gravitation,

while the buoyancy force acts in the same direction as the magnetic force. The overall force in z-direction can be described by

$$F_z(z, v, t) = F_{\mathrm{m},y}(z, t) - F_{\mathrm{d},y}(v) + F_{\mathrm{b},z} - F_{\mathrm{g},z}, \tag{6.10}$$

where the buoyancy force and the gravitation force can be combined to one force

$$F_{\mathrm{bg},z} = V_{\mathrm{p}} g(\rho_{\mathrm{p}} - \rho_{\mathrm{water}}). \tag{6.11}$$

The force in z-direction can then be modelled as

$$F_z(z, \dot{z}, t) = F_{\mathrm{m},y}(z, t) - F_{\mathrm{d},y}(\dot{z}) + F_{\mathrm{bg},z}, \tag{6.12}$$

where the velocity v is written as first derivative of z. If one assumes $F = ma = m\ddot{z}(t)$, Eq. (6.12) can be rearranged to an ordinary second order differential equation

$$\ddot{z}(t) = kz(t)s(t) - l\dot{z}(t) + q \tag{6.13}$$

$$\text{with} \quad k = \frac{4\pi\mu_0 r_{\mathrm{c}}^3 \Delta\chi_{\mathrm{v}} G_z^2}{3m_{\mathrm{p}}}, \tag{6.14}$$

$$l = \frac{6\pi\eta_{\mathrm{water}} r_{\mathrm{h}}}{m_{\mathrm{p}}}, \tag{6.15}$$

$$q = \frac{V_{\mathrm{p}} g(\rho_{\mathrm{p}} - \rho_{\mathrm{water}})}{m_{\mathrm{p}}}. \tag{6.16}$$

Note that the function $s(t)$ comes from the Eq. (2.49) for the magnetic force. This differential equation can be numerically solved with Runge-Kutta's method with the boundary conditions $z(0) = z_0$, $\dot{z}(0) = 0$ and $\ddot{z}(0) = 0$.

6.2.4. Equation of motion of magnetic particles

The equation of motion of the particles within a gradient magnetic field, can be explicitly solved, if only the magnetic force on the particle is considered. In this case, the drag force is not considered and for simplification, the behavior in the y-direction is analyzed where buoyancy and gravity force are neglected as well. In chapter 2.6, the Eq. (2.48) for the magnetic force

$$F_{m,y} = \frac{4\mu_0}{3}\pi r_{\mathrm{c}}^3 \Delta\chi_{\mathrm{v}} G_y^2 y. \tag{6.17}$$

has been described. From this equation, it is now desirable to derive the kind of motion the particles perform within the gradient field. With $F = m_p a$, Eq. (6.17) can be written as

$$a(y) = \frac{F_{m,y}(y)}{m_\mathrm{p}} \tag{6.18}$$

where m_p is the mass of the particles. Since $a(t)$ is the second time derivative of $y(t)$, Eq. (6.18) becomes a differential equation

$$\ddot{y}(t) = \frac{4\mu_0 \pi r_\mathrm{c}^3 \Delta\chi_\mathrm{v} G_y^2}{3m_\mathrm{p}} y(t). \tag{6.19}$$

The starting point y_0 of the particles is defined as the distance from the center of the gradient magnetic field. If the particles would start in the center of gradient field at $y_0 = 0$, the particles would not move because no magnetic force acts on them. With initial conditions $y(0) = y_0$ and $\dot{y}(0) = 0$, the second-order linear ordinary differential equation can be solved to

$$y(t) = \frac{y_0}{2} e^{kt} + \frac{y_0}{2} e^{-kt} \tag{6.20}$$

with $k = \sqrt{\frac{4\mu_0 \pi r_\mathrm{c}^3 \Delta\chi_\mathrm{v} G_y^2}{3m_\mathrm{p}}}$ using an exponential approach [P1]. Consequently, the function for velocity and acceleration are then given by

$$v(t) = \frac{y_0}{2} k e^{kt} + \frac{y_0}{2} k e^{-kt} \tag{6.21}$$

and

$$a(t) = \frac{y_0}{2} k^2 e^{kt} + \frac{y_0}{2} k^2 e^{-kt}. \tag{6.22}$$

These equation of motion show that the particles have an exponential movement $y(t) \propto e^t$ inside the magnetic gradient field as long as no other forces counteract.

6.2.5. Transversal navigation of particles through bifurcation

In the following scenario, it is intended to navigate magnetic particles to one side of a vessel bifurcation within a flowing medium. In dependency of the vessel diameter d_v and all magnetic field parameters, it is desired to estimate the limiting flow velocity up to which the magnetic force is capable of moving the particles to one side of the bifurcation. The bifurcation scheme and all parameters of the designed flow experiment are shown in Fig. 6.2. In order to maneuver all particles through only one part of the bifurcation, the magnetic force needs to move the particles from one side of the vessel to the other.

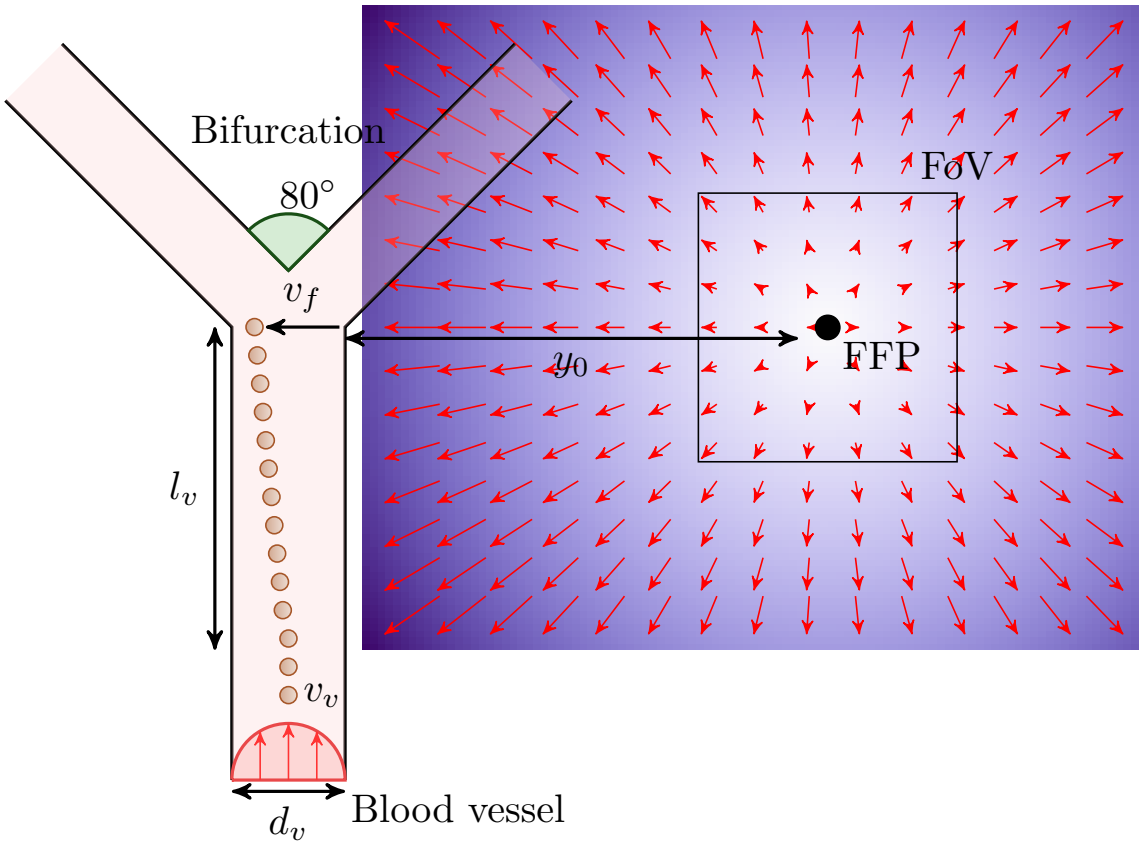

Figure 6.2.: Schematic image of manipulation of particles in bifurcation flow phantom. The magnetic force induces the particles movement over a distance of d_v, while the particles flow with a velocity of v_v inside a rectangular shape vessel with side length l_v. The bifurcation junction is placed in the xy-plane and the flow velocity generated by the magnetic field in y-direction is given by v_f. The flow through the inbound tube is in x-direction in the middle branch.

With the previously determined Eq. (6.20) of motion for the particles within a magnetic gradient field, equation

$$y(t_m) = \frac{y_0}{2} e^{kt_m} + \frac{y_0}{2} e^{-kt_m} = d_v + y_0 \tag{6.23}$$

can be derived. The vessel diameter d_v plus the distance to the FFP y_0 is set equal to $y(t)$. The time t_m is the time necessary for the magnetic force to navigate the particles over the distance d_v. As the drag force is not considered in Eq. (6.23), the time t_m describes only a minimum estimate for the movement time. By rearranging Eq. (6.23) for t_m, it becomes

$$t_m = k^{-1} \ln \left(\frac{\sqrt{d_v(2y_0 + d_v)} + y_0 + d_v}{y_0} \right). \tag{6.24}$$

The particles are carried by the volume flow with flow velocity v_v towards the bifurcation. At first, a length l_v is defined, at which the magnetic field starts to exert a force on the particle, then the time

$$t_v = \frac{l_v}{v_v} \tag{6.25}$$

can be calculated, where the particles are influenced by the magnetic force. The volume flow velocity v_v is assumed to be laminar and denotes the average linear velocity given over the cross section A_v of the vessel. By setting both times equal, $t_m = t_v$, the limiting velocity of the flowing liquid can be estimated by

$$v_{v,t_m} = \frac{l_v}{t_m} = l_v \frac{k}{\ln\left(\frac{\sqrt{d_v(2y_0+d_v)}+y_0+d_v}{y_0}\right)} \tag{6.26}$$

in dependency of the geometry parameter and the magnetic field parameters. When a gradient strength of $G_y = 1.2\,\mathrm{T\,m^{-1}}/\mu_0$ in y-direction is assumed, a starting distance away from the FFP of $y_0 = 12\,\mathrm{mm}$, a vessel length of $l_v = 15\,\mathrm{mm}$, a particle core radius $r_\mathrm{c} = 1000\,\mathrm{nm}$, a particle mass of $m_p = \frac{4}{3}\pi r_\mathrm{c}^3 \rho_p$ with $\rho_p = 5200\,\mathrm{kg\,m^{-3}}$ as particle density, the following velocity values can be estimated as summarized in Table 6.1.

Table 6.1.: The diameters and flow velocities in different human vessel types. With the parameters for the particles and the gradient field, the limiting velocities are estimated for each vessel type. The diameters and flow velocities are provided by [88, 198, 199, 99]

Vessels type	Diameter d_v [mm]	Flow velocity v_v [mm/s] ([ml/s])	Time t_v [s]	Est. flow velocity v_{v,t_m} [mm/s]
Aorta	20	300 (94)	0.05	1138
Arteries (ICA)	4.6-5.1	268-223 (4.58)	0.055-0.067	2178-2086
Arteries (VA)	6.1-6.5	52-46 (1.51)	0.09-0.1	1920-1865
Arteriols	0.1	1 ($7.85 \cdot 10^{-6}$)	15	14440
Capillaries	0.01	0.5 ($3.9 \cdot 10^{-8}$)	30	45637

6.2.6. Stopping particles transversal in volume flow

Additionally to the navigation in the y-direction, the particles can be stopped or slowed down by positioning the FFP away from the particles in the opposite direction of the flow direction. In this case, the magnetic force needs to be equal to the drag force exerted by the volume flow. Setting the drag force from Eq. (6.1) equal to the magnetic force from Eq. (2.48) in x-direction leads to

$$F_{m,x} = \frac{4\mu_0}{3}\pi r_\mathrm{c}^3 \Delta\chi_\mathrm{v} G_x^2 x_0 = 6\pi\eta_\mathrm{water} r_\mathrm{h} \Delta v_{m,x} = F_{d,x}, \tag{6.27}$$

where x_0 is the distance away from the FFP in x-direction. This equation can be rearranged to

$$x_0 = \frac{6\pi\eta_{\text{water}} r_{\text{h}} \Delta v_{m,x}}{\frac{4\mu_0}{3}\pi r_{\text{c}}^3 \Delta\chi_{\text{v}} G_x^2} \tag{6.28}$$

to estimate the necessary distance of the FFP to stop the particles. The schematic sketch of stopping the particles can be seen in Fig. 6.3. If the particle parameters and magnetic

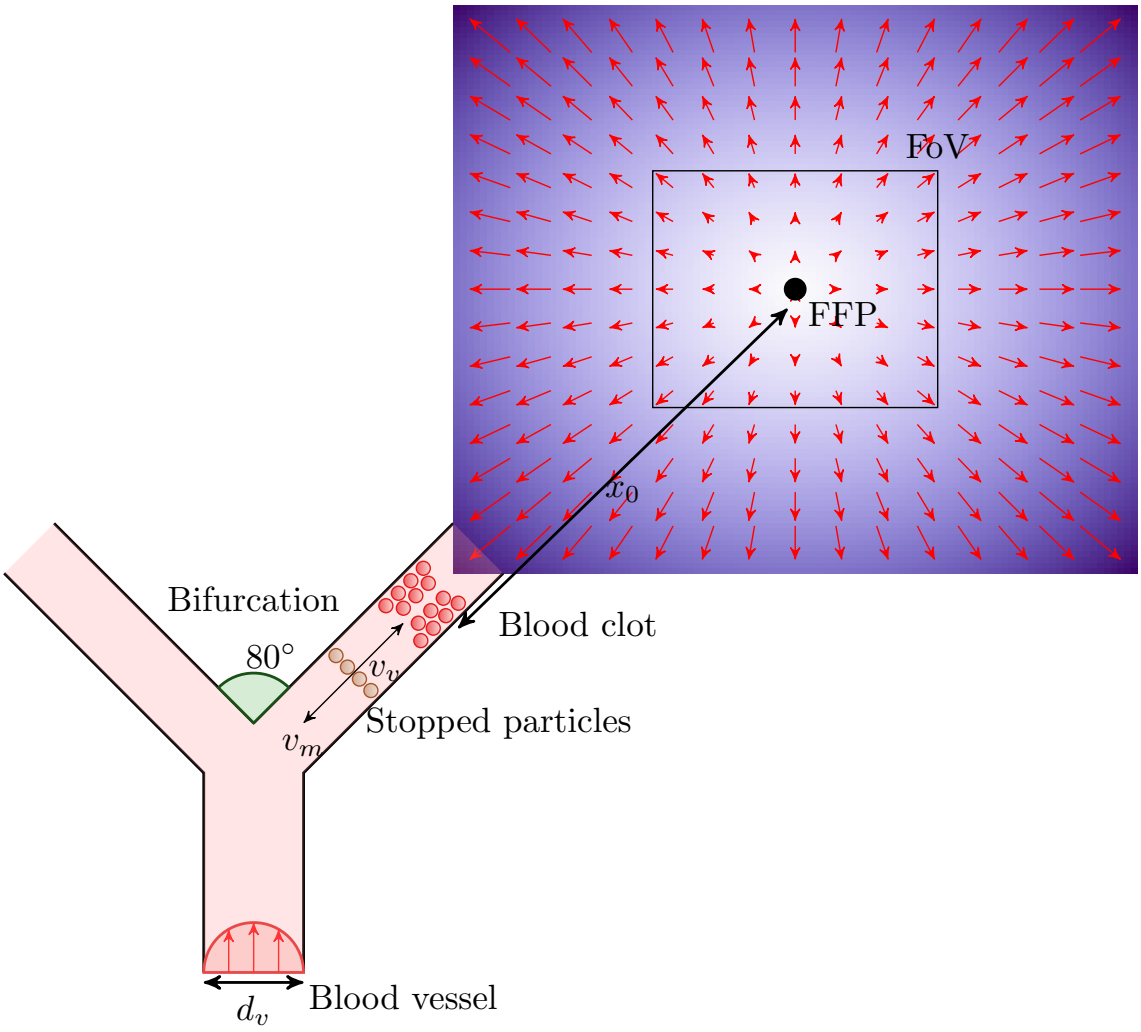

Figure 6.3.: Schematic sketch of stopping the particles at a stenosis due to a blood clot with magnetic forces induced by the shifted FFP. The magnetic force acts in the opposite direction of the flow direction. If the magnetically induced velocity v_m is equal to the flow velocity v_v inside the vessel, the particles are stopped otherwise they are only slowed down.

field parameters from section 6.2.5 are assumed, the FFP distance x_0 necessary to stop the particles for the different vessel type can be calculated. Exemplarily, the FFP needs to be adjusted to $x_0 = 49.6\,\text{m}$ for the arteries. Here, it is assume that a particle is set into a volume flow of $200\,\text{mm}\,\text{s}^{-1}$ with a gradient of $G_x = 1.2\,\text{T}\,\text{m}^{-1}/\mu_0$, a viscosity $\eta = 0.001\,\text{kg}\,\text{s}^{-1}\,\text{m}$ and particle diameter $r_{\text{c}} = 1000\,\mu\text{m}$ ($r_{\text{h}} = 1100\,\mu\text{m}$). Since the scanner

used in this thesis is only capable of positioning the FFP to a maximum of $14.1\,\mathrm{mm}$ in x-direction, the particles are only slowed down and not fully stopped.

6.2.7. Magnetic particles and magnetic particle spectrometry

For the MPIN experiments, two types of particles with different compositions and magnetic core diameters are used. As a reference, Dynabeads MyOne (ThermoFisher, US) with a hydrodynamic diameter of about $1\,\mu\mathrm{m}$ are selected as a first particle type. The second particle types are customized nanomag/synomag-D particles (micromod Partikeltechnologie GmbH, Germany) with hydrodynamic diameters around $700\,\mathrm{nm}$. These particles are biocompatible and consist of iron oxide cores with a dextran shell. Synomag-D particles have excellent chracteristics as blood pool tracers for MPI [140], but exert a quite slow magnetic mobility. In contrast, nanomag-D particles with diameters in the range of $250\,\mathrm{nm}$ to $500\,\mathrm{nm}$ show a high magnetic mobility [141]. In order to combine the imaging properties of synomag-D with the high magneto-mobility of nanomag-D particles, various amounts of synomag-D are embedded in the iron oxide multi-cores of nanomag. Finally, all particles are coated with a dextran shell. An overview of the synthesized particles is given in Table 6.2. Further, MPS measurements are conducted to analyze the imaging

Table 6.2.: Different synthesized particles with their relevant properties used for the MPIN experiments.

Sample name	Lot	Surface	Hydrodynamic diameter [nm]	Polydispersity index (PDI)	Percentage of iron from synomag [%]
nanomag-D	308	dextran	405	0.12	-
nanomag/synomag-D	332	dextran	649	0.14	44
nanomag/synomag-D	333	dextran	698	0.24	61
nanomag/synomag-D	334	dextran	641	0.32	40
Dynabeads MyOne	017	COOH	1048	0.13	-

capabilities of the particles. The design of the custom-designed MPS is outlined in [143] and has been described in 2.7.2. The particles are excited with a sinusoidal signal with a frequency of $26.042\,\mathrm{kHz}$ and an amplitude of $20\,\mathrm{mT}$. The measurements are performed with background subtraction and 1000 averages. To analyze the spectra of the particles, a dilution series of all particle types is prepared. This dilution series is summarized in Table 6.3. In a first measurement series, a volume of $20\,\mu\mathrm{L}$ for each concentration is analyzed within an Eppendorf tube. In a second measurement series, the sample with the highest concentration for each particle is magnetized with a conventional magnet. The particles remain at the bottom of the tube while the remaining suspension becomes transparent. In a third measurement series, the particles are stirred up with a vortexer. In a fourth measurement cycle, the whole process of magnetization and vortexing is repeated

Table 6.3.: Iron concentrations of the dilution series used for MPS measurements.

Num	c_0	c_1	c_2	c_3	c_4	c_5
Dilution factor	0	1	2	4	8	16
Iron concentration [$\mathrm{mmol\,L^{-1}}$]	179.05	89.52	44.76	22.38	11.19	5.59
Num	c_6	c_7	c_8	c_9	c_{10}	
Dilution factor	32	64	128	256	512	
Iron concentration [$\mathrm{mmol\,L^{-1}}$]	2.79	1.39	0.69	0.35	0.18	

twice. With these second, third, and fourth measurement series, it should be ensured that all particle types have no strong remanence caused by the strong magnetic field of the conventional magnet. The strong magnetic field of the conventional magnet is supposed to simulate the field of the force mode in the following experiments. If the particles would have a strong remanence after being exposed to the strong magnetic field, they would not be suitable for quantitative imaging. Finally, a background measurement containing noise is subtracted from all measurements.

6.2.8. Magnetic mobility of particles

The theory of magnetic mobility and its connection the magnetophoretic mobility are discussed in section 6.2.2. Specifically, the magnetic mobility, regrading its half separation time, is measured with a Q 100 ml device (SEPMAG Technologies, Spain). For these experiments, a volume of $100\,\mathrm{mL}$ with an iron concentration of $0.03\,\mathrm{mg\,mL^{-1}}$ is placed inside the cavity. During the measurement, the opaque suspension becomes more and more transparent until all particles are driven towards the borders. A light source illuminates the cavity from one side to the other and the detector on the other side monitors the magnetophoresis process. Consequently, the suspension homogeneity is measured over time. Afterwards, the half separation time t_{50} is calculated by using the Qualitance software by SEPMAG, that fits a sigmoidal curve to the measured values. A decreasing half separation time indicates an increase of the magnetophoretic mobility. Additionally, the size distribution of the particle suspension before and after the magnetic separation is determined by Dynamic Light Scattering (Nano-S 90, Malvern Panalytical Ltd, UK).

6.2.9. MPN transversal in tube

In a first proof of concept experiment, the Dynabeads MyOne particles with a diameter of $1000\,\mathrm{nm}$ are placed inside a glass capillary with a diameter of $25\,\mathrm{mm}$ [P1]. The capillary is filled with water and is then sealed. Afterwards, the capillary is mounted inside the scanner in the y-direction. The right side of the capillary with the particles is placed in the center of the FoV. The FoV has a size of $20\,\mathrm{mm} \times 20\,\mathrm{mm} \times 10\,\mathrm{mm}$ resulting from

the gradient strength of $2.4\,\mathrm{T\,m^{-1}}$ in z-direction and an amplitude of $12\,\mathrm{mT}$. The experimental setup can be seen in Fig. 6.4. The FFP during the navigation mode is positioned at

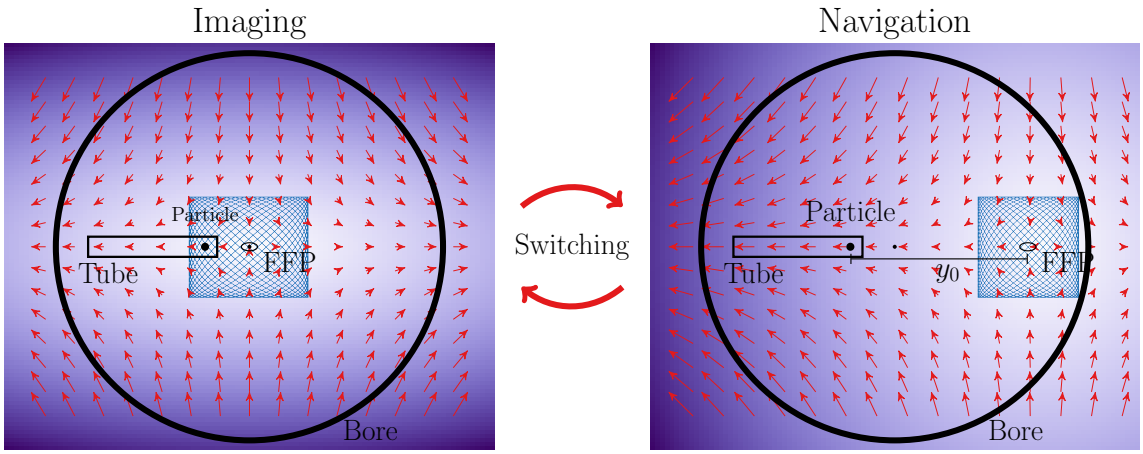

Figure 6.4.: The particles inside the capillary tube are moved and imaged by the magnetic fields during the MPIN method. The tube is place inside the scanner bore in y-direction.

$\mathrm{FFP}_{F,y} = 14.1\,\mathrm{mm}$ and at position $\mathrm{FFP}_{F,y} = 0\,\mathrm{mm}$ during the imaging mode. The MPIN method uses a ratio of $N_{\mathrm{nc}} = 5$ and $N_{\mathrm{ic}} = 1$ for navigation and imaging cycles. The resulting temporal resolution is about $2\,\mathrm{Hz}$. The experiment is recorded with an optical digital camera mounted in front of the scanner bore.

6.2.10. MPN against gravity through vertical bifurcation junction

For the second proof of concept experiment, Dynabeads MyOne particles are placed at the bottom of a bifurcation phantom. The designed bifurcation phantom is 3D-printed with the SL technique (Form 2, Formslabs, US). The used material (clear 4, Formlabs, US) is translucent and waterproof. A quadric cross-section with a side length of $4\,\mathrm{mm}$ is chosen to facilitate the vision through the material. A schematic setup of the experiment can be seen in Fig. 6.5. The angle between the bifurcation branches is $80°$. The phantom is filled with water and it is sealed afterwards. The bifurcation phantom is placed $14\,\mathrm{mm}$ left from the FoV center inside the bore. In this experiment, the force mode is activated with $N_{\mathrm{nc}} = 4$ cycles while the imaging cycles is set $N_{\mathrm{ic}} = 1$. The FFP position is at $\mathrm{FFP}_{F,xyz} = (0\,\mathrm{mm}, 14.1\,\mathrm{mm}, -17.5\,\mathrm{mm})$. Again, the experiment is recorded with an optical camera from outside of the bore.

6.2.11. MPN in flow within transversal bifurcation junction

The first two proof of concept experiments used the Dynabeads MyOne particles. The third experiment uses the results from the MPS study and the mobility study. Previously, the particles are analyzed in the MPS system to determine their imaging capabilities.

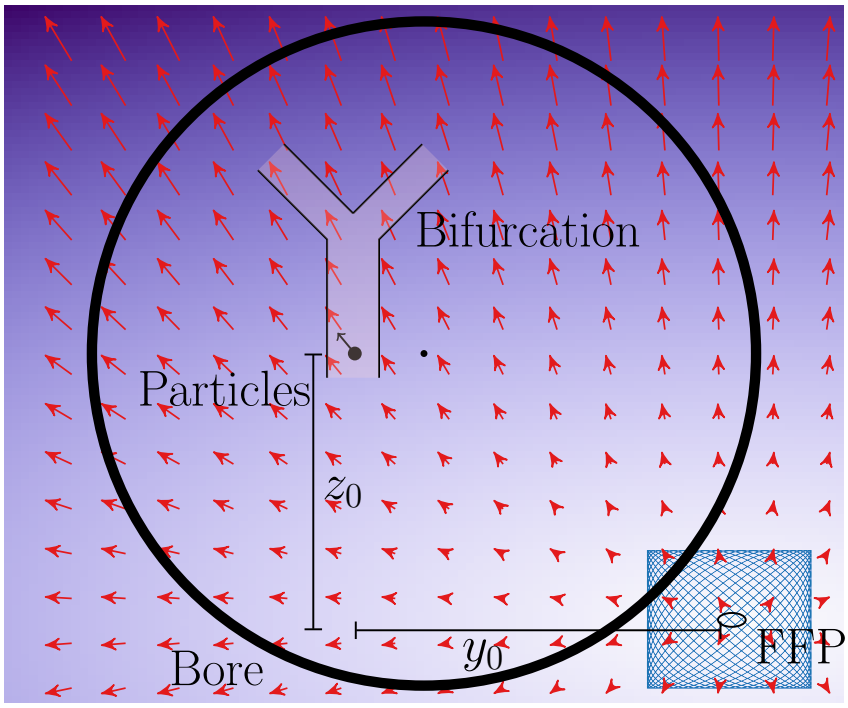

Figure 6.5.: The bifurcation junction in the yz-plane is place inside the scanner while the FFP is shifted the right bottom corner to induce a magnetic force upwards to the left.

Further, their usability for navigation is determined by the magnetic separation device as described in section 6.2.2. Therefore, all subsequent experiments are performed using only the particles best suited for quasi-simultaneous imaging and navigation from the insight gained in the aforementioned experiments. The third experiment makes the step from a static to a dynamic flow experiments, but as a next step only the navigation mode is used in this studies. For navigating particles in flow through a bifurcation using MPN, three different bifurcation phantoms are designed. They are 3D-printed by the SL technique (Forms 2, Formlabs, US). All bifurcation phantoms have a quadratic cross-section of $A = a^2 = 12.544\,\mathrm{mm}^2$ with a side length of $d_v = a = 3.544\,\mathrm{mm}$. This cross-section corresponds to a circular cross-section with a diameter of $d = 4\,\mathrm{mm}$. A squared cross-section is selected to avoid optical refraction. It simplifies the identification of the particles in flow with the optical camera. The first bifurcation phantom splits into two equally-sized branches with a crossing angle of $80°$ (seen Fig. 6.6a). The second bifurcation phantom is designed similarly and has a 60% stenosis in the right branch. Its cross-section of $A_{60} = 7.52\,\mathrm{mm}^2$ is designed circularly with a diameter of $1.54\,\mathrm{mm}$. It is supposed to mimic a more realistic vessel. The capability to follow the particles without optical refraction is less important in this case. The 60% stenosis phantom is presented in Fig. 6.6b. The third bifurcation phantom mimics a 100% stenosis in the right branch. A circular cross-section of $A_{100} = 3.76\,\mathrm{mm}^2$ with a diameter of $1.09\,\mathrm{mm}$ is glued to achieve a full blockage. Again, all stenosis phantoms split with a crossing angle of $80°$. A centric catheter mount in the middle branch is designed in all three phantoms in the inbound

flowing branch (seen Fig. 6.6c). This catheter mount ensures that the particles are injected centrically.

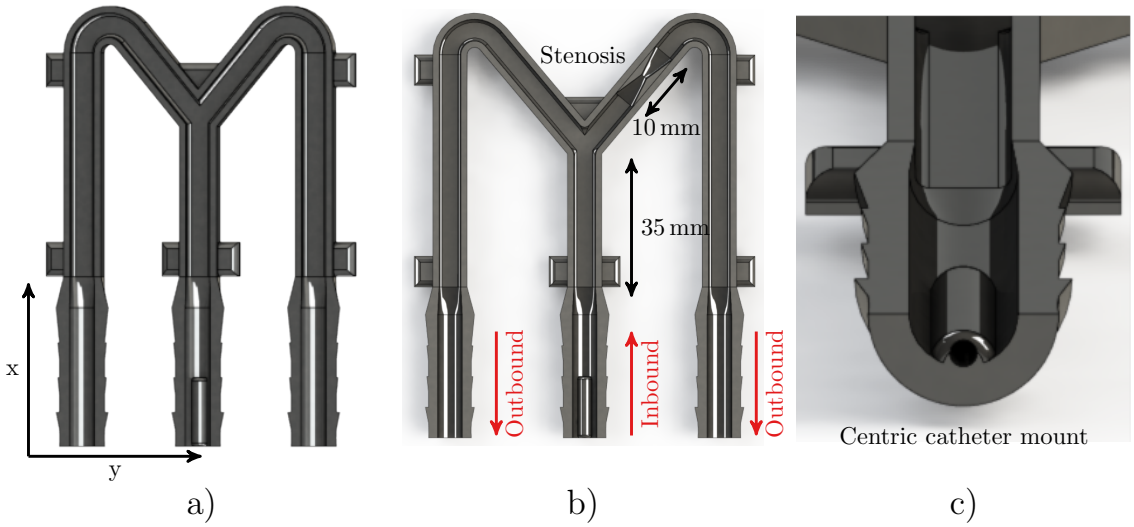

Figure 6.6.: a) 3D CAD sketch of the bifurcation phantom. b) 3D CAD sketch of the bifurcation with 60% stenosis in the right branch of the phantom. c) The centric catheter mount is built centrically at the bottom of the inbound tube of every phantom to ensure centric injection of particles.

In addition, a phantom mount is built that positions the phantom in the center of the FoV (seen Fig. 6.7a). To be able to follow the experiments through the scanner bore, a mirror is fixed at a $45°$ angle above the phantom to make the volume flow visible from the outside. The bore is illuminated by a conventional light source. The bifurcation phantom is positioned horizontally in the xy-plane. By this means, the influence of the gravity force is avoided. Further, the center of the bifurcation is positioned $10\,\mathrm{mm}$ off-center in the y-direction and $5\,\mathrm{mm}$ in the x-direction. Three flow sensors (BB BioTech, Switzerland) with a measurement range of $0.25\,\mathrm{mL\,s^{-1}}$ to $13.33\,\mathrm{mL\,s^{-1}}$ are used to monitor the volume flow. They are connected to the dynamic flow bifurcation phantom via three hoses. Two outbound hoses are connected back to one hose and back to the pump. The flow sensors are controlled by an Arduino (Arduino LLC, Italy). It logs the flow rates and starts when the MPI scanner sends a trigger at the beginning of the measurement. The inbound hose is connected to the inlet of the bifurcation phantom. Additionally, the inbound hose has a bypass, in which a catheter can be inserted. This catheter, (Armada 14, Abbott, US) with a diameter of $1.35\,\mathrm{mm}$, is attached in the bottom middle of the 3D-printed phantom (seen in Fig. 6.6c). By this means, an unbiased particle flow is ensured at the time of the injection. The whole experiment setup is illustrated in a photo in Fig. 6.7a and as a scheme in Fig. 6.7b. The preclinical MPI scanner creates a maximum gradient of $2.4\,\mathrm{T\,m^{-1}}$ in the z-direction ($-1.2\,\mathrm{T\,m^{-1}}$ in the x- and y-directions). The FFP offset can be adjusted to a maximum of $-42\,\mathrm{mT}$ to $42\,\mathrm{mT}$ ($-17.5\,\mathrm{mm}$ to $17.5\,\mathrm{mm}$) in the z-direction. It can be set to $-17\,\mathrm{mT}$ to $17\,\mathrm{mT}$ ($-14.1\,\mathrm{mm}$ to $14.1\,\mathrm{mm}$) in the x- and y-directions. This

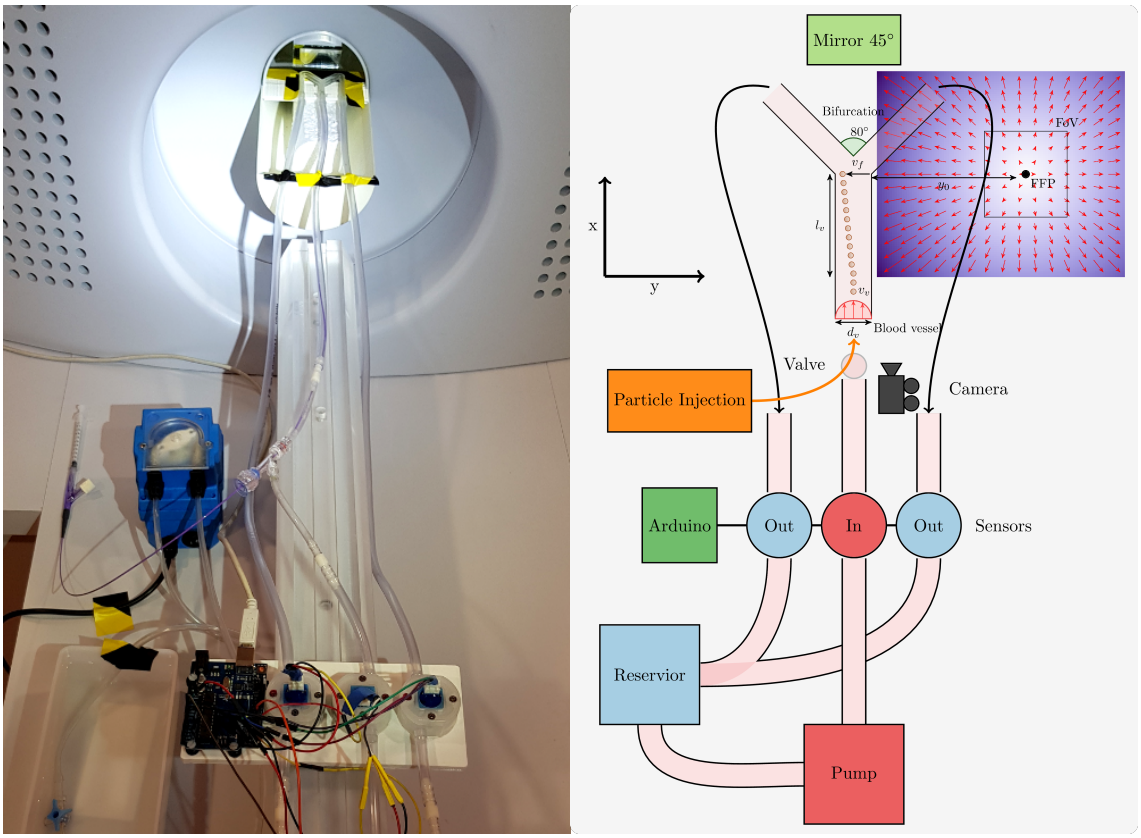

a) b)

Figure 6.7.: a) Bifurcation flow experiment setup with Arduino connected to flow sensors, bifurcation phantom visible inside the mirror placed inside the bore and light source. b) Schematic image of navigation of particles in bifurcation flow phantom.

induces a maximum force of $1.18 \cdot 10^{-12}$ N on the particles in the z-direction. In the y-direction, a force of $2.96 \cdot 10^{-13}$ N is induced, if a particle diameter of $1\,\mu\mathrm{m}$ is assumed. For the experiments, the FFP in navigation mode is set $14.16\,\mathrm{mm}$ away in the opposed y-direction. This sums up to a total distance from bifurcation center to the FFP of $22.16\,\mathrm{mm}$ ($4.64 \cdot 10^{-13}$ N). In the x-direction, the FFP is also positioned $14.16\,\mathrm{mm}$ away from the MPI FoV center. This shift leads to a total distance between FFP and bifurcation center of $9.16\,\mathrm{mm}$. For all experiments, only the MPN is used (DF cycles $N_{\mathrm{nc}} = 20$, DF cycles $N_{\mathrm{ic}} = 0$). Therefore, no imaging is performed and the magnetic force is induced on the particles all the time.

The described flow experiments with the bifurcation phantoms are performed with five different flow velocities from $5.45\,\mathrm{mL\,s^{-1}}$ to $10.22\,\mathrm{mL\,s^{-1}}$ in the inflowing branch. For each flow velocity, the experiment is repeated twice. In the first experiment, the magnetic forces are switched off to obtain the ground truth about the flow behavior. By this means, any bias in the flow direction is excluded. Consequently, it is ensured that the particles flow equally through both branches. Second, in the actual experiment, the magnetic forces are switched on to analyze the particles' flow properties. The experiment is conducted for

both branches of the bifurcation for the flow velocity $5.45\,\mathrm{mL\,s^{-1}}$, in order to eliminate a bias to one branch. Therefore, it validates that the MPN method functions in both directions of the bifurcation.

Table 6.4.: Volumetric flow velocities used in the experiments and the time duration the particles are influenced by the magnetic force.

Degree of stenosis	Flow velocity inbound [$\mathrm{mL\,s^{-1}}$]	Flow velocity outbound [$\mathrm{mL\,s^{-1}}$]	Time [ms]
100%	1.36	1.36	161
0%, 60%, 100%	2.72	1.36, 1.36, 2.72	161, 161, 80
0%, 60%	5.45	2.72, 2.72	80, 80
0%, 60%	6.87	3.40, 3.40	63, 63
0%, 60%	8.18	4.09, 4.09	53, 53
0%	10.22	5.11	42

The flow velocity rates measured by the sensors correspond with the theory. The flow velocity in both branches are equal. Their sum corresponds to the flow velocity rates inbound to the bifurcation. The five analyzed flow velocities are presented in Table 6.4. The distance from the position where the particles are released to the junction of the bifurcation is l_v = $35\,\mathrm{mm}$. The particles are injected with a catheter mounted centrically inside the phantom. The time duration from particle release to the junction of the bifurcation is also stated in the last column of Table 6.4.

6.2.12. MPI parameters

For the following flow experiments using the MPIN method, the imaging of static particles without navigation application is performed in advance to check the imaging capabilities of the particles in the MPI scanner. The results from the MPS measurements indicates good imaging properties, which have to be validated with the MPI scanner. Therefore, two system matrices are acquired on a grid of $24 \times 24 \times 14$ positions, which cover a volume of $24\,\mathrm{mm} \times 24\,\mathrm{mm} \times 14\,\mathrm{mm}$. The delta samples have a size of $1\,\mathrm{mm} \times 1\,\mathrm{mm} \times 1\,\mathrm{mm}$ and are filled with $1\,\mu\mathrm{L}$ of Dynabeads MyOne and nanomag/synomag-D 333. The gradient strength is adjusted to $2.4\,\mathrm{T\,m^{-1}}/\mu_0$ and the drive-field amplitude is set to $12\,\mathrm{mT}/\mu_0$. These parameters result in a FoV size of $20\,\mathrm{mm} \times 20\,\mathrm{mm} \times 10\,\mathrm{mm}$. For the imaging measurement, the delta samples of $1\,\mathrm{mm} \times 1\,\mathrm{mm} \times 1\,\mathrm{mm}$ are used as well. The imaging sequence is performed with the same imaging parameters to enable reconstruction using a regularized iterative Kaczmarz algorithm. Previous to the reconstruction, the measurement data from 100 DF cycles is averaged. Additionally, frequencies with an SNR above two are selected from the frequency range of $80\,\mathrm{kHz}$ to $1250\,\mathrm{kHz}$. This choice leads to 423 frequency components. The relative regularization parameter is set to 0.001. The

Kaczmarz algorithm runs for three iterations. Finally, the FWHM is calculated in the x- and z-directions in the image.

6.2.13. Simultaneous MPIN in flow with bifurcation junction

The last experiment brings all aspects from the previous experiments together. However, the simultaneous MPIN bifurcation studies with flow are only performed for a flow velocity of $1.36\,\mathrm{mL\,s^{-1}}$ and only with the bifurcation phantom with a 100% stenosis. The position of the imaging FoV is set to $\mathrm{FF_{I,xyz}} = 0\,\mathrm{mm} \times 14.1\,\mathrm{mm} \times 0\,\mathrm{mm}$ by using the focus fields to cover the phantom branch with the simulated stenosis. Because of the field deviations, the system matrix acquired for the previous imaging experiments cannot be used for the imaging part of the experiments with simultaneous navigation application. Therefore, a system matrix with the identical imaging parameters is acquired at the shifted focus fields position. The focus field position for navigation is adjusted to $\mathrm{FF_{F,xyz}} = 14.1\,\mathrm{mm} \times -14.1\,\mathrm{mm} \times 0\,\mathrm{mm}$. For simultaneous imaging and navigation, the number of imaging DF cycles is given with $N_{\mathrm{ic}} = 1$, while the number of navigation DF cycles is adjusted to $N_{\mathrm{nc}} = 20$. Consequently, the FFP switches between $\mathrm{FF_{I,xyz}}$ and $\mathrm{FF_{F,xyz}}$ with the ratio of 20:1. That means only snapshots are taken at the 100% stenosis. Overall, this leads to a temporal resolution for imaging of $2.15\,\mathrm{s}$ per 3D Volume.

6.3. Results

6.3.1. Magnetic particles and magnetic particle spectrometry

The spectra of Dynabeads MyOne and four different nanomag/synomag-D particle types in a concentration of $179.05\,\mathrm{mmol\,L^{-1}}$ are presented in Fig. 6.8. The batches (332, 308) only generate up to 28 harmonics above the noise level and the signal decline has no linear form. The spectra of the Dynabeads MyOne and the nanomag/synomag-D batches (333, 334) produce up to 35 harmonics above the noise level. The nanomag/synomag-D batch 333 has the strongest signal of all batches but also the steepest decrease of the signal strength (see Fig. 6.8). Batch 334 has a lower signal in the first harmonics. However, its steepness is lower than in the other spectra and it has a kink at the 18^{th} harmonic, where the curvature of the signal strength becomes even less steep. For further analysis, only the measurements of nanomag/synomag-D batch 333 are presented because batch 333 provides the best result of all batches in terms of the spectrum. Therefore, it is the most promising candidate with respect to its imaging abilities. The linearity within several frequencies over different concentrations is analyzed for Dynabeads MyOne and nanomag/synomag-D batch 333 in Fig. 6.9a and Fig. 6.9b. It demonstrates that the signal strength is linear in all investigated frequencies, with coefficients of determi-

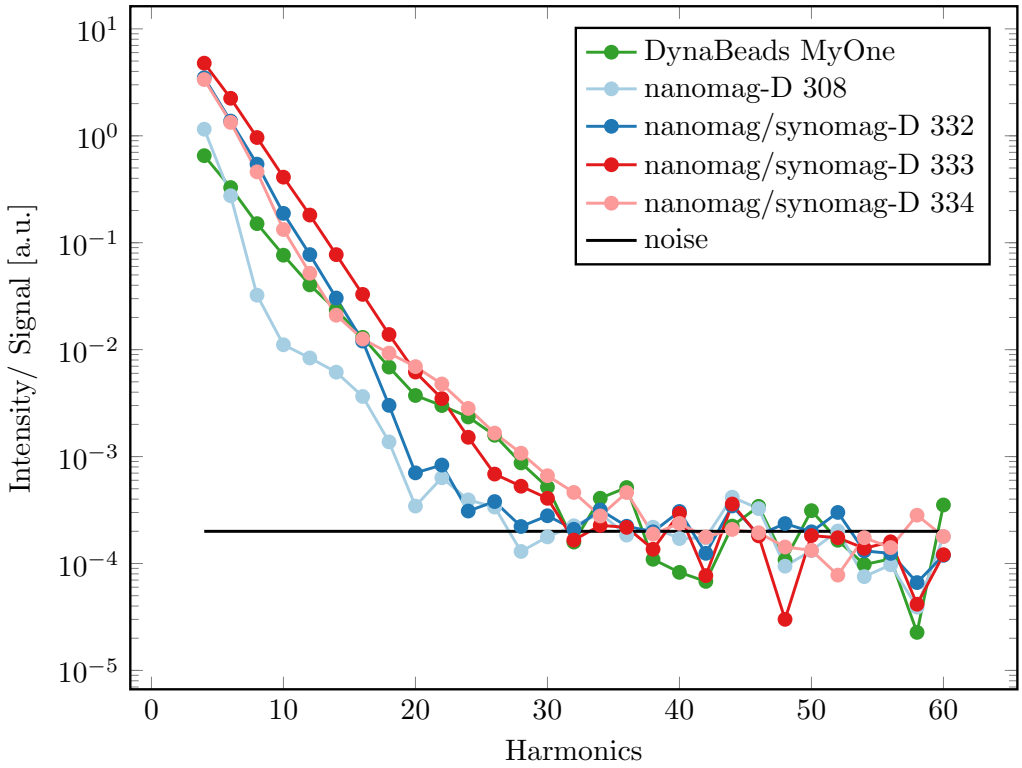

Figure 6.8.: Visualization of the spectra of Dynabeads MyOne, nanomag/synomag-D batches 332, 333, 334, 308.

nation between 0.971 and 0.997. Further, the imaging properties of magnetic particles

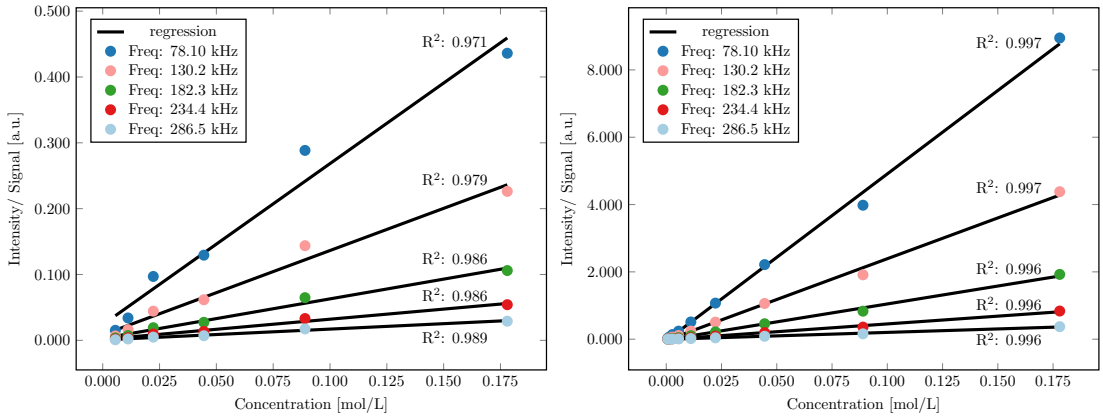

(a) Dynabeads MyOne. (b) nanomag/synomag-D 333.

Figure 6.9.: (a) Linear signal strength decrease for various frequencies depending on the concentration of beads. (b) Linear signal strength decline for various frequencies depending on the concentration of nanomag/synomag-D batch 333.

are analyzed for any effects of magnetization, since the particles should be used for magnetic navigation applications. The time signal of Dynabeads MyOne at concentration $179.05\,\mathrm{mmol\,L^{-1}}$ is shown for different stages in Fig. 6.10a. The light blue line shows the signal of non-magnetized particles, while for the dark blue line the particles have been magnetized. The measurements shown as a green line are generated by particles

that have been magnetized and vertexed once. The results shown as a red line derive from particles that have gone through this procedure twice. In all four time signals, only small deviations occur. Apart from that the signals seem similar. The mean standard deviation using the 4 measurements per time point reveals a mean relative error of 3.1% by considering the measurement range. In Fig. 6.10b, the same four lines are shown for the nanomag/synomag-D batch 333 particles. All graphs also turn out to be very similar with only very small discrepancies. The mean relative error is 1.7%. The relative error for repeated measurements without magnetization or vortexing is 0.75%. Therefore, the nanomag/synomag-D particles are only minimally influenced by magnetization or vortexing.

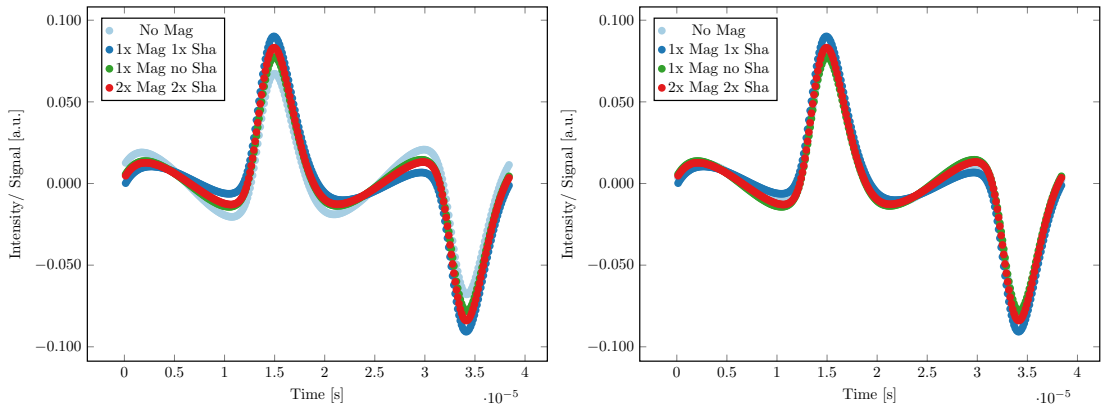

(a) Dynabeads MyOne. (b) nanomag/synomag-D 333.

Figure 6.10.: Time signal for Dynabeads MyOne (a) and (b) nanomag/synomag-D 333 in four different stages: non-magnetized, magnetized, magnetized and vertex, 2x magnetized and 2x vertex.

6.3.2. Magnetic mobility of particles

The suspension homogeneity during the separation procedure for all particles is presented in Fig. 6.11. The homogeneity is normalized with the initial homogeneity. The relevant navigation parameters are determined based on these time curves (the half separation time values) (see Table 6.5). Additionally, the size distribution of the particle suspension before and after the magnetic separation with the polydispersity index (PdI) are given in Table 6.5. The half separation times ($75\,\mathrm{s}$, $83\,\mathrm{s}$) of nanomag/synomag-D batches (333, 334) are similar to the half separation of the Dynabeads MyOne at $79\,\mathrm{s}$. In contrast, the half separation time of nanomag/synomag-D (332) particles is shorter at $57\,\mathrm{s}$. With $194.4\,\mathrm{s}$ the half separation time of plain nanomag-D is much longer. The separation process influences the size distribution, which results in an increase of Z_{average}. Except for nanomag/synomag-D 333 particles the increase of Z_{average} is $130\,\mathrm{nm}$ at its maximum after the magnetic separation for all other particles. For nanomag/synomag-D 333 particles, the difference is $405\,\mathrm{nm}$ before and after the magnetic separation procedure.

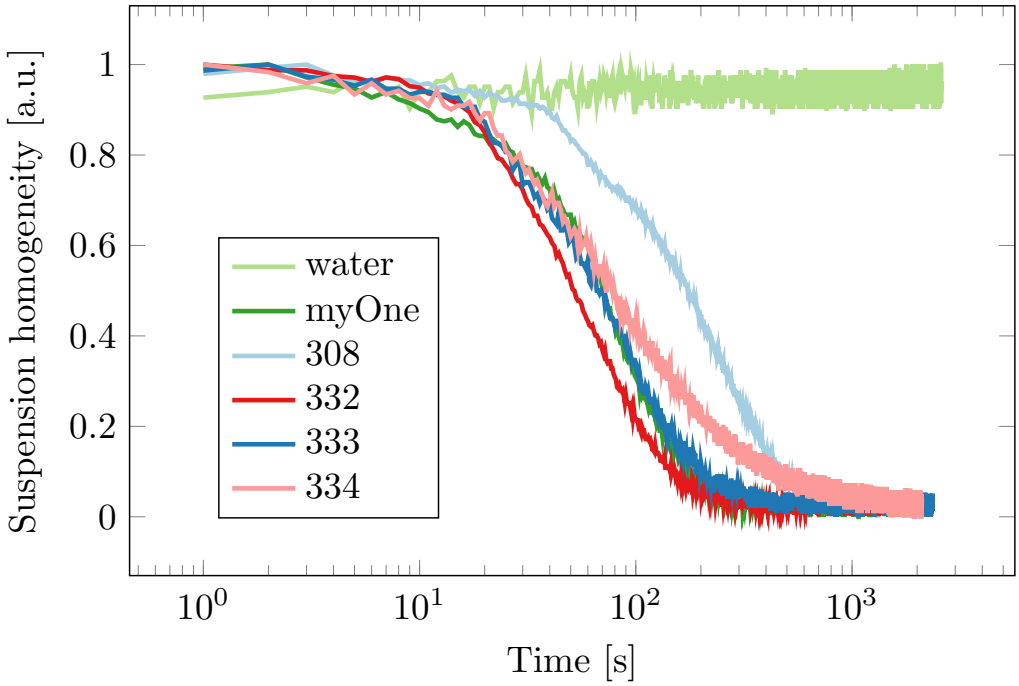

Figure 6.11.: The homogeneity of the suspension is measured over time during the magnetic separation. The suspension homogeneity is plotted for all particle batches, while water is used as a blank value for comparison.

Table 6.5.: Half separation times t_{50} of the different suspensions of iron oxide particles and size distribution before and after separation.

Sample name	Lot	t_{50}[s]	Z_{average}[nm] / PdI before separation	Z_{average}[nm] / PdI after separation
Dynabeads MyOne COOH	017	79.0	1048 / 0.126	1105.0 / 0.280
nanomag-D	308	194.4	405.4 / 0.118	505.0 / 0.229
nanomag/synomag-D	332	57.0	649.2 / 0.143	679.2 / 0.171
nanomag/synomag-D	333	75.0	698.2 / 0.240	1104.0 / 0.297
nanomag/synomag-D	334	83.0	641.3 / 0.325	770.2 / 0.481

6.3.3. MPN transversal in tube

To analyze the particle behavior, the results of the first proof of concept MPIN experiment are recorded with a digital camera using 25 images per second. This video sequence is synchronized to the 4D MPI imaging data of the MPIN sequence, where only the data from the imaging phase is used. The 4D MPI volume images are shown as MIP images in the xz-plane. The combined video is presented in Fig. 6.12. Three snapshots of the video at different time points 0 s, 6 s and 12 s are given in Fig. 6.13. In the experiment shown in the video the magnetic particles are moved towards the left side of the glass capillary. The magnetic force acts towards the left and drives the particles against the drag force and frictions at bottom of the capillary tube to the left. By taking a very close

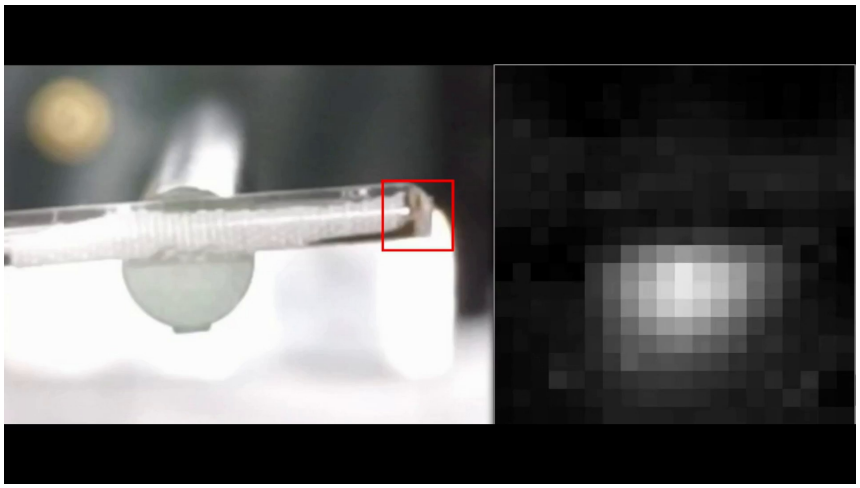

Figure 6.12.: Combined video of the digital camera and maximum intensity xz-projection of the MPI imaging footage (video length: 18 s).

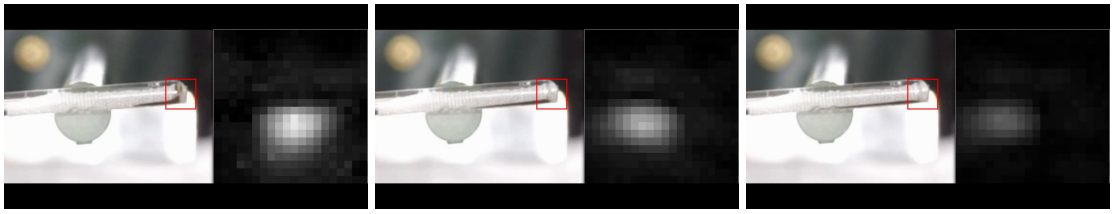

(a) $t_1 = 0\,\mathrm{s}$. (b) $t_2 = 6\,\mathrm{s}$. (c) $t_3 = 12\,\mathrm{s}$.

Figure 6.13.: Snapshots of the combined footage of optical camera and maximum intensity xz-projection of the MPI imaging during the MPIN sequence at different time points a), b) and c).

look, the change between navigation and imaging mode can be identified as the movement is always shortly interrupted for a certain time. The magnetic particles gain velocity as they are moved further away from the FFP. Furthermore, the acceleration increases with increasing distance to the FFP. Synchronously, at the beginning of the MPI video sequence a high concentration of particles is visible as the images show high pixel intensities at the right side of the tube. The intensities within the MPI images is reduced over time because more particles have been moved outside the FoV to the other side of the tube. The sum of all intensity values, that are within the FoV, is shown as function over time in Fig. 6.14.

6.3.4. MPN against gravity through vertical bifurcation junction

The second proof of concept MPIN experiment the results is again recorded with a camera. In this case only the footage of the camera is shown in video 6.15 because the images from the imaging sequence revealed no useful results. Nevertheless, the movement of the particles can be clearly seen in the video. As the MPIN sequence starts, the particles are

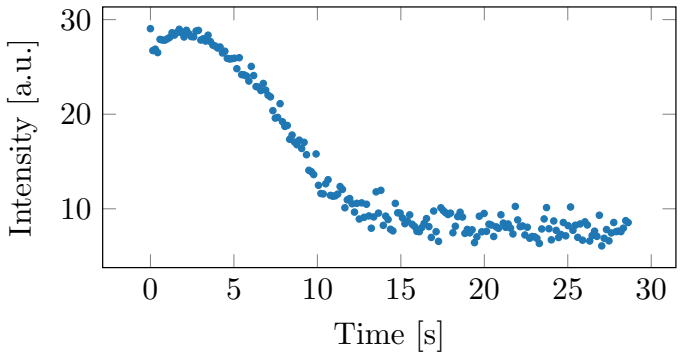

Figure 6.14.: Intensity changes over time for all voxels within the FoV.

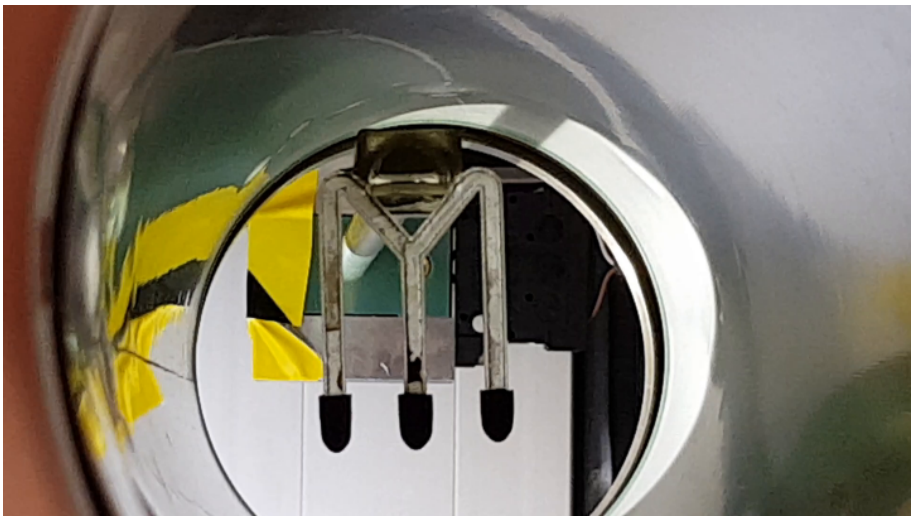

Figure 6.15.: Upward movement of particles on the left side against gravity. The movement and velocity increase when the particle particle move further up since the magnetic force increases linear with the distance from the FFP (video length: $80\,\mathrm{s}$).

moved up and down in the frequency of the alternating imaging and navigation mode. The particles are pushed to the left side because a magnetic force is induced as the FFP is positioned in the down right position. In the course of the MPIN measurement, the particles start to climb up the tube on the left side in small steps. The particles are pumped up slowly against the gravity on the left side of the tube into the left branch of the bifurcation. During the imaging phase the particles are dropping slightly back down as the gravity pulls them downwards. However, as the particles are moved further up the tube, their velocity increases because the magnetic force increases linearly with distance to the FFP. The experiment works as well for the right side, but only result pushing particles to the left branch of the bifurcation are presented. Further, snapshots of three different time points are presented in Fig. 6.16. In these snapshots a large chunk of particles (red circle) is visible. Based on this chunk an average velocity of $8\,\mathrm{mm\,s^{-1}}$ can be estimated as the particles moved over $24\,\mathrm{mm}$ in $3\,\mathrm{s}$. To analyze the entire movement of the particles with up and down movement, the chunk of particles is identified in every frame of the

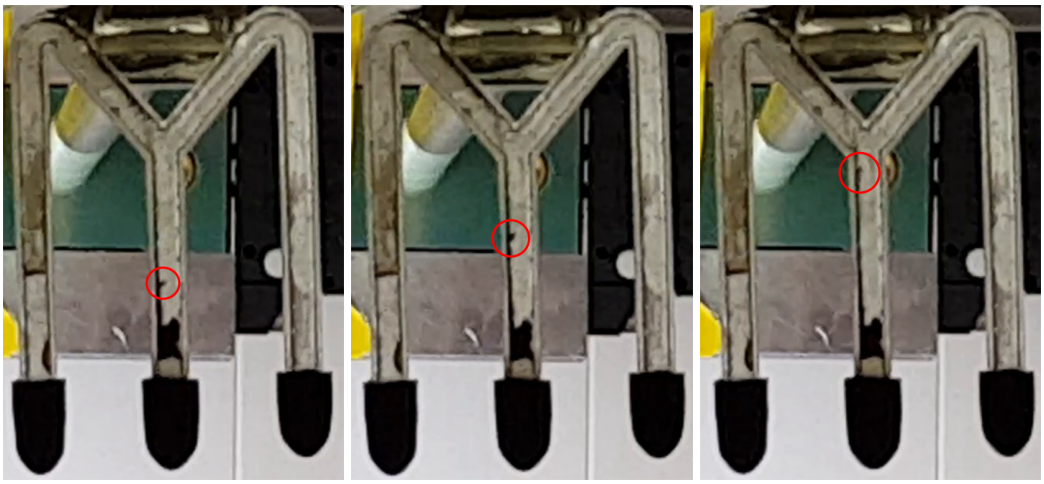

(a) $t_1 = 0.46\,\mathrm{s}$. (b) $t_2 = 0.86\,\mathrm{s}$. (c) $t_3 = 1.36\,\mathrm{s}$.

Figure 6.16.: Upward movement of particles at a) $t_1 = 0.46\,\mathrm{s}$ b) $t_2 = 0.86\,\mathrm{s}$ and c) $t_3 = 1.36\,\mathrm{s}$ on the left side against gravity. A large chunk of particles is highlighted with a red circle.

video 6.15. The position of the chuck is determined manually by identifying the pixel position in the every frame. With the help of the known distance of the phantom and the video frame rate of $30\,\mathrm{Hz}$, the distance in dependence of time is plotted in the upper graph in Fig. 6.17.

These graphs illustrate the up and down movement of the particles quite well. In the distance-time graph, the alternating imaging and navigation mode phase can be identified clearly. During the imaging phase, the movement in z stagnates, while during the navigation phase, the distance increases. By being further away from the FFP, the stagnation becomes less and lesser during the imaging phase, while the distance in z increases even steeper and steeper during the force phases. In addition, the development of the velocity over time can be seen in the middle of Fig. 6.17. It shows that the velocity alternates with the frequency of the changing imaging and navigation mode, but increases in a general trend over the whole measurement time. A similar behavior can be identified in the acceleration over time, where the acceleration alternates as the switching magnetic fields but increases in magnitude slowly over time. The general behavior of the particle movement corresponds with the theoretical force Eq. (2.49) from section 2.6.

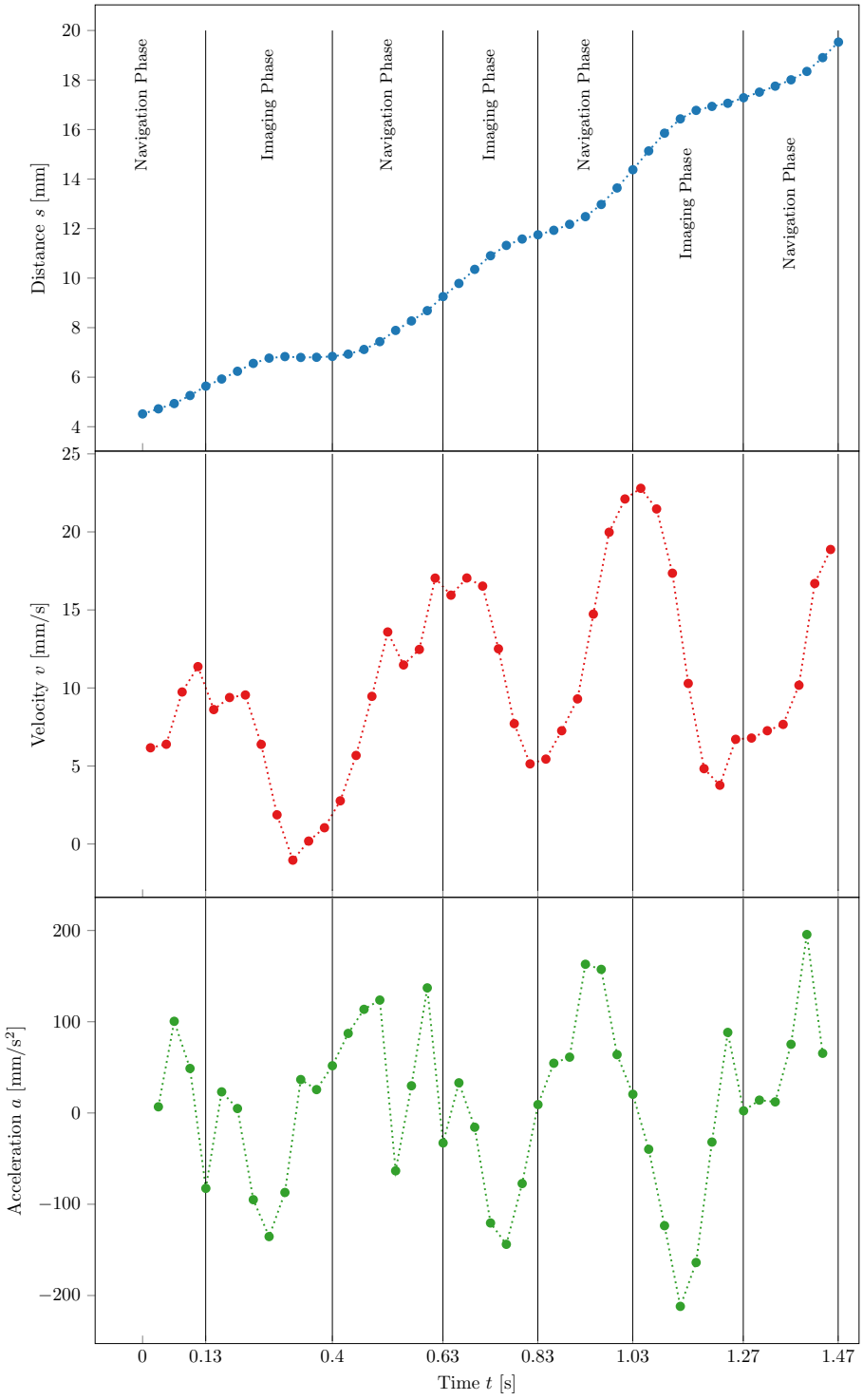

Figure 6.17.: The distance time graph of the movement of the particles at the side of the phantom (top) and its velocity time diagram (middle). The acceleration time graph (bottom) reflects the switching magnetic navigation and imaging mode. During the magnetic force phase the particles are accelerated and during the imaging phase the particles are decelerated due to gravity. Due to the ratio of 4:1, the acceleration phase is longer.

6.3.5. MPN in flow within bifurcation junction

The results for the MPN bifurcation flow experiments in the xy-plane are presented in videos. A summary of the videos of the flow experiments is given in Table 6.6 with video reference, flow velocity parameters for inbound and outbound bifurcation branches, left or right bifurcation and description.

Table 6.6.: Summary of videos for bifurcation flow experiments in xy-plane and their control measurements for five different flow velocities.

Video ref	Flow velocity inbound / outbound [ml/s]	Bifurcation side	Description of results
v1.1.0R	2.72 / 1.36	right	Particles flow only through the right branch
v1.1.1R	2.72 / 1.36	right	Control No Force: Particles flow through both branches equally
v1.1.0L	2.72 / 1.36	left	Particles flow only through the left branch
v1.1.1L	2.72 / 1.36	left	Control No Force: Particles flow through both branches equally
v1.2.0L	5.45 / 2.72	left	Particles flow only through the left branch
v.1.2.1L*	5.45 / 2.72	left	Control No Force: Particles flow through both branches equally
v1.3.0L	6.87 / 3.40	left	Particles flow only through the left branch
v1.3.1L	6.87 / 3.40	left	Control No Force: Particles flow through both branches equally
v1.4.0L	8.18 / 4.09	left	Particles flow mainly through the left branch, depending on injection pressure
v1.4.1L	8.18 / 4.09	left	Control No Force: Particles flow through both branches equally
v1.5.0L	10.22 / 5.11	left	Effect still visible but, due to the high flow velocity, not all particles are navigated to the left.

* video broken

Overall, the magnetic forces from the FFP move the particles to one branch of the bifurcation for flow velocities up to $8.18\,\mathrm{mL\,s^{-1}}$ in the inbound branch. The MPN method works for both branches of the bifurcation, because the FFP can be shifted to both sides. The control experiments validate that the particles flow equally through both branches. The bias for one direction is negligibly low. At the flow velocity $10.22\,\mathrm{mL\,s^{-1}}$ inbound, the majority of particles are moved to the left branch. The other particles flow too fast

through the navigation window and travel with the current in the right branch. As an

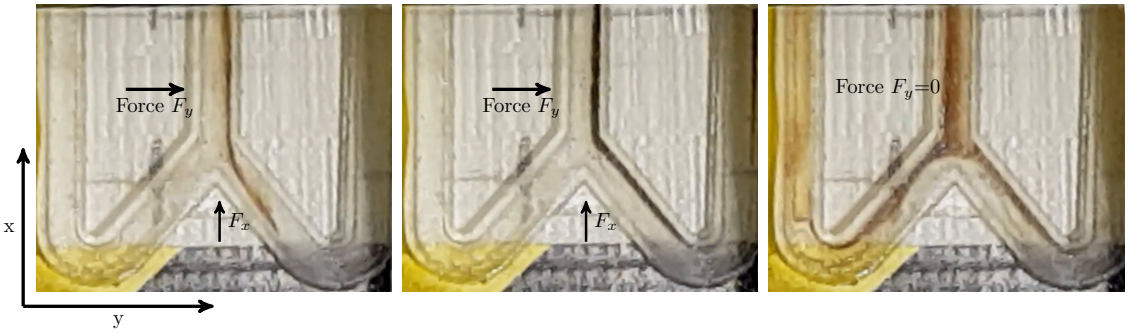

(a) $F_y > 0$, no stenosis, flow velocity $2.72\,\mathrm{mL\,s^{-1}}$.

(b) $F_y > 0$, no stenosis, flow velocity $2.72\,\mathrm{mL\,s^{-1}}$.

(c) Control: $F_y = 0$, no stenosis, flow velocity $2.72\,\mathrm{mL\,s^{-1}}$.

Figure 6.18.: a) First time point in the flow experiment with magnetic forces applied in the x and y directions and a flow velocity of $2.72\,\mathrm{mL\,s^{-1}}$. The particles are injected centrically in the inbound branch and flow through the right branch of the bifurcation. (b) Second time point where particles are injected centrically in the inbound branch and pushed to the right side. Some particles remain motionless at the side, as long as the magnetic fields are switched on. c) Control experiment, where the magnetic forces are switched off. The particles are flowing equally through both bifurcation branches.

examples, two time points during the injection of particles are presented for the flow velocity $2.72\,\mathrm{mL\,s^{-1}}$ inbound in Fig. 6.18a and Fig. 6.18b. As the particles are always injected centrically, the particles are pushed to the right side. Afterwards, they enter the right branch (see in Fig. 6.18a). At the second time point, the particles also enter the right branch but they remain on the right side despite the flow. These particles stay motionless at the right side, as shown in Fig. 6.18b, as long as the magnetic field is turned on. After the magnetic fields are switched off, the particles are carried away by the outbound flow. In the control experiment with force $F_y = 0$ (see Fig. 6.18c), the particles interfuse with water. They are distributed equally towards both branches of the bifurcation. As examples, the videos v1.1.0R and v1.1.1R are shown in Fig. 6.19. The particles are successfully navigated towards one of the bifurcation branches with a maximal flow velocity of $8.18\,\mathrm{mL\,s^{-1}}$. The video of this experiment can be seen in Fig. 6.20a. In the control experiment shown in Fig. 6.20b with no force acting on the particles, the particles are distributed equally to both branches of the bifurcation. The particles are only stopped at the side of the inbound tube at the flow velocity $2.72\,\mathrm{mL\,s^{-1}}$. However, this effect can not be observed at higher flow velocities.

Flow analysis with bifurcation and 60%/100% stenosis

Additional flow experiments are performed using a bifurcation phantom with a 60% stenosis in the right branch. These experiments are conducted using four different flow velocities. In general, it is possible to navigate the particles to the right branch for all

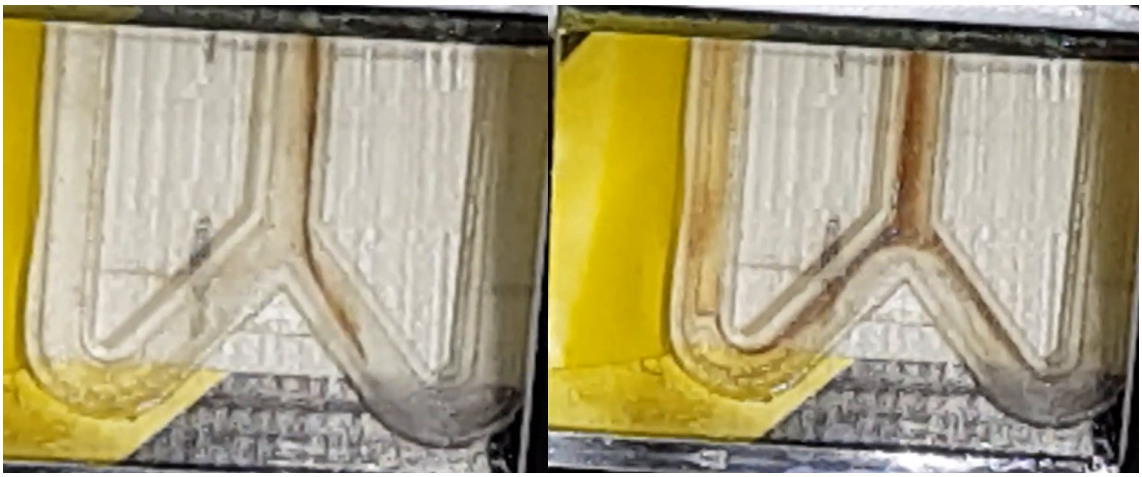

a) v1.1.0R. b) v1.1.1R.

Figure 6.19.: (a) During the MPN experiment at flow velocity $2.72\,\mathrm{mL\,s^{-1}}$the particles are moved into the right branch and some particles are stopped at right side of the tube (video length: 73 s). (b) In the control experiment at flow velocity $2.72\,\mathrm{mL\,s^{-1}}$ all particles flow equally through both bifurcation branches (video length: 21 s).

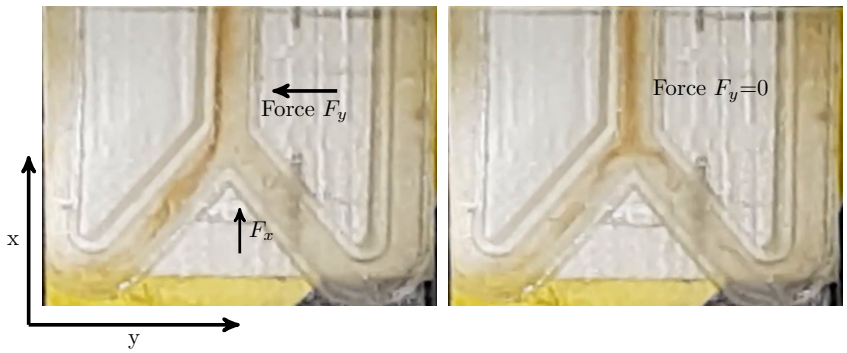

(a) $F_y > 0$, no stenosis, flow velocity $8.18\,\mathrm{mL\,s^{-1}}$.

(b) Control: $F_y = 0$, no stenosis, flow velocity $8.18\,\mathrm{mL\,s^{-1}}$.

Figure 6.20.: (a) The particles are completely moved to the left branch of the bifurcation at a flow velocity of $8.18\,\mathrm{mL\,s^{-1}}$. (b) When the magnetic fields are switches off in the control experiment, the particles distribute equally to both branches at a flow velocity of $8.18\,\mathrm{mL\,s^{-1}}$.

velocities up to $6.87\,\mathrm{mL\,s^{-1}}$. However, all particles flow through the left branch in the control experiments. This can be explained by the changed flow behavior in the left branch that is caused by the 60% stenosis. At a flow velocity of $8.18\,\mathrm{mL\,s^{-1}}$, the particles flow through both branches, the left and right branch. The video references of the 60% stenosis experiments and their control experiments for four different velocities are presented in Table 6.7. The description of the results is given in Table 6.7. A snapshot of the 60% stenosis experiment is illustrated for flow velocity $6.87\,\mathrm{mL\,s^{-1}}$ in Fig. 6.21a. It shows that the magnetic force moves the particles through the bifurcation branch of the stenosis, although the flow velocity is reduced in that branch. The control experiment

Table 6.7.: Video for 60% stenosis experiments and their controls experiments for four flow velocities.

Video ref	Flow velocity inbound/ outbound [ml/s]	Bifurcation Bifurcation	Description of results
v2.1.0R	2.72 / 1.36	right	Particles flow only through stenosis in right branch
v2.1.1R	2.72 / 1.36	right	Control: Particles flow mainly through left branch
v2.2.0R	5.45 / 2.72	right	Particles flow only through stenosis in right branch
v2.2.1R	5.45 / 2.72	right	Control: Particles flow mainly through left branch
v2.3.0R	6.87 / 3.40	right	Particles flow mostly through stenosis in right branch
v2.3.1R	6.87 / 3.40	right	Control: Particles flow mainly through left branch
v2.4.0R	8.18 / 4.09	right	Particles flow through left branch and stenosis in right branch
v2.4.1R	8.18 / 4.09	right	Control: Particles flow mainly through left branch

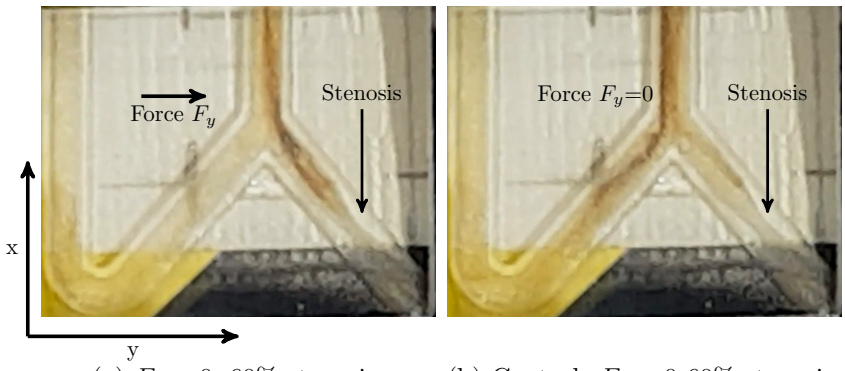

(a) $F_y > 0$, 60% stenosis, flow velocity $6.87\,\mathrm{mL\,s^{-1}}$.

(b) Control: $F_y = 0$ 60% stenosis, flow velocity $6.87\,\mathrm{mL\,s^{-1}}$.

Figure 6.21.: (a) The particles are pushed into the right branch containing the 60% stenosis at a flow velocity of $6.87\,\mathrm{mL\,s^{-1}}$. In the control experiment at a flow velocity of $6.87\,\mathrm{mL\,s^{-1}}$ the majority of the particles flows through the left branch and only a small amount enters the right branch with the stenosis.

underlines that more particles flow through the left side with no stenosis (see Fig. 6.21b). The videos for these experiments are shown in Fig. 6.22. The results of the experiments conducted using the bifurcation phantom with a 100% stenosis in the right branch are presented in Fig. 6.23. In Fig. 6.23a and Fig. 6.23b, the flow velocity is $1.36\,\mathrm{mL\,s^{-1}}$, whereas it is $2.72\,\mathrm{mL\,s^{-1}}$ for the images in Fig. 6.23c and Fig. 6.23d. Even though the flow velocity inside the right branch is zero due to the full blockage, the magnetic force

(a) v2.3.0R. (b) v2.3.1R.

Figure 6.22.: (a) During the MPN experiment at flow velocity $6.87\,\mathrm{mL\,s^{-1}}$ the particles are moved into the right branch with the 60% stenosis (video length: $12\,\mathrm{s}$). (b) In the control experiment at flow velocity $6.87\,\mathrm{mL\,s^{-1}}$ only a small amount enter the 60% stenosis. The majority of the particles enters the left branch with no stenosis (video length: $17\,\mathrm{s}$).

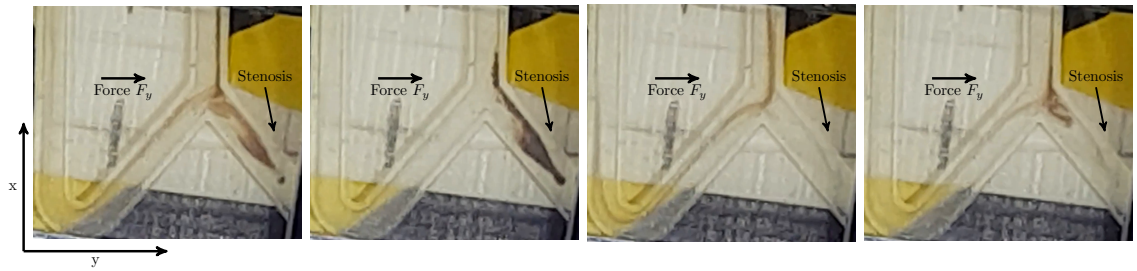

(a) 100% stenosis, flow velocity $1.36\,\mathrm{mL\,s^{-1}}$, $t_1 = 5\,\mathrm{s}$.

(b) 100% stenosis, flow velocity $1.36\,\mathrm{mL\,s^{-1}}$, $t_2 = 45\,\mathrm{s}$.

(c) 100% stenosis, flow velocity $2.72\,\mathrm{mL\,s^{-1}}$, $t_1 = 16\,\mathrm{s}$.

(d) 100% stenosis, flow velocity $2.72\,\mathrm{mL\,s^{-1}}$, $t_2 = 18\,\mathrm{s}$.

Figure 6.23.: (a) and (b) Most of the particles accumulate in the 100% stenosis during the flow experiment with flow velocity $1.36\,\mathrm{mL\,s^{-1}}$. (c) and (d) Only a small amount of particles ends up in the 100% stenosis, if the flow velocity is higher than $2.72\,\mathrm{mL\,s^{-1}}$. The majority of the particles are drifted towards the left branch.

is strong enough to navigate the particles towards the right branch into the stenosis for the flow velocity of $1.36\,\mathrm{mL\,s^{-1}}$. In the inbound tube of the phantom, the particles are moved to the right side, but as soon as they reach the inlet of the right branch they turn towards the left branch. The majority of the particles still ends up in the stenosis (see Fig. 6.23a and Fig. 6.23b) at a flow velocity of $2.72\,\mathrm{mL\,s^{-1}}$. The movement towards the left branch can be clearly identified in Fig. 6.23c and Fig. 6.23d. In this case, the flow dynamics cause the majority of particles to be pushed away from the inlet of the right branch to the left side. Due to these turbulent whirls, only a small amount of particles ends up at the 100% stenosis. The video references of the 100% stenosis experiments for the two different velocities can be found in Table 6.8 together with its description, while the videos are presented in Fig. 6.24.

Table 6.8.: Videos for 100% stenosis experiments for flow velocities $1.36\,\mathrm{mL\,s^{-1}}$ and $2.72\,\mathrm{mL\,s^{-1}}$.

Video ref	Flow velocity inbound/ outbound [ml/s]	Bifurcation	Description of results
v3.0.0R	1.36 / 1.36	right	Large amount of particles flow to 100% stenosis in right branch
v3.1.0R	2.72 / 2.72	right	Particles flow through left branch. Only a small amount ends up in the 100% stenosis

a) v3.0.0R. b) v3.1.0R.

Figure 6.24.: (a) The majority of particles accumulates in the 100% stenosis during the flow experiment with flow velocity $1.36\,\mathrm{mL\,s^{-1}}$ (video length: $136\,\mathrm{s}$). (b) During the flow experiment with flow velocity $2.72\,\mathrm{mL\,s^{-1}}$ only a small amount of particles ends up in the 100% stenosis. If the flow velocity is higher, most of the particles are bended towards the left branch (video length: $39\,\mathrm{s}$).

6.3.6. Magnetic Particle Imaging

To evaluate the imaging capabilities of the most promising particles, MPI experiments are conducted without MPN. For these experiments, the reconstructed images are presented in Fig. 6.25 and the spatial resolution in terms of the FWHM is determined. For this purpose, delta samples are used in the reconstructed image. In Fig. 6.25a, a reconstructed image of a static delta sample filled with nanomag/synomag-D 333 is presented in the xz-plane. To determine the FWHM of the sample, profiles in the x- and z-directions are determined and visualized (see Fig. 6.25a above and left of the image). The FWHM in the x-direction is $6.7\,\mathrm{mm}$ and in the z-direction it is $2.6\,\mathrm{mm}$. This indicates a higher spatial resolution in the z-direction compared to the x-direction. In Fig. 6.25b, the reconstructed image for the sample with beads is shown in the xz-plane. Their profiles yield a FWHM of $6.3\,\mathrm{mm}$ and $3.0\,\mathrm{mm}$ in the x-direction and the z-direction, respectively (above and left of the image in Fig. 6.25b). The spatial resolution in the x-direction and y-direction is

supposed to be the similar because the gradient strength in the x-direction and y-direction are the same.

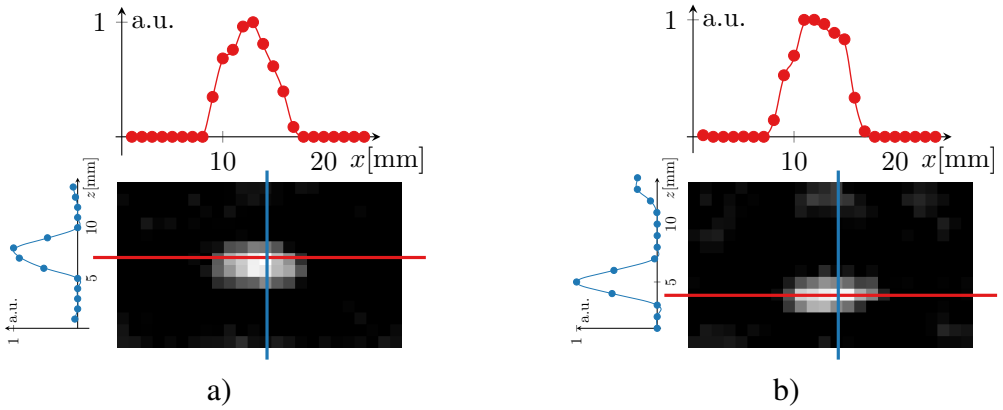

Figure 6.25.: (a) Image of a delta sample filled with MyOne beads in the xz-plane with profile in the x-direction (above) and profile in the z-direction (left). b) Image of delta sample containing nanomag/synomag-D 333 in the xz-plane with profile in the x-direction (above) and profile in the z-direction (left).

6.3.7. Simultaneous MPIN in flow with bifurcation junction

In this flow bifurcation experiment, the imaging and navigation method MPIN is used to navigate the particles towards a 100% stenosis at flow velocity $1.36\,\mathrm{mL\,s^{-1}}$ while the distribution of the particles is imaged (see Fig. 6.26). The induced magnetic force acts sufficiently long enough to move the particles towards the stenosis, despite no force acting on the particles during the short time of the imaging mode. The ratio between navigation cycle is $N_{\mathrm{nc}} = 20$ to the imaging cycles $N_{\mathrm{ic}} = 1$. The particles are pushed towards the

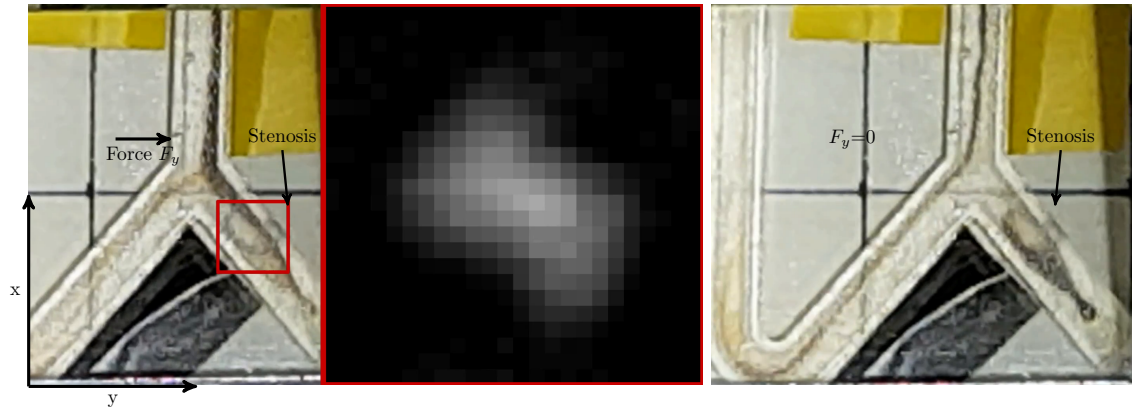

(a) 100% stenosis, flow velocity $1.36\,\mathrm{mL\,s^{-1}}$, MPI image.

(b) F_y=0, 100% stenosis, flow velocity $1.36\,\mathrm{mL\,s^{-1}}$.

Figure 6.26.: (a) The majority of particles is moved into the right branch towards the 100% stenosis at flow velocity $1.36\,\mathrm{mL\,s^{-1}}$ while the distribution of the particles is imaged by MPI. (b) In the control experiment, all particles flow through the left branch.

right branch of the bifurcation. Quasi-simultaneously, the intensities within the MPI image are increased as the particles enter the right branch (see Fig. 6.27). They are pushed into the 100% stenosis (see Fig. 6.26a). In the control experiment afterwards, presented in Fig. 6.26b, the particles are flowing entirely through the left branch of the bifurcation. The videos can be found in Fig. 6.27 and their references are given in Table 6.9 with descriptions of the results.

Table 6.9.: Videos for 100% stenosis experiments for flow velocity $1.36\,\mathrm{mL\,s^{-1}}$. Additionally, snapshots are taking within the imaging cycle.

Video ref	Flow velocity inbound/ outbound [ml/s]	Bifurcation	Description of results
v4.0.0R	1.36 / 1.36	right	Large amount of particles flow to 100% stenosis in right branch
v4.0.1R	1.36 / 1.36	right	Control: With no force, all particles flow through left branch

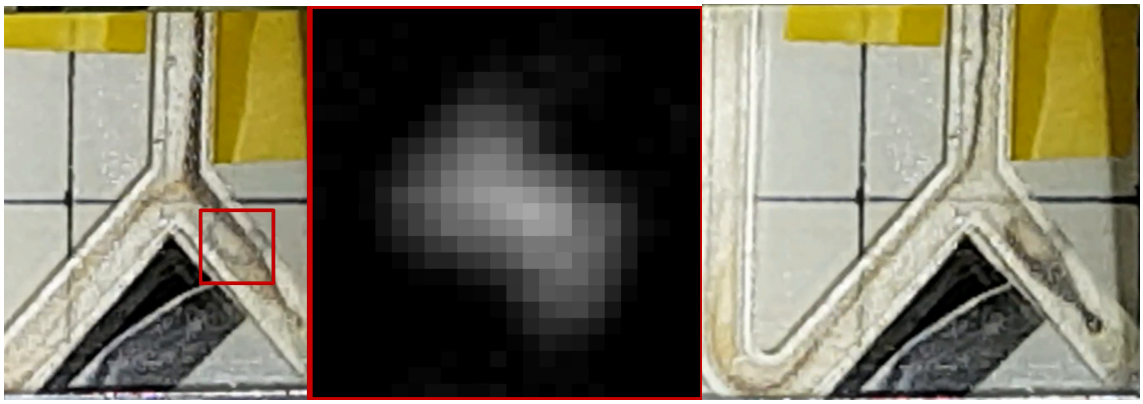

a) v4.0.0R. b) v4.0.1R.

Figure 6.27.: (a) At flow velocity $1.36\,\mathrm{mL\,s^{-1}}$ the majority of particles is maneuvered into the right branch towards the 100% stenosis. Parallel, the distribution of the particles is imaged by MPI during the imaging cycles (video length: $60\,\mathrm{s}$). (b) In the control experiment afterwards all particles are flowing through the left branch of the bifurcation (video length: $20\,\mathrm{s}$).

6.4. Discussion

The results from the MPS measurements demonstrate that nanomag/synomag-D 333 particles provide the best compromise between imaging abilities and magnetic mobility of all analyzed nanomag/synomag-D particles. In the spectrum of nanomag/synomag-D 333, particles 35 harmonics above the noise level can be identified, which is sufficient for MPI

imaging. The imaging performance of Dynabeads MyOne particles is a little inferior, but the spectrum shows enough harmonics for MPI imaging. The imaging properties, in terms of the spectra of both particle types, are not strongly affected by magnetizing or vertexing. Therefore, both particle types indicate only a negligible remaining remanence. The nanomag/synomag-D 333 particles show a strong linearity at the intensities of the first five harmonics. The intensities are dependent on the particle concentration. Their regression lines show coefficients of determination of $R = 0.996$ to $R = 0.997$. This linearity is desired for MPI, because the quantification of the particles relies on this linearity [16]. This criterion is also met by the DynaBeads MyOne particles, where the frequency signals show a linear tendency to the iron concentration. However, their coefficients of determination for the regression lines are smaller with $R = 0.971$ to $R = 0.986$. The similar half separation times of the DynaBeads and nanomag/synomag-D batches (333,334) particles imply an equal magnetic mobility for both particle types. The nanomag/synomag-D 333 batch is therefore suitable for magnetic navigation. Additionally, the batch has shown the most promising imaging abilities for MPI since it generates the most harmonics above the noise level. In contrast to the nanomag/synomag-D 333 particles, the analyzed polystyrene Dynabeads MyOne particles are not biodegradable, thus they are not suitable for human use. The nanomag/synomag-D particles do have a biocompatible coating layer. They can be resolved in the liver and are therefore much more suited for human use. In conclusion, the nanomag/synomag-D 333 particles are used for further MPN bifurcation flow and MPIN flow bifurcation experiments because they show a better performance in imaging, have a similar half time separation and are biocompatible.

The first proof of concept experiment shows the feasibility to navigate magnetic particles with the magnetic forces of the used MPI scanner. At the same time, the distribution of the particles is imaged. The magnetic force is sufficiently strong to overcome the friction of the particles at the bottom of the tube. Further, the magnetic force overcomes the drag force induced by the water. As the particles are still accelerated at the far left of the tube (see Fig. 6.12), it can be concluded that a balance between magnetic force and drag force has not been reach yet. Otherwise, the particles would travel with a constant velocity, after they have been accelerated shortly. The visual movement of the particles indicates an exponential behavior stated by Eq. (6.20).

The results from the second proof of concept experiments demonstrate that the magnetic force of the MPI scanner is even strong enough to overcome the gravitational force in addition to the drag force. Further, the particles are directed towards one branch of the bifurcation by magnetic forces in the y-direction. Unfortunately, the MPI imaging during the imaging cycles of the MPIN method yielded only noisy images, probably due to complications with the focus fields in the z-direction of the MPI scanner during that time. Overall, the movement of the particles shows an exponential behavior, but not as clearly as in the first experiment. The magnetic force, the drag force and the gravity are probably

quite close to an equilibrium that would result in a constant velocity. During the imaging cycles, the particles are dropping down. Here, the gravity pulls them down again but the time span, in which the particles descend, becomes shorter as the particles are moved further up. This can be explained by the increased distance to the FFP and the associated increase of the magnetic force. A detailed analysis of the differential equation involving all force and the switching of the magnetic force could verify the particle behavior with the theory.

The results of the MPN experiments show that nanomag/synomag-D 333 particles can be maneuvered to one branch of the bifurcation within a liquid medium flowing with a flow velocity of up to $8.18\,\mathrm{mL\,s^{-1}}$ ($652.1\,\mathrm{mm\,s^{-1}}$). The rectangular cross-section $A_{\text{exp}} = (3.544\,\mathrm{mm})^2 = 12.5\,\mathrm{mm}^2$ of the phantom corresponds to a cross-section of a circular vessel with diameter of $4\,\mathrm{mm}$. For the internal carotid artery with a circular diameter of about $5\,\mathrm{mm}$ [198], a flow velocity of $4.58\,\mathrm{mL\,s^{-1}}$ ($233.2\,\mathrm{mm\,s^{-1}}$) is stated in [199]. Therefore, it is auspicious to analyze MPIN under more realistic circumstances, e.g. blood circulation.

It is possible that the effect of the magnetic navigation could be a little bit stronger in more realistic conditions, because the heart pumps with a frequency of about $60\,\mathrm{Hz}$, whereas the peristaltic pump produces a constant volume current. During diastole, the flow volume is noticeably lower. During that time, the magnetic force has more time to maneuver the particles in the wanted direction. Under these conditions, it could be possible to navigate particles from the aorta into the common carotid artery.

For a flow velocity of $2.72\,\mathrm{mL\,s^{-1}}$ ($217\,\mathrm{mm\,s^{-1}}$), the results demonstrate that particles can be stopped by pressing them against the side wall of the phantom. The reduced flow velocity profile close to the side and the friction at the border are probably responsible for this effect. These findings could increase the prospect for TDD applications in small arteries. Here, the effect of the drug could be amplified. The effect can be further analyzed by trying to stop particles against the flow direction explicitly. However, it has also to be considered that the functionalization of the particles would increase the hydrodynamic radius. In general, that depends on the type of drug and would only add a layer of about $10\,\mathrm{nm}$ to $20\,\mathrm{nm}$. Nevertheless, an increased hydrodynamic radius would reduce the navigation capabilities by the magnetic force. Consequently, the limiting flow velocity would be decreased.

Further, the flow bifurcation experiment with a stenosis of 60% demonstrate that the nanomag/synomag-D 333 particles can be moved to one side of a bifurcation up to a flow velocity of $6.87\,\mathrm{mL\,s^{-1}}$ ($546.6\,\mathrm{mm\,s^{-1}}$). Due to increased flow resistance in the bifurcation branch of the 60% stenosis, a larger portion of the volume prefers to flow through side without a stenosis. Therefore, it becomes more challenging to maneuver the particles through the stenosis under these circumstances. If the stenosis in one branch is a 100% stenosis, the particles can still be magnetically forced towards the stenosis at a

maximal flow velocity of $1.36\,\mathrm{mL\,s^{-1}}$ ($108.2\,\mathrm{mm\,s^{-1}}$). With these results, a blood clot in a medium-sized artery could be resolved in a stenosis. Thus, drug-loaded particles could clear the blockages. The drug is normally injected intravenously and would hardly reach the stenosis under these circumstances. Therefore, even if a small dose of particles loaded with tissue plasminogen activator (tPA) reaches the blood clot at the stenosis, the dissolution would benefit highly. Both particle types demonstrate that their MPI signal is sufficient enough to reconstruct an image. However, the spatial resolutions, in terms of FWHM in the x-direction at $6.7\,\mathrm{mm}$ and $2.6\,\mathrm{mm}$ in the z-direction for Dynabeads MyOne particles, are not as great as dedicated imaging particles. Several groups achieved spatial resolutions in the sub-millimeter range [26, 20, 25]. For nanomag/synomag-D 333 particles the spatial resolutions in terms of FWHM in the x-direction at $6.3\,\mathrm{mm}$ and $3.0\,\mathrm{mm}$ in the z-direction, are comparable to ones of Dynabeads MyOne particles. Finally, the results of the MPIN studies show that particles can be controlled and imaged through a bifurcation at a flow velocity of $1.36\,\mathrm{mL\,s^{-1}}$ ($108.2\,\mathrm{mm\,s^{-1}}$) quasi-simultaneously. Even when one branch is 100% blocked, the particles are navigated through a bifurcation towards the 100% stenosis branch. It can be challenging to move the particles to towards the 100% stenosis (see video v4.0.0R) because the total blockage leads to a high resistance. Consequently, turbulances occur at the boundary surface of the bifurcation. Further, the particles are pulled out of the stenosis back into the flowing current due to negative pressure generated by the flowing water. The ratio between navigation and imaging is set to 20 to 1. This results in an imaging rate of $2.15\,\mathrm{s}$ per image in which the position of the particles can be identified. Regrading an improvement of the experiments, the limiting flow velocity of $1.36\,\mathrm{mL\,s^{-1}}$ ($108.2\,\mathrm{mm\,s^{-1}}$) could be increased by stronger gradient fields. By this means, a greater force could be induced on the particles. However, such an upgrade can not be easily implemented in the commerical system used for these experiments. Nevertheless, it could be introduced in a custom built human scanner [66, C7]. Then, stronger additional magnetic fields could use the MPIN method for human brain applications.

In conclusion, it has been demonstrated that the nanomag/synomag-D 333 particles provide a good compromise between magnetic mobility and imaging performance for MPI. Further, it has been shown that these particles can be maneuvered within a volume flow with flow velocity of up to $8.18\,\mathrm{mL\,s^{-1}}$ ($652.1\,\mathrm{mm\,s^{-1}}$). The particles have been moved towards one side of a bifurcation by using the MPN method of an MPI scanner. In addition, the MPIN method has been successfully utilized to navigate particles towards a 100% stenosis within a bifurcation. During that movement the particles' distribution is imaged in the stenosis every $2.15\,\mathrm{s}$ at a flow velocity of $1.36\,\mathrm{mL\,s^{-1}}$ ($108.2\,\mathrm{mm\,s^{-1}}$). In further experiments, magnetic particles attached with a tPA could be used to dissolve blood clots in hard-to-reach locations, while monitoring the liquidation of the clot with MPIN.

7. Orientation as MPI Contrast

Contents

7.1. Introduction and motivation

The magnetic response of SPIONs to an oscillating magnetic field is composed by a mixture of Néel rotation and Brownian rotation [95]. As stated in section 2.1.1, the Néel rotation reorients the magnetic moment internally, while the Brownian rotation reorients the particle itself. Whether Néel rotation or Brownian rotation dominates is usually dependent on the particle size, excitation frequency and mobilization state. When the SPIONs are immobilized, Néel rotation dominates the relaxation process, because the particles can no longer rotate themselves freely. This characteristic can be utilized as an MPI contrast and is described in the multi-contrast section 2.5.3. So far, a contrast between mobilized and immobilized SPIONs has been established. Lately, however, it has been demonstrated that the alignment of the magnetic easy-axis also influences the relaxation dynamics of the immobilized particles [132, 207]. When the easy-axis is aligned parallel to the excitation field in immobilized particles, the particles exhibit larger harmonic spectra compared to randomly and perpendicularly oriented immobilized particle. The perpendicularly oriented particles showed the smallest harmonic magnetization spectra of all three. The same effect has been identified for the width of the hysteresis in the magnetization curve. The hysteresis grew from small to large in the order of perpendicularly, randomly to parallelly oriented [132]. The immobilization of the easy-axis is also helpful by modeling

the multi-dimensional excitation patterns of SPIONs [208]. In this chapter, it is investigated whether these findings can be utilized for a novel MPI contrast [C15]. The idea is to estimate the orientation of the easy-axis of immobilized particles in discrete angles. Therefore, different system matrices with delta samples of differently aligned easy-axes are acquired. This novel MPI contrast can be utilized for instrumental MPI applications.

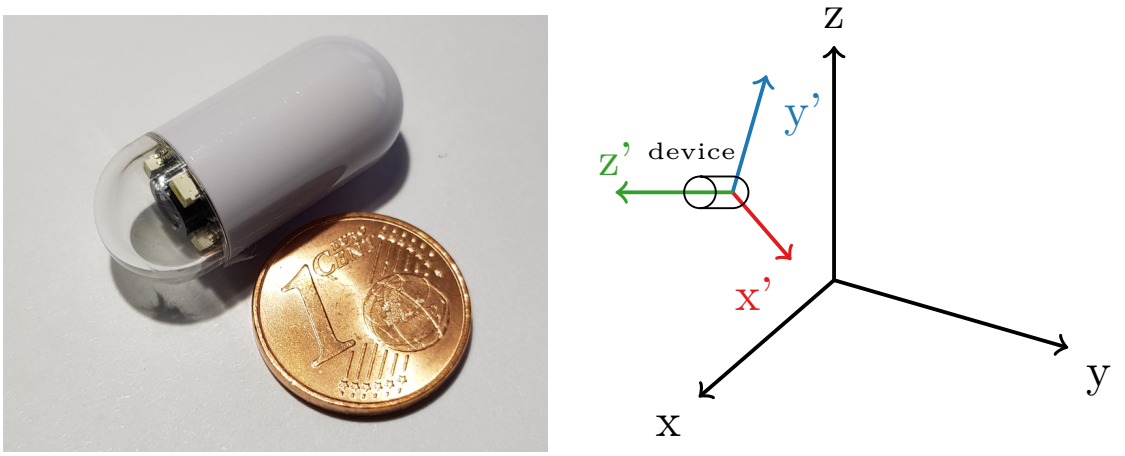

(a) (b)

Figure 7.1.: a) PillCam as an example for magnetic swimmer [65, 66] b) The axis determination could help to identify the position and orientation in 3D of magnetic swimmers within the FoV. Thus, three markers with known immobilized easy-axis would be necessary for the pose determination.

Thus, the easy-axis alignment of the immobilized particles is known within the medical instrument or device. With its help, the axis direction of fiducials (compare section 4.2.2) or the orientation of a catheter could be determined. For an IVOCT catheter (compare section 5.3.4), the rotation could be tracked with an easy-axis alignment marker that is oriented orthogonal to the catheter direction. In Fig. 7.1a, a PillCam (Given Imaging Ltd, Israel) is shown, which illustrates a possible application scenario for the magnetic schwimmers [65, 66]. The easy-axis orientation MPI contrast could play a key role in estimating the 3D orientation of magnetic swimmers with MPI (see Fig. 7.1b).

7.2. Material and methods

Perimag (micromod GmbH, Germany) with an iron concentration of $50\,\mathrm{mmol\,L^{-1}}$ is used as an MPI tracer. For the delta sample and the other three samples, cylindric containers are 3D-printed by the SL printing technique. The samples have a cavity with a radius of $1.7\,\mathrm{mm}$ and a height of $1.5\,\mathrm{mm}$. In these cavities, four immobilized samples are prepared to align the easy-axis of the SPIONs. For the immobilization and alignment of the easy-axis the cavities are filled with dental cement (alginic acid) and mixed with $13.5\,\mu\mathrm{L}$ of perimag. The mixing and curing is performed in the presence of a static homogeneous

magnetic field H_{app} with a strength of $0.18\,\text{T}$ to align the easy-axis of the nanoparticles in the direction of the magnetic field. This easy-axis direction is then fixated by immobilizing the particles within the dental cement. The particles have to be within the homogeneous magnetic field field while the dental cement is curing. Otherwise, they would point in random directions again. For this purpose, a sample holder with two strong magnets in Helmholtz setting is designed and 3D-printed. The direction of the static homogeneous magnetic field is marked on each sample. The sample holder is shown in Fig. 7.2. The

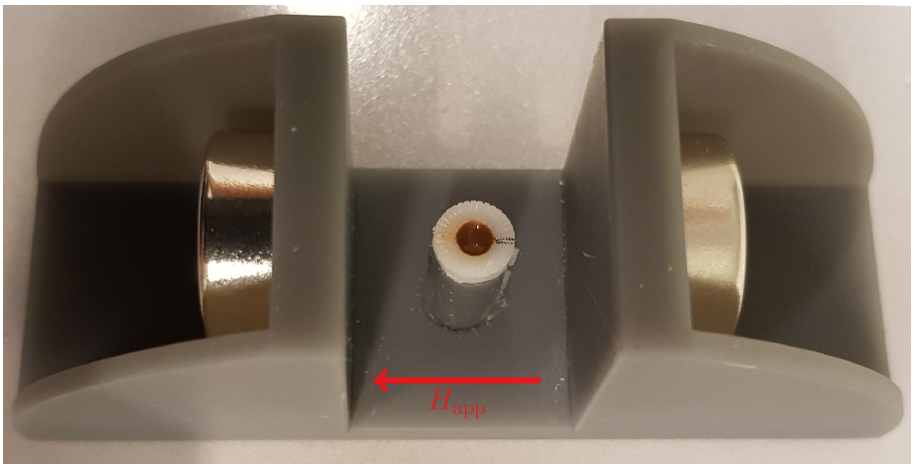

Figure 7.2.: Sample holder to fixate the easy-axis of the samples in a defined direction in dental cement. The homogeneous magnetic field H_{app} has a strength of $0.18\,\text{T}$.

process of fixating the easy-axis in the direction of the static homogeneous magnetic field is illustrated in Fig. 7.3. At first, the particles are oriented randomly within the sam-

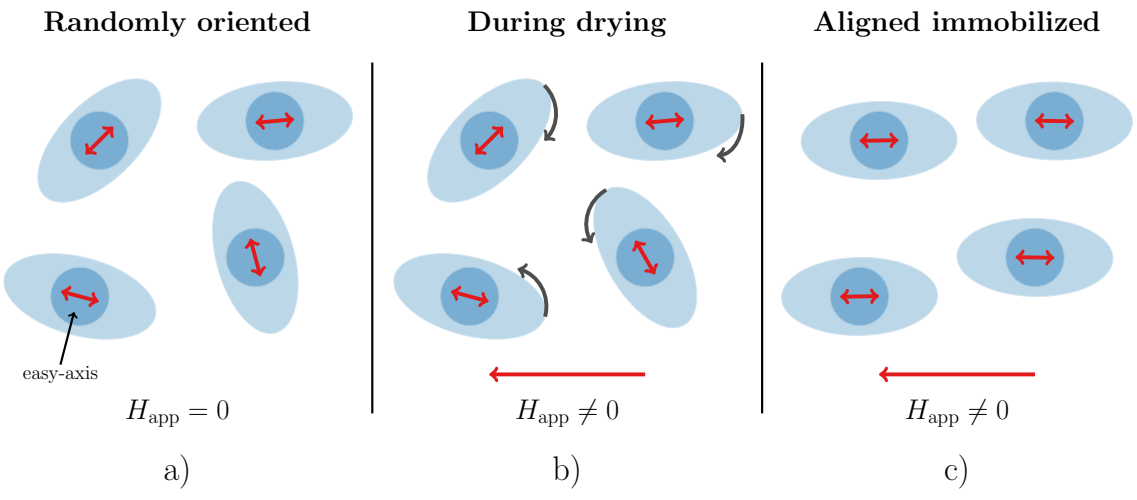

Figure 7.3.: a) The particles are randomly oriented along with their easy-axis. b) The particles undergo Brownian rotation to align their easy-axis with the axis of the homogeneous magnetic field. c) When the dental cement has been cured, the easy-axis direction is fixated within the immobilized particles along the axis of the magnetic field.

ple. Secondly, as a magnetic field with a fixed direction is applied, the particles undergo Brownian rotation until their easy-axis is colinear with the direction of the magnetic field.

Thirdly, as the dental cement is curing, the easy-axis is fixated in the direction of the magnetic field and will not reorient itself again when the magnetic field is removed. It is worth noting that only the easy-axis is fixated, the magnetic moments of the particles are still able to rotate via the Néel rotation in order to follow the oscillating magnetic field.

To acquire system matrices with different angles with respect to the y-axis, a dedicated delta sample holder is constructed. The dedicated delta sample holder enables a manual positioning of the radial container in discrete $10°$ steps. A CAD rendering of the dedicated delta sample holder is shown in Fig. 7.4. Based on the delta sample holder, a phantom

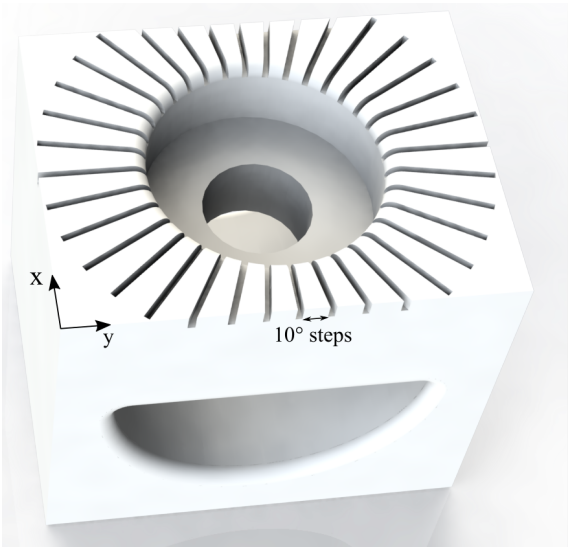

Figure 7.4.: Special delta sample holder with auxiliary lines in steps of $10°$ to adjust the delta samples in different angles with respect to the y-axis.

with three cavities for three samples is constructed and shown in Fig. 7.5. The samples

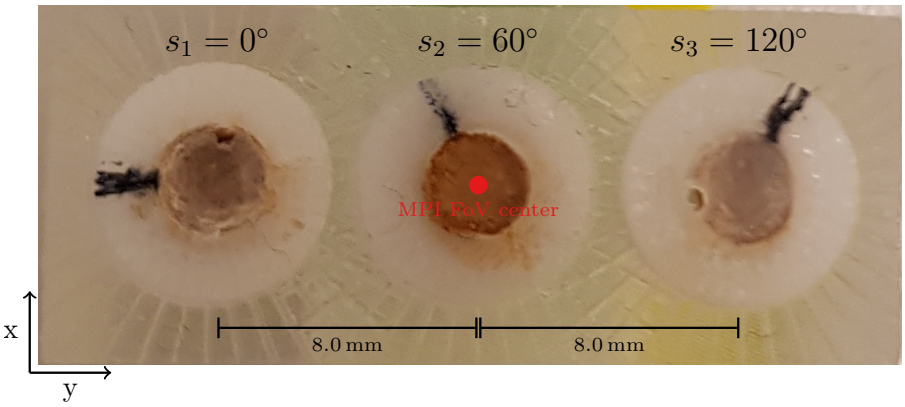

Figure 7.5.: Visualization of the constructed phantom with three samples s_1, s_2 and s_3 with particles immobilized in easy-axis direction $0°$, $60°$, $120°$.

can be rotated freely within the cavities. Therefore, the cavities are equipped with marks in $10°$ angle steps. The cavities are placed inside the MPI scanner aligned to the y-axis. The phantom with cavities s_1, s_2 and s_3 is placed along the y-axis with distances from the

center of $-8\,\mathrm{mm}$, $0\,\mathrm{mm}$, and $8\,\mathrm{mm}$, respectively. In Fig. 7.5, the three samples inside the cavities are oriented in direction $s_1 = 0°$, $s_2 = 60°$, and $s_3 = 120°$ with respect to the y-axis.

7.2.1. MPI parameters and system matrices

The experiments are conducted with the preclinical MPI scanner (see section 2.7.3) set to the gradient strength of $-1.0\,\mathrm{T\,m^{-1}}$ in the x- and the y-directions and $2.0\,\mathrm{T\,m^{-1}}$ in the z-direction. The excitation is performed with 2D Lissajous patterns with excitation frequencies $2.5/99\,\mathrm{MHz}$ and $2.5/102\,\mathrm{MHz}$ in the x- and y-directions, respectively. In this setting, the Lissajous pattern covers a FoV of $24\,\mathrm{mm} \times 24\,\mathrm{mm}$. One Lissajous cycle has a repetition time of $652.8\,\mu\mathrm{s}$. To receive the MPI signal, a gradiometric pickup coil is used [136]. The receive coil is inserted parallel to the x-axis inside the scanner. 18 system matrices with overscan are acquired on a 30×30 pixel grid. The grid covers a FoV of $30\,\mathrm{mm} \times 30\,\mathrm{mm}$. At each position of the grid, 500 MPI Lissajous cycles are averaged to incease the SNR. For each system matrix, the delta sample s_{delta} is rotated in the xy-plane from $0°$ to $340°$ in $20°$ steps with respect to the y-axis.

7.2.2. Periodic fitting

The reconstruction with 18 system matrices results in a multi-channel image with 18 channels. For each channel image, a circular region of interest (ROI) with a radius of 4 voxels is defined. In case of the phantom with three cavities, this is done for each sample position s_1, s_2, and s_3. The intensity signal of the ROI is summed for each channel and each sample position individually. This leads to 18 weights per sample position s_1, s_2, and s_3, where each weight w_{0-340} corresponds to an angle alignment between $0°$ to $340°$. The weights per sample location are then least square fitted with a periodic function

$$w_{s_i}(\alpha_\mathrm{d}) = b_\mathrm{w} \left(\left(\cos\left(\frac{\pi(\alpha_\mathrm{d} - \alpha_\mathrm{e})}{180°} \right) \right)^2 \right)^{c_\mathrm{w}}, \quad i = 1, 2, 3 \tag{7.1}$$

where α_d is the angle in ° of the delta sample, α_e, b_w and c_w are model parameters. The parameter α_e is the estimated angle of the sample. The error of the angle determination is then calculated between the true sample alignment and the estimated angle α_e.

7.2.3. Experiments

After the 18 system matrices are acquired with angles between $0°$ to $340°$ in $20°$ steps, the phantom with three cavities is measured with three samples set to angles of $0°$, $60°$ and $120°$. All of the six possible permutations, as listed in Table 7.1, are measured twice. Each measurement is acquired with 10.000 excitation cycles. The measurements are

Table 7.1.: Permutation of the angles $0°$, $60°$ and $120°$ for all three sample positions s_1, s_2 and s_3.

num	1	2	3	4	5	6
s_1 [°]	0	0	60	60	120	120
s_2 [°]	60	120	0	120	60	0
s_3 [°]	120	60	120	0	0	60

block-averaged with 500 Lissajous cycles. The multi-channel images are reconstructed with the open source reconstruction framework described in [C14, C13]. As reconstruction parameters, an SNR of 3, a relative Tikhonov regularization parameter of 0.01 and 10.000 iteration are chosen. These parameters have been determined heuristically by visual inspection. This yields to a total of 40 18-channel images per angle combination measurement. For the quantitative evaluation, the combination of the angles $0°$, $20°$, $40°$ and $80°$, as listed in Table 7.2, are also measured inside the phantom with three cavities.

Table 7.2.: Two measurements in the angle interval $40°$ and $20°$.

num	1	2
s_1 [°]	80	20
s_2 [°]	0	0
s_3 [°]	40	40

7.3. Results

7.3.1. System matrices

In Fig. 7.6, the frequency component of $90\,\mathrm{kHz}$ is shown for all 18 system matrices acquired from the angle $0°$ to $340°$ in $20°$ steps. The frequency patterns seem to be fringing from $20°$ to $60°$ in every $20°$ step, while the patterns with the same phase are connected diagonally. Between $40°$ and $60°$, a phase shift is visible as the frequency patterns change their color. In these representations of the frequency patterns, the color encodes the phase. Further, the frequency patterns between $100°$ and $160°$ seem to fringe as well but $180°$ shifted to the ones between $20°$ to $60°$. Between $120°$ to $140°$ the phase changes back to the original phase. All frequency patterns look very similar to the frequency patterns from the sample rotated by $180°$ (compare columns in Fig. 7.6). The fringing changes of the frequency patterns and the shift of the phase can be easily identified in the animation provided in Fig. 7.7. The same behavior can be seen in other frequency components.

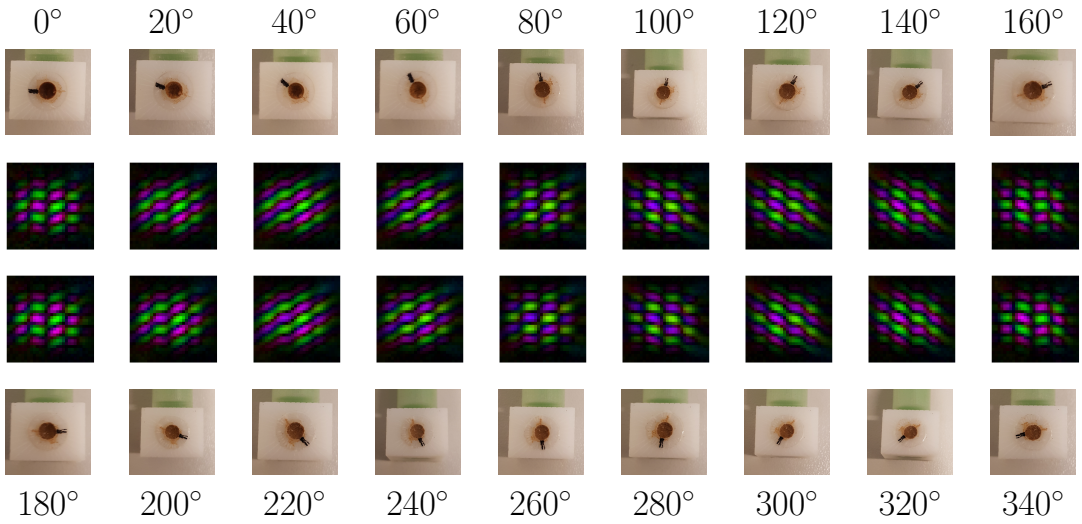

Figure 7.6.: Frequency patterns of frequency component of 90 kHz for all 18 system matrices acquired from the angle 0° to 340° in 20° steps. The phase is encoded within the color of the pattern.

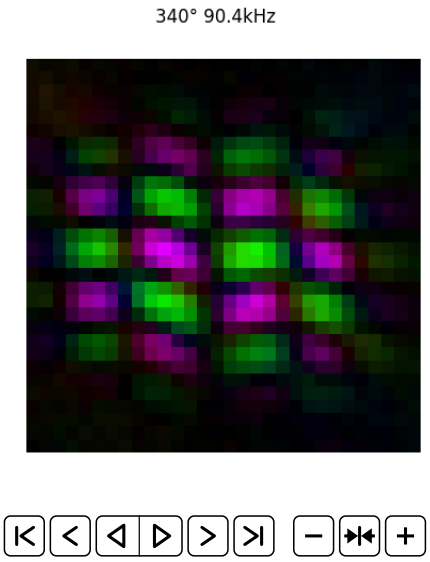

Figure 7.7.: Animation of frequency component 90 kHz of system matrices from the angle 0° to 340° in 20° steps.

7.3.2. Qualitative results

In Fig. 7.8a, the phantom with three cavities is filled with samples in angle positions $s_1 = 0°$, $s_2 = 60°$ and $s_3 = 120°$. This multi-contrast image is only reconstructed with the corresponding three system matrices acquired with angles 0°, 60° and 120°. All three channels are blended, while the first channel with a system matrix acquired with the delta sample at 0° is assigned the red color, the second channel with 60° is assigned green and the third channel with 120° is assigned blue. The different colors indicate that the axis orientation with a maximal spacing of 60° can be clearly discerned from each other. In Fig. 7.8b, the spacing of the axis angles is set to 40° with samples in angle positions $s_1 =$

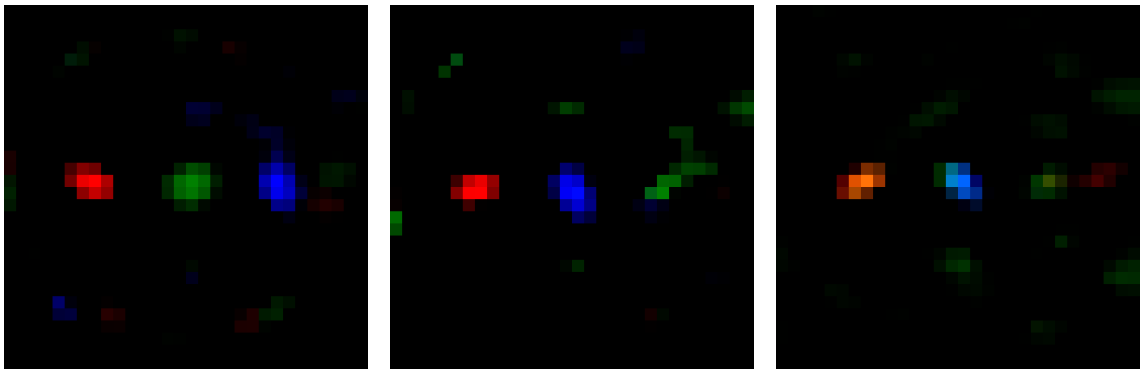

(a) (b) (c)

Figure 7.8.: The samples are measured in a) $s_1 = 0°$, $s_2 = 60°$ and $s_3 = 120°$, b) $s_1 = 80°$, $s_2 = 0°$ and $s_3 = 40°$ and c) $s_1 = 20°$, $s_2 = 0°$ and $s_3 = 40°$ orientation. In each case, the three multi-contrast images are reconstructed with the respective system matrices acquired with that delta sample angle. Afterwards the three multi-contrast images are blended into one image.

$80°$, $s_2 = 0°$ and $s_3 = 40°$. Again, the multi-contrast image is only reconstructed with the corresponding system matrices acquired with delta sample angles $80°$ (red), $0°$ (blue) and $40°$ (green). As the three multi-contrast images are blended, the three samples are still distinguishable, but the quality of the images has dropped especially for the channel with $40°$. In Fig. 7.8c, the angle spacing is further reduced to $20°$. Here, the samples have the angle positions $s_1 = 20°$, $s_2 = 0°$ and $s_3 = 40°$. When the three multi-contrast images from system matrices acquired with delta sample angles $20°$ (red), $0°$ (blue) and $40°$ (green) are blended, the colors red and green at position s_1 are superimposed to orange. Additionally, the blue color at position s_2 appears more light and partly green than in Fig. 7.8a and Fig. 7.8b.

7.3.3. Quantitative error estimation

The weights of the three sample positions are shown for all sample angle combinations (see Table 7.1) in Fig. 7.9a-f. It is worth noting that only the first measurement of the block-averaged measurements are presented. For the statistics, all measurements are evaluated for the alignments $0°$, $60°$ $120°$ and yielded estimation angles of $-8° \pm 6°$, $52° \pm 4°$ and $115° \pm 7°$, respectively. The error plot in Fig. 7.10 shows the absolute error in dependence of the true alignment angle and the sample locations s_1, s_2, and s_3. The absolute error plot indicates that no spatial dependence on the alignment estimation could be identified. For the sample positions s_1, s_2, s_3, the estimation angles are $-5° \pm 7°$, $-8° \pm 6°$, and $-7° \pm 6°$, respectively. Overall, taking all absolute errors from all alignments and location into account, the systematic underestimation of the true alignment is $-7° \pm 6°$. It should be noted that the standard deviation between different measurements is quite high,

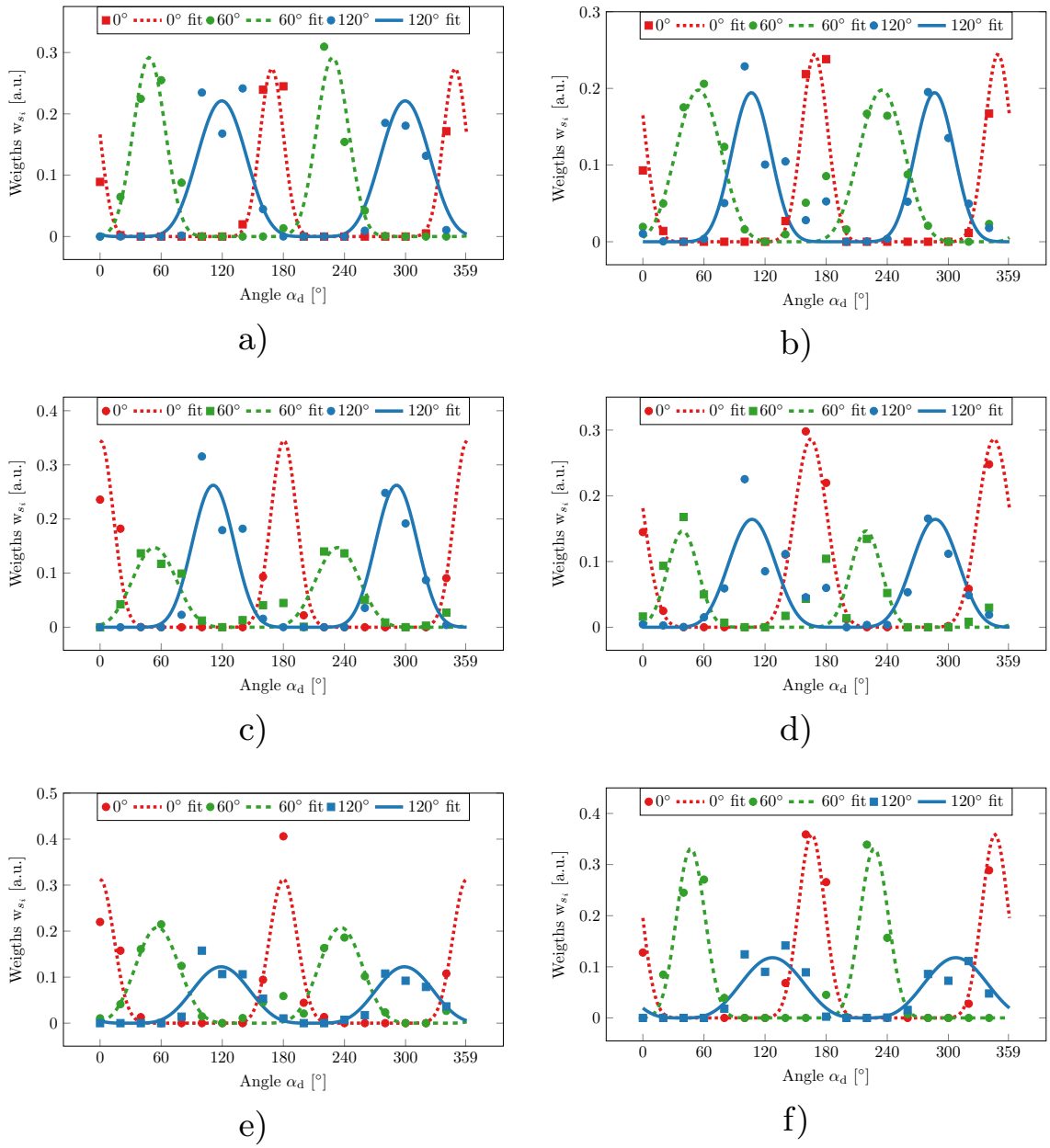

Figure 7.9.: The weights of the three sample positions are presented for the angle combination a) $s_1 = 0°$, $s_2 = 60°$ and $s_3 = 120°$ b) $s_1 = 0°$, $s_2 = 120°$ and $s_3 = 60°$ c) $s_1 = 60°$, $s_2 = 0°$ and $s_3 = 120°$ d) $s_1 = 60°$, $s_2 = 120°$ and $s_3 = 0°$ e) $s_1 = 120°$, $s_2 = 0°$ and $s_3 = 60°$ f) $s_1 = 120°$, $s_2 = 60°$ and $s_3 = 0°$. Only the first of the block-averaged measurements are shown. The estimated angles of alignment are taken from the parameters of the fitting curves (lines).

but within a measurement, the alignment estimates have only a minor standard deviation of below 1°.

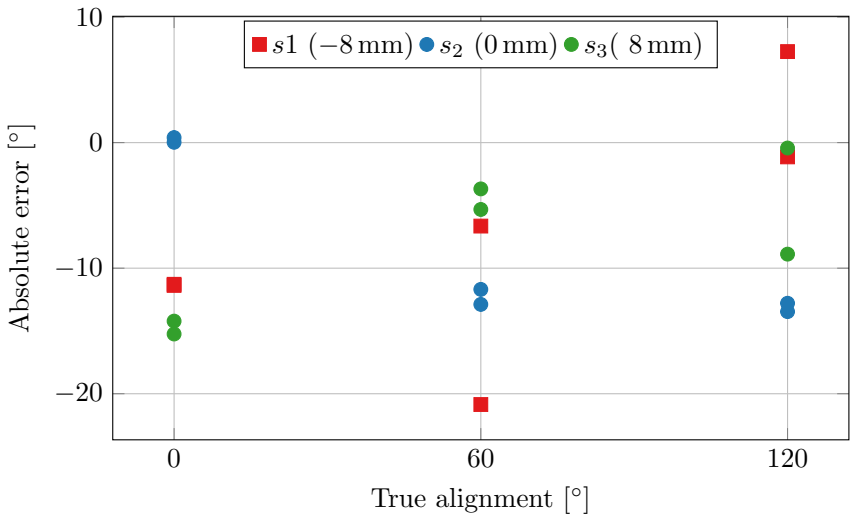

Figure 7.10.: Absolute error in dependence of the spatial locations s_1, s_2 s_3 and the true alignments 0°, 60°, 120°.

7.4. Discussion

The experiments represent a proof of concept that the easy-axis alignment can be used as a novel imaging contrast for multi-contrast MPI. However, the accuracy of the axis estimation could be improved with a more sophisticated experimental setup. The main source of error in these experiments is the manual adjustment of the samples within the cavities. The auxiliary lines are only provided in 10° intervals and the precision relies on the visual inspection of the freely rotatable samples. The impact of this error is even tripled. The sample is aligned manually during the preparation process, the acquisition of the system matrix and during the preparation of the measurement itself. A systematic misalignment of the easy-axis explains most likely the systematic underestimation of the estimated angles. Therefore, the error is mainly dominated by the manual alignment procedure. Although this experimental setup provides a great flexibility, the systematic error could be avoid by fixed sample holders, one for every angle. These need to be constructed for the curing process, the system matrix acquisition and the preparation of the phantoms. Then, by minimizing the systematic error, an accuracy of about 1° could be reached since the spread within one measurement is below 1°. This error will then only be influenced by the noise within the images.

As the MPI signal of the easy-axis alignment is also dependent on the direction of the pickup coils [132], the measurements would benefit from a receive coil arrangement with three receive coils, one in each direction. The presented experiments have only been performed in 2D so far, but the method could be easily expanded to 3D with an orbital easy-axis alignment. In 3D, the easy-axis alignment MPI contrast is suitable to determine the pose of three spherical fiducials, as presented in section 4.2.2. With the easy-axis alignment in three orbital directions perpendicular in x-, y- and z-axis, the sanity check

to identify the spheres labeling could be avoided, since the markers can be identified uniquely. The second application scenario for the easy-axis contrast in 3D could be the orientation determination of catheters and especially their rotation angle in the case of IVOCT catheters (compare section 5.3.4). Three layers of immobilized particles with easy-axis alignments $0°$, $60°$ and $120°$ could be attached to the IVOCT catheter tip orthogonal to the catheter direction. By this means, the rotation could be tracked with three channel multi-contrast information. As a third application, the navigation of medical devices and magnetic swimmers [65, 66] would highly benefit from the pose estimation with the easy-axis contrast. However, the high iteration number of the multi-contrast reconstruction remains a challenge, as it would not be real-time capable in 3D.

In summary, a proof of concept for the novel easy-axis alignment MPI contrast is provided. The alignment of samples is estimated with immobilized SPIONs, which have a fixated easy-axis alignment. The improvement of the experimental setup could yield an angle precision of down to $1°$ for the easy-axis MPI contrast. The easy-axis MPI contrast is a promising method for instrumental MPI applications in 3D, such as fiducials, catheters and magnetic swimmers.

8. Summary and Outlook

Contents

8.1. Summary

MPI shows great potential as a functional imaging modality, but the possible medical application in which MPI can fully exploit its unique strengths has not yet been identified. One strength is that MPI provides radiation free modality based on oscillating magnetic fields. Further, the magnetic particles feature a high contrast as biocompatible tracer. Overall, MPI achieves a high spatial and temporal resolution while providing 3D volume images. In this work, the potential of MPI is investigated for instrumental applications, such as fiducial marker identification, IVOCT catheter tracking, and magnetic navigation. Further, the tracking estimation in MPI is improved with a submillimeter-accurate marker localization. Likewise, MPI is studied in the field of magnetic navigation. In this context, MPI is utilized for TTD with magnetic particles in the application scenario of ischemic stroke. This work shows that it is possible to navigate and image magnetic particles quasi-simultaneously through bifurcations.

In chapter 2, the fundamental principles of MPI were explained. Beginning with the physical response model of the magnetic particles, the signal generation based on oscillating magnetic fields was described. Further, the spatial encoding through a strong gradient field along with the Lissajous sampling trajectory was presented. After the explanation of the image reconstruction process, multi-contrast MPI and magnetic navigation were outlined. Furthermore, the potential of MPI in terms of resolution and sensitivity was discussed in dependence of various MPI parameters. Additional MPI features, such as multi-contrast MPI, were presented along with the joint algebraic reconstruction approach. Finally, the basic theory of how the magnetic field induces a magnetic force on the particles was outlined.

In chapter 3, an algorithm for submillimeter-accurate marker localization was derived. It uses a subvoxel strategy to determine the position of markers in connected-component regions with a center of mass approach. The results showed that positions can be tracked

10-times more accurately for low-gradient MPI images with an precision of about $\pm 0.27\,\mathrm{mm}$ in the x- and y-directions and $\pm 0.12\,\mathrm{mm}$ in the z-direction.

The findings from chapter 3 were exploited in chapter 4, where three fiducial markers can be tracked with submillimeter-accuracy for the registration of sequentially acquired MRI and MPI volumes. Further, the registration workflow was greatly enhanced with the developed mouse bed adapter and the extended online registration software. This facilitated the workflow and handling of preclinical rodent experiments. As an example experiment for the achieved improvements in terms of workflow, registration and fiducials, an inflammation detection in mouse brains with magnetic particles were carried out successfully. The results demonstrated the feasibility to detect brain inflammations with functionalized MPIO particles with MPI.

In chapter 5, the 4D position of an IVOCT catheter was accurately tracked with help of the subvoxel approach from chapter 3. For the first time, the feasibility of combining IVOCT and MPI simultaneously was demonstrated in *in-vitro* phantom experiments. The bimodal imaging approach was used to minimize motion artifacts usually induced by catheter bending and heart beat motion. The results showed a considerable improvement in the IVOCT reconstruction in terms of vessel shape and stenosis length. Both modalities were able to synergize their full potential with regard to no ionizing radiation, high temporal resolution and high spatial resolution.

In chapter 6, MPI focus fields were utilized to induce magnetic forces on particles. The feasibility for magnetic navigation was analyzed in detail in phantom-based bifurcation experiments within vascular flow. Before the flow experiments, suitable magnetic particles with sufficient potential for mobility and imaging applications had been developed and analyzed. It is demonstrated that MPI can be used to maneuver magnetic particles against gravity towards one branch of a bifurcation. Similarly, magnetic particles were navigated towards one branch of a bifurcation while the particles flow within a realistic current of $217\,\mathrm{mm\,s^{-1}}$. In an additional experiment, magnetic particles were successfully navigated towards a 100% stenosis, while the distribution of the particles inside the phantom was quasi-simultaneously imaged with MPI within a flowing current of $108\,\mathrm{mm\,s^{-1}}$. The presented MPIN method promises an auspicious tool for TTD with magnetic particles.

In a proof of concept experiment, a novel MPI contrast with immobilized aligned easy-axis particles was shown in chapter 7. For this contrast, magnetic particles were immobilized within a static homogeneous magnetic field to fixate and align the easy-axis of the particles. The results of this study demonstrated that MPI is able to determine the immobilized angle of the easy-axis with a sufficient precision. This novel MPI contrast could be especially helpful in determining the pose and orientation of one magnetic swimmer.

In summary, the presented work highlights different aspects of MPI in the context of possible medical applications, such as IVOCT catheter tracking, orientation determina-

tion, and magnetic navigation. In the future, many of these aspects can be combined to achieve a unique, sophisticated medical application for MPI.

8.2. Outlook

As this work provides insights in the current possibilities to utilize MPI in several medical applications, this section focuses on the combination of different MPI properties and their further developments.

The MRI and MPI image registration can be improved by using the immobilized aligned easy-axis contrast to construct the fiducials. This allows the unique identification of the three markers and makes a sanity check obsolete. Further, it is necessary to develop a sophisticated and robust segmentation algorithm to extract the fiducials position from the MRI images. Then, an automatic registration with the spherical fiducials can be performed.

Even though the IVOCT catheter tracking based on MPI has proven to be very promising, there is still room for improvement. The catheter could be labeled with three immobilized easy-axis aligned markers, where each marker orientation differs about $60°$. This would facilitate the catheter orientation tracking and improve the compensation of the NURD artifacts. Additionally, a second liquid tracer could be used as a blood pool tracer to achieve a multi-contrast MPI image with channels for the three markers and the blood pool tracer. Based on this, the pose and orientation of the catheter could be determined while the shape of the vessel could be imaged simultaneously. In a more advanced application, the rotating focus fields could be utilized to rotate only the microprism of the IVOCT catheter. This could eliminate the proximal rotation via actuators and also minimize NURD artifacts.

The principle of TTD using magnetic particles and MPIN needs to be further developed in order to gain insights into this technique. As a first step, the MPIO particles have to be functionalized with tPA and the dissolution of clotted blood has to be investigated in various *in-vitro* experiments. Secondly, the artificial stenosis needs to be replaced with a real blood clot within the artificial bifurcation phantom. Then, the bifurcation flow experiments have be repeated in order to demonstrate the effect of the functionalized MPIOs on a real blood clot. Once the effectiveness and robustness of this method has been proven, the final validation could be done in *in-vivo* mouse experiments. As an MPI human head scanner is currently under development [C7] for the detection of ischemic strokes, the TTD feature could be added to the current scanner design by adding strong focus field coils. Such a mobile head scanner without the need of additional shielding could provide the functionality of stroke monitoring and therapy in one system.

Besides the application of magnetic forces for TDD, the rotational focus fields have been used for the navigation of magnetic swimmers [65, 66]. In this case, the immobi-

lized aligned easy-axis contrast provides an excellent feature to determine the pose and orientation of one magnetic swimmer. Even though there is still a lot of research work to be done, MPI could be used to navigate a small object, such as a PillCam, through the human body while estimating the pose and direction of the device.

Bibliography

Own Publications

Journal Publications

[J1] F. Griese, T. Knopp, R. Werner, A. Schlaefer, and M. Möddel. “Submillimeter-Accurate Marker Localization within Low Gradient Magnetic Particle Imaging Tomograms.” In: *International Journal on Magnetic Particle Imaging* 3.1 (2017) (cit. on pp. 6, 72, 123).

[J2] S. Latus[1], F. Griese[1], M. Schlüter, C. Otte, M. Möddel, M. Graeser, T. Saathoff, T. Knopp, and A. Schlaefer. “Bimodal intravascular volumetric imaging combining OCT and MPI.” In: *Medical Physics* 46.3 (2019), pp. 1371–1383. DOI: 10.1002/mp.13388 (cit. on pp. 6, 91, 96, 97, 99, 100, 102–104, 111–114, 124).

[J3] F. Griese[1], S. Latus[1], M. Schlüter, M. Graeser, M. Lutz, A. Schlaefer, and T. Knopp. “In-Vitro MPI-guided IVOCT catheter tracking in real time for motion artifact compensation.” In: *PLOS ONE* 15.3 (2020). DOI: 10.1371/journal.pone.0230821 (cit. on pp. 6, 92, 99, 100, 102, 103, 120, 121).

[J4] F. Griese, T. Knopp, C. Gruettner, F. Thieben, K. Müller, S. Loges, P. Ludewig, and N. Gdaniec. “Simultaneous Magnetic Particle Imaging and Navigation of large superparamagnetic nanoparticles in bifurcation flow experiments.” In: *Journal of Magnetism and Magnetic Materials* 498 (2020), p. 166206. DOI: 10.1016/j.jmmm.2019.166206 (cit. on p. 6).

Proceedings Publications

[P1] F. Griese, P. Ludewig, F. Thieben, N. Gdaniec, and T. Knopp. “Imaging and moving magnetic beads with magnetic particle imaging for targeted drug delivery.” In: *2018 IEEE 15th International Symposium on Biomedical Imaging (ISBI 2018)*. 2018, pp. 1293–1296. DOI: 10.1109/ISBI.2018.8363808 (cit. on pp. 3, 6, 129, 134, 139).

[1] Shared first authorship

[P2] F. Griese, M. Prieske, M. Möddel, R. Werner, and T. Knopp. “MRI-based field of view selection for precise, real-time targeting in MPI.” In: *9th International Workshop on Magnetic Particle Imaging (IWMPI 2019)*. 2019, pp. 207–208 (cit. on p. 6).

[P3] F. Griese, S. Latus, M. Gräser, M. Möddel, M. Schlüter, C. Otte, T. Saathoff, A. Schlaefer, and T. Knopp. “Stenosis Analysis by synergizing MPI and intravascular OCT.” In: *8th International Workshop on Magnetic Particle Imaging (IWMPI 2018)*. 2018, pp. 217–218 (cit. on p. 6).

[P4] F. Griese, A. Dreyer, J. Salamon, H. Ittrich, and T. Knopp. “CoPLA coating material for interventional multi-spectral MPI.” In: *World Molecular Imaging Congress (WMIC) 2018*. 2018 (cit. on p. 6).

Collaborative Publications

[C1] S. Latus, F. Griese, M. Gräser, M. Möddel, M. Schlüter, C. Otte, N. Gessert, T. Saathoff, T. Knopp, and A. Schlaefer. “Towards bimodal intravascular OCT MPI volumetric imaging.” In: *Proceedings of SPIE Medical Imaging*. 2018 (cit. on pp. 6, 103, 124).

[C2] I. M. Baltruschat, P. Szwargulski, F. Griese, M. Grosser, R. Werner, and T. Knopp. “3d-SMRnet: Achieving a new quality of MPI system matrix recovery by deep learning.” In: *MICCAI (accepted)* (2020) (cit. on pp. 6, 31).

[C3] I. M. Baltruschat, F. Griese, P. Szwargulski, R. Werner, and T. Knopp. “Wrestling the Devil of Wasting Time: MPI System Matrix Recovery by Deep Learning.” In: *9th International Workshop on Magnetic Particle Imaging (IWMPI 2019)*. 2019, pp. 109–110 (cit. on pp. 6, 31).

[C4] P. Szwargulski, N. Gdaniec, M. Graeser, M. Möddel, F. Griese, and T. Knopp. “Enlarging the field of view in magnetic particle imaging using a moving table approach.” In: *Proceedings of SPIE Medical Imaging*. 2018, pp. 10578–51 (cit. on p. 6).

[C5] P. Szwargulski, N. Gdaniec, M. Graeser, M. Möddel, F. Griese, K. M. Krishnan, T. M. Buzug, and T. Knopp. “Moving table magnetic particle imaging: a stepwise approach preserving high spatio-temporal resolution.” In: *Journal of Medical Imaging (Bellingham, Wash.)* 5.4 (2018), p. 046002. DOI: 10.1117/1.JMI.5.4.046002 (cit. on p. 6).

[C6] P. Szwargulski, N. Gdaniec, M. Graeser, M. Möddel, F. Griese, and T. Knopp. “Erweiterung des Bildgebungsbereiches bei der Magnetpartikelbildgebung durch externe axiale Verschiebungen.” In: *BVM Workshop 2018*. 2018, p. 202 (cit. on p. 6).

[C7] M. Graeser et al. “Human-sized magnetic particle imaging for brain applications.” In: *Nature Communications* 10.1 (2019), p. 1936. DOI: 10.1038/s41467-019-09704-x (cit. on pp. 7, 163, 179).

[C8] M. Graeser et al. “First human-sized Magnetic Particle Imaging Device for Cerebral Applications.” In: *9th International Workshop on Magnetic Particle Imaging (IWMPI 2019)*. 2019, pp. 15–16 (cit. on p. 7).

[C9] P. Szwargulski, M. Graeser, F. Thieben, N. Gdaniec, F. Werner, M. Boberg, F. Griese, M. Möddel, and T. Knopp. “Interpretation of Cartesian Data based on a Simulated Human-Sized MPI Brain Imager.” In: *9th International Workshop on Magnetic Particle Imaging (IWMPI 2019)*. 2019, pp. 37–38 (cit. on p. 7).

[C10] N. Gdaniec et al. “Determining Perfusion Parameters using Magnetic Particle Imaging: A Phantom Study using a Human-Sized Flow Phantom.” In: *9th International Workshop on Magnetic Particle Imaging (IWMPI 2019)*. 2019, pp. 151–152 (cit. on p. 7).

[C11] F. Werner et al. “Stroke Detection using Magnetic Particle Imaging: A Phantom Study using a Human-sized Brain Phantom.” In: *9th International Workshop on Magnetic Particle Imaging (IWMPI 2019)*. 2019, pp. 141–142 (cit. on p. 7).

[C12] T. Knopp, P. Szwargulski, F. Griese, and M. Gräser. “OpenMPIData: An initiative for freely accessible magnetic particle imaging data.” In: *Data in Brief* (2019), p. 104971. DOI: 10.1016/j.dib.2019.104971 (cit. on p. 7).

[C13] T. Knopp, M. Möddel, F. Griese, F. Werner, P. Szwargulski, N. Gdaniec, and M. Boberg. “MPIFiles.jl: A Julia Package for Magnetic Particle Imaging Files.” In: *Journal of Open Source Software* 4.38 (2019), p. 1331. DOI: 10.21105/joss.01331 (cit. on pp. 7, 170).

[C14] T. Knopp, P. Szwargulski, F. Griese, M. Grosser, M. Boberg, and M. Möddel. “MPIReco.jl: Julia Package for Image Reconstruction in MPI.” In: *International Journal on Magnetic Particle Imaging* 5.1 (2019). DOI: 10.18416/IJMPI.2019.1907001 (cit. on pp. 7, 170).

[C15] M. Möddel, F. Griese, T. Kluth, and T. Knopp. “Estimating orientation using multi-contrast MPI.” In: *International Journal on Magnetic Particle Imaging* 6.2 (2020). DOI: 10.18416/IJMPI.2020.2009023 (cit. on p. 166).

General Publications

[1] T. Salditt, T. Aspelmeier, and S. Aeffner. *Biomedical Imaging, Principles of Radiography, Tomography and Medical Physics*. Berlin, Boston: De Gruyter, 2017. DOI: 10.1515/9783110426694 (cit. on p. 1).

[2] Paul C. Lauterbur and Z.-P. Liang. *Principles of Magnetic Resonance Imaging: A Signal Processing Perspective*. Wiley-IEEE Press, 1999. 416 pp. (cit. on p. 1).

[3] O. Dössel. *Bildgebende Verfahren in der Medizin: Von der Technik zur medizinischen Anwendung*. 2nd ed. Springer Vieweg, 2016. p.239. DOI: 10.1007/978-3-642-54407-1 (cit. on pp. 1, 48).

[4] A. R. Kherlopian, T. Song, Q. Duan, M. A. Neimark, M. J. Po, J. K. Gohagan, and A. F. Laine. "A review of imaging techniques for systems biology." In: *BMC Systems Biology* 2.1 (2008), p. 74. DOI: 10.1186/1752-0509-2-74 (cit. on p. 1).

[5] K. Doi. "Diagnostic imaging over the last 50 years: research and development in medical imaging science and technology." In: *Physics in Medicine and Biology* 51.13 (2006), R5–R27. DOI: 10.1088/0031-9155/51/13/R02 (cit. on p. 1).

[6] R. A. Smith, V. Cokkinides, and H. J. Eyre. "American Cancer Society Guidelines for the Early Detection of Cancer, 2006." In: *CA: A Cancer Journal for Clinicians* 56.1 (2006), pp. 11–25. DOI: 10.3322/canjclin.56.1.11 (cit. on p. 1).

[7] T. M. Buzug. *Computed Tomography: From Photon Statistics to Modern Cone-Beam CT*. Berlin Heidelberg: Springer-Verlag, 2008. DOI: 10.1007/978-3-540-39408-2 (cit. on p. 1).

[8] G. Müller and M. Möser, eds. *Ultraschall in Medizin und Technik*. Fachwissen Technische Akustik. Springer Vieweg, 2017. DOI: 10.1007/978-3-662-55442-5 (cit. on p. 1).

[9] J. A. Izatt and M. A. Choma. "Theory of Optical Coherence Tomography." In: *Optical Coherence Tomography: Technology and Applications*. Ed. by W. Drexler and J. G. Fujimoto. Biological and Medical Physics, Biomedical Engineering. Berlin, Heidelberg: Springer Berlin Heidelberg, 2008, pp. 47–72. DOI: 10.1007/978-3-540-77550-8_2 (cit. on pp. 1, 95).

[10] D. L. Bailey, D. W. Townsend, P. E. Valk, and M. N. Maisey, eds. *Positron Emission Tomography: Basic Sciences*. London: Springer-Verlag, 2005. DOI: 10.1007/b136169 (cit. on p. 2).

[11] M. N. Wernick and J. N. Aarsvold. *Emission Tomography: The Fundamentals of PET and SPECT*. Elsevier, 2004. 596 pp. (cit. on p. 2).

[12] T. K. Jain, J. Richey, M. Strand, D. L. Leslie-Pelecky, C. Flask, and V. Labhasetwar. “Magnetic Nanoparticles with Dual Functional Properties: Drug Delivery and Magnetic Resonance Imaging.” In: *Biomaterials* 29.29 (2008), pp. 4012–4021. DOI: 10.1016/j.biomaterials.2008.07.004 (cit. on p. 2).

[13] B. Chertok, B. A. Moffat, A. E. David, F. Yu, C. Bergemann, B. D. Ross, and V. C. Yang. “Iron oxide nanoparticles as a drug delivery vehicle for MRI monitored magnetic targeting of brain tumors.” In: *Biomaterials* 29.4 (2008), pp. 487–496. DOI: 10.1016/j.biomaterials.2007.08.050 (cit. on p. 2).

[14] M. Gauberti, A. P. Fournier, F. Docagne, D. Vivien, and S. Martinez de Lizarrondo. “Molecular Magnetic Resonance Imaging of Endothelial Activation in the Central Nervous System.” In: *Theranostics* 8.5 (2018), pp. 1195–1212. DOI: 10.7150/thno.22662 (cit. on pp. 2, 43, 65, 72, 83).

[15] B. Gleich and J. Weizenecker. “Tomographic imaging using the nonlinear response of magnetic particles.” In: *Nature* 435.7046 (2005), pp. 1214–1217. DOI: 10.1038/nature03808 (cit. on p. 2).

[16] K. Lu, P. W. Goodwill, E. U. Saritas, B. Zheng, and S. M. Conolly. “Linearity and Shift Invariance for Quantitative Magnetic Particle Imaging.” In: *IEEE transactions on medical imaging* 32.9 (2013). DOI: 10.1109/TMI.2013.2257177 (cit. on pp. 2, 161).

[17] T. Knopp, N. Gdaniec, and M. Möddel. “Magnetic particle imaging: from proof of principle to preclinical applications.” In: *Physics in Medicine and Biology* 62.14 (2017), R124–R178. DOI: 10.1088/1361-6560/aa6c99 (cit. on pp. 2, 89, 102, 125).

[18] N. Panagiotopoulos et al. “Magnetic particle imaging: current developments and future directions.” In: *International Journal of Nanomedicine* 10 (2015), pp. 3097–3114. DOI: 10.2147/IJN.S70488 (cit. on p. 2).

[19] D. Huang, E. A. Swanson, C. P. Lin, J. S. Schuman, W. G. Stinson, W. Chang, M. R. Hee, T. Flotte, K. Gregory, and C. A. Puliafito. “Optical coherence tomography.” In: *Science (New York, N.Y.)* 254.5035 (1991), pp. 1178–1181. DOI: 10.1126/science.1957169 (cit. on pp. 2, 88).

[20] R. M. Ferguson et al. “Magnetic Particle Imaging With Tailored Iron Oxide Nanoparticle Tracers.” In: *IEEE Transactions on Medical Imaging* 34.5 (2015), pp. 1077–1084. DOI: 10.1109/TMI.2014.2375065 (cit. on pp. 2, 163).

[21] E. U. Saritas, P. W. Goodwill, G. Z. Zhang, and S. M. Conolly. “Magnetostimulation limits in magnetic particle imaging.” In: *IEEE transactions on medical imaging* 32.9 (2013), pp. 1600–1610. DOI: 10.1109/TMI.2013.2260764 (cit. on pp. 2, 23, 61, 89).

[22] I. Schmale, B. Gleich, J. Rahmer, C. Bontus, J. Schmidt, and J. Borgert. “MPI Safety in the View of MRI Safety Standards.” In: *IEEE Transactions on Magnetics* 51.2 (2015), pp. 1–4. DOI: 10.1109/TMAG.2014.2322940 (cit. on pp. 2, 23, 61, 89).

[23] J. Weizenecker, B. Gleich, J. Rahmer, H. Dahnke, and J. Borgert. “Three-dimensional real-time in vivo magnetic particle imaging.” In: *Physics in Medicine and Biology* 54.5 (2009), pp. L1–L10. DOI: 10.1088/0031-9155/54/5/L01 (cit. on pp. 2, 3, 37).

[24] J. Borgert et al. “Perspectives on clinical magnetic particle imaging.” In: *Biomedizinische Technik. Biomedical Engineering* 58.6 (2013), pp. 551–556. DOI: 10.1515/bmt-2012-0064 (cit. on p. 2).

[25] P. Vogel, M. A. Rückert, S. J. Kemp, A. P. Khandhar, R. M. Ferguson, S. Herz, A. Vilter, P. Klauer, T. A. Bley, K. M. Krishnan, and V. C. Behr. “Micro-Traveling Wave Magnetic Particle Imaging—Sub-Millimeter Resolution With Optimized Tracer LS-008.” In: *IEEE Transactions on Magnetics* 55.10 (2019), pp. 1–7. DOI: 10.1109/TMAG.2019.2924198 (cit. on pp. 2, 163).

[26] J. Rahmer, J. Weizenecker, B. Gleich, and J. Borgert. “Analysis of a 3-D system function measured for magnetic particle imaging.” In: *IEEE transactions on medical imaging* 31.6 (2012), pp. 1289–1299. DOI: 10.1109/TMI.2012.2188639 (cit. on pp. 2, 48, 49, 163).

[27] J. Rahmer, J. Weizenecker, B. Gleich, and J. Borgert. “Signal encoding in magnetic particle imaging: properties of the system function.” In: *BMC Medical Imaging* 9.1 (2009), p. 4. DOI: 10.1186/1471-2342-9-4 (cit. on pp. 2, 15, 16, 36, 37, 49).

[28] J. Weizenecker, B. Gleich, and J. Borgert. “Magnetic particle imaging using a field free line.” In: *Journal of Physics D: Applied Physics* 41.10 (2008), p. 105009. DOI: 10.1088/0022-3727/41/10/105009 (cit. on p. 2).

[29] B. Gleich, J. Weizenecker, H. Timminger, B. Bontus, I. Schmale, J. Rahmer, J. Schmidt, J. Kanzenbach, and J. Borgert. “Fast mpi demonstrator with enlarged field of view,” in: *Proceedings of the International Society for Magnetic Resonance in Medicine* 18 (2010), p. 218 (cit. on pp. 2, 24).

[30] J. Rahmer, B. Gleich, C. Bontus, I. Schmale, J. Schmidt, J. Kanzenbach, O. Woywode, J. Weizenecker, and J. Borgert. “Results on rapid 3D magnetic particle imaging with a large field of view.” In: Proceedings of the International Society for Magnetic Resonance in Medicine. Vol. 19. 2011, p. 629 (cit. on pp. 2, 24).

[31] H. Arami, E. Teeman, A. Troksa, H. Bradshaw, K. Saatchi, A. Tomitaka, S. S. Gambhir, U. O. Häfeli, D. Liggitt, and K. M. Krishnan. "Tomographic magnetic particle imaging of cancer targeted nanoparticles." In: *Nanoscale* 9.47 (2017), pp. 18723–18730. DOI: 10.1039/C7NR05502A (cit. on p. 3).

[32] J. Zhong, M. Schilling, and F. Ludwig. "Magnetic nanoparticle temperature imaging with a scanning magnetic particle spectrometer." In: *Measurement Science and Technology* 29.11 (2018), p. 115903. DOI: 10.1088/1361-6501/aae3bd (cit. on pp. 3, 33, 34).

[33] J. Wells, H. Paysen, O. Kosch, L. Trahms, and F. Wiekhorst. "Temperature dependence in magnetic particle imaging." In: *AIP Advances* 8.5 (2017), p. 056703. DOI: 10.1063/1.5004506 (cit. on pp. 3, 33, 34).

[34] C. Stehning, B. Gleich, and J. Rahmer. "Simultaneous magnetic particle imaging (MPI) and temperature mapping using multi-color MPI." In: *International Journal on Magnetic Particle Imaging* 2.2 (2016) (cit. on pp. 3, 33, 34).

[35] A. M. Rauwerdink, E. W. Hansen, and J. B. Weaver. "Nanoparticle temperature estimation in combined ac and dc magnetic fields." In: *Physics in medicine and biology* 54.19 (2009), pp. L51–L55. DOI: 10.1088/0031-9155/54/19/L01 (cit. on pp. 3, 33, 34).

[36] J. B. Weaver, A. M. Rauwerdink, and E. W. Hansen. "Magnetic nanoparticle temperature estimation." In: *Medical Physics* 36.5 (2009), pp. 1822–1829. DOI: 10.1118/1.3106342 (cit. on pp. 3, 33, 34).

[37] M. Möddel, C. Meins, J. Dieckhoff, and T. Knopp. "Viscosity quantification using multi-contrast magnetic particle imaging." In: *New Journal of Physics* 20.8 (2018), p. 083001. DOI: 10.1088/1367-2630/aad44b (cit. on pp. 3, 33, 34).

[38] A. M. Rauwerdink and J. B. Weaver. "Viscous effects on nanoparticle magnetization harmonics." In: *Journal of Magnetism and Magnetic Materials* 322.6 (2010), pp. 609–613. DOI: 10.1016/j.jmmm.2009.10.024 (cit. on pp. 3, 33, 34).

[39] A. M. Rauwerdink and J. B. Weaver. "Measurement of molecular binding using the Brownian motion of magnetic nanoparticle probes." In: *Applied Physics Letters* 96.3 (2010), p. 033702. DOI: 10.1063/1.3291063 (cit. on pp. 3, 33).

[40] C. Shasha, E. Teeman, K. M. Krishnan, P. Szwargulski, T. Knopp, and M. Möddel. "Discriminating nanoparticle core size using multi-contrast MPI." In: *Physics in Medicine & Biology* 64.7 (2019), p. 074001. DOI: 10.1088/1361-6560/ab0fc9 (cit. on pp. 3, 33, 34).

[41] J. Rahmer, A. Halkola, B. Gleich, I. Schmale, and J. Borgert. “First experimental evidence of the feasibility of multi-color magnetic particle imaging.” In: *Physics in Medicine & Biology* 60.5 (2015), p. 1775 (cit. on pp. 3, 33, 34, 47, 124).

[42] P. Vogel, M. A. Rückert, T. Kampf, S. Herz, A. Stang, L. Wöckel, T. A. Bley, S. Dutz, and V. C. Behr. “Superspeed Bolus Visualization for Vascular Magnetic Particle Imaging.” In: *IEEE Transactions on Medical Imaging* (2020), pp. 1–1. DOI: 10.1109/TMI.2020.2965724 (cit. on p. 3).

[43] M. G. Kaul, T. Mummert, C. Jung, J. Salamon, A. P. Khandhar, R. M. Ferguson, S. J. Kemp, H. Ittrich, K. M. Krishnan, G. Adam, and T. Knopp. “In vitro and in vivo comparison of a tailored magnetic particle imaging blood pool tracer with Resovist.” In: *Physics in Medicine and Biology* 62.9 (2017), pp. 3454–3469. DOI: 10.1088/1361-6560/aa5780 (cit. on pp. 3, 15, 88, 125).

[44] P. Goodwill, R. M. Ferguson, E. Yu, R. Orendorff, B. Zheng, K. Lu, D. Hensley, A. Khandhar, S. Kemp, K. Krishnan, and S. Conolly. “In Vivo and Ex vivo experimental MPI angiography with high selection field strength and tailored SPIO nanoparticles.” In: *2015 5th International Workshop on Magnetic Particle Imaging (IWMPI)*. 2015, pp. 1–1. DOI: 10.1109/IWMPI.2015.7106988 (cit. on p. 3).

[45] J. Haegele, R. L. Duschka, M. Graeser, C. Schaecke, N. Panagiotopoulos, K. Lüdtke-Buzug, T. M. Buzug, J. Barkhausen, and F. M. Vogt. “Magnetic particle imaging: kinetics of the intravascular signal in vivo.” In: *International Journal of Nanomedicine* 9 (2014), pp. 4203–4209. DOI: 10.2147/IJN.S49976 (cit. on pp. 3, 87).

[46] P. Ludewig et al. “Magnetic Particle Imaging for Real-Time Perfusion Imaging in Acute Stroke.” In: *ACS nano* 11.10 (2017), pp. 10480–10488. DOI: 10.1021/acsnano.7b05784 (cit. on p. 3).

[47] Z. W. Tay, P. Chandrasekharan, A. Chiu-Lam, D. W. Hensley, R. Dhavalikar, X. Y. Zhou, E. Y. Yu, P. W. Goodwill, B. Zheng, C. Rinaldi, and S. M. Conolly. “Magnetic Particle Imaging Guided Heating In Vivo using Gradient Fields For Arbitrary Localization of Magnetic Hyperthermia Therapy.” In: *ACS nano* 12.4 (2018), pp. 3699–3713. DOI: 10.1021/acsnano.8b00893 (cit. on pp. 3, 11).

[48] D. Hensley, Z. W. Tay, R. Dhavalikar, B. Zheng, P. Goodwill, C. Rinaldi, and S. Conolly. “Combining magnetic particle imaging and magnetic fluid hyperthermia in a theranostic platform.” In: *Physics in Medicine and Biology* 62.9 (2017), pp. 3483–3500. DOI: 10.1088/1361-6560/aa5601 (cit. on pp. 3, 11).

[49] L. M. Bauer, S. F. Situ, M. A. Griswold, and A. C. S. Samia. “High-performance iron oxide nanoparticles for magnetic particle imaging - guided hyperthermia (hMPI).” In: *Nanoscale* 8.24 (2016), pp. 12162–12169. DOI: 10.1039/c6nr01877g (cit. on pp. 3, 11).

[50] A. P. Khandhar, R. M. Ferguson, J. A. Simon, and K. M. Krishnan. “Tailored magnetic nanoparticles for optimizing magnetic fluid hyperthermia.” In: *Journal of Biomedical Materials Research. Part A* 100.3 (2012), pp. 728–737. DOI: 10.1002/jbm.a.34011 (cit. on pp. 3, 11).

[51] A. J. Giustini, A. A. Petryk, S. M. Cassim, J. A. Tate, I. Baker, and P. J. Hoopes. “Magnetic Nanoparticle Hyperthermia In Cancer Treatment.” In: *Nano LIFE* 1.1 (2010). DOI: 10.1142/S1793984410000067 (cit. on pp. 3, 11).

[52] B. Zheng, M. P. von See, E. Yu, B. Gunel, K. Lu, T. Vazin, D. V. Schaffer, P. W. Goodwill, and S. M. Conolly. “Quantitative Magnetic Particle Imaging Monitors the Transplantation, Biodistribution, and Clearance of Stem Cells In Vivo.” In: *Theranostics* 6.3 (2016), pp. 291–301. DOI: 10.7150/thno.13728 (cit. on p. 3).

[53] B. Zheng, T. Vazin, P. W. Goodwill, A. Conway, A. Verma, E. U. Saritas, D. Schaffer, and S. M. Conolly. “Magnetic Particle Imaging tracks the long-term fate of in vivo neural cell implants with high image contrast.” In: *Scientific Reports* 5.1 (2015), pp. 1–9. DOI: 10.1038/srep14055 (cit. on pp. 3, 38).

[54] B. Zheng, T. Vazin, W. Yang, P. W. Goodwill, E. U. Saritas, L. R. Croft, D. V. Schaffer, and S. M. Conolly. “Quantitative stem cell imaging with magnetic particle imaging.” In: *2013 International Workshop on Magnetic Particle Imaging (IWMPI)*. 2013, pp. 1–1. DOI: 10.1109/IWMPI.2013.6528323 (cit. on p. 3).

[55] J. W. M. Bulte, P. Walczak, M. Janowski, K. M. Krishnan, H. Arami, A. Halkola, B. Gleich, and J. Rahmer. “Quantitative "Hot Spot" Imaging of Transplanted Stem Cells using Superparamagnetic Tracers and Magnetic Particle Imaging (MPI).” In: *Tomography (Ann Arbor, Mich.)* 1.2 (2015), pp. 91–97. DOI: 10.18383/j.tom.2015.00172 (cit. on p. 3).

[56] A. Tomitaka, H. Arami, S. Gandhi, and K. M. Krishnan. “Lactoferrin conjugated iron oxide nanoparticles for targeting brain glioma cells in magnetic particle imaging.” In: *Nanoscale* 7.40 (2015), pp. 16890–16898. DOI: 10.1039/C5NR02831K (cit. on p. 3).

[57] E. Y. Yu, M. Bishop, B. Zheng, R. M. Ferguson, A. P. Khandhar, S. J. Kemp, K. M. Krishnan, P. W. Goodwill, and S. M. Conolly. "Magnetic Particle Imaging: A Novel in Vivo Imaging Platform for Cancer Detection." In: *Nano Letters* 17.3 (2017), pp. 1648–1654. DOI: 10.1021/acs.nanolett.6b04865 (cit. on p. 3).

[58] J. Haegele, S. Biederer, H. Wojtczyk, M. Gräser, T. Knopp, T. M. Buzug, J. Barkhausen, and F. M. Vogt. "Toward cardiovascular interventions guided by magnetic particle imaging: first instrument characterization." In: *Magnetic Resonance in Medicine* 69.6 (2013), pp. 1761–1767. DOI: 10.1002/mrm.24421 (cit. on pp. 3, 4, 87).

[59] J. Haegele, J. Rahmer, B. Gleich, J. Borgert, H. Wojtczyk, N. Panagiotopoulos, T. M. Buzug, J. Barkhausen, and F. M. Vogt. "Magnetic particle imaging: visualization of instruments for cardiovascular intervention." In: *Radiology* 265.3 (2012), pp. 933–938. DOI: 10.1148/radiol.12120424 (cit. on pp. 3, 4, 47, 87).

[60] J. Rahmer, D. Wirtz, C. Bontus, J. Borgert, and B. Gleich. "Interactive Magnetic Catheter Steering With 3-D Real-Time Feedback Using Multi-Color Magnetic Particle Imaging." In: *IEEE Transactions on Medical Imaging* 36.7 (2017), pp. 1449–1456. DOI: 10.1109/TMI.2017.2679099 (cit. on pp. 3, 87, 124, 129).

[61] J. Salamon, M. Hofmann, C. Jung, M. G. Kaul, F. Werner, K. Them, R. Reimer, P. Nielsen, A. v. Scheidt, G. Adam, T. Knopp, and H. Ittrich. "Magnetic Particle / Magnetic Resonance Imaging: In-Vitro MPI-Guided Real Time Catheter Tracking and 4D Angioplasty Using a Road Map and Blood Pool Tracer Approach." In: *PLOS ONE* 11.6 (2016), e0156899. DOI: 10.1371/journal.pone.0156899 (cit. on pp. 3, 4, 34, 47, 87, 124).

[62] S. Herz, P. Vogel, P. Dietrich, T. Kampf, M. A. Rückert, R. Kickuth, V. C. Behr, and T. A. Bley. "Magnetic Particle Imaging Guided Real-Time Percutaneous Transluminal Angioplasty in a Phantom Model." In: *CardioVascular and Interventional Radiology* 41.7 (2018), pp. 1100–1105. DOI: 10.1007/s00270-018-1955-7 (cit. on pp. 3, 4, 87, 124).

[63] S. Herz, P. Vogel, T. Kampf, P. Dietrich, S. Veldhoen, M. A. Rückert, R. Kickuth, V. C. Behr, and T. A. Bley. "Magnetic Particle Imaging–Guided Stenting." In: *Journal of Endovascular Therapy* 26.4 (2019), pp. 512–519. DOI: 10.1177/1526602819851202 (cit. on pp. 3, 4, 124).

[64] K. Bente, A. Codutti, F. Bachmann, and D. Faivre. “Biohybrid and Bioinspired Magnetic Microswimmers.” In: *Small* 14.29 (2018), p. 1704374. DOI: 10.1002/smll.201704374 (cit. on pp. 3, 38, 129).

[65] A. C. Bakenecker, A. v. Gladiss, T. Friedrich, U. Heinen, H. Lehr, K. Lüdtke-Buzug, and T. M. Buzug. “Actuation and Visualization of a Magnetically Coated Swimmer with Magnetic Particle Imaging.” In: *Journal of Magnetism and Magnetic Materials* (2018). DOI: 10.1016/j.jmmm.2018.10.056 (cit. on pp. 3, 129, 166, 175, 179).

[66] J. Rahmer, C. Stehning, and B. Gleich. “Spatially selective remote magnetic actuation of identical helical micromachines.” In: *Science Robotics* 2.3 (2017), eaal2845. DOI: 10.1126/scirobotics.aal2845 (cit. on pp. 3, 38, 125, 129, 163, 166, 175, 179).

[67] N. Nothnagel, J. Rahmer, B. Gleich, A. Halkola, T. M. Buzug, and J. Borgert. “Steering of Magnetic Devices With a Magnetic Particle Imaging System.” In: *IEEE Transactions on Biomedical Engineering* 63.11 (2016), pp. 2286–2293. DOI: 10.1109/TBME.2016.2524070 (cit. on pp. 3, 38, 40, 129).

[68] J. Rahmer, C. Stehning, and B. Gleich. “Remote magnetic actuation using a clinical scale system.” In: *PLOS ONE* 13.3 (2018), e0193546. DOI: 10.1371/journal.pone.0193546 (cit. on pp. 3, 129).

[69] T.-A. Le, X. Zhang, A. K. Hoshiar, J. Yoon, T.-A. Le, X. Zhang, A. K. Hoshiar, and J. Yoon. “Real-Time Two-Dimensional Magnetic Particle Imaging for Electromagnetic Navigation in Targeted Drug Delivery.” In: *Sensors* 17.9 (2017), p. 2050. DOI: 10.3390/s17092050 (cit. on pp. 3, 129).

[70] A. Mahmood, M. Dadkhah, M. O. Kim, and J. Yoon. “A Novel Design of an MPI-Based Guidance System for Simultaneous Actuation and Monitoring of Magnetic Nanoparticles.” In: *IEEE Transactions on Magnetics* 51.2 (2015), pp. 1–5. DOI: 10.1109/TMAG.2014.2358252 (cit. on pp. 3, 129).

[71] X. Zhang, T.-A. Le, and J. Yoon. “Development of a real time imaging-based guidance system of magnetic nanoparticles for targeted drug delivery.” In: *Journal of Magnetism and Magnetic Materials* 427 (2017), pp. 345–351. DOI: 10.1016/j.jmmm.2016.10.056 (cit. on pp. 3, 129).

[72] T. Kuboyabu, A. Ohki, N. Banura, and K. Murase. “Usefulness of Magnetic Particle Imaging for Monitoring the Effect of Magnetic Targeting.” In: *Open Journal of Medical Imaging* 06 (2016), p. 33. DOI: 10.4236/ojmi.2016.62004 (cit. on pp. 3, 129).

[73] G. D. Dangas, C. D. Mario, N. N. Kipshidze, P. Barlis, and T. Addo. *Interventional Cardiology: Principles and Practice*. 2. Chichester, West Sussex ; Ames, Iowa: Wiley-Blackwell, 2017. 816 pp. (cit. on p. 4).

[74] T. Simard, B. Hibbert, F. D. Ramirez, M. Froeschl, Y.-X. Chen, and E. R. O'Brien. "The Evolution of Coronary Stents: A Brief Review." In: *Canadian Journal of Cardiology* 30.1 (2014), pp. 35–45. DOI: 10.1016/j.cjca.2013.09.012 (cit. on p. 4).

[75] The Lancet. "40 years of percutaneous coronary intervention: where next?" In: *The Lancet* 390.10096 (2017), p. 715. DOI: 10.1016/S0140-6736(17)32238-9 (cit. on p. 4).

[76] S. Ui, M. Chino, and T. Isshiki. "Rates of primary percutaneous coronary intervention worldwide." In: *Circulation Journal: Official Journal of the Japanese Circulation Society* 69.1 (2005), pp. 95–100. DOI: 10.1253/circj.69.95 (cit. on p. 4).

[77] G. J. Tearney et al. "Consensus standards for acquisition, measurement, and reporting of intravascular optical coherence tomography studies: a report from the International Working Group for Intravascular Optical Coherence Tomography Standardization and Validation." In: *Journal of the American College of Cardiology* 59.12 (2012), pp. 1058–1072. DOI: 10.1016/j.jacc.2011.09.079 (cit. on pp. 4, 88, 95).

[78] L. M. Bauer, S. F. Situ, M. A. Griswold, and A. C. S. Samia. "Magnetic Particle Imaging Tracers: State-of-the-Art and Future Directions." In: *The Journal of Physical Chemistry Letters* 6.13 (2015), pp. 2509–2517. DOI: 10.1021/acs.jpclett.5b00610 (cit. on pp. 10, 11, 14).

[79] P. Somasundaran. *Encyclopedia of Surface and Colloid Science*. CRC Press, 2015. DOI: 10.1081/E-ESCS3 (cit. on p. 10).

[80] S. P. Gubin. *Magnetic Nanoparticles*. 1. Weinheim: Wiley-VCH, 2009. 484 pp. (cit. on p. 11).

[81] C. P. Bean and J. D. Livingston. "Superparamagnetism." In: *Journal of Applied Physics* 30.4 (1959), pp. 120–129. DOI: 10.1063/1.2185850 (cit. on p. 11).

[82] R. M. Ferguson, K. R. Minard, and K. M. Krishnan. "Optimization of nanoparticle core size for magnetic particle imaging." In: *Journal of magnetism and magnetic materials* 321.10 (2009), pp. 1548–1551. DOI: 10.1016/j.jmmm.2009.02.083 (cit. on p. 11).

[83] N. Kurti. *Selected Works of Louis Neel*. CRC Press, 1988. 536 pp. (cit. on pp. 11, 12).

[84] L. NEEL. “Theorie du trainage magnetique des ferromagnetiques en grains fins avec application aux terres cuites.” In: *Ann. Geophys.* 5 (1949), pp. 99–136 (cit. on pp. 11, 12).

[85] W. T. Coffey and Y. P. Kalmykov. “Thermal fluctuations of magnetic nanoparticles: Fifty years after Brown.” In: *Journal of Applied Physics* 112.12 (2012), p. 121301. DOI: 10.1063/1.4754272 (cit. on p. 11).

[86] J. F. Schenck. “The role of magnetic susceptibility in magnetic resonance imaging: MRI magnetic compatibility of the first and second kinds.” In: *Medical Physics* 23.6 (1996), pp. 815–850. DOI: 10.1118/1.597854 (cit. on p. 11).

[87] K. J. Buschow, ed. *Encyclopedia of Materials: Science and Technology*. Elsevier, 2001 (cit. on p. 11).

[88] D. C. Giancoli. *Physik: Lehr-und Übungsbuch*. München: Boston: Pearson Studium, 2009 (cit. on pp. 11, 136).

[89] T. Knopp and T. M. Buzug. *Magnetic Particle Imaging: An Introduction to Imaging Principles and Scanner Instrumentation*. Berlin Heidelberg: Springer-Verlag, 2012. DOI: 10.1007/978-3-642-04199-0 (cit. on pp. 12, 26, 28, 31, 32, 38).

[90] T. Kluth. “Mathematical models for magnetic particle imaging.” In: *Inverse Problems* 34.8 (2018), p. 083001. DOI: 10.1088/1361-6420/aac535 (cit. on pp. 12, 15).

[91] T. Hülser. “Strukturelle und magnetische eigenschaften von eisenkarbid- und eisenoxid nanopartikeln.” In: *Fakultät für Naturwissenschften der Universität Duisburg-Essen, Duisburg-Essen* (2003) (cit. on p. 13).

[92] A. Einstein. *Investigations on the Theory of the Brownian Movement*. Courier Corporation, 1956. 148 pp. (cit. on p. 13).

[93] P. Kopčanský et al. “Néel and Brownian rotations in ferronematics.” In: *Physics Procedia*. 12th International Conference on Magnetic Fluids (ICMF12) 9 (2010), pp. 82–86. DOI: 10.1016/j.phpro.2010.11.020 (cit. on p. 13).

[94] D. B. Reeves and J. B. Weaver. “Combined Néel and Brown rotational Langevin dynamics in magnetic particle imaging, sensing, and therapy.” In: *Applied Physics Letters* 107.22 (2015). DOI: 10.1063/1.4936930 (cit. on pp. 13, 14).

[95] S. A. Shah, D. B. Reeves, R. M. Ferguson, J. B. Weaver, and K. M. Krishnan. “Mixed Brownian alignment and Néel rotations in superparamagnetic iron oxide nanoparticle suspensions driven by an ac field.” In: *Physical review. B, Condensed matter and materials physics* 92.9 (2015). DOI: 10.1103/PhysRevB.92.094438 (cit. on pp. 13, 33, 165).

[96] J. Weizenecker, B. Gleich, J. Rahmer, and J. Borgert. “Particle dynamics of mono-domain particles in magnetic particle imaging.” In: *Magnetic Nanoparticles*. 0 vols. WORLD SCIENTIFIC, 2010, pp. 3–15. DOI: 10.1142/9789814324687_0001 (cit. on p. 14).

[97] D. Eberbeck, F. Wiekhorst, S. Wagner, and L. Trahms. “How the size distribution of magnetic nanoparticles determines their magnetic particle imaging performance.” In: *Applied Physics Letters* 98.18 (2011), p. 182502. DOI: 10.1063/1.3586776 (cit. on p. 14).

[98] A. Lindemann, K. Lüdtke-Buzug, B. M. Fräderich, K. Gräfe, R. Pries, and B. Wollenberg. “Biological impact of superparamagnetic iron oxide nanoparticles for magnetic particle imaging of head and neck cancer cells.” In: *International Journal of Nanomedicine* 9 (2014), pp. 5025–5040. DOI: 10.2147/IJN.S63873 (cit. on p. 14).

[99] K. M. Krishnan. *Fundamentals and applications of magnetic materials*. Oxford University Press, 2016 (cit. on pp. 15, 38, 39, 43, 45, 130, 131, 136).

[100] J. Weizenecker, B. Gleich, J. Rahmer, and J. Borgert. “Micro-magnetic simulation study on the magnetic particle imaging performance of anisotropic mono-domain particles.” In: *Physics in Medicine & Biology* 57.22 (2012), p. 7317. DOI: 10.1088/0031-9155/57/22/7317 (cit. on pp. 16, 48).

[101] M. Graeser, K. Bente, and T. M. Buzug. “Dynamic single-domain particle model for magnetite particles with combined crystalline and shape anisotropy.” In: *Journal of Physics D: Applied Physics* 48.27 (2015), p. 275001. DOI: 10.1088/0022-3727/48/27/275001 (cit. on pp. 16, 48).

[102] L. R. Croft, P. W. Goodwill, and S. M. Conolly. “Relaxation in X-Space Magnetic Particle Imaging.” In: *IEEE transactions on medical imaging* 31.12 (2012), pp. 2335–2342. DOI: 10.1109/TMI.2012.2217979 (cit. on p. 16).

[103] D. B. Reeves and J. B. Weaver. “Simulations of magnetic nanoparticle Brownian motion.” In: *Journal of Applied Physics* 112.12 (2012), p. 124311. DOI: 10.1063/1.4770322 (cit. on p. 16).

[104] J. Weizenecker, B. Gleich, and J. Borgert. “Magnetic particle imaging using a field free line.” In: *Journal of Physics D: Applied Physics* 41.10 (2008), p. 105009. DOI: 10.1088/0022-3727/41/10/105009 (cit. on p. 20).

[105] M. Weber. *Magnetic Particle Imaging: Neuartige Bildgebungskonzepte mit einer feldfreien Linie*. 1st ed. Lübeck: Infinite Science Publishing, 2017 (cit. on p. 20).

[106] C. B. Top, S. Ilbey, and H. E. Güven. "Electronically rotated and translated field-free line generation for open bore magnetic particle imaging." In: *Medical Physics* 44.12 (2017), pp. 6225–6238. DOI: 10.1002/mp.12604 (cit. on p. 20).

[107] M. Weber. *Power-Loss Optimized Field-Free Line Generation for Magnetic Particle Imaging*. 1st ed. Lübeck: Infinite Science Publishing, 2015. 74 pp. (cit. on p. 20).

[108] M. Erbe. *Field Free Line Magnetic Particle Imaging*. Aktuelle Forschung Medizintechnik – Latest Research in Medical Engineering, Research. Springer Vieweg, 2014 (cit. on p. 20).

[109] T. Knopp, S. Biederer, T. Sattel, J. Weizenecker, B. Gleich, J. Borgert, and T. M. Buzug. "Trajectory analysis for magnetic particle imaging." In: *Physics in Medicine and Biology* 54.2 (2009), pp. 385–397. DOI: 10.1088/0031-9155/54/2/014 (cit. on p. 23).

[110] F. Werner, N. Gdaniec, and T. Knopp. "First experimental comparison between the Cartesian and the Lissajous trajectory for magnetic particle imaging." In: *Physics in Medicine and Biology* 62.9 (2017), pp. 3407–3421. DOI: 10.1088/1361-6560/aa6177 (cit. on p. 23).

[111] F. Werner, N. Gdaniec, and T. Knopp. "Improving the Spatial Resolution of Bidirectional Cartesian MPI Data using Fourier Techniques." In: *International Journal on Magnetic Particle Imaging* 3.1 (2017), pp. 1–6. DOI: 10.18416/ijmpi.2017.1703007 (cit. on p. 23).

[112] J. Bohnert, B. Gleich, J. Weizenecker, J. Borgert, and O. Dössel. "Evaluation of Induced Current Densities and SAR in the Human Body by Strong Magnetic Fields around 100 kHz." In: *4th European Conference of the International Federation for Medical and Biological Engineering*. Ed. by J. Vander Sloten, P. Verdonck, M. Nyssen, and J. Haueisen. IFMBE Proceedings. Springer Berlin Heidelberg, 2009, pp. 2532–2535 (cit. on pp. 23, 89).

[113] J. Bohnert, B. Gleich, J. Weizenecker, J. Borgert, and O. Dössel. "Optimizing Coil Currents for reduced SAR in Magnetic Particle Imaging." In: *World Congress on Medical Physics and Biomedical Engineering, September 7 - 12, 2009, Munich, Germany*. Ed. by O. Dössel and W. C. Schlegel. IFMBE Proceedings. Springer Berlin Heidelberg, 2010, pp. 249–252 (cit. on pp. 23, 89).

[114] T. Knopp, K. Them, M. Kaul, and N. Gdaniec. "Joint reconstruction of non-overlapping magnetic particle imaging focus-field data." In: *Physics in Medicine and Biology* 60.8 (2015), pp. L15–21. DOI: 10.1088/0031-9155/60/8/L15 (cit. on p. 24).

[115] M. Ahlborg, C. Kaethner, and T. M. Buzug. “Simultaneous patch reconstruction in Magnetic Particle Imaging.” In: *2015 5th International Workshop on Magnetic Particle Imaging (IWMPI)*. 2015, pp. 1–1. DOI: 10.1109/IWMPI.2015.7107017 (cit. on p. 24).

[116] P. Szwargulski, M. Moddel, N. Gdaniec, and T. Knopp. “Efficient Joint Image Reconstruction of Multi-Patch Data Reusing a Single System Matrix in Magnetic Particle Imaging.” In: *IEEE transactions on medical imaging* 38.4 (2019), pp. 932–944. DOI: 10.1109/TMI.2018.2875829 (cit. on p. 24).

[117] N. Gdaniec, P. Szwargulski, and T. Knopp. “Fast multiresolution data acquisition for magnetic particle imaging using adaptive feature detection.” In: *Medical Physics* 44.12 (2017), pp. 6456–6460. DOI: 10.1002/mp.12628 (cit. on p. 25).

[118] M. Gräser. *Mehrdimensionale Magnet-Partikel-Spektroskopie und -Bildgebung: Physikalische Modellierung und Instrumentierung*. Springer-Verlag, 2017 (cit. on pp. 28, 45).

[119] N. Löwa, P. Radon, O. Kosch, and F. Wiekhorst. “Concentration Dependent MPI Tracer Performance.” In: *International Journal on Magnetic Particle Imaging* 2.1 (2016) (cit. on p. 28).

[120] A. Weber, F. Werner, J. Weizenecker, T. M. Buzug, and T. Knopp. “Artifact free reconstruction with the system matrix approach by overscanning the field-free-point trajectory in magnetic particle imaging.” In: *Physics in Medicine and Biology* 61.2 (2015), pp. 475–487. DOI: 10.1088/0031-9155/61/2/475 (cit. on pp. 29, 102).

[121] M. Ahlborg. *Bildgebungskonzepte und Rekonstruktionsansätze für große Bildgebungsvolumen bei Magnetic Particle Imaging*. 1st ed. Lübeck: Infinite Science Publishing, 2016. 156 pp. (cit. on p. 30).

[122] M. Boberg, T. Knopp, P. Szwargulski, and M. Möddel. “Generalized MPI Multi-Patch Reconstruction using Clusters of similar System Matrices.” In: *IEEE Transactions on Medical Imaging* (2019), pp. 1–1. DOI: 10.1109/TMI.2019.2949171 (cit. on p. 30).

[123] T. Knopp, S. Biederer, T. F. Sattel, J. Rahmer, J. Weizenecker, B. Gleich, J. Borgert, and T. M. Buzug. “2D model-based reconstruction for magnetic particle imaging.” In: *Medical Physics* 37.2 (2010), pp. 485–491. DOI: 10.1118/1.3271258 (cit. on p. 30).

[124] T. Knopp, T. F. Sattel, S. Biederer, J. Rahmer, J. Weizenecker, B. Gleich, J. Borgert, and T. M. Buzug. “Model-based reconstruction for magnetic particle imaging.” In: *IEEE transactions on medical imaging* 29.1 (2010), pp. 12–18. DOI: 10.1109/TMI.2009.2021612 (cit. on p. 30).

[125] A. v. Gladiss, M. Graeser, P. Szwargulski, T. Knopp, and T. M. Buzug. “Hybrid system calibration for multidimensional magnetic particle imaging.” In: *Physics in Medicine & Biology* 62.9 (2017), p. 3392. DOI: 10.1088/1361-6560/aa5340 (cit. on pp. 31, 37, 45).

[126] M. Graeser, A. v. Gladiss, M. Weber, and T. M. Buzug. “Two dimensional magnetic particle spectrometry.” In: *Physics in Medicine & Biology* 62.9 (2017), p. 3378. DOI: 10.1088/1361-6560/aa5bcd (cit. on pp. 31, 45).

[127] T. Knopp, J. Rahmer, T. F. Sattel, S. Biederer, J. Weizenecker, B. Gleich, J. Borgert, and T. M. Buzug. “Weighted iterative reconstruction for magnetic particle imaging.” In: *Physics in Medicine and Biology* 55.6 (2010), pp. 1577–1589. DOI: 10.1088/0031-9155/55/6/003 (cit. on p. 31).

[128] P. C. Hansen. *Discrete Inverse Problems*. Fundamentals of Algorithms. Society for Industrial and Applied Mathematics, 2010. 219 pp. DOI: 10.1137/1.9780898718836 (cit. on p. 31).

[129] S. Kaczmarz. “Angenäherte Auflösung von Systemen linearer Gleichungen.” In: *Bull. Internat. Acad. Polon. Sci. Let.* A35 (1937), pp. 355–357 (cit. on p. 31).

[130] T. Knopp and M. Hofmann. “Online reconstruction of 3D magnetic particle imaging data.” In: *Physics in Medicine and Biology* 61.11 (2016), N257–267. DOI: 10.1088/0031-9155/61/11/N257 (cit. on pp. 32, 65, 73).

[131] A. M. Rauwerdink, A. J. Giustini, and J. B. Weaver. “Simultaneous quantification of multiple magnetic nanoparticles.” In: *Nanotechnology* 21.45 (2010), p. 455101. DOI: 10.1088/0957-4484/21/45/455101 (cit. on p. 33).

[132] T. Yoshida, Y. Matsugi, N. Tsujimura, T. Sasayama, K. Enpuku, T. Viereck, M. Schilling, and F. Ludwig. “Effect of alignment of easy axes on dynamic magnetization of immobilized magnetic nanoparticles.” In: *Journal of Magnetism and Magnetic Materials* 427 (2017), pp. 162–167. DOI: 10.1016/j.jmmm.2016.10.040 (cit. on pp. 33, 165, 174).

[133] J. Haegele, S. Vaalma, N. Panagiotopoulos, J. Barkhausen, F. M. Vogt, Jörn Borgert, and J. Rahmer. “Multi-color magnetic particle imaging for cardiovascular interventions.” In: *Physics in Medicine & Biology* 61.16 (2016), N415. DOI: 10.1088/0031-9155/61/16/N415 (cit. on pp. 34, 87, 124).

[134] P. W. Goodwill and S. M. Conolly. “The X-space formulation of the magnetic particle imaging process: 1-D signal, resolution, bandwidth, SNR, SAR, and magnetostimulation.” In: *IEEE transactions on medical imaging* 29.11 (2010), pp. 1851–1859. DOI: 10.1109/TMI.2010.2052284 (cit. on pp. 36, 48).

[135] M. Graeser, A. v. Gladiss, T. Friedrich, and T. M. Buzug. “SNR and Discretization Enhancement for System Matrix Determination by Decreasing the Gradient in Magnetic Particle Imaging.” In: *International Journal on Magnetic Particle Imaging* 3.1 (2017) (cit. on p. 37).

[136] M. Graeser, T. Knopp, P. Szwargulski, T. Friedrich, A. v. Gladiss, M. Kaul, K. M. Krishnan, H. Ittrich, G. Adam, and T. M. Buzug. “Towards Picogram Detection of Superparamagnetic Iron-Oxide Particles Using a Gradiometric Receive Coil.” In: *Scientific Reports* 7.1 (2017), p. 6872. DOI: 10.1038/s41598-017-06992-5 (cit. on pp. 38, 78, 101, 107, 169).

[137] A. Bakenecker, T. Friedrich, A. von Gladiss, and T. M. Buzug. “Lateral Movement of a Helical Swimmer Induced by Rotating Focus Fields in a Preclinical MPI Scanner.” In: *International Workshop on Magnetic Particle Imaging*. 2018, pp. 99–100 (cit. on p. 38).

[138] *Dynabeads Produkte und Technologie zur Separation mit Magnetbeads - DE*. Library Catalog: www.thermofisher.com. URL: https://www.thermofisher.com/de/de/home/brands/product-brand/dynal/dynabeads-technology.html (visited on 04/08/2020) (cit. on p. 42).

[139] P. S. Gilmour et al. “Pulmonary and systemic effects of short-term inhalation exposure to ultrafine carbon black particles.” In: *Toxicology and Applied Pharmacology* 195.1 (2004), pp. 35–44. DOI: 10.1016/j.taap.2003.10.003 (cit. on p. 43).

[140] C. Grüttner. “synomag® Nanoflower Particles: A new Tracer for MPI, Physical characterization and initial in vitro Toxicity Studies.” In: *International Workshop on Magnetic Particle Imaging (IWMPI)* (2018), pp. 17–18 (cit. on pp. 43, 138).

[141] J. R. Henstock, M. Rotherham, H. Rashidi, K. M. Shakesheff, and A. J. El Haj. “Remotely Activated Mechanotransduction via Magnetic Nanoparticles Promotes Mineralization Synergistically With Bone Morphogenetic Protein 2: Applications for Injectable Cell Therapy.” In: *Stem Cells Translational Medicine* 3.11 (2014), pp. 1363–1374. DOI: 10.5966/sctm.2014-0017 (cit. on pp. 43, 138).

[142] S. Biederer, T. Sattel, T. Knopp, K. Lüdtke-Buzug, B. Gleich, J. Weizenecker, J. Borgert, and T. M. Buzug. "A Spectrometer for Magnetic Particle Imaging." In: *4th European Conference of the International Federation for Medical and Biological Engineering*. Ed. by J. Vander Sloten, P. Verdonck, M. Nyssen, and J. Haueisen. IFMBE Proceedings. Berlin, Heidelberg: Springer, 2009, pp. 2313–2316. DOI: 10.1007/978-3-540-89208-3_555 (cit. on pp. 44, 45).

[143] S. Biederer. *Magnet-Partikel-Spektrometer: Entwicklung eines Spektrometers zur Analyse superparamagnetischer Eisenoxid-Nanopartikel für Magnetic Particle Imaging*. Aktuelle Forschung Medizintechnik – Latest Research in Medical Engineering. Vieweg+Teubner Verlag, 2012 (cit. on pp. 45, 138).

[144] F. Werner et al. "Geometry planning and image registration in magnetic particle imaging using bimodal fiducial markers." In: *Medical Physics* 43.6 (2016), pp. 2884–2893. DOI: 10.1118/1.4948998 (cit. on pp. 47, 63, 72).

[145] M. Graeser, P. Ludewig, P. Szwargulski, F. Foerger, T. Liebing, N. D. Forkert, F. Thieben, T. Magnus, and T. Knopp. "Organ Specific Head Coil for High Resolution Mouse Brain Perfusion Imaging using Magnetic Particle Imaging." In: *arXiv:2004.11728 [physics]* (2020) (cit. on p. 48).

[146] M. Y. Wang, C. R. Maurer, J. M. Fitzpatrick, and R. J. Maciunas. "An automatic technique for finding and localizing externally attached markers in CT and MR volume images of the head." In: *IEEE transactions on bio-medical engineering* 43.6 (1996), pp. 627–637. DOI: 10.1109/10.495282 (cit. on pp. 48, 83).

[147] W. R. Brody. "Digital Subtraction Angiography." In: *IEEE Transactions on Nuclear Science* 29.3 (1982), pp. 1176–1180. DOI: 10.1109/TNS.1982.4336336 (cit. on p. 48).

[148] J.-P. Fillard. "Sub-pixel accuracy location estimation from digital signals." In: *Optical Engineering* 31.11 (1992), pp. 2465–2472. DOI: 10.1117/12.59956 (cit. on pp. 50, 83).

[149] J. Rauschenberg, A. O. De, S. Müller, W. Semmler, and M. Bock. "[An algorithm for passive marker localization in interventional MRI]." In: *Zeitschrift fur medizinische Physik* 17.3 (2007), pp. 180–189. DOI: 10.1016/j.zemedi.2007.04.002 (cit. on p. 50).

[150] A. Mattern, R. Sandig, A. Joos, N. Löwa, O. Kosch, A. Weidner, J. Wells, F. Wiekhorst, and S. Dutz. "Magnetic Nanoparticle-Gel Materials for Development of MPI and MRI Phantoms." In: *International Journal on Magnetic Particle Imaging* 4.2 (2018). DOI: 10.18416/IJMPI.2018.1811001 (cit. on p. 64).

[151] M. Gauberti, A. P. Fournier, D. Vivien, and S. Martinez de Lizarrondo. "Molecular Magnetic Resonance Imaging (mMRI)." In: *Methods in Molecular Biology (Clifton, N.J.)* 1718 (2018), pp. 315–327. DOI: 10.1007/978-1-4939-7531-0_19 (cit. on pp. 65, 72, 77).

[152] P. Chandrasekharan, Z. W. Tay, X. Y. Zhou, E. Yu, R. Orendorff, D. Hensley, Q. Huynh, K. L. B. Fung, C. C. VanHook, P. Goodwill, B. Zheng, and S. Conolly. "A perspective on a rapid and radiation-free tracer imaging modality, magnetic particle imaging, with promise for clinical translation." In: *The British Journal of Radiology* 91.1091 (2018), p. 20180326. DOI: 10.1259/bjr.20180326 (cit. on p. 65).

[153] A. Meola, J. Rao, N. Chaudhary, G. Song, X. Zheng, and S. D. Chang. "Magnetic Particle Imaging in Neurosurgery." In: *World Neurosurgery* 125 (2019), pp. 261–270. DOI: 10.1016/j.wneu.2019.01.180 (cit. on p. 65).

[154] L. C. Wu et al. "A Review of Magnetic Particle Imaging and Perspectives on Neuroimaging." In: *American Journal of Neuroradiology* 40.2 (2019), pp. 206–212. DOI: 10.3174/ajnr.A5896 (cit. on p. 65).

[155] M. F. Reiser, W. Semmler, and H. Hricak, eds. *Magnetic Resonance Tomography*. Berlin Heidelberg: Springer-Verlag, 2008. DOI: 10.1007/978-3-540-29355-2 (cit. on pp. 66, 67, 70).

[156] D. Weishaupt, V. D. Köchli, and B. Marincek. *How does MRI work?: An Introduction to the Physics and Function of Magnetic Resonance Imaging*. 2nd ed. Berlin Heidelberg: Springer-Verlag, 2006. DOI: 10.1007/978-3-540-37845-7 (cit. on pp. 66, 70).

[157] S. Zhang, A. A. Joseph, D. Voit, S. Schaetz, K.-D. Merboldt, C. Unterberg-Buchwald, A. Hennemuth, J. Lotz, and J. Frahm. "Real-time magnetic resonance imaging of cardiac function and flow—recent progress." In: *Quantitative Imaging in Medicine and Surgery* 4.5 (2014), pp. 313–329. DOI: 10.3978/j.issn.2223-4292.2014.06.03 (cit. on p. 66).

[158] A. Niebergall, S. Zhang, E. Kunay, G. Keydana, M. Job, M. Uecker, and J. Frahm. "Real-time MRI of speaking at a resolution of 33 ms: Undersampled radial FLASH with nonlinear inverse reconstruction." In: *Magnetic Resonance in Medicine* 69.2 (2013), pp. 477–485. DOI: 10.1002/mrm.24276 (cit. on p. 66).

[159] M. Uecker, S. Zhang, D. Voit, A. Karaus, K.-D. Merboldt, and J. Frahm. "Real-time MRI at a resolution of 20 ms." In: *NMR in biomedicine* 23.8 (2010), pp. 986–994. DOI: 10.1002/nbm.1585 (cit. on p. 66).

[160] L. G. Hanson. “Is quantum mechanics necessary for understanding magnetic resonance?” In: *Concepts in Magnetic Resonance Part A* 32A.5 (2008), pp. 329–340. DOI: 10.1002/cmr.a.20123 (cit. on pp. 66, 67).

[161] M. H. Levitt. *Spin dynamics basics of nuclear magnetic resonance*. Reprinted. Wiley, 2002 (cit. on p. 66).

[162] V. Kuperman. *Magnetic resonance imaging*. Electromagnetism. Academic Press, 2000 (cit. on p. 70).

[163] J. Modersitzki. *Fair: Flexible Algorithms for Image Registration*. USA: Society for Industrial and Applied Mathematics, 2009 (cit. on p. 74).

[164] S. Rusinkiewicz and M. Levoy. “Efficient variants of the ICP algorithm.” In: *Proceedings Third International Conference on 3-D Digital Imaging and Modeling*. Proceedings Third International Conference on 3-D Digital Imaging and Modeling. 2001, pp. 145–152. DOI: 10.1109/IM.2001.924423 (cit. on p. 83).

[165] P. J. Besl and N. D. McKay. “Method for registration of 3-D shapes.” In: *Sensor Fusion IV: Control Paradigms and Data Structures*. Sensor Fusion IV: Control Paradigms and Data Structures. Vol. 1611. International Society for Optics and Photonics, 1992, pp. 586–607. DOI: 10.1117/12.57955 (cit. on p. 83).

[166] J. W. Nichols and Y. H. Bae. “EPR: Evidence and fallacy.” In: *Journal of Controlled Release*. 30th Anniversary Special Issue 190 (2014), pp. 451–464. DOI: 10.1016/j.jconrel.2014.03.057 (cit. on p. 84).

[167] D. De Cock, S. Tu, G. J. Ughi, and T. Adriaenssens. “Development of 3D IVOCT Imaging and Co-Registration of IVOCT and Angiography in the Catheterization Laboratory.” In: *Current Cardiovascular Imaging Reports* 7.10 (2014), p. 9290. DOI: 10.1007/s12410-014-9290-0 (cit. on p. 87).

[168] L. Hebsgaard et al. “Co-registration of optical coherence tomography and X-ray angiography in percutaneous coronary intervention. the Does Optical Coherence Tomography Optimize Revascularization (DOCTOR) fusion study.” In: *International Journal of Cardiology* 182 (2015), pp. 272–278. DOI: 10.1016/j.ijcard.2014.12.088 (cit. on pp. 87, 124).

[169] L. Athanasiou, F. R. Nezami, M. Z. Galon, A. C. Lopes, P. A. Lemos, J. M. de la Torre Hernandez, E. Ben-Assa, and E. R. Edelman. “Optimized Computer-Aided Segmentation and Three-Dimensional Reconstruction Using Intracoronary Optical Coherence Tomography.” In: *IEEE Journal of Biomedical and Health Informatics* 22.4 (2018), pp. 1168–1176. DOI: 10.1109/JBHI.2017.2762520 (cit. on p. 87).

[170] M. Kunio, C. C. O'Brien, A. C. Lopes, L. Bailey, P. A. Lemos, G. J. Tearney, and E. R. Edelman. "Vessel centerline reconstruction from non-isocentric and non-orthogonal paired monoplane angiographic images." In: *The International Journal of Cardiovascular Imaging* 34.5 (2018), pp. 673–682. DOI: 10.1007/s10554-017-1275-z (cit. on pp. 87, 123).

[171] S. Latus, M. Neidhardt, M. Lutz, N. Gessert, N. Frey, and A. Schlaefer. "Quantitative Analysis of 3D Artery Volume Reconstructions Using Biplane Angiography and Intravascular OCT Imaging." In: *Annual International Conference of the IEEE Engineering in Medicine and Biology Society* 2019 (2019), pp. 6004–6007. DOI: 10.1109/EMBC.2019.8857712 (cit. on pp. 87, 124).

[172] C. V. Bourantas, M. I. Papafaklis, L. Athanasiou, F. G. Kalatzis, K. K. Naka, P. K. Siogkas, S. Takahashi, S. Saito, D. I. Fotiadis, C. L. Feldman, P. H. Stone, and L. K. Michalis. "A new methodology for accurate 3-dimensional coronary artery reconstruction using routine intravascular ultrasound and angiographic data: implications for widespread assessment of endothelial shear stress in humans." In: *EuroIntervention: Journal of EuroPCR in Collaboration with the Working Group on Interventional Cardiology of the European Society of Cardiology* 9.5 (2013), pp. 582–593. DOI: 10.4244/EIJV9I5A94 (cit. on p. 88).

[173] R. W. Katzberg and C. Haller. "Contrast-induced nephrotoxicity: clinical landscape." In: *Kidney International. Supplement* 100 (2006), S3–7. DOI: 10.1038/sj.ki.5000366 (cit. on pp. 88, 125).

[174] P. A. McCullough, R. Wolyn, L. L. Rocher, R. N. Levin, and W. W. O'Neill. "Acute renal failure after coronary intervention: incidence, risk factors, and relationship to mortality." In: *The American Journal of Medicine* 103.5 (1997), pp. 368–375 (cit. on pp. 88, 125).

[175] P. A. McCullough. "Contrast-induced acute kidney injury." In: *Journal of the American College of Cardiology* 51.15 (2008), pp. 1419–1428. DOI: 10.1016/j.jacc.2007.12.035 (cit. on p. 88).

[176] J. Fujimoto and W. Drexler. "Introduction to Optical Coherence Tomography." In: *Optical Coherence Tomography: Technology and Applications*. Ed. by W. Drexler and J. G. Fujimoto. Biological and Medical Physics, Biomedical Engineering. Berlin, Heidelberg: Springer Berlin Heidelberg, 2008, pp. 1–45. DOI: 10.1007/978-3-540-77550-8_1 (cit. on pp. 88, 92–95, 97).

[177] T. Wang, T. Pfeiffer, E. Regar, W. Wieser, H. van Beusekom, C. T. Lancee, G. Springeling, I. Krabbendam, A. F. van der Steen, R. Huber, and G. van Soest. "Heartbeat OCT: in vivo intravascular megahertz-optical coherence tomography."

In: *Biomedical Optics Express* 6.12 (2015), pp. 5021–5032. DOI: 10.1364/BOE.6.005021 (cit. on pp. 88, 90, 125).

[178] T. Pfeiffer, M. Petermann, W. Draxinger, C. Jirauschek, and R. Huber. "Ultra low noise Fourier domain mode locked laser for high quality megahertz optical coherence tomography." In: *Biomedical Optics Express* 9.9 (2018), pp. 4130–4148. DOI: 10.1364/BOE.9.004130 (cit. on p. 88).

[179] G. J. Tearney, I. .-K. Jang, and B. E. Bouma. "Imaging Coronary Atherosclerosis and Vulnerable Plaques with Optical Coherence Tomography." In: *Optical Coherence Tomography: Technology and Applications*. Ed. by W. Drexler and J. G. Fujimoto. Biological and Medical Physics, Biomedical Engineering. Berlin, Heidelberg: Springer Berlin Heidelberg, 2008, pp. 1083–1101. DOI: 10.1007/978-3-540-77550-8_34 (cit. on p. 88).

[180] T. Knopp, S. M. Conolly, and T. M. Buzug. "Recent progress in magnetic particle imaging: from hardware to preclinical applications." In: *Physics in Medicine & Biology* 62.9 (2017), E4. DOI: 10.1088/1361-6560/aa62c7 (cit. on pp. 89, 125).

[181] E. A. Neuwelt, B. E. Hamilton, C. G. Varallyay, W. R. Rooney, R. D. Edelman, P. M. Jacobs, and S. G. Watnick. "Ultrasmall superparamagnetic iron oxides (USPIOs): a future alternative magnetic resonance (MR) contrast agent for patients at risk for nephrogenic systemic fibrosis (NSF)?" In: *Kidney International* 75.5 (2009), pp. 465–474. DOI: 10.1038/ki.2008.496 (cit. on p. 89).

[182] M. Lu, M. H. Cohen, D. Rieves, and R. Pazdur. "FDA report: Ferumoxytol for intravenous iron therapy in adult patients with chronic kidney disease." In: *American Journal of Hematology* 85.5 (2010), pp. 315–319. DOI: 10.1002/ajh.21656 (cit. on p. 89).

[183] N. S. van Ditzhuijzen, A. Karanasos, N. Bruining, M. van den Heuvel, O. Sorop, J. Ligthart, K. Witberg, H. M. Garcia-Garcia, F. Zijlstra, D. J. Duncker, H. M. M. van Beusekom, and E. Regar. "The impact of Fourier-Domain optical coherence tomography catheter induced motion artefacts on quantitative measurements of a PLLA-based bioresorbable scaffold." In: *The International Journal of Cardiovascular Imaging* 30.6 (2014), pp. 1013–1026. DOI: 10.1007/s10554-014-0447-3 (cit. on p. 90).

[184] J. Ha, H. Yoo, G. J. Tearney, and B. E. Bouma. "Compensation of motion artifacts in intracoronary optical frequency domain imaging and optical coherence tomography." In: *The International Journal of Cardiovascular Imaging* 28.6 (2012), pp. 1299–1304. DOI: 10.1007/s10554-011-9953-8 (cit. on p. 90).

[185] J. Peng, L. Ma, X. Li, H. Tang, Y. Li, and S. Chen. “A Novel Synchronous Micro Motor for Intravascular Ultrasound Imaging.” In: *IEEE Transactions on Biomedical Engineering* 66.3 (2019), pp. 802–809. DOI: 10.1109/TBME.2018.2856930 (cit. on p. 90).

[186] A. F. Fercher, C. K. Hitzenberger, G. Kamp, and S. Y. El-Zaiat. “Measurement of intraocular distances by backscattering spectral interferometry.” In: *Optics Communications* 117.1 (1995), pp. 43–48. DOI: 10.1016/0030-4018(95)00119-S (cit. on p. 94).

[187] N. Nassif, B. Cense, B. H. Park, S. H. Yun, T. C. Chen, B. E. Bouma, G. J. Tearney, and J. F. d. Boer. “In vivo human retinal imaging by ultrahigh-speed spectral domain optical coherence tomography.” In: *Optics Letters* 29.5 (2004), pp. 480–482. DOI: 10.1364/OL.29.000480 (cit. on p. 94).

[188] B. Cense, N. A. Nassif, T. C. Chen, M. C. Pierce, S.-H. Yun, B. H. Park, B. E. Bouma, G. J. Tearney, and J. F. d. Boer. “Ultrahigh-resolution high-speed retinal imaging using spectral-domain optical coherence tomography.” In: *Optics Express* 12.11 (2004), pp. 2435–2447. DOI: 10.1364/OPEX.12.002435 (cit. on p. 94).

[189] M. Wojtkowski, V. J. Srinivasan, T. H. Ko, J. G. Fujimoto, A. Kowalczyk, and J. S. Duker. “Ultrahigh-resolution, high-speed, Fourier domain optical coherence tomography and methods for dispersion compensation.” In: *Optics Express* 12.11 (2004), pp. 2404–2422. DOI: 10.1364/OPEX.12.002404 (cit. on p. 94).

[190] M. I. Papafaklis et al. “Anatomically correct three-dimensional coronary artery reconstruction using frequency domain optical coherence tomographic and angiographic data: head-to-head comparison with intravascular ultrasound for endothelial shear stress assessment in humans.” In: *EuroIntervention: Journal of EuroPCR in Collaboration with the Working Group on Interventional Cardiology of the European Society of Cardiology* 11.4 (2015), pp. 407–415. DOI: 10.4244/EIJY14M06_11 (cit. on p. 103).

[191] M. M. G. d. Macedo, C. K. Takimura, P. A. Lemos, M. A. Gutierrez, M. M. G. d. Macedo, C. K. Takimura, P. A. Lemos, and M. A. Gutierrez. “A robust fully automatic lumen segmentation method for in vivo intracoronary optical coherence tomography.” In: *Research on Biomedical Engineering* 32.1 (2016), pp. 35–43. DOI: 10.1590/2446-4740.0759 (cit. on p. 103).

[192] L. S. Athanasiou, C. V. Bourantas, P. K. Siogkas, A. I. Sakellarios, T. P. Exarchos, K. K. Naka, M. I. Papafaklis, L. K. Michalis, F. Prati, and D. I. Fotiadis. “3D reconstruction of coronary arteries using frequency domain optical coherence tomography images and biplane angiography.” In: *Annual International Conference*

of the IEEE Engineering in Medicine and Biology Society 2012 (2012), pp. 2647–2650. DOI: 10.1109/EMBC.2012.6346508 (cit. on p. 104).

[193] A. Šolcová. "The Founders of the Conjugate Gradient Method." In: *Conjugate Gradient Algorithms and Finite Element Methods*. Ed. by M. Křížek, P. Neittaanmäki, S. Korotov, and R. Glowinski. Scientific Computation. Berlin, Heidelberg: Springer, 2004, pp. 3–10. DOI: 10.1007/978-3-642-18560-1_1 (cit. on p. 110).

[194] J. Yang, W. Cong, Y. Chen, J. Fan, Y. Liu, and Y. Wang. "External force back-projective composition and globally deformable optimization for 3-D coronary artery reconstruction." In: *Physics in Medicine and Biology* 59.4 (2014), pp. 975–1003. DOI: 10.1088/0031-9155/59/4/975 (cit. on p. 123).

[195] S. Ozkok and A. Ozkok. "Contrast-induced acute kidney injury: A review of practical points." In: *World Journal of Nephrology* 6.3 (2017), pp. 86–99. DOI: 10.5527/wjn.v6.i3.86 (cit. on p. 125).

[196] J. M. Wardlaw, V. Murray, E. Berge, G. del Zoppo, P. Sandercock, R. L. Lindley, and G. Cohen. "Recombinant tissue plasminogen activator for acute ischaemic stroke: an updated systematic review and meta-analysis." In: *Lancet* 379.9834 (2012), pp. 2364–2372. DOI: 10.1016/S0140-6736(12)60738-7 (cit. on p. 128).

[197] P. Deb, S. Sharma, and K. M. Hassan. "Pathophysiologic mechanisms of acute ischemic stroke: An overview with emphasis on therapeutic significance beyond thrombolysis." In: *Pathophysiology* 17.3 (2010), pp. 197–218. DOI: 10.1016/j.pathophys.2009.12.001 (cit. on p. 128).

[198] J. Krejza, M. Arkuszewski, S. E. Kasner, J. Weigele, A. Ustymowicz, R. W. Hurst, B. L. Cucchiara, and S. R. Messe. "Carotid artery diameter in men and women and the relation to body and neck size." In: *Stroke* 37.4 (2006), pp. 1103–1105. DOI: 10.1161/01.STR.0000206440.48756.f7 (cit. on pp. 128, 136, 162).

[199] M. D. Ford, N. Alperin, S. H. Lee, D. W. Holdsworth, and D. A. Steinman. "Characterization of volumetric flow rate waveforms in the normal internal carotid and vertebral arteries." In: *Physiological Measurement* 26.4 (2005), p. 477. DOI: 10.1088/0967-3334/26/4/013 (cit. on pp. 129, 136, 162).

[200] C. Zhou, E. D. Boland, P. W. Todd, and T. R. Hanley. "Magnetic particle characterization—magnetophoretic mobility and particle size." In: *Cytometry Part A* 89.6 (2016), pp. 585–593. DOI: 10.1002/cyto.a.22866 (cit. on p. 130).

[201] K. E. McCloskey, J. J. Chalmers, and M. Zborowski. “Magnetic Cell Separation: Characterization of Magnetophoretic Mobility.” In: *Analytical Chemistry* 75.24 (2003), pp. 6868–6874. DOI: 10.1021/ac034315j (cit. on p. 130).

[202] J. J. Chalmers, Y. Zhao, M. Nakamura, K. Melnik, L. Lasky, L. Moore, and M. Zborowski. “An instrument to determine the magnetophoretic mobility of labeled, biological cells and paramagnetic particles.” In: *Journal of Magnetism and Magnetic Materials* 194.1 (1999), pp. 231–241. DOI: 10.1016/S0304-8853(98)00557-5 (cit. on p. 131).

[203] G. De Las Cuevas, J. Faraudo, and J. Camacho. “Low-Gradient Magnetophoresis through Field-Induced Reversible Aggregation.” In: *The Journal of Physical Chemistry C* 112.4 (2008), pp. 945–950. DOI: 10.1021/jp0755286 (cit. on p. 131).

[204] M. Benelmekki, A. Montras, A. J. Martins, P. J. G. Coutinho, and L. M. Martinez. “Magnetophoresis behaviour at low gradient magnetic field and size control of nickel single core nanobeads.” In: *Journal of Magnetism and Magnetic Materials* 323.15 (2011), pp. 1945–1949. DOI: 10.1016/j.jmmm.2011.02.027 (cit. on p. 131).

[205] J. S. Andreu, J. Camacho, J. Faraudo, M. Benelmekki, C. Rebollo, and L. M. Martínez. “Simple analytical model for the magnetophoretic separation of superparamagnetic dispersions in a uniform magnetic gradient.” In: *Physical Review. E, Statistical, Nonlinear, and Soft Matter Physics* 84.2 (2011), p. 021402. DOI: 10.1103/PhysRevE.84.021402 (cit. on pp. 131, 132).

[206] K. Witte, K. Müller, C. Grüttner, F. Westphal, and C. Johansson. “Particle size- and concentration-dependent separation of magnetic nanoparticles.” In: *Journal of Magnetism and Magnetic Materials* 427 (2017), pp. 320–324. DOI: 10.1016/j.jmmm.2016.11.006 (cit. on p. 132).

[207] A. v. Gladiss, M. Graeser, K. Lüdtke-Buzug, and T. M. Buzug. “Contribution of brownian rotation and particle assembly polarisation to the particle response in magnetic particle spectrometry.” In: *Current Directions in Biomedical Engineering* 1.1 (2015), pp. 298–301. DOI: 10.1515/cdbme-2015-0074 (cit. on p. 165).

[208] T. Kluth, P. Szwargulski, and T. Knopp. “Towards accurate modeling of the multidimensional magnetic particle imaging physics.” In: *New Journal of Physics* 21.10 (2019), p. 103032. DOI: 10.1088/1367-2630/ab4938 (cit. on p. 166).

A. Videos

A.1. Experiment v1.*

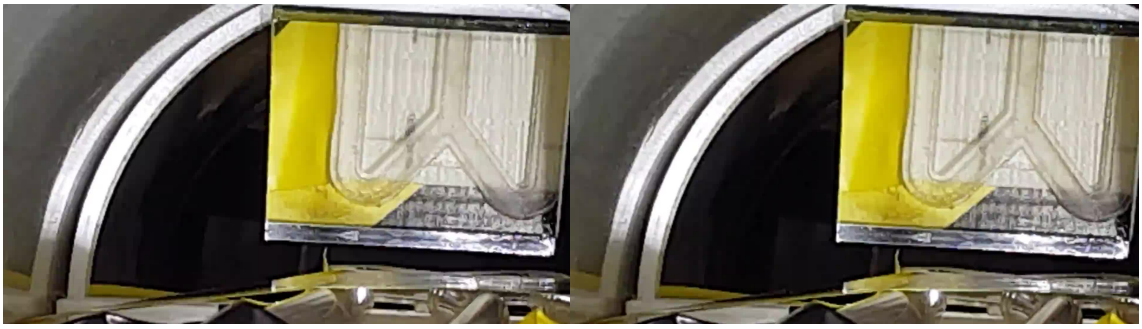

a) v1.1.0R b) v1.1.1R

Figure A.1.: a) To right branch, $F_y > 0$, no stenosis, flow velocity $2.72\,\mathrm{mL\,s^{-1}}$ b) Control: $F_y = 0$, no stenosis, flow velocity $2.72\,\mathrm{mL\,s^{-1}}$.

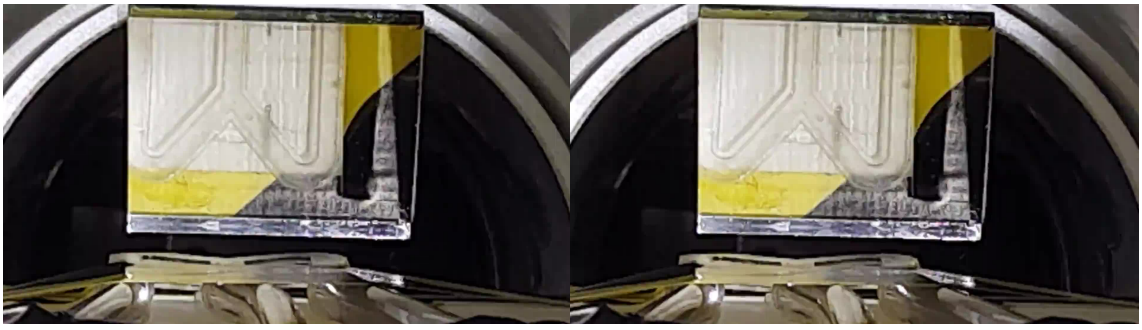

a) v1.1.0L b) v1.1.1L

Figure A.2.: a) To left branch, $F_y > 0$, no stenosis, flow velocity $2.72\,\mathrm{mL\,s^{-1}}$ b) Control: $F_y = 0$, no stenosis, flow velocity $2.72\,\mathrm{mL\,s^{-1}}$.

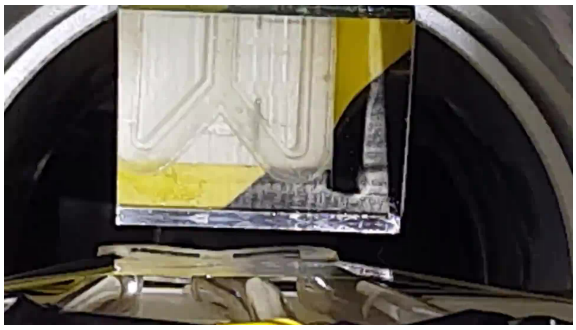

a) v1.2.0L b) v1.2.1L (broken)

Figure A.3.: a) To left branch, $F_y > 0$, no stenosis, flow velocity $5.45\,\mathrm{mL\,s^{-1}}$ b) Control: $F_y = 0$, no stenosis, flow velocity $5.45\,\mathrm{mL\,s^{-1}}$.

a) v1.3.0L b) v1.3.1L

Figure A.4.: a) To left branch, $F_y > 0$, no stenosis, flow velocity $6.87\,\mathrm{mL\,s^{-1}}$ b) Control: $F_y = 0$, no stenosis, flow velocity $6.87\,\mathrm{mL\,s^{-1}}$.

a) v1.4.0L b) v1.4.1L

Figure A.5.: a) To left branch, $F_y > 0$, no stenosis, flow velocity $8.18\,\mathrm{mL\,s^{-1}}$ b) Control: $F_y = 0$, no stenosis, flow velocity $8.18\,\mathrm{mL\,s^{-1}}$.

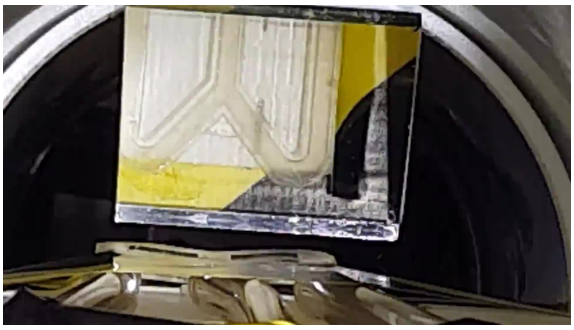

a) v1.5.0L

Figure A.6.: a) To left branch, $F_y > 0$, no stenosis, flow velocity $10.22\,\mathrm{mL\,s^{-1}}$.

A.2. Experiment v2.*

a) v2.1.0R b) v2.1.1R

Figure A.7.: a) To right branch, $F_y > 0$, 60% stenosis, flow velocity $2.72\,\mathrm{mL\,s^{-1}}$ b) Control: $F_y = 0$, 60% stenosis, flow velocity $2.72\,\mathrm{mL\,s^{-1}}$.

a) v2.2.0R b) v2.2.1R

Figure A.8.: a) To right branch, $F_y > 0$, 60% stenosis, flow velocity $5.45\,\mathrm{mL\,s^{-1}}$ b) Control: $F_y = 0$, 60% stenosis, flow velocity $5.45\,\mathrm{mL\,s^{-1}}$.

a) v2.3.0R b) v2.3.1R

Figure A.9.: a) To right branch, $F_y > 0$, 60% stenosis, flow velocity $6.87\,\mathrm{mL\,s^{-1}}$ b) Control: $F_y = 0$, 60% stenosis, flow velocity $6.87\,\mathrm{mL\,s^{-1}}$.

a) v2.4.0R b) v2.4.1R

Figure A.10.: a) To right branch, $F_y > 0$, 60% stenosis, flow velocity $8.18\,\mathrm{mL\,s^{-1}}$ b) Control: $F_y = 0$, 60% stenosis, flow velocity $8.18\,\mathrm{mL\,s^{-1}}$.

A.3. Experiment v3.*

a) v3.0.0R b) v3.1.0R

Figure A.11.: a) To right branch, $F_y > 0$, 100% stenosis, flow velocity $1.36\,\mathrm{mL\,s^{-1}}$ b) To right branch, $F_y > 0$, 100% stenosis, flow velocity $2.72\,\mathrm{mL\,s^{-1}}$.

A.4. Experiment v4.*

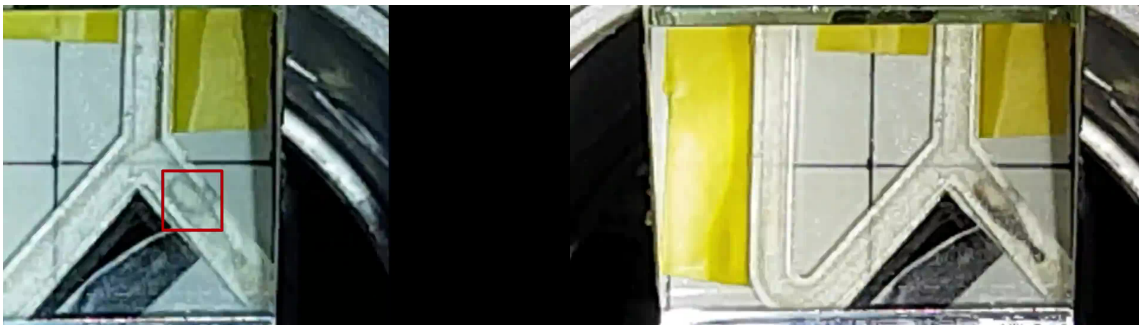

a) v4.0.0R b) v4.0.1R

Figure A.12.: a) To right branch, $F_y > 0$, 100% stenosis, flow velocity $1.36\,\mathrm{mL\,s^{-1}}$ b) Control: $F_y = 0$, 100% stenosis, flow velocity $1.36\,\mathrm{mL\,s^{-1}}$.